Karlsruher Institut für Technologie

Higher-Order QCD Corrections to *B* Meson Mixing and Decays

Zur Erlangung des akademischen Grades eines

Doktors der Naturwissenschaften
(Dr. rer. nat.)

von der KIT-Fakultät für Physik
des Karlsruher Instituts für Technologie (KIT)

genehmigte

Dissertation

von

Pascal Reeck MMath,
geboren am 27.05.1999 in Borna.

Tag der mündlichen Prüfung:	30. Januar 2026
Erstgutachter:	Prof. Dr. Matthias Steinhauser
Zweitgutachter:	Prof. Dr. Ulrich Nierste

Abstract

In this thesis, next-to-next-to-leading-order corrections to the mixing and decay of bottom-flavoured hadrons are calculated in perturbative quantum chromodynamics. For the mixing of B mesons, the absorptive part of the off-diagonal decay matrix element, Γ_{12}, is computed. The focus of the analysis of the decays is on the lifetime ratios for B^+ and B_d mesons as well as for the corresponding baryons, Ξ_b^0 and Ξ_b^-. The calculations yield matching coefficients for the $|\Delta B| = 2$ and $|\Delta B| = 0$ transition operators to leading power within the Heavy Quark Expansion. Therefore, two-loop amplitudes are computed for the transition operators while the other side of the matching involves three-loop corrections to diagrams calculated in the $|\Delta B| = 1$ effective field theory. General projectors for spinor structures of up to eleven γ matrices on two spin lines, applicable to two-point functions with four external fermions, are constructed as part of the computation. Moreover, the renormalisation procedure developed here, which preserves Fierz symmetry and deals with subtleties arising from power-suppressed corrections, is applicable to a broad range of processes.

The perturbative corrections are furthermore employed to obtain theoretical predictions of mixing observables and lifetime ratios. For B meson mixing, the most precise calculation of $\Delta\Gamma$ and a_{fs} to date for both the B_s and B_d systems are presented. Additionally, stringent constraints on the apex of the Cabibbo-Kobayashi-Maskawa unitarity triangle are obtained from the perturbative matching coefficients and measurements of a_{fs}^d and $\Delta\Gamma_d/\Delta\Gamma_s$. The relevance of Γ_{12} for Beyond Standard Model physics is further emphasised through the discussion of new physics in the chromoelectric vertex. For the lifetime ratios, the predictions of $\tau(B^+)/\tau(B_d)$ and $\tau(\Xi_b^0)/\tau(\Xi_b^-)$ are updated to next-to-next-to-leading order. The theoretical predictions agree with current measurements within the uncertainty, confirming the Standard Model and the validity of the Heavy Quark Expansion.

Zusammenfassung

In dieser Dissertation werden Korrekturen der nächst-zu-nächst-zu-führenden Ordnung in der perturbativen Quantenchromodynamik für die Mischung und die Zerfälle von Hadronen, die Bottom-Quarks beinhalten, berechnet. Für die Mischung von B-Mesonen wird der absorptive Teil des nicht-diagonalen Elements der Zerfallsmatrix, Γ_{12}, berechnet. Der Fokus der Analyse der Zerfälle liegt auf den Lebensdauerverhältnissen der B^+- und B_d-Mesonen sowie der entsprechenden Baryonen Ξ_b^0 und Ξ_b^-. Die Rechnung liefert Matching-Koeffizienten für die $|\Delta B| = 2$ und $|\Delta B| = 0$ Übergangsoperatoren der führenden Ordnung in der Heavy-Quark-Entwicklung. Hierfür werden Zweischleifenamplituden für die Übergangsoperatoren berechnet, während die andere Seite des Matchings Dreischleifenkorrekturen zu Diagrammen umfasst, die in der $|\Delta B| = 1$ Effektivfeldtheorie ausgewertet werden. Für die Berechnung werden allgemeine Projektoren für Spinorstrukturen mit bis zu elf γ-Matrizen auf zwei Spinlinien konstruiert, die für Zweipunktfunktionen mit vier externen Fermionen anwendbar sind. Darüber hinaus ist das hier entwickelte Renormierungsverfahren, welches die Fierz-Symmetrie erhält und Subtilitäten im Zusammenhang mit Massen-unterdrückten Korrekturen berücksichtigt, auch für weitere Prozesse anwendbar.

Die perturbativen Korrekturen werden ferner zur Ableitung theoretischer Vorhersagen für Mischungsobservablen und Lebensdauerverhältnisse verwendet. Für die B-Mesonmischung werden die bislang präzisesten Berechnungen von $\Delta\Gamma$ und a_{fs} sowohl für das B_s- als auch für das B_d-System dargelegt. Zudem lassen sich aus den perturbativen Matching-Koeffizienten in Kombination mit Messungen von a_{fs}^d und $\Delta\Gamma_d/\Delta\Gamma_s$ strenge Einschränkungen für die Spitze des Cabibbo-Kobayashi-Maskawa-Unitaritätsdreiecks aufstellen. Die Relevanz von Γ_{12} für Physik jenseits des Standardmodells wird außerdem anhand der Diskussion neuer Physik im chromoelektrischen Vertex hervorgehoben. Für die Lebensdauerverhältnisse werden die Vorhersagen für $\tau(B^+)/\tau(B_d)$ und $\tau(\Xi_b^0)/\tau(\Xi_b^-)$ auf die nächst-zu-nächst-zu-führende Ordnung aktualisiert. Die theoretischen Vorhersagen stimmen innerhalb der Unsicherheiten mit den aktuellen Messungen überein, was das Standardmodell und die Gültigkeit der Heavy-Quark-Entwicklung bestätigt.

Contents

1 Introduction and Motivation

In the following, a brief introduction to particle physics with a focus on B mesons is presented together with a theoretical description of the decay and mixing processes. By outlining the current status of experimental and theoretical determinations of the relevant observables and their phenomenological importance, the need for high-precision calculations is motivated. The chapter concludes with an overview of the strategy employed in this work to reduce the theoretical uncertainty.

1.1 B mesons in the Standard Model

The Standard Model (SM) of particle physics provides the best description of nature as we observe it at the smallest lengths and highest energy scales [1–3]. It offers an explanation of many physical phenomena based on so-called fundamental particles, as shown in Tab. 1.1 with the quantum numbers as given in Tab. 1.2. The quarks and leptons form the basis of all observed regular matter around us while the bosons mediate interactions between those particles. A particular focus of this thesis is the strong interaction between quarks, which is mediated by gluons. The theory describing the strong interaction is called quantum chromodynamics (QCD) in reference to the colour charge under $\mathrm{SU}(3)_C$ [4–6].

Quarks		**Leptons**	
Up (u)	Down (d)	Electron (e)	Electron neutrino (ν_e)
Charm (c)	Strange (s)	Muon (μ)	Muon neutrino (ν_μ)
Top (t)	Bottom (b)	Tau (τ)	Tau neutrino (ν_τ)
Vector Bosons			
Photon (γ)	Gluon (g)	$W^\pm$	Z^0
Scalar Boson			
Higgs (H)			

Table 1.1: The Standard Model of elementary particles, arranged by generation.

An interesting feature of the strong interaction is the formation of bound states. Since the interaction displays asymptotic freedom, i.e. particles are non-interacting in the ultraviolet (UV) limit, at low energies, quarks do not occur as free particles, and colour is not observed. Hence, the theory shows confinement in the infrared (IR) regime, and quarks are found in hadrons, mostly made up of either three or two quarks although there have been reports of higher numbers in short-lived bound states [7]. Those particles consisting of three quarks are called baryons, which include protons and neutrons, while combinations of a quark and anti-quark are called mesons. Since quarks are in the fundamental **3** representation of

Name	**Label**	$\mathbf{SU(3)_C}$, $\mathbf{SU(2)_L}$, $\mathbf{U(1)_Y}$	**Spin**
Quarks	$Q_L^i = \begin{pmatrix} u_L^i \\ d_L^i \end{pmatrix}$	$(\mathbf{3}, \mathbf{2}, +\frac{1}{6})$	$\frac{1}{2}$
	u_R^i	$(\bar{\mathbf{3}}, \mathbf{1}, \frac{2}{3})$	$\frac{1}{2}$
	d_R^i	$(\bar{\mathbf{3}}, \mathbf{1}, -\frac{1}{3})$	$\frac{1}{2}$
Leptons	$L_L^i = \begin{pmatrix} \nu_L^i \\ e_L^i \end{pmatrix}$	$(\mathbf{1}, \mathbf{2}, -\frac{1}{2})$	$\frac{1}{2}$
	e_R^i	$(\mathbf{1}, \mathbf{1}, -1)$	$\frac{1}{2}$
	ν_R^{i*}	$(\mathbf{1}, \mathbf{1}, 0)$	$\frac{1}{2}$
Higgs	H	$(\mathbf{1}, \mathbf{2}, +\frac{1}{2})$	0
Gluons	g_α	$(\mathbf{8}, \mathbf{1}, 0)$	1
W/Z-Bosons	$W^\pm$, Z^0	$(\mathbf{1}, \mathbf{3}, 0)$	1
Photon	γ	$(\mathbf{1}, \mathbf{1}, 0)$	1

Table 1.2: Quantum numbers of Standard Model fields under the gauge group $SU(3)_C \times SU(2)_L \times U(1)_Y$. Note that the label i enumerates the three generations of quarks and leptons.

$SU(3)_C$, a quark-antiquark pair can be either in the octet or singlet representation,

$$\mathbf{3} \otimes \bar{\mathbf{3}} = \mathbf{8} \oplus \mathbf{1}\,. \tag{1.1}$$

The interaction potential as calculated from the scattering amplitude of a quark-antiquark pair reveals that the potential for the singlet state is attractive whereas it is repulsive for the octet state. Similarly, a triplet of quarks is can be decomposed as

$$\mathbf{3} \otimes \mathbf{3} \otimes \mathbf{3} = \mathbf{10} \oplus \mathbf{8} \oplus \mathbf{8} \oplus \mathbf{1}\,, \tag{1.2}$$

and again only the singlet state has an attractive potential. This is consistent with the observation that the colourless singlet states are bound states.

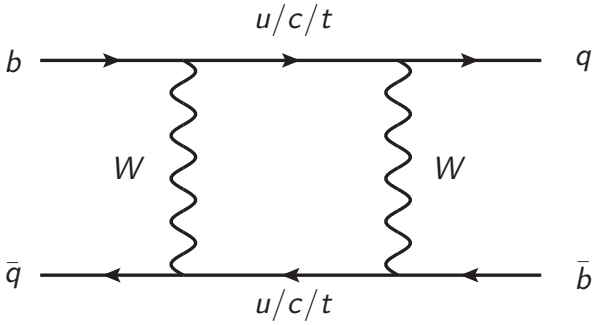

Figure 1.1: Leading-order B meson mixing from a box diagram. Note that the down-type quark q can be either d or s.

In this thesis, we consider the phenomenology of B_q and B^+ mesons. These have the quark content $(\bar{b}q)$, where q can stand for either d (down) or s (strange) quarks, and $(\bar{b}u)$ respectively. All B mesons contain one $\bar{b}$ anti-quark. The bottom quark was first discovered in 1977 at Fermilab by the E288 experiment [8], and since then flavour physics involving bottom quarks has been a focus of many particle detectors, including CDF at the Tevatron, BaBar, Belle I and II, and LHCb [9–12]. The phenomenology of the neutral B mesons is mostly characterised by the mixing between the meson and its corresponding antiparticle, which was experimentally confirmed for the B_s system by CDF at Fermilab in 2006 [13].

The contribution of this thesis is to improve the predictions of B meson mixing and decays, and to enable stronger conclusions to be drawn from experimental measurements of the mixing and decay properties. For B meson mixing, the focus is on the absorptive part, i.e. on the width difference $\Delta\Gamma$ and the flavour-specific CP asymmetry a_{fs} while for the decays the lifetime ratios are considered.

1.2 Particle-antiparticle mixing in B meson systems

In the Standard Model, B mesons oscillate between the particle and antiparticle state because W boson exchanges allow for transitions which change the number of bottom quarks by two. In the following, B mesons with a generic down-type quark will be discussed. The Feynman diagram in Fig. 1.1 shows a leading-order contribution to B meson mixing. That this type of diagram leads to a mixing between particle and antiparticle states can be seen from the self-energy matrix Σ, which is related to the scattering matrix $\mathcal{S}$ in the Wigner-Weisskopf approximation [14, 15] through

$$-i\,(2\pi)^4\,\delta^{(4)}(p_i - p_j)\,\Sigma_{ij} = \frac{1}{2M_B}\langle B_i|\mathcal{S}|B_j\rangle\,, \tag{1.3}$$

where M_B is the mass of the B meson and $|B_i\rangle$, $|B_j\rangle$ denotes either a B meson or $\bar{B}$ anti-meson state with the four-momentum p_i, p_j [16]. Using time-dependent perturbation theory in quantum field theory (QFT), the time evolution of the two-state system is given by

$$i\,\frac{\mathrm{d}}{\mathrm{d}t}\begin{pmatrix}|B(t)\rangle\\|\bar{B}(t)\rangle\end{pmatrix} = \Sigma\begin{pmatrix}|B(t)\rangle\\|\bar{B}(t)\rangle\end{pmatrix}\,, \tag{1.4}$$

where natural units $\hbar = 1$ are used.

Inspecting the self-energy matrix more closely, we can observe how the states mix into each other and how physical observables are related to the scattering matrix. The self-energy matrix is commonly parametrised as

$$\Sigma = M - i\,\frac{\Gamma}{2}\,, \tag{1.5}$$

where M is called the mass matrix and Γ the decay matrix. Both matrices are taken to be Hermitian, and their diagonal elements are identical due to charge-parity-time reversal (CPT) invariance. Hence, this parametrisation offers a unique decomposition of the Hermitian self-energy matrix,

$$\Sigma = \begin{pmatrix} M_{11} - i\,\dfrac{\Gamma_{11}}{2} & M_{12} - i\,\dfrac{\Gamma_{12}}{2} \\[2ex] M_{12}^* - i\,\dfrac{\Gamma_{12}^*}{2} & M_{11} - i\,\dfrac{\Gamma_{11}}{2} \end{pmatrix}\,. \tag{1.6}$$

From a practical standpoint, the off-diagonal elements of the mass and decay matrix are obtained from the dispersive and absorptive part of the self-energy, i.e.

$$\begin{aligned} M_{12} &= (\Sigma_{12} + \Sigma_{21}^*)/2 \equiv \mathrm{Disp}\,(\Sigma_{12})\,, \\ \Gamma_{12} &= i\,(\Sigma_{12} - \Sigma_{21}^*) \quad \equiv -2\,\mathrm{Abs}\,(\Sigma_{12})\,. \end{aligned} \tag{1.7}$$

Since Σ has non-zero off-diagonal elements, the time evolution in Eq. (1.4) mixes the flavour eigenstates. In other words, diagonalising the self-energy matrix leads to the mass eigenstates

$$|B_{\mathrm{L,H}}\rangle = p|B\rangle \pm q|\bar{B}\rangle\,, \tag{1.8}$$

which are linear combinations of the flavour eigenstates. The subscripts L, H denote the light and heavy states with the eigenvalues

$$E_{\mathrm{L,H}} = M_{\mathrm{L,H}} - i\,\frac{\Gamma_{\mathrm{L,H}}}{2}\,, \tag{1.9}$$

where $M_{\mathrm{L,H}}$ and $\Gamma_{\mathrm{L,H}}$ are respectively the mass and decay width of the light and heavy states. The mass and decay width differences are defined as

$$\Delta M \equiv M_{\mathrm{H}} - M_{\mathrm{L}}\,, \qquad\qquad \Delta\Gamma \equiv \Gamma_{\mathrm{L}} - \Gamma_{\mathrm{H}}\,. \tag{1.10}$$

Defining the charge-parity (CP) violating phase

$$\phi \equiv \arg\left(-\frac{\Gamma_{12}}{M_{12}}\right), \tag{1.11}$$

and neglecting corrections of order $|\Gamma_{12}/M_{12}|^2 \sim 10^{-5}$, the mass and width differences can be written as

$$\Delta M = 2|M_{12}|, \qquad \Delta\Gamma = 2|\Gamma_{12}|\cos\phi, \tag{1.12}$$

and hence their ratio is

$$\frac{\Delta\Gamma}{\Delta M} = -\,\mathrm{Re}\,\frac{\Gamma_{12}}{M_{12}}. \tag{1.13}$$

Additionally, up to linear order in $\mathrm{Im}\,(\Gamma_{12}/M_{12}) \lesssim 10^{-3}$, the flavour-specific CP asymmetry a_{fs} is given by

$$a_{\mathrm{fs}} = \mathrm{Im}\,\frac{\Gamma_{12}}{M_{12}}. \tag{1.14}$$

It is instructive to see how the observables derived above appear in measurements. The self-energy matrix from Eq. (1.6) can be diagonalised with the eigenvectors (p, q) and $(p, -q)$, i.e.

$$Q^{-1}\Sigma Q = \begin{pmatrix} M_L - i\frac{\Gamma_L}{2} & 0 \\ 0 & M_H - i\frac{\Gamma_H}{2} \end{pmatrix}, \tag{1.15}$$

where

$$Q = \begin{pmatrix} p & q \\ q & -p \end{pmatrix}. \tag{1.16}$$

Note that a_{fs} is defined in terms of p and q as [17]

$$a_{\mathrm{fs}} \equiv 1 - \left|\frac{q}{p}\right|^2, \tag{1.17}$$

which leads to Eq. (1.14).

The time evolution in the flavour basis is solved as

$$\begin{pmatrix} |B(t)\rangle \\ |\bar{B}(t)\rangle \end{pmatrix} = Q \begin{pmatrix} M_L - i\frac{\Gamma_L}{2} & 0 \\ 0 & M_H - i\frac{\Gamma_H}{2} \end{pmatrix} Q^{-1} \begin{pmatrix} |B\rangle \\ |\bar{B}\rangle \end{pmatrix}, \tag{1.18}$$

and the matrix can be expressed as

$$Q \begin{pmatrix} M_L - i\frac{\Gamma_L}{2} & 0 \\ 0 & M_H - i\frac{\Gamma_H}{2} \end{pmatrix} Q^{-1} = \begin{pmatrix} g_+(t) & \frac{q}{p}g_-(t) \\ \frac{p}{q}g_-(t) & g_+(t) \end{pmatrix}, \tag{1.19}$$

where the quantities $g_\pm(t)$ encode the oscillations,

$$g_+(t) = e^{-iMt}e^{-\Gamma t/2}\left(\cosh\frac{\Delta\Gamma t}{4}\cos\frac{\Delta M t}{2} - i\sinh\frac{\Delta\Gamma t}{4}\sin\frac{\Delta M t}{2}\right),$$
$$g_-(t) = e^{-iMt}e^{-\Gamma t/2}\left(-\sinh\frac{\Delta\Gamma t}{4}\cos\frac{\Delta M t}{2} + i\cosh\frac{\Delta\Gamma t}{4}\sin\frac{\Delta M t}{2}\right), \tag{1.20}$$

and the shorthand notation $\Gamma = \Gamma_{11}$ and $M = M_{11}$ was used. If we start in a pure state $|B\rangle$ at time $t = 0$, the state oscillates, and the probability of observing either a particle or antiparticle is proportional to

$$|g_\pm(t)|^2 = \frac{e^{-\Gamma t}}{2}\left[\cosh\left(\frac{\Delta\Gamma t}{2}\right) \pm \cos(\Delta M t)\right]. \tag{1.21}$$

Meanwhile, the flavour-specific CP asymmetry can be measured in the decays of B mesons to final states f and their respective antiparticle states [16, 18],

$$a_{CP}^{\text{dir}} + a_{\text{fs}} = \frac{\Gamma(\bar{B}(t)\to f) - \Gamma(B(t)\to \bar{f})}{\Gamma(\bar{B}(t)\to f) + \Gamma(B(t)\to \bar{f})}, \tag{1.22}$$

where the direct CP asymmetry

$$a_{CP}^{\text{dir}} = \frac{\Gamma(B\to f) - \Gamma(\bar{B}\to \bar{f})}{\Gamma(B\to f) + \Gamma(\bar{B}\to \bar{f})} \tag{1.23}$$

was introduced. For a derivation of the individual decay widths, see e.g. Ref. [17]. Note that flavour-specific decays are such processes where $B \to f$ is allowed while $\bar{B} \to f$ and $B \to \bar{f}$ are not. However, it is not necessary to tag the initial states to measure a_{fs}. Defining the untagged decay width

$$\Gamma[f, t] \equiv \Gamma(\bar{B}(t)\to f) + \Gamma(B(t)\to f), \tag{1.24}$$

the untagged CP asymmetry is further defined as

$$a_{\text{fs, untagged}} \equiv \frac{\Gamma[f,t] - \Gamma[\bar{f},t]}{\Gamma[f,t] + \Gamma[\bar{f},t]}. \tag{1.25}$$

This quantity can be expressed in terms of the previously defined CP asymmetries [16],

$$a_{\text{fs, untagged}} = a_{CP}^{\text{dir}} + \frac{a_{\text{fs}}}{2}\left(1 - (a_{CP}^{\text{dir}})^2\right)\left(1 - \frac{\cos(\Delta M t)}{\cosh(\Delta\Gamma t/2)}\right). \tag{1.26}$$

This is useful for experimental measurements because the need to tag the initial states is eliminated, making the measurement of the CP asymmetry more tractable. In the measurement of $a_{\text{fs, untagged}}$, the time dependence does not cancel, in contrast with Eq. (1.22). The tagging of initial states can therefore be traded with the need to measure

the time dependence of the decays. With the full time dependence, it becomes possible to distinguish a_{fs} from a_{CP}^{dir} and detector asymmetries [19].

To illustrate the discussion above, we highlight potential measurements of a_{fs}. The traditional way of measuring the flavour-specific CP asymmetry is to investigate semileptonic decays with $f = X\ell^+\nu_\ell$ and $\bar{f} = \bar{X}\ell^-\bar{\nu}_\ell$. However, other decay channels like $B_d \to J/\psi K^+\pi^-$, $B_d \to D_s^+ D^-$, $B_d \to D^- K^+$ and many more can be included in the analysis to increase the statistics. It is worth noting that the semileptonic decays have the advantage that the direct CP asymmetry a_{CP}^{dir} vanishes for those decays. This is not the case for example in the decay channels $B_d \to J/\psi K^+\pi^-$ and $B_d \to D_s^+ D^-$ [20].

The B meson mixing observables are sensitive to the Cabibbo-Kobayashi-Maskawa (CKM) matrix V, which encodes the differences in the weak interaction when it comes to coupling different flavours of quarks [21, 22]. The CKM matrix is unitary, so there exist six unitarity triangles, which can be written as

$$\begin{aligned} V_{ui}^* V_{uj} + V_{ci}^* V_{cj} + V_{ti}^* V_{tj} &= 0\,, \\ V_{kd}^* V_{ld} + V_{ks}^* V_{ls} + V_{kb}^* V_{lb} &= 0\,, \end{aligned} \tag{1.27}$$

where $i, j \in \{u, c, t\}$ are up-type quarks while $k, l \in \{d, s, b\}$ are down-type quarks. It will be convenient to introduce the notation

$$\lambda_i^q \equiv V_{iq}^* V_{ib}\,, \tag{1.28}$$

where q is either d or s. When q is not specified, the superscript is not show. The CKM coefficients from Eq. (1.28) appear in both M_{12} and Γ_{12}. This can be seen from considering the off-diagonal part of the self-energy matrix, which is obtained from box diagrams like the one shown in Fig. 1.1 and QCD corrections to it. The CP-violating CKM matrix elements factor out of the amplitudes

$$\begin{aligned} \mathcal{M}(\bar{B} \to B) &= -\sum_{i,j} \lambda_i \lambda_j \, \mathcal{M}^{ij}(\bar{B} \to B)\,, \\ \mathcal{M}(B \to \bar{B}) &= -\sum_{i,j} \lambda_i^* \lambda_j^* \, \mathcal{M}^{ij}(B \to \bar{B})\,, \end{aligned} \tag{1.29}$$

where we have introduced the amplitude $\mathcal{M}$ in the parametrisation of the scattering matrix from Eq. (1.3),

$$\langle B_i | \mathcal{S} | B_j \rangle = i\,(2\pi)^4\, \delta^{(4)}(p_i - p_j)\, \mathcal{M}\,. \tag{1.30}$$

Since QCD obeys CP invariance, the factorised amplitude $\mathcal{M}^{ij}$ in Eq. (1.29) must be CP-invariant. This implies that

$$\mathcal{M}^{ij}(\bar{B} \to B) = \mathcal{M}^{ij}(B \to \bar{B}) \equiv \mathcal{M}^{ij}\,. \tag{1.31}$$

The CKM elements can hence be factored out from M_{12} and Γ_{12}. Note that while for M_{12} all three up-type quarks can appear in the internal loop, Γ_{12} only obtains contributions

from u and c. This is because the imaginary part of a diagram is given by the sum of all cuts which allow physical on-shell states [23]. Since the top quark is heavier than the external bottom quark, there are no allowed cuts and the imaginary part of those diagrams vanishes. Therefore, we have

$$M_{12} = \lambda_t^2 M_{12}^{tt} + 2\lambda_t\lambda_c M_{12}^{tc} + 2\lambda_t\lambda_u M_{12}^{tu} + \lambda_c^2 M_{12}^{cc} + 2\lambda_u\lambda_c M_{12}^{uc} + \lambda_u^2 M_{12}^{uu}\,, \quad (1.32)$$

and using the unitarity triangle Eq. (1.27) to remove λ_u,

$$\begin{aligned} M_{12} = {} & \lambda_t^2(M_{12}^{tt} - 2M_{12}^{ut} + M_{12}^{uu}) \\ & + 2\lambda_c\lambda_t(M_{12}^{uu} - M_{12}^{uc} - M_{12}^{ut} + M_{12}^{ct}) \\ & + \lambda_c^2(M_{12}^{uu} - 2M_{12}^{uc} + M_{12}^{cc})\,. \end{aligned} \quad (1.33)$$

If all quarks had the same mass, all terms M_{12}^{ij} would be identical, and the expression would vanish. This is an example of the Glashow-Iliopoulos-Maiani (GIM) mechanism [24]. Since the top quark is much heavier than the up and charm quarks, the leading contribution to M_{12} stems from the λ_t^2 term. Meanwhile for Γ_{12} the factorisation is

$$\Gamma_{12} = -\left(\lambda_c^2\,\Gamma_{12}^{cc} + 2\lambda_u\lambda_c\,\Gamma_{12}^{uc} + \lambda_u^2\,\Gamma_{12}^{uu}\right)\,. \quad (1.34)$$

Since the CKM elements have been factored out in Eqs. (1.29), (1.32) and (1.34), we can obtain simple expressions for the individual CKM contributions,

$$\begin{aligned} M_{12}^{ij} &= \frac{1}{4M_B}\left(\mathcal{M}^{ij} + \mathcal{M}^{ij,*}\right) = \frac{1}{2M_B}\mathrm{Re}\left(\mathcal{M}^{ij}\right)\,, \\ \Gamma_{12}^{ij} &= -\frac{i}{2M_B}\left(\mathcal{M}^{ij} - \mathcal{M}^{ij,*}\right) = \frac{1}{M_B}\mathrm{Im}\left(\mathcal{M}^{ij}\right)\,. \end{aligned} \quad (1.35)$$

1.3 Decays of B mesons

Lifetimes of B mesons are interesting to study because the Standard Model enables predictions of differences in lifetimes, or equivalently their ratios, to a very high precision. The inverse of the lifetime, the total decay width Γ of B mesons is given by the diagonal part Γ_{11} of the self-energy as defined in Eq. (1.6). It is clear that this is indeed the decay width from the exponential in Eq. (1.21), but we can also derive this from the optical theorem.

The optical theorem in the general case can be derived from the unitarity of the scattering matrix,

$$\mathcal{S}^\dagger\mathcal{S} = \mathbb{1} \quad \Longleftrightarrow \quad i\left(T^\dagger - T\right) = T^\dagger T\,, \quad (1.36)$$

where the transfer matrix T is defined by $\mathcal{S} = \mathbb{1} + iT$. Evaluating $i(T^\dagger - T)$ between initial and final states, $|a\rangle$ and $|b\rangle$ respectively, yields

$$\langle b|i\left(T^\dagger - T\right)|a\rangle = i(2\pi)^4\delta^{(4)}(p_a - p_b)\left(\mathcal{M}^*(b\to a) - \mathcal{M}(a\to b)\right)\,. \quad (1.37)$$

We can use the completeness relation for multi-particle states $|X\rangle$ to evaluate the other side of Eq. (1.36),

$$\begin{aligned}\langle b|\,T^\dagger\,T|a\rangle &= \sum_X \int \mathrm{d}P_X \langle b|\,T^\dagger|X\rangle\langle X|\,T|a\rangle \\ &= \sum_X (2\pi)^4\delta^{(4)}(p_b - p_X)(2\pi)^4\delta^{(4)}(p_a - p_X)\int \mathrm{d}P_X \mathcal{M}(a\to X)\mathcal{M}^*(b\to X)\,,\end{aligned} \tag{1.38}$$

where the relativistically normalised integral measure is given by

$$\mathrm{d}P_X = \prod_{j\in X}\frac{\mathrm{d}^3 p_j}{(2\pi)^3}\frac{1}{2E_j}\,. \tag{1.39}$$

The unitarity condition Eq. (1.36) hence yields the generalised optical theorem

$$\mathcal{M}(a\to b) - \mathcal{M}^*(b\to a) = i\sum_X (2\pi)^4\delta^{(4)}(p_a - p_X)\int \mathrm{d}P_X \mathcal{M}(a\to X)\mathcal{M}^*(b\to X)\,, \tag{1.40}$$

which has the special case $|a\rangle = |b\rangle = |B\rangle$:

$$\mathrm{Im}\Big(\mathcal{M}(B\to B)\Big) = M_B\,\Gamma\,. \tag{1.41}$$

This also allows us to view Eq. (1.3) as a generalisation of the optical theorem.

Lifetime ratios are especially attractive from a theoretical standpoint because the leading term drops out of such ratios when using the Heavy Quark Expansion (HQE), which is to be discussed in Section 2.5. In this thesis, the lifetime ratios

$$\frac{\tau(B^+)}{\tau(B_d)} \qquad \text{and} \qquad \frac{\tau(\Xi_b^0)}{\tau(\Xi_b^-)} \tag{1.42}$$

are considered, where the baryons have the quark contents $\Xi_b^0 \sim (bus)$ and $\Xi_b^- \sim (bds)$.

1.4 The need for precision physics

1.4.1 Current status of B meson mixing

The B_s and B_d meson systems have been studied in detail experimentally, and the current status with regards to the mixing parameters in the B_s system is as follows:

$$\Delta M_s^{\mathrm{exp}} = (17.7656 \pm 0.0057)\,\mathrm{ps}^{-1}\,, \qquad [25] \tag{1.43}$$

$$\Delta\Gamma_s^{\mathrm{exp}} = (0.0781 \pm 0.0035)\,\mathrm{ps}^{-1}\,, \qquad [26] \tag{1.44}$$

$$a_{\mathrm{fs}}^{s,\mathrm{exp}} = (-60 \pm 280)\times 10^{-5}\,, \qquad [26] \tag{1.45}$$

while for the B_d system, the most recent experimental measurements are:

$$\Delta M_d^{\text{exp}} = (0.5065 \pm 0.0019)\,\text{ps}^{-1}\,, \quad [26] \tag{1.46}$$
$$\Delta \Gamma_d^{\text{exp}} = (0.7 \pm 6.6) \times 10^{-3}\,\text{ps}^{-1}\,, \quad [26] \tag{1.47}$$
$$a_{\text{fs}}^{d,\text{exp}} = (-21 \pm 17) \times 10^{-4}\,. \quad [26] \tag{1.48}$$

These value can be confronted with theoretical predictions that this thesis aims to update, specifically for the B_s system:

$$\Delta M_s^{\text{theo}} = (18.23 \pm 0.63)\,\text{ps}^{-1}\,, \quad [27] \tag{1.49}$$
$$\Delta \Gamma_s^{\text{theo}} = (0.076 \pm 0.017)\,\text{ps}^{-1}\,, \quad [28] \tag{1.50}$$
$$a_{\text{fs}}^{s,\text{theo}} = (2.19 \pm 0.14) \times 10^{-5}\,, \quad [29] \tag{1.51}$$

and for the B_d system:

$$\Delta M_d^{\text{theo}} = (0.535 \pm 0.021)\,\text{ps}^{-1}\,, \quad [27] \tag{1.52}$$
$$\Delta \Gamma_d^{\text{theo}} = (2.16 \pm 0.47) \times 10^{-3}\,\text{ps}^{-1}\,, \quad [29] \tag{1.53}$$
$$a_{\text{fs}}^{d,\text{theo}} = (-5.04 \pm 0.33) \times 10^{-4}\,. \quad [29] \tag{1.54}$$

From these values and referring to Fig. 1.2, we can observe that the largest theoretical uncertainty in relative terms persists in $\Delta\Gamma$, followed by a_{fs}. Moreover, there is a large discrepancy in the central values for $\Delta\Gamma_d$, and historical data from experiments showed a greater deviation from the predicted value for $\Delta\Gamma_s$ too, see Ref. [30]. The central values for a_{fs} agree within the experimental uncertainty, which is, however, much larger than the theoretical prediction. The most accurately determined quantity with the best agreement is ΔM. It should be noted that $\Delta\Gamma$ presents an opportunity to reduce a large theoretical uncertainty to clear up a potential tension with the experiment. Moreover, new physics models involving B mesons for baryogenesis and dark matter can be probed via Γ_{12} [31].

1.4.2 Current status of B and Ξ_b lifetime ratios

The current experimental data related to the lifetimes and their ratios are

$$\left(\frac{\tau(B^+)}{\tau(B_d)}\right)^{\text{exp}} = 1.076 \pm 0.004\,, \quad [26] \tag{1.55}$$
$$\left(\frac{\tau(\Xi_b^0)}{\tau(\Xi_b^-)}\right)^{\text{exp}} = 0.936 \pm 0.022\,, \quad [26] \tag{1.56}$$
$$\left(\tau(B^+)\right)^{\text{exp}} = (1.638 \pm 0.004)\,\text{ps}\,, \quad [26] \tag{1.57}$$
$$\left(\tau(\Xi_b^0)\right)^{\text{exp}} = (1.477 \pm 0.032)\,\text{ps}\,. \quad [26] \tag{1.58}$$

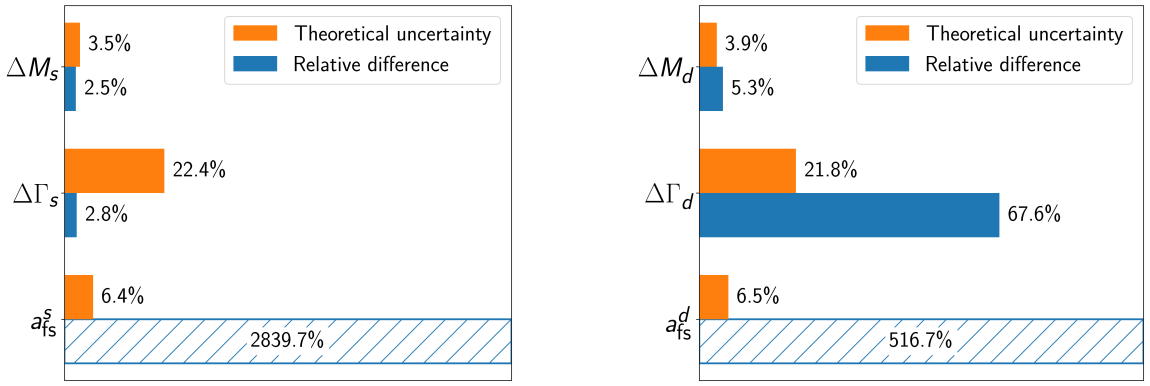

(a) B_s system (b) B_d system

Figure 1.2: Relative differences between theory and experiment and theoretical uncertainties for B_s and B_d observables. Note that the relative differences are calculated with respect to the theoretical predictions. The hatched bars extend beyond the area of the plot and are not to scale.

The most recent theoretical predictions of the lifetime ratios in the HQE are

$$\left(\frac{\tau(B^+)}{\tau(B_d)}\right)^{\text{theo}} = 1.086 \pm 0.022\,, \qquad [32] \tag{1.59}$$

$$\left(\frac{\tau(\Xi_b^0)}{\tau(\Xi_b^-)}\right)^{\text{theo}} = 0.929 \pm 0.028\,. \qquad [33] \tag{1.60}$$

Confronting theory with experiment, we see that the uncertainty of the B meson lifetime ratio is more than five times as large on the theoretical prediction, motivating a more precise determination in this thesis.

1.4.3 Phenomenological importance of the observables

An accurate determination of $\Delta\Gamma$ and $a_{\rm fs}$ has a different relevance for the B_s and B_d systems. Considering the B_s system first, the ratio $\Delta\Gamma_s/\Delta M_s$ is almost independent of any CKM parameters, including $|V_{cb}|$. This can be seen from Eqs. (1.32) and (1.34) since λ_t^s cancels in the ratio Γ_{12}/M_{12} and the ratio $|\lambda_u^s/\lambda_t^s| \simeq 0.02$ is small. As $\Delta\Gamma_s/\Delta M_s$ is well-measured experimentally, a comparison of theory and experiment serves as a probe of SM parameters [28]. On the other hand, $a_{\rm fs}^s$ is tiny in the SM, but Beyond Standard Model (BSM) physics can increase the CP asymmetry by two orders of magnitude [34]. Therefore, a precise parametrisation of $a_{\rm fs}^s$ in terms of effective operators will allow for a more precise implementation of BSM theories too.

Given the experimental status and the different CKM elements involved, the B_d system can be studied to provide constraints on the CKM unitarity triangle. In particular, we can

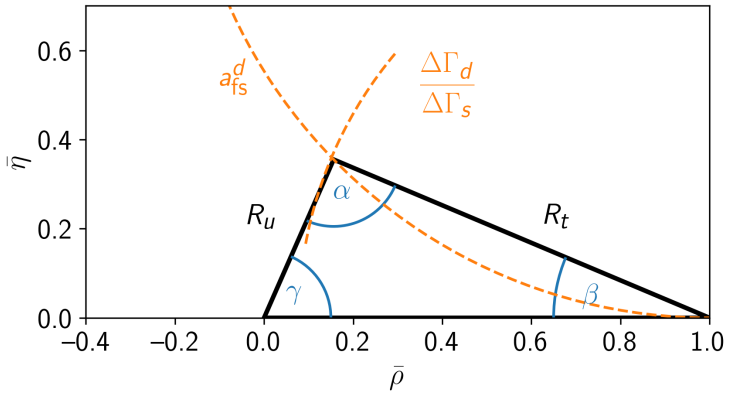

Figure 1.3: The CKM unitarity triangle probed by B_d mixing. The triangle shown represents the current global average [35]. The constraints in orange are curves on which the apex of the CKM triangle would need to lie for hypothetical measurements of a_{fs}^d and $\Delta\Gamma_d/\Delta M_d$.

obtain constraints on the CKM unitarity triangle involving λ_u^d, λ_c^d and λ_t^d from future measurements of a_{fs} and $\Delta\Gamma_d$. The corresponding triangle is show in Fig. 1.3. Following the notation of Ref. [36], we introduce the parametrisation

$$\frac{\Gamma_{12}}{M_{12}} \equiv \left[a\,\frac{\lambda_u}{\lambda_t} + b\,\frac{\lambda_u^2}{\lambda_t^2} + c\right] \times 10^{-4}\,, \tag{1.61}$$

such that the flavour-specific CP asymmetry can be written as

$$a_{\mathrm{fs}}^d = \left[a\,\mathrm{Im}\frac{\lambda_u^d}{\lambda_t^d} + b\,\mathrm{Im}\frac{(\lambda_u^d)^2}{(\lambda_t^d)^2}\right] \times 10^{-4}\,, \tag{1.62}$$

and a measurement of a_{fs}^d can be used to constrain the apex of the CKM triangle, see Section 4.6. An additional constraint can be constructed from the ratio $\Delta\Gamma_d/\Delta\Gamma_s$, which can be parametrised using Eq. (1.61) as

$$\frac{\Delta\Gamma_d}{\Delta\Gamma_s} = \left|\frac{\lambda_t^d}{\lambda_t^s}\right|^2 \frac{1 + \frac{a}{c}\mathrm{Re}\frac{\lambda_u^d}{\lambda_t^d} + \frac{b}{c}\mathrm{Re}\frac{(\lambda_u^d)^2}{(\lambda_t^d)^2}}{1 + \frac{a}{c}\mathrm{Re}\frac{\lambda_u^s}{\lambda_t^s} + \frac{b}{c}\mathrm{Re}\frac{(\lambda_u^s)^2}{(\lambda_t^s)^2}}\,. \tag{1.63}$$

Measurements of $\Delta\Gamma_d$ and $\Delta\Gamma_s$ can hence be used to yield another constraint on the CKM triangle, which is also shown in detail in Section 4.6. Since the two constraints are almost orthogonal to each other, the apex of the CKM triangle can be determined with high precision from B meson mixing observables alone. This serves as an excellent test of the Standard Model.

The inclusion of penguin operators in particular in the calculation of Γ_{12} is important for constraining certain types of BSM models. Such models could introduce an additional

contribution to e.g. C_4, see Section 2.2, but only couple b and $q = d, s$ quarks to down-type quarks. The new physics effects would not impact M_{12} significantly, which is dominated by the top quark loops; however, they contribute to Γ_{12}. The largest contribution would be expected from the interference with the SM matching coefficient C_2. There would be no leading order contribution as the one-particle reducible diagram vanishes, so the leading effect comes from NLO diagrams like the one shown in Fig. 1.4 as the interference with a penguin operator at LO will be smaller than the NLO diagram with a current-current operator due to the smaller Wilson coefficient of SM penguins. To improve the accuracy of constraints on such BSM theories, it is hence desirable to calculate the first correction to this contribution too, i.e. to calculate current-current penguin diagrams at NNLO.

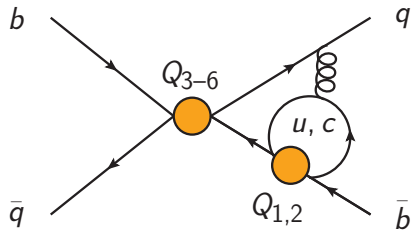

Figure 1.4: Leading effect from a BSM contribution to a penguin operator Q_{3-6} that only couples to down-type quarks.

A cornerstone of the B meson mixing calculations is the HQE, so it is important to independently verify the validity of this operator product expansion. This can be done through the comparison of experiment and theory for the lifetime ratios. The lifetime ratios offer a clean way of probing the validity of the HQE since any BSM effects are expected to be of the per mille level in the lifetime ratios [27, 32]. The main criticism of the HQE, which should be addressed with precise calculations of the lifetime ratios, is the possibility of the violation of quark-hadron duality (QHD) as proposed in Refs. [37–39]. As proving QHD in general is very difficult, additional evidence from lifetime ratios is a valuable contribution to our understanding of QCD.

1.5 Reducing the theoretical uncertainty on B meson observables

1.5.1 Overview of theoretical determinations of B meson mixing

Calculations of B meson observables consist of a non-perturbative and a perturbative part, connecting the high- and low-energy regimes. While the non-perturbative calculations are usually done using QCD sum rules or lattice QCD, perturbative calculations proceed via an asymptotic expansion in the coupling parameter, amounting to the evaluation of

increasingly complicated Feynman diagrams. Our focus lies on the perturbative part of the calculations, which are discussed in the following. The non-perturbative counterparts are described for example in Refs. [40–46]. For more details on the perturbative part and how perturbative and non-perturbative results are combined to yield physical results, see Chapter 2.

Previous calculations of B meson mixing observables have included various contributions of the weak interaction to at most next-to-next-to-leading order (NNLO) with the most involved calculations being limited to certain kinematic limits. The various contributions of the weak interaction are captured through effective operators, which will be introduced in detail in Section 2.2, most notably the current-current and penguin operators. A smaller contribution arises from the chromomagnetic operator, which has also been considered before. The observable Γ_{12} is calculated in the HQE, where successive terms are suppressed by the ratio of the fundamental QCD scale (at around 400 MeV) to the bottom quark mass, Λ_{QCD}/m_b. The sub-leading contributions in the HQE have been calculated to LO in QCD [34, 47, 48] and the leading-power terms are discussed in the following.

The current-current operator contributions to Γ_{12} have previously been determined to leading order (LO) and next-to-leading order (NLO) [36, 47, 49, 50]. The NNLO contributions have been calculated for the fermionic parts, i.e. in the large flavour limit, in Refs. [51–53] and for the non-fermionic parts in Ref. [28], both in an expansion in the charm-to-bottom mass ratio m_c/m_b up to second order.

Contributions involving penguin operators have been calculated to LO [47, 49] and to NLO in an expansion in m_c/m_b up to second order [28, 54]. The chromomagnetic operator has been included to NLO in Ref. [49]. Its NNLO and next-to-next-to-next-to-leading (N3LO) contributions have been considered in Ref. [54] in the expansion up to $(m_c/m_b)^2$.

1.5.2 Extending the B meson mixing calculations of Γ_{12}

Because of the larger theoretical uncertainties on $\Delta\Gamma$ and a_{fs}, the focus of this thesis lies on the accurate determination of these two observables. They are closely related to the quantities Γ_{12} and M_{12}, as can be seen from Eqs. (1.12) and (1.14). Since M_{12} has been accurately determined from theoretical predictions [55], Γ_{12} is a focus topic of this thesis. Building on previous works, this thesis completes the perturbative NNLO QCD corrections to the leading-power term of Γ_{12} in the HQE, including a deep expansion in the mass ratio m_c/m_b for all contributions. To this extent, the following improvements are presented:

1. Penguin operator contributions are calculated at NNLO for the first time.
2. The current-current contributions at NNLO are calculated to a deeper expansion up to $(m_c/m_b)^{20}$.

3. Contributions involving penguin operators at NLO are calculated to a deeper expansion up to $(m_c/m_b)^{20}$.

4. Contributions involving the chromomagnetic operator up to N3LO are calculated to a deeper expansion up to $(m_c/m_b)^{20}$.

Additionally, the question of an unambiguous choice of basis for the leading-power transition operator in the HQE is resolved, allowing for an accurate combination of perturbative results from this thesis with non-perturbative matrix elements, see Sections 2.4.2 and 2.4.3. It is worth noting here that the expansion depth of $(m_c/m_b)^{20}$ is sufficient to achieve a relative precision of better than 10^{-6} at NNLO.

The significance of the added expansion depth in m_c/m_b for previously calculated contributions is underscored by the fact that the leading term of a_{fs} is proportional to $(m_c/m_b)^2$. However, also $\Delta\Gamma$ is expected to benefit from the higher precision. The entirely novel contribution involving penguin operators at NNLO contributes to both observables for diagrams involving one penguin and one current-current operator, providing another precision boost. Meanwhile, the NNLO double penguin contribution has no effect on a_{fs} because the CKM factor λ_t^2 cancels in the ratio Γ_{12}/M_{12}, which is therefore purely real. However, in BSM theories, the Wilson coefficients might pick up a complex phase such that penguin double insertions contribute to the imaginary part of Γ_{12} and thereby a_{fs}.

In order to calculate the penguin operator contributions at NNLO, novel projector methods had to be developed. The algorithm presented in Section 3.3 is applicable to any process with four external fermions and is particularly relevant for higher-order QCD corrections involving effective operators and dimensional regularisation.

1.5.3 Overview of theoretical determinations of lifetime ratios

As for the calculations concerning the B meson mixing observables, the focus of this thesis is on the high-energy perturbative QCD corrections to the lifetime ratios. For an overview of all the components which enter the B meson lifetimes, see Ref. [32]. Recently, all LO non-leptonic matching coefficients of the two-quark $|\Delta B| = 0$ transition operator up to dimension six were computed [56]; however, these mostly cancel in the lifetime ratio $\tau(B^+)/\tau(B_d)$ due to isospin symmetry. For this lifetime ratio, the most relevant matching coefficients are those of the four-quark dimension-six $|\Delta B| = 0$ transition operator, which for the non-leptonic part have been computed to LO [57] and to NLO [58, 59] for the CKM-leading contribution of the current-current operators. The penguin and chromomagnetic operators were also considered in Ref. [59] at one-loop order. The next step in improving the precision of the lifetime differences is hence the calculation of the CKM-leading NNLO contributions of the current-current operators together with the CKM-suppressed terms at NLO.

Similar to the theoretical calculations of the mixing observables, non-perturbative matrix elements are required to yield physical results in combination with the high-energy matching coefficients. For the lifetime ratios, the $|\Delta B| = 0$ matrix elements were recently updated using QCD sum rules in Ref. [60].

Further motivation for an NNLO calculation of the dimension-six terms stems from the recent calculation of the dimension-three contributions to B meson decays [61, 62]. Theoretical predictions of the decay width to NNLO are hence partially possible now, and with the addition of the NNLO terms from the four-quark operators, a full NNLO calculation of the total decay width draws closer.

1.5.4 Increasing the precision of lifetime ratios

In this thesis, the current-current operator contributions to the non-leptonic decay width are calculated to NNLO in QCD and analysed in terms of their phenomenological implications for the lifetime ratios of B mesons and Ξ_b baryons. The calculation involves the imaginary part of the three-loop weak annihilation (WA) and Pauli interference (PI) diagrams, see Section 2.5. The following novel contributions are presented:

1. The leading-CKM contributions of the current-current operators are calculated to NNLO.
2. The CKM-suppressed contributions of the current-current operators are calculated to NLO.

The calculation also makes use of the advanced projector methodology developed for the mixing calculations, see Section 3.3.

The results of this high-precision calculation present a major update of the work carried out in Ref. [58] and allow for a more robust test of the validity of quark-hadron duality and the Heavy Quark Expansion.

1.6 Summary and overall approach

This thesis describes the methods necessary to complete high-precision calculations for B meson observables within the framework of the weak effective Hamiltonian in the perturbative regime up to NNLO. Moreover, the phenomenological implications are discussed. The calculations proceed via two operator product expansions, where the W boson and heavier particles are integrated out first to obtain an effective $|\Delta B| = 1$ theory. Subsequently, the HQE is employed to match onto an effective $|\Delta B| = 2$ and $|\Delta B| = 0$ transition operator for B meson mixing and decays respectively. The theoretical foundations of these theories are discussed in Chapter 2. These transition operators allow a factorisation of the

high-energy and low-energy physics, where our focus is on the perturbative high-energy regime. In Chapter 3, the calculation of amplitudes in terms of Feynman diagrams is presented with a particular focus on the novel projector methods developed as part of this thesis. The phenomenological implications of the results in B meson mixing and their relevance for BSM physics are analysed in Chapter 4 and Chapter 5, while the phenomenology of B meson and Ξ_b baryon lifetime ratios follows in Chapter 6. The thesis concludes with a discussion of the results and an outlook on future work in Chapter 7.

2 Operator Product Expansions and Effective Field Theories

In this chapter, the theoretical foundations of the effective operators employed in calculating the B meson decay and mixing amplitudes are presented. Starting from a general introduction to effective field theories (EFTs), the weak effective Hamiltonian of the $|\Delta B| = 1$ basis as well as the $|\Delta B| = 2$ and $|\Delta B| = 0$ transition operators in the Heavy Quark Expansion (HQE) are developed. The matching calculation which connects the $|\Delta B| = 1$ theory to the transition operators is discussed for both the mixing observables and lifetime ratios. Additionally, field theoretic challenges in the evaluation of amplitudes, e.g. the correct implementation of Fierz symmetry and the preservation of the Λ_{QCD}/m_b suppression of renormalised matrix elements, are highlighted.

2.1 Fundamentals of operator product expansions and effective field theories

2.1.1 Describing low-energy physics with effective operators

To introduce the concepts of an operator product expansion, the derivation of the weak effective Hamiltonian is discussed in the following. The effective $|\Delta B| = 1$ Hamiltonian is a useful tool to describe the mixing and decay processes at the typical mass scales of B mesons. Many calculations in quantum field theory are simplified by working at the correct scale of the problem, and EFTs offer a convenient path to achieving this. In the case of the weak effective Hamiltonian, a Type-I EFT [63] where heavy degrees of freedom are fully removed, the W boson and all particles heavier than it are integrated out. In doing so, the number of scales is reduced when calculating QCD corrections to the mixing and decay processes.

In order to construct the effective field theory, a short-distance operator product expansion is employed, which can be illustrated by examining the W boson exchange shown in Fig. 2.1, see also Refs. [63, 64] for further details. The weak interaction in the Standard

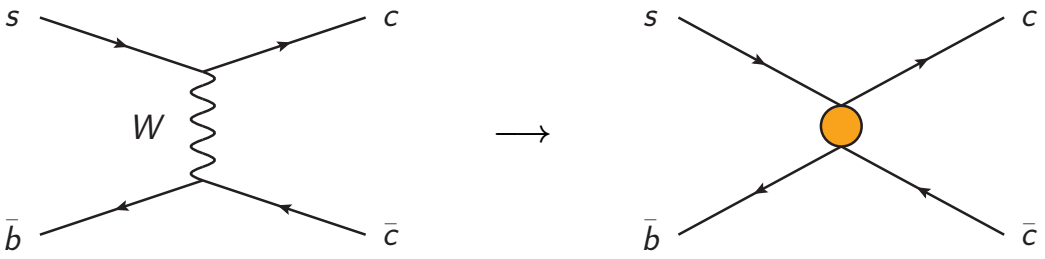

Figure 2.1: Effective current-current operator in orange as generated from the exchange of a W boson.

Model Hamiltonian takes the form

$$\mathcal{H} \supset -\frac{g_w}{\sqrt{2}}\left[W_\mu^+\left(\bar{u}_L^a\gamma_\mu V_{ab}d_L^b\right) + W_\mu^-\left(\bar{d}_L^a\gamma_\mu V_{ab}^\dagger u_L^b\right)\right], \tag{2.1}$$

where g_w is the electroweak coupling constant. The matrix element of the Feynman diagram on the left of Fig. 2.1 is given by

$$\mathcal{M} = \left(\frac{ig_w}{\sqrt{2}}\right)^2 V_{cs}V_{cb}^*\left(\bar{c}\gamma^\mu P_L s\right)\left(\bar{b}\gamma^\nu P_L c\right) \times \frac{-ig_{\mu\nu}}{p^2 - M_W^2}, \tag{2.2}$$

where the chirality projector $P_{R/L} = (1 \pm \gamma_5)/2$ was introduced. The momentum and mass of the W boson are denoted by p and M_W respectively. In the low-energy limit $p^2 \ll M_W^2$, the denominator of the W propagator can be expanded in a Taylor series,

$$\frac{1}{p^2 - M_W^2} = -\frac{1}{M_W^2}\left(1 + \frac{p^2}{M_W^2} + \dots\right), \tag{2.3}$$

which allows us to write the matrix element from Eq. (2.2) as

$$\mathcal{M} = \frac{i}{M_W^2}\left(\frac{ig_w}{\sqrt{2}}\right)^2 V_{cs}V_{cb}^*\left(\bar{c}\gamma^\mu P_L s\right)\left(\bar{b}\gamma_\mu P_L c\right) + \mathcal{O}\left(\frac{p^2}{M_W^4}\right). \tag{2.4}$$

We observe that the W boson generates operators which are suppressed by increasing powers of p^2/M_W^2. This illustrates the Appelquist–Carazzone decoupling theorem [65], which states that heavy fields of mass M generate at low energies operators that are $1/M$-suppressed, with the exception of renormalisation effects.

Using the example above, the concepts of an operator product expansion and an effective field theory will be introduced. First, it can be observed that the non-local interaction mediated by the W boson in Eq. (2.2) is replaced by a series expansion of local operators in Eq. (2.4). This is an example of an operator product expansion (OPE), which reads in generic terms as

$$\mathcal{O}_i(x)\,\mathcal{O}_j(y) \sim \sum_k C_{ij}^k(x-y)\,\mathcal{O}_k(y), \tag{2.5}$$

where the operators $\mathcal{O}_i$ and $\mathcal{O}_j$ are expressed as an asymptotic expansion in an open neighbourhood U of y such that $x \in U\backslash\{y\}$ [66–69]. While the OPE is defined in position space, the relation above can be Fourier-transformed to momentum space, which is more practical for loop calculations. Since the definition holds in an open neighbourhood of y, the OPE will be valid for spacetime points x close to y, which intuitively makes sense for the type of short-distance OPEs that we are considering. The advantage of using such OPEs is that the high-energy and low-energy physics can be factorised into the Wilson coefficients C_{ij}^k and operator matrix elements $\langle \mathcal{O}_k(y) \rangle$ respectively. This allows us to combine perturbative with non-perturbative results.

After integrating out the W boson, the low-energy physics are described by the electroweak $|\Delta B| = 1$ effective Hamiltonian. Continuing with the example from above, consider the Hamiltonian

$$\mathcal{H}_{\text{eff}} = -\frac{4G_F}{\sqrt{2}} V_{cs} V_{cb}^* \left(\bar{c}\gamma^\mu P_L s\right) \left(\bar{b}\gamma_\mu P_L c\right) + \text{h.c.}\,, \tag{2.6}$$

which generates the same matrix element as given in Eq. (2.4) when

$$G_F = \frac{g_W^2}{4\sqrt{2}M_W^2}\,. \tag{2.7}$$

The constant G_F is called the Fermi constant, and the Hamiltonian in Eq. (2.6) can be generalised for all quarks and leptons to the effective field theory proposed by Enrico Fermi [70, 71]. While OPEs are generally only valid inside correlation functions, EFTs are standalone quantum field theories, with their own action and perturbative Feynman rules, valid below a cutoff scale. When constructing EFTs, the most general Hamiltonian consistent with the symmetries of the theory is written down and organised in powers of the heavy cutoff scale, which will be presented in Section 2.2. On the other hand, the $|\Delta B| = 2$ and $|\Delta B| = 0$ transition operators presented in Section 2.4 and Section 2.5 are examples for where an OPE is used inside a correlation function to evaluate an amplitude.

Amplitudes calculated using effective operators need to be renormalised to yield finite results. In the following sections, the renormalisation procedure is discussed, including the evanescent operators appearing in dimensional regularisation.

2.1.2 Renormalisation of the QCD Lagrangian

As the main focus of this thesis is the calculation of QCD corrections to B meson mixing and decays, the renormalisation of the QCD Lagrangian is discussed first before moving on to special considerations for effective field theories. The QCD Fadeev-Popov Lagrangian is given by [72]

$$\mathcal{L}_{\text{QCD}} = -\frac{1}{4}\left(G_{\mu\nu}^a\right)^2 - \frac{1}{2\xi}\left(\partial^\mu G_\mu^a\right)^2 + \bar{\psi}\left(i\not{D} - m\right)\psi + \bar{c}^a\left(-\partial^\mu D_\mu^{ac}\right)c^c\,, \tag{2.8}$$

where c^a are the Fadeev-Popov ghosts and ψ denotes a generic quark field of mass m. The gauge choice $\xi = 1$ corresponds to Feynman-t'Hooft gauge. The covariant derivative acting on the fundamental representation is

$$D_\mu = \partial_\mu - ig_s G_\mu^a T^a \,, \tag{2.9}$$

while for the adjoint representation it is defined as

$$D_\mu^{ac} = \delta^{ac}\partial_\mu + g_s f^{abc} G_\mu^a \,, \tag{2.10}$$

where f^{abc} are the structure constants of the Lie algebra of SU(3). The field strength tensor is given by

$$G_{\mu\nu}^a = \partial_\mu G_\nu^a - \partial_\nu G_\mu^a + g_s f^{abc} G_\mu^b G_\nu^c \,. \tag{2.11}$$

In order to renormalise the Lagrangian, the fields and coupling constants are expressed in terms of bare quantities and renormalisation constants,

$$\begin{aligned} \psi^0 &= \sqrt{Z_2}\,,\psi & G_\mu^{a,0} &= \sqrt{Z_3}\,G_\mu^a \,, \\ c^{a,0} &= \sqrt{\tilde{Z}_3}\,c^a \,, & m^0 &= Z_m\, m \,, \\ g_s^0 &= \mu^\epsilon \sqrt{Z_{\alpha_s}}\, g_s \,, & \xi^0 &= Z_3\,\xi \,. \end{aligned} \tag{2.12}$$

Here, we have introduced the renormalisation scale μ and the parameter ϵ, which is used in dimensional regularisation in $d = 4 - 2\epsilon$ dimensions. This parameter acts as a regulator of divergences, which appear as poles in ϵ and need to be renormalised. After the renormalisation procedure, physical results are recovered by taking the limit $\epsilon \to 0$. For the calculations carried out as part of this thesis, the constant $\tilde{Z}_3$ is not required and only mentioned here for completeness. Additionally, the field strength renormalisation of the gauge field G_μ^a does not appear, but the constant Z_3 enters through the renormalisation of the gauge parameter ξ.

The renormalisation constants can be expanded as a series in the strong coupling constant and the UV pole regulator,

$$Z = \sum_{i=0}^{\infty} \sum_{k=-\infty}^{i} \left(\frac{\alpha_s}{4\pi}\right)^i \frac{1}{\epsilon^k} Z^{(i,k)} \,, \tag{2.13}$$

where $\alpha_s = g_s^2/(4\pi)$. The renormalisation constants in this thesis are taken to be in the modified minimal subtraction ($\overline{\text{MS}}$) scheme in most cases, which removes all poles and terms with the Euler-Mascheroni constant γ_E as well as certain logarithms that can be absorbed by rescaling the renormalisation scale

$$\mu^2 \to \mu^2 \frac{e^{\gamma_\text{E}}}{4\pi} \,. \tag{2.14}$$

This corresponds to subtracting only poles in

$$\frac{1}{\tilde{\epsilon}} \equiv \frac{1}{\epsilon} - \gamma_{\mathsf{E}} + \ln(4\pi)\,, \tag{2.15}$$

and we have $Z^{(i,k)} = 0\,\forall\, k > 0$ as well as $Z^{(0,0)} = 1$. The QCD renormalisation constants are known up to α_s^5, see Refs. [73–77].

For the mass renormalisation, we find it convenient to work in the on-shell (OS) scheme when computing the amplitudes as outlined in Chapter 3. This is because the external bottom quark is taken to be on-shell, such that its momentum squared is equal to the on-shell mass squared, i.e. $q^2 = m_b^2$. In particular, applying the equation of motion $\not{q} u_b = m_b u_b$ will yield additional factors of the on-shell mass. Therefore, it is practical to also use the OS mass for internal propagators and consequently the mass renormalisation. The OS mass m^{OS} is defined such that the pole in the two-point function occurs at the physical mass m and has residue 1. If we denote all one-particle irreducible insertions into the fermion propagator by $-iM(p^2)$, the full two-point function A can be written as a geometric series

$$A = \frac{i}{\not{p} - m^{\mathsf{OS}}} \sum_{n=0}^{\infty} \left(-iM(p^2)\right)^n \left(\frac{i}{\not{p} - m^{\mathsf{OS}}}\right)^n = \frac{i}{\not{p} - m^{\mathsf{OS}} - M(p^2)}\,, \tag{2.16}$$

where p is the external momentum of the particle. The renormalisation conditions are hence

$$M(p^2)\Big|_{p^2=(m^{\mathsf{OS}})^2} = 0\,, \qquad \frac{\mathrm{d}}{\mathrm{d}p^2} M(p^2)\Big|_{p^2=(m^{\mathsf{OS}})^2} = 0\,. \tag{2.17}$$

The mass renormalisation constants in the OS scheme up to α_s^4 can be found in Ref. [78]. Additionally, Ref. [79] gives contributions at α_s^3 from on-shell diagrams with two mass scales, e.g. the bottom and charm quark masses.

For phenomenological applications, different renormalisation schemes of the bottom quark mass can be used. While the poles must cancel in any renormalisation scheme, the finite parts may differ, and the remaining dependence on the renormalisation scale due to the truncation of the perturbation series at a finite order in α_s is also specific to the chosen scheme. Hence, certain schemes are more suitable for processes at particular scales. The conversion between the previously discussed $\overline{\mathrm{MS}}$ and OS schemes can be found in Ref. [79].

The third scheme that is interesting to consider in the context of bottom flavour physics is the potential subtracted (PS) scheme, where large corrections from the heavy quark potential are removed [80]. Large perturbative corrections to the OS mass cancel with those in the potential, making the PS mass a well-determined quantity even when truncating the perturbation series. The PS mass m^{PS} is obtained by subtracting the low-energy part of the heavy quark potential $\tilde{V}(q)$ below a factorisation scale μ_f from the OS mass,

$$m^{\mathsf{PS}}(\mu_f) = m^{\mathsf{OS}} - \delta m(\mu_f)\,, \tag{2.18}$$

where the subtraction term is given by

$$\delta m(\mu_f) = -\frac{1}{2} \int\limits_{|\vec{q}|<\mu_f} \frac{\mathrm{d}^3\vec{q}}{(2\pi)^3}\, \tilde{V}(q)\,. \tag{2.19}$$

The heavy quark potential in momentum space $\tilde{V}(q)$ has been computed to order $\mathcal{O}(\alpha_s^2)$ in Ref. [80], and the three-loop corrections were obtained in Refs. [81, 82]. The conversion to the $\overline{\text{MS}}$ mass is given in Ref. [78], and a convenient implementation of quark mass relations as well as the running of the strong coupling constants and the quark masses called is provided in Ref. [83] in the form of a program called `RunDec`. The finite charm mass effects in the definition of the PS mass are presented in Ref. [84].

2.1.3 Renormalisation of EFTs and evanescent operators

In order to renormalise an EFT, additional renormalisation constants are necessary for the effective operators, which need to be treated differently. The effective operators mix under renormalisation since higher-order corrections to any operator may yield colour and spinor structures different from the original one. Therefore, it becomes necessary to renormalise the Wilson coefficients or equivalently the effective operators through a renormalisation matrix,

$$C_i^0 = C_j Z_{ji}\,. \tag{2.20}$$

To define the renormalisation scheme used for the operator mixing, a special class of operators called evanescent operators needs to be introduced too.

When working with Dirac spinors in $d = 4 - 2\epsilon$ dimensions, the Dirac algebra becomes infinite-dimensional and additional spinor structures appear, which give rise to evanescent operators [85]. This is because the four-dimensional identities that could be used to reduce the number of γ matrices in a so-called Dirac chain are not applicable to d dimensions. For example, the Chisholm identity [86]

$$\gamma^\mu\gamma^\nu\gamma^\rho \overset{d\equiv 4}{=} g^{\mu\nu}\gamma^\rho - g^{\mu\rho}\gamma^\nu + g^{\mu\rho}\gamma^\mu + i\epsilon^{\sigma\mu\nu\rho}\gamma_\sigma\gamma_5 \tag{2.21}$$

does not hold in $d \neq 4$ dimensions. Similarly, without a particular choice of evanescent operators, the four-dimensional Fierz identities as derived in Appendix C are not valid outside of four dimensions. Therefore, evanescent operators are introduced as the difference between the spinor structures in d dimensions and their counterpart after applying four-dimensional identities [85, 87, 88]. The tree-level matrix elements of evanescent operators hence vanish in four dimensions, i.e. they are $\mathcal{O}(\epsilon)$; however, in intermediate steps they may be multiplied by poles in the regulator ϵ. For a correct physical result, the renormalisation procedure must include the evanescent operators.

When extending the renormalisation scheme to include evanescent operators, we follow the prescription outlined in Ref. [89], which extends the $\overline{\text{MS}}$ scheme:

- Renormalised amplitudes of physical matrix elements are UV-finite, i.e. the renormalisation constants only remove poles in $1/\tilde{\epsilon}_{\text{UV}}$.
- Renormalised amplitudes of evanescent matrix elements vanish as $\epsilon_{\text{UV}} \to 0$, i.e. the renormalisation constants have poles as well as finite parts that cancel the finite bare amplitude.

It is worth stressing here that amplitudes can still contain IR poles after the UV divergences have been removed in the renormalisation procedure. In fact, when using the same regulator for UV and IR divergences $\epsilon_{\text{UV}} = \epsilon_{\text{IR}} \equiv \epsilon$, one cannot differentiate between the divergences, and the evanescent operators need to be retained until the IR poles are removed in the matching, see Section 2.6.

Returning to the renormalisation matrix which describes the operator mixing, we can write down an explicit parametrisation of the necessary terms for the physical and evanescent operators. Schematically, the renormalisation constants are defined via

$$\begin{aligned}\left((\vec{C}^{\text{bare}})^T, (\vec{C}_E^{\text{bare}})^T\right) &= \left((\vec{C}^{\text{ren}})^T, (\vec{C}_E^{\text{ren}})^T\right) Z \\ &\equiv \left((\vec{C}^{\text{ren}})^T, (\vec{C}_E^{\text{ren}})^T\right) \begin{pmatrix} Z_{QQ} & Z_{QE} \\ Z_{EQ} & Z_{EE} \end{pmatrix}, \end{aligned} \tag{2.22}$$

where the sub-matrices Z_{QQ} and Z_{EE} can be expanded in α_s and ϵ,

$$(Z_{AA})_{ij} = \delta_{ij} + \frac{\alpha_s}{4\pi}\frac{1}{\epsilon}\left(Z_{AA}^{(1,1)}\right)_{ij} + \mathcal{O}(\alpha_s^2)\,. \tag{2.23}$$

The off-diagonal sub-matrix Z_{QE} has a similar expansion,

$$(Z_{QE})_{ij} = \frac{\alpha_s}{4\pi}\frac{1}{\epsilon}\left(Z_{QE}^{(1,1)}\right)_{ij} + \mathcal{O}(\alpha_s^2)\,. \tag{2.24}$$

The sub-matrix Z_{EQ} is different because it introduces the finite counterterms which are needed to fulfil the renormalisation condition for the vanishing finite part of the evanescent operators, which is easier to see when renormalising the operators instead of the Wilson coefficients. In either case, the matrix reads

$$(Z_{EQ})_{ij} = \frac{\alpha_s}{4\pi}\left(Z_{EQ}^{(1,0)}\right)_{ij} + \mathcal{O}(\alpha_s^2)\,. \tag{2.25}$$

This sub-matrix is special as its highest pole in $1/\epsilon^k$ is $k = i-1$, where i is the order in α_s, and it contains a finite ϵ^0 part as well. For the second-oder α_s^2 terms this means that there are both ϵ^0 and $1/\epsilon$ terms. Since we are working in the modified $\overline{\text{MS}}$ scheme, there are no terms with positive powers of ϵ at any order.

Finally, it is worth considering which evanescent operators need to be included in order to renormalise certain amplitudes. Formally there is an infinite number of evanescent

operators because the Dirac algebra in d dimensions is infinite-dimensional. However, when considering a limited set of operators to a finite maximum order in α_s, the number of evanescent operators to be included is also finite. To renormalise an nth generation evanescent operator up to $\mathcal{O}(\alpha_s^i)$, evanescent operators $E^{(k)}$ up to generation $k = n+i-\ell$ need to be included in the order ℓ diagrams, where $\ell = 0$ corresponds to leading order and $n = 0$ are the physical operators. To illustrate this point, the required operators at each loop order are shown for a few examples in Tab. 2.1.

Matrix element at order $i = 2$	Highest at LO $\ell = 0$	Highest at NLO $\ell = 1$	Highest at NNLO $\ell = 2$
$\langle Q \rangle^{\text{ren}}$ $(n = 0)$	$E^{(2)}$	$E^{(1)}$	Q
$\langle E^{(1)} \rangle^{\text{ren}}$ $(n = 1)$	$E^{(3)}$	$E^{(2)}$	$E^{(1)}$
$\langle E^{(2)} \rangle^{\text{ren}}$ $(n = 2)$	$E^{(4)}$	$E^{(3)}$	$E^{(2)}$
$\langle E^{(3)} \rangle^{\text{ren}}$ $(n = 3)$	$E^{(5)}$	$E^{(4)}$	$E^{(3)}$

Table 2.1: Highest generation evanescent operators required to renormalise different matrix elements up to α_s^2.

2.1.4 Renormalisation group equations for Wilson coefficients

The renormalisation matrices in Eq. (2.22) can also be used to relate Wilson coefficients at different scales through the renormalisation group equations (RGE). This is useful because the low-energy and high-energy physics involve scales which differ significantly but need to be connected. For example, when integrating out a heavy particle, the full theory side will involve logarithms like $\ln(M/\mu)$ where M is the mass of the heavy particle which is no longer present on the effective side. On the effective theory side we get logarithms of the form $\ln(m/\mu)$ where m is a low-energy scale, e.g. the mass of a light particle. It is therefore impossible to choose a single value of μ which suppresses both logarithms. Instead, we use renormalisation group equations to relate quantities at different renormalisation scales, which automatically sums up the large logarithms.

The bare Wilson coefficients must be independent of the renormalisation scale μ; therefore,

$$\mu \frac{\mathrm{d}\vec{C}^0}{\mathrm{d}\mu} = \mu \frac{\mathrm{d}}{\mathrm{d}\mu} \left(\vec{C}^T Z \right) \stackrel{!}{=} 0 \,, \tag{2.26}$$

which implies that the scale evolution of the renormalised Wilson coefficients is given by the renormalisation group equation

$$\mu \frac{\mathrm{d}}{\mathrm{d}\mu} \vec{C} = -\vec{C}^T \left(\mu \frac{\mathrm{d}}{\mathrm{d}\mu} Z \right) Z^{-1} \equiv \vec{C}^T \gamma \,, \tag{2.27}$$

where the anomalous dimension matrix γ was defined. With the QCD beta function

$$\beta(\alpha_s, \epsilon) \equiv \mu \frac{\mathrm{d}\alpha_s}{\mathrm{d}\mu}\,, \tag{2.28}$$

we can also write

$$\gamma = -\beta(\alpha_s, \epsilon) \left(\frac{\mathrm{d}}{\mathrm{d}\alpha_s} Z\right) Z^{-1}\,, \tag{2.29}$$

which is more useful since the renormalisation matrix is usually given as a function of α_s. We need the beta function up to $\mathcal{O}(\alpha_s^2)$, i.e.

$$\beta(\alpha_s, \epsilon) = -2\alpha_s \left[\epsilon + \left(\frac{\alpha_s}{4\pi}\right)\beta_0 + \left(\frac{\alpha_s}{4\pi}\right)^2 \beta_1 + \mathcal{O}(\alpha_s^3)\right]\,. \tag{2.30}$$

Corrections to the QCD beta function are known to five-loop order [90–92], and the relevant parts for our calculation are

$$\beta_0 = \frac{11}{3} C_A - \frac{4}{3} T_F N_f\,, \tag{2.31}$$

$$\beta_1 = \frac{34}{3} C_A^2 - \frac{20}{3} C_A T_F N_f - 4 C_F T_F N_f\,, \tag{2.32}$$

where $C_A = N_c$ and $C_F = (N_c^2 - 1)/(2N_c)$ are the quadratic Casimirs of the adjoint and fundamental representations respectively, and $T_F = 1/2$ is the Dynkin index of the fundamental representation. The number of colours is denoted by N_c, and the number of active quark flavours is N_f.

The solution to Eq. (2.28) for α_s at the scale μ_2 provided the coupling strength at the scale μ_1 is given by

$$\begin{aligned}\alpha_s(\mu_2) = \alpha_s(\mu_1) &- \frac{\alpha_s^2(\mu_1)}{2\pi}\beta_0 \ln\left(\frac{\mu_2}{\mu_1}\right) \\ &+ \frac{\alpha_s^3(\mu_1)}{8\pi^2}\left[2\beta_0^2 \ln^2\left(\frac{\mu_2}{\mu_1}\right) - \beta_1 \ln\left(\frac{\mu_2}{\mu_1}\right)\right] + \mathcal{O}(\alpha_s^4)\,.\end{aligned} \tag{2.33}$$

The RGE for the Wilson coefficients in Eq. (2.27) is be solved by

$$\vec{C}(\mu_2) = \vec{C}(\mu_1)^T U(\mu_2, \mu_1), \tag{2.34}$$

where U can be written as a perturbative expansion in α_s. For this purpose, we expand the anomalous dimension matrix:

$$\gamma = \sum_{i=0}^{\infty} \left(\frac{\alpha_s}{4\pi}\right)^{i+1} \gamma_i. \tag{2.35}$$

We obtain

$$\begin{aligned}\vec{C}(\mu_2) &= \vec{C}(\mu_1)^T \exp\left[\int_{\mu_1}^{\mu_2} \mathrm{d}\mu \frac{\gamma}{\mu}\right] = \vec{C}(\mu_1)^T \exp\left[\int_{\alpha_s(\mu_1)}^{\alpha_s(\mu_2)} \mathrm{d}\alpha_s \frac{\gamma}{\beta(\alpha_s,0)}\right] \\ &= \vec{C}(\mu_1)^T \exp\left[\int_{\alpha_s(\mu_1)}^{\alpha_s(\mu_2)} \mathrm{d}\alpha_s \left(-\frac{\gamma_0}{2\beta_0\alpha_s} - \frac{\beta_0\gamma_1-\beta_1\gamma_0}{8\pi\beta_0^2} + \mathcal{O}(\alpha_s)\right)\right] \\ &= \vec{C}(\mu_1)^T \exp\left[-\frac{\gamma_0}{2\beta_0}\ln\left(\frac{\alpha_s(\mu_2)}{\alpha_s(\mu_1)}\right) - \frac{\beta_0\gamma_1-\beta_1\gamma_0}{8\pi\beta_0^2}(\alpha_s(\mu_2)-\alpha_s(\mu_1)) + \mathcal{O}(\alpha_s^2)\right].\end{aligned} \tag{2.36}$$

We can set $\epsilon = 0$ here since all quantities are finite. Inserting Eq. (2.33) and expanding in α_s, the final expression for the running of the Wilson coefficients is

$$\begin{aligned}\vec{C}(\mu_2) = \vec{C}(\mu_1)^T \Bigg[\mathbb{1} &+ \frac{\alpha_s(\mu_2)}{4\pi}\gamma_0 \ln\left(\frac{\mu_2}{\mu_1}\right) \\ &+ \left(\frac{\alpha_s(\mu_1)}{4\pi}\right)^2 \left\{\gamma_1 \ln\left(\frac{\mu_2}{\mu_1}\right) + \left(\frac{\gamma_0^2}{2} - \gamma_0\beta_0\right)\ln^2\left(\frac{\mu_2}{\mu_1}\right)\right\} + \mathcal{O}(\alpha_s^3)\Bigg].\end{aligned} \tag{2.37}$$

This solution to the RGE running is used to connect low-energy matrix elements with the perturbative matching coefficients obtained at a high-energy scale, see Section 2.6.

2.1.5 The choice of scheme for γ_5

In dimensional regularisation, the Dirac algebra also needs to be treated accordingly in d spacetime dimensions, and an additional challenge arises for the matrix γ_5. The issue is that for $d \neq 4$, γ_5 is not well defined, so a particular scheme needs to be chosen to treat the matrix in intermediate expressions. The scheme we choose is naive dimensional regularisation (NDR), where γ_5 is taken to be anti-commuting

$$\{\gamma_\mu, \gamma_5\} = 0\,, \tag{2.38}$$

and the Dirac algebra is extended naively to d dimensions,

$$\begin{aligned}\{\gamma^\mu, \gamma^\nu\} &= 2g^{\mu\nu}\,, & g^\mu_\mu &= d\,, \\ \gamma^\mu\gamma_\mu &= d\,, & \mathrm{Tr}_d(\mathbb{1}) &= 4\,.\end{aligned}$$

When applying the NDR scheme to loop calculations of higher orders, ambiguities appear in traces over γ_5 with four or more γ matrices, so the scheme may only be used where these ambiguities do not appear [93–97].

Care must be taken to avoid such inconsistencies, and we treat this issue with two different approaches for the mixing and decay processes. For B meson mixing, we choose a basis

which avoids γ_5 in the penguin operators, see Section 2.2.3. In the case of B meson decays, there is no such issue when considering current-current operators only.

Alternative schemes to treat γ_5 are the 't Hooft-Veltman scheme [98], where the Dirac matrices are split into four- and $(d-4)$-dimensional parts, and dimensional reduction [99], where only four-vectors are treated as d-dimensional while the Dirac algebra is purely four-dimensional. However, NDR is the most easily implemented scheme in an automated calculation of a large number of diagrams, so it is the preferred scheme for higher-order QCD corrections considered in this thesis.

2.2 The effective $|\Delta B| = 1$ Hamiltonian

The weak effective Hamiltonian at scales below the W boson mass is given by

$$\mathcal{H}_{\text{full}}^{|\Delta B|=1} = \mathcal{H}_{\text{NL}}^{|\Delta B|=1} + \mathcal{H}_{\text{SL}}^{|\Delta B|=1} + \mathcal{H}_{\text{rare}}^{|\Delta B|=1}\,, \tag{2.39}$$

where the labels NL, SL and rare stand for the non-leptonic, semi-leptonic and rare decay modes of the bottom quark [100]. The dominant contribution to the mixing stems from the non-leptonic decays since they are mediated by the strong interaction, and the lifetime differences in bottom-flavoured hadrons with different spectator quarks depend mostly on the non-leptonic parts of the Hamiltonian too. Rare decays mediated by $\mathcal{H}_{\text{rare}}^{|\Delta B|=1}$ like $B \to K\ell^+\ell^-$ have small branching fractions below the theoretical uncertainty [32]. Therefore, only the non-leptonic part of the Hamiltonian is considered in the following.

2.2.1 The historical basis of the $|\Delta B| = 1$ Hamiltonian

Below the scale of the W boson mass, the effective Hamiltonian is traditionally written as

$$\begin{aligned}\mathcal{H}_{\text{hist}}^{|\Delta B|=1} = \frac{4G_F}{\sqrt{2}}\Bigg[&-\lambda_t \sum_{i=1}^{8} C_i O_i - \lambda_u \sum_{i=1}^{2} C_i (O_i - O_i^{uu}) \\ &+ V_{uq}^* V_{cb} \sum_{i=1}^{2} C_i O_i^{cu} + V_{cq}^* V_{ub} \sum_{i=1}^{2} C_i O_i^{uc} + \sum_i C_{E_i} \tilde{E}_i \Bigg] + \text{h.c.}\,,\end{aligned} \tag{2.40}$$

with q denoting either the down or strange quark. The current-current operators are generated by diagrams like the one in Fig. 2.1 on page 20 as well as QCD corrections to them. They are defined as

$$\begin{aligned} O_1 &\equiv \left(\bar{q}_i \gamma_\mu P_L c_j\right)\left(\bar{c}_j \gamma^\mu P_L b_i\right), & O_2 &\equiv \left(\bar{q}\gamma_\mu P_L c\right)\left(\bar{c}\gamma^\mu P_L b\right), \\ O_1^{uu} &\equiv \left(\bar{q}_i \gamma_\mu P_L u_j\right)\left(\bar{u}_j \gamma^\mu P_L b_i\right), & O_2^{uu} &\equiv \left(\bar{q}\gamma_\mu P_L u\right)\left(\bar{u}\gamma^\mu P_L b\right), \\ O_1^{cu} &\equiv \left(\bar{q}_i \gamma_\mu P_L u_j\right)\left(\bar{c}_j \gamma^\mu P_L b_i\right), & O_2^{cu} &\equiv \left(\bar{q}\gamma_\mu P_L u\right)\left(\bar{c}\gamma^\mu P_L b\right), \\ O_1^{uc} &\equiv \left(\bar{q}_i \gamma_\mu P_L c_j\right)\left(\bar{u}_j \gamma^\mu P_L b_i\right), & O_2^{uc} &\equiv \left(\bar{q}\gamma_\mu P_L c\right)\left(\bar{u}\gamma^\mu P_L b\right), \end{aligned} \tag{2.41}$$

where the colour indices i, j are contracted across the two spinor products when they are explicitly shown. Suppressed colour indices are contracted within the spinor products. The Wilson coefficients do not depend on the external quark fields, so they are identical for all O_1 and O_2 operators respectively. However, they have to be treated differently for the purpose of renormalisation since they do not mix with the operators with different CKM factors.

The penguin operators, which are defined as

$$\begin{aligned} O_3 &\equiv \left(\bar{q}\gamma_\mu P_L b\right) \sum_f \left(\bar{f}\gamma^\mu P_L f\right), \\ O_4 &\equiv \left(\bar{q}_i\gamma_\mu P_L b_j\right) \sum_f \left(\bar{f}_j\gamma^\mu P_L f_i\right), \\ O_5 &\equiv \left(\bar{q}\gamma_\mu P_L b\right) \sum_f \left(\bar{f}\gamma^\mu P_R f\right), \\ O_6 &\equiv= \left(\bar{q}_i\gamma_\mu P_L b_j\right) \sum_f \left(\bar{f}_j\gamma^\mu P_R f_i\right), \end{aligned} \tag{2.42}$$

where the sum runs over the quark flavours $f \in \{u, d, c, s, b\}$, stem from diagrams in the full theory as shown in Fig. 2.2a and higher-order QCD corrections to them. The electromagnetic penguin operator is

$$O_7 \equiv \frac{e}{16\pi^2}\, m_b\, \left(\bar{q}\sigma^{\mu\nu} P_R b\right)\, F_{\mu\nu}\,, \tag{2.43}$$

with $\sigma^{\mu\nu} = i[\gamma^\mu, \gamma^\nu]/2$ and the electromagnetic field strength tensor $F_{\mu\nu} = \partial_\mu A_\nu - \partial_\nu A_\mu$. This operator stems from penguin diagrams involving photons, see for example Fig. 2.2b. Since the strong coupling constant g_s is much larger than the electric coupling constant e, this operator will be neglected in the following calculations. Lastly, the chromomagnetic operator is generated from diagrams like Fig. 2.2c and is given by

$$O_8 \equiv -\frac{g_s}{16\pi^2}\, m_b\, \left(\bar{q}\sigma^{\mu\nu} T^a P_R b\right)\, G^a_{\mu\nu}\,, \tag{2.44}$$

where the field strength tensor $G^a_{\mu\nu}$ is defined as

$$G^a_{\mu\nu} = \partial_\mu G^a_\nu - \partial_\nu G^a_\mu + g_s f^{abc} G^b_\mu G^c_\nu\,, \tag{2.45}$$

with the structure constants f^{abc} of the Lie algebra of SU(3).

The operators $\tilde{E}_i$ are the so-called evanescent operators which are needed to renormalise the theory in dimensional regularisation with $d = 4 - 2\epsilon$ dimensions. The evanescent

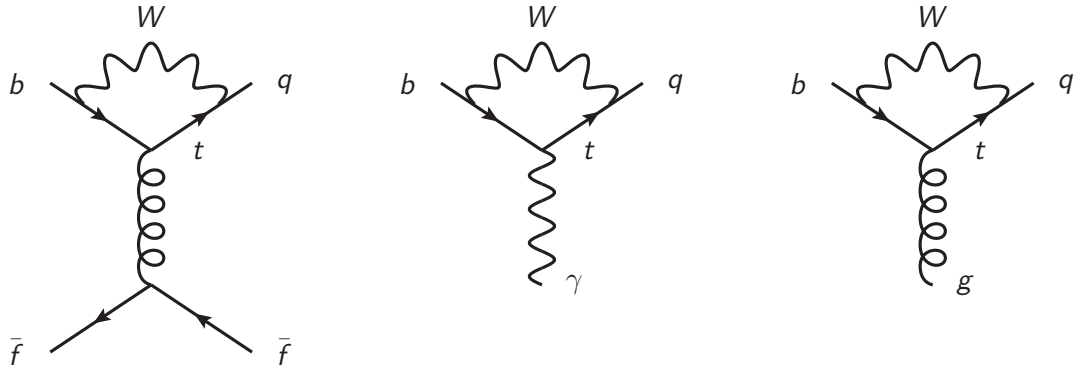

(a) QCD penguin (b) Electromagnetic penguin (c) Chromomagnetic penguin

Figure 2.2: Leading-order diagrams in the full theory which give rise to the effective operators $Q_{3\text{–}8}$.

operators corresponding to the current-current operators are

$$\begin{aligned}
\tilde{E}_1^{(1)} &\equiv \left(\bar{q}_i\gamma^{\mu_1}\gamma^{\mu_2}\gamma^{\mu_3}P_L c_j\right)\left(\bar{c}_j\gamma_{\mu_1}\gamma_{\mu_2}\gamma_{\mu_3}P_L b_i\right) - \left(16 - 4\epsilon + A_2\epsilon^2\right)O_1\,, \\
\tilde{E}_2^{(1)} &\equiv \left(\bar{q}\gamma^{\mu_1}\gamma^{\mu_2}\gamma^{\mu_3}P_L c\right)\left(\bar{c}\gamma^{\mu_1}\gamma^{\mu_2}\gamma^{\mu_3}P_L b\right) - \left(16 - 4\epsilon + A_2\epsilon^2\right)O_2\,, \\
\tilde{E}_1^{(2)} &\equiv \left(\bar{q}_i\gamma^{\mu_1}\gamma^{\mu_2}\gamma^{\mu_3}\gamma^{\mu_4}\gamma^{\mu_5}P_L b_j\right)\left(\bar{c}_j\gamma_{\mu_1}\gamma_{\mu_2}\gamma_{\mu_3}\gamma_{\mu_4}\gamma_{\mu_5}P_L b_i\right) \qquad (2.46) \\
&\quad - \left(256 - 224\epsilon + B_1\epsilon^2\right)O_1\,, \\
\tilde{E}_2^{(2)} &\equiv \left(\bar{q}\gamma^{\mu_1}\gamma^{\mu_2}\gamma^{\mu_3}\gamma^{\mu_4}\gamma^{\mu_5}P_L b\right)\left(\bar{c}\gamma_{\mu_1}\gamma_{\mu_2}\gamma_{\mu_3}\gamma_{\mu_4}\gamma_{\mu_5}P_L b\right) \qquad (2.47) \\
&\quad - \left(256 - 224\epsilon + B_2\epsilon^2\right)O_2\,, \qquad (2.48)
\end{aligned}$$

which can be generalised to the other up-type flavour combinations by analogy with the current-current operators. The constants A_2, B_1 and B_2 have been solved for in Ref. [61], and the solution we choose in our calculation is

$$A_2 = -4\,, \qquad B_1 = -\frac{45936}{115}\,, \qquad B_2 = -\frac{115056}{115}\,. \qquad (2.49)$$

The logic behind the calculation of Ref. [61] is explained in the following section. The corresponding renormalisation constants of the full basis in the $\overline{\text{MS}}$ scheme can be found in Appendix A.

2.2.2 Fierz transformations at diagram level

In order to calculate $|\Delta B| = 0$ amplitudes from two insertions of $|\Delta B| = 1$ operators in the historical basis, it is convenient to Fierz-transform one of the two operator insertions, see Section 3.2.4. This is because we want to map onto the $|\Delta B| = 0$ basis used in Ref. [58] where each spin line connects a bottom to a light quark. The reason for this

is that otherwise we would encounter evanescent operators which vanish under a Fierz transformation and subsequent application of the equations of motion, i.e. they have the form

$$(\bar{b}\Gamma b)(\bar{q}\not{p}\Gamma q) - m_b(\bar{b}\Gamma q)(\bar{q}\Gamma b)\,. \tag{2.50}$$

This can be avoided by Fierz-transforming the $|\Delta B| = 1$ operators at the diagram level. For a derivation of the Fierz identites, see Appendix C.

Requiring Fierz symmetry at the diagram level determines the $\mathcal{O}(\epsilon)$ parts of the evanescent operators given in Eq. (2.48) with the NNLO solution first determined in Ref. [61]. The procedure we follow is outlined in Ref. [85] and rests on a particular symmetry of the anomalous dimension of the current-current operators. Note that this procedures only works when considering current-current operators up to NNLO because it does not treat penguin operators.

In the most general scenario, what we want to achieve is to identify an operator $\mathcal{O}_i$ with it's counterpart that has the external spinors contracted in a different manner, $\mathcal{O}_i^F$, which we call the Fierz-transformed operator. This means we have two equivalent Hamiltonians with identical Wilson coefficients,

$$\mathcal{H} = \sum_j C_j \mathcal{O}_j \qquad \text{and} \qquad \mathcal{H}^F = \sum_j C_j^F \mathcal{O}_j^F\,. \tag{2.51}$$

Calculating a correlation function of two operator insertions and Fierz-transforming one of the operators is the same as picking out one operator from $\mathcal{H}$ and one from $\mathcal{H}^F$.

Buras and Weisz show to NLO that this can be achieved through a particular symmetry of the anomalous dimension [85]. Consider the current-current operators O_1^{cu} and O_2^{cu} from Eq. (2.41), which differ only in colour structure. The Fierz-transformed basis is then

$$\begin{aligned} O_1^{cu,\,F} &= \left(\bar{q}\gamma_\mu P_L b\right)\left(\bar{c}\gamma^\mu P_L u\right), \\ O_2^{cu,\,F} &= \left(\bar{q}_i\gamma_\mu P_L b_j\right)\left(\bar{c}_j\gamma^\mu P_L u_i\right). \end{aligned} \tag{2.52}$$

Note that the colour structures have flipped between the two operators, i.e. apart from the quark flavours, the operators O_1^{cu} and $O_2^{cu,\,F}$ are identical.

For the Wilson coefficients of the regular and Fierz-transformed operators to be the same, we require the initial condition and the running of the operators to be the same. We will show that fixing the running given by the anomalous dimension is actually sufficient to achieve this. Hence, we demand that

$$\gamma(O_1^{cu,\,F}, O_2^{cu,\,F}) \stackrel{!}{=} \gamma(O_1^{cu}, O_2^{cu})\,. \tag{2.53}$$

Since the QCD corrections that contribute to the anomalous dimension are independent of the external flavours, we know that

$$\gamma(O_1^{cu,\,F}, O_2^{cu,\,F}) = \gamma(O_2^{cu}, O_1^{cu})\,, \tag{2.54}$$

so by combining the two equations we obtain the symmetry condition for the anomalous dimension

$$\gamma(O_1^{cu}, O_2^{cu}) = \gamma(O_2^{cu}, O_1^{cu}) \ . \tag{2.55}$$

The anomalous dimension hence has the form

$$\gamma(O_1^{cu}, O_2^{cu}) = \begin{pmatrix} a & b \\ b & a \end{pmatrix} \ . \tag{2.56}$$

To higher orders, the constants A_2, B_1 and B_2 from the definition of the evanescent operators in Eq. (2.48) enter the 2×2 anomalous dimension. It is only necessary to consider the anomalous dimension for the physical operators, and all required evanescent operators are fixed if we consider the anomalous dimension to a sufficiently high order in α_s. Note that if we go to the $O_\pm^{cu} = O_1^{cu} \pm O_2^{cu}$ basis, the two operators do not mix under running if the anomalous dimension has the above symmetric form.

To complete the argument, we also need to show that this indeed fixes the initial conditions for the Wilson coefficients too. Following the notation of Ref. [64], the Wilson coefficients at a scale μ are given by

$$\vec{C}(\mu) = U(\mu, \mu_0) \left[\vec{C}^{(0)}(\mu_0) + \frac{\alpha_s(\mu_0)}{4\pi} \vec{C}^{(1)}(\mu_0) + \left(\frac{\alpha_s(\mu_0)}{4\pi} \right)^2 \vec{C}^{(2)}(\mu_0) + \dots \right] , \tag{2.57}$$

where the evolution matrix is given by

$$U(\mu, \mu_0) = \mathbb{1} + \frac{\alpha_s(\mu_0)}{4\pi} J^{(1)} + \left(\frac{\alpha_s(\mu_0)}{4\pi} \right)^2 J^{(2)} + \dots \ . \tag{2.58}$$

The matrix $J^{(i)}$ is determined by the anomalous dimension and depends on the choice of the evanescent operators. Since the left-hand side of Eq. (2.57) does not depend on μ_0, all terms related to μ_0 must drop out from the right-hand side. This means that the initial conditions, i.e. the $\vec{C}^{(i)}(\mu_0)$, are fixed through the anomalous dimension that enters $J^{(i)}$. In other words, the scale dependence in $\vec{C}^{(i)}(\mu_0)$ stems from the pole structure of the diagrams, which is also encoded in the renormalisation constants and thus the anomalous dimension. Hence, fixing the anomalous dimension according to Eq. (2.56) guarantees that the Wilson coefficients of the regular and Fierz-transformed operators are the same at all scales.

2.2.3 The CMM basis of the $|\Delta B| = 1$ Hamiltonian

The effective Hamiltonian obtained from the Standard Model theory below the mass of the W boson M_W can also be written down in the Chetyrkin-Misiak-Münz (CMM) basis [101].

It is given by

$$\begin{aligned}\mathcal{H}^{|\Delta B|=1} = \frac{4G_F}{\sqrt{2}} \Bigg[&- \lambda_t \sum_{i=1}^{8} C_i Q_i - \lambda_u \sum_{i=1}^{2} C_i (Q_i - Q_i^{uu}) \\ &+ V_{uq}^* V_{cb} \sum_{i=1}^{2} C_i Q_i^{cu} + V_{cq}^* V_{ub} \sum_{i=1}^{2} C_i Q_i^{uc} + \sum_i C_{E_i} E_i \Bigg] + \text{h.c.}\,,\end{aligned} \tag{2.59}$$

where the quark q is either down or strange. The current-current operators are defined as

$$\begin{aligned} Q_1 &\equiv \left(\bar{q}\gamma_\mu T^a P_L c\right)\left(\bar{c}\gamma^\mu T^a P_L b\right), & Q_2 &\equiv \left(\bar{q}\gamma_\mu P_L c\right)\left(\bar{c}\gamma^\mu P_L b\right), \\ Q_1^{uu} &\equiv \left(\bar{q}\gamma_\mu T^a P_L u\right)\left(\bar{u}\gamma^\mu T^a P_L b\right), & Q_2^{uu} &\equiv \left(\bar{q}\gamma_\mu P_L u\right)\left(\bar{u}\gamma^\mu P_L b\right), \\ Q_1^{cu} &\equiv \left(\bar{q}\gamma_\mu T^a P_L u\right)\left(\bar{c}\gamma^\mu T^a P_L b\right), & Q_2^{cu} &\equiv \left(\bar{q}\gamma_\mu P_L u\right)\left(\bar{c}\gamma^\mu P_L b\right), \\ Q_1^{uc} &\equiv \left(\bar{q}\gamma_\mu T^a P_L c\right)\left(\bar{u}\gamma^\mu T^a P_L b\right), & Q_2^{uc} &\equiv \left(\bar{q}\gamma_\mu P_L c\right)\left(\bar{u}\gamma^\mu P_L b\right), \end{aligned} \tag{2.60}$$

where T^a denotes the generator of SU(3). Additionally, we have the penguin operators

$$\begin{aligned} Q_3 &\equiv \left(\bar{q}\gamma_\mu P_L b\right) \sum_f \left(\bar{f}\gamma^\mu f\right), \\ Q_4 &\equiv \left(\bar{q}\gamma_\mu T^a P_L b\right) \sum_f \left(\bar{f}\gamma^\mu T^a f\right), \\ Q_5 &\equiv \left(\bar{q}\gamma_{\mu_1}\gamma_{\mu_2}\gamma_{\mu_3} P_L b\right) \sum_f \left(\bar{f}\gamma^{\mu_1}\gamma^{\mu_2}\gamma^{\mu_3} f\right), \\ Q_6 &\equiv \left(\bar{q}\gamma_{\mu_1}\gamma_{\mu_2}\gamma_{\mu_3} T^a P_L b\right) \sum_f \left(\bar{f}\gamma^{\mu_1}\gamma^{\mu_2}\gamma^{\mu_3} T^a f\right), \end{aligned} \tag{2.61}$$

where $f \in \{u, d, c, s, b\}$. The electromagnetic penguin operator is identical to the historical basis,

$$Q_7 \equiv \frac{e}{16\pi^2}\, m_b\, \left(\bar{q}\sigma^{\mu\nu} P_R b\right)\, F_{\mu\nu}\,, \tag{2.62}$$

and the same holds true for the chromomagnetic operator

$$Q_8 \equiv -\frac{g_s}{16\pi^2}\, m_b\, \left(\bar{q}\sigma^{\mu\nu} T^a P_R b\right)\, G^a_{\mu\nu}\,. \tag{2.63}$$

The Wilson coefficients of the effective operators in the $|\Delta B| = 1$ Hamiltonian from Eq. (2.59) are known to NNLO in QCD [101–105]. Numerically, the Wilson coefficients of the current-current operators at $\mathcal{O}(1)$ are larger than those of the penguin operators at $\lesssim \mathcal{O}(10^{-1})$, which is why diagrams involving current-current operators are more significant for phenomenological applications.

The main advantage of using the CMM basis is that for the B meson mixing processes it avoids issues with γ_5 in closed loops, which cannot be uniquely determined in dimensional

regularisation. The traditional basis, as discussed in Section 2.2.1, has a γ_5 in the quark-antiquark product of the penguin operators. Therefore, NLO and higher-order diagrams like the one shown in Fig. 2.3 may involve traces over γ_5 and four or more γ matrices,

$$\mathrm{Tr}_d\left(\gamma_5\gamma^\mu\gamma^\nu\gamma^\rho\gamma^\sigma\right) . \tag{2.64}$$

When using dimensional regularisation for the UV poles, the trace needs to be evaluated in d dimensions as indicated. This is problematic because the Dirac algebra is infinite-dimensional in d spacetime dimensions, so the definition of the trace in four spacetime dimensions in terms of the completely antisymmetric tensor $\epsilon^{\mu\nu\rho\sigma}$,

$$\mathrm{Tr}_4\left(\gamma_5\gamma^\mu\gamma^\nu\gamma^\rho\gamma^\sigma\right) = -4i\epsilon^{\mu\nu\rho\sigma} , \tag{2.65}$$

cannot be extended to d dimensions. However, this problem arises only because of the choice of basis and can be circumvented by working in the CMM basis. This is possible because the full theory diagrams underlying e.g. Fig. 2.3 do not contain any problematic traces. The reason why the CMM basis does not have the same issue as the traditional

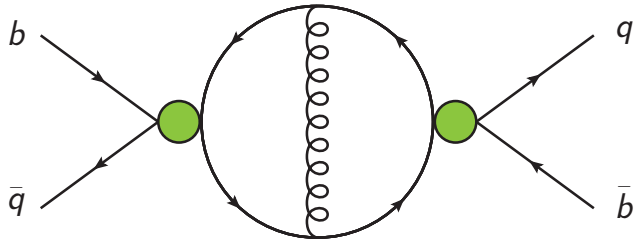

Figure 2.3: NLO diagram which will give rise to ambiguous traces over γ_5 in the traditional basis. The green operator insertions correspond to penguin operators in the traditional basis.

basis is because the spin line with the quark anti-quark pair $\bar{f}\Gamma f$ does not contain a chirality projector inside Γ in the CMM basis. Therefore, closed fermion loops stemming from this part of the penguin operators lead to traces over large numbers of γ matrices, but they do not contain γ_5. For current-current operators, both the traditional and the CMM basis have chirality projectors on either spin lines; however, those never lead to closed fermion loops. Instead, on each spin line one of the quarks is contracted with an external state while the other quark becomes an internal line.

As discussed in Section 2.1.3, a number of evanescent operators is required to renormalise the physical operators. Since the calculations in this thesis are carried out to NNLO, two generations of evanescent operators are included in the calculations. The first generation

is given by [101]

$$
\begin{aligned}
E_1^{(1)} &\equiv \left(\bar{q}\gamma^{\mu_1}\gamma^{\mu_2}\gamma^{\mu_3}P_L T^a c\right)\left(\bar{c}\gamma_{\mu_1}\gamma_{\mu_2}\gamma_{\mu_3}P_L T^a b\right) - 16Q_1\,,\\
E_2^{(1)} &\equiv \left(\bar{q}\gamma^{\mu_1}\gamma^{\mu_2}\gamma^{\mu_3}P_L c\right)\left(\bar{c}\gamma_{\mu_1}\gamma_{\mu_2}\gamma_{\mu_3}P_L b\right) - 16Q_2\,,\\
E_3^{(1)} &\equiv \left(\bar{q}\gamma^{\mu_1}\gamma^{\mu_2}\gamma^{\mu_3}\gamma^{\mu_4}\gamma^{\mu_5}P_L b\right)\sum_f\left(\bar{f}\gamma_{\mu_1}\gamma_{\mu_2}\gamma_{\mu_3}\gamma_{\mu_4}\gamma_{\mu_5} f\right)\\
&\quad - 20Q_5 + 64Q_3\,,\\
E_4^{(1)} &\equiv \left(\bar{q}\gamma^{\mu_1}\gamma^{\mu_2}\gamma^{\mu_3}\gamma^{\mu_4}\gamma^{\mu_5}P_L T^a b\right)\sum_f\left(\bar{f}\gamma_{\mu_1}\gamma_{\mu_2}\gamma_{\mu_3}\gamma_{\mu_4}\gamma_{\mu_5} T^a f\right)\\
&\quad - 20Q_6 + 64Q_4\,.
\end{aligned}
\tag{2.66}
$$

For the current-current operators coupling to up quarks, there are additional evanescent operators $E_1^{q_1q_2,(1)}$ and $E_2^{q_1q_2,(1)}$ defined analogously to $E_1^{(1)}$ and $E_2^{(1)}$ but with the charm quarks substituted with up quarks according to the flavour structure q_1q_2 of the current-current operator to be renormalised:

$$
\begin{aligned}
E_1^{uu,(1)} &\equiv \left(\bar{q}\gamma^{\mu_1}\gamma^{\mu_2}\gamma^{\mu_3}T^a P_L u\right)\left(\bar{u}\gamma^{\mu_1}\gamma^{\mu_2}\gamma^{\mu_3}T^a P_L b\right) - 16Q_1^{uu}\,,\\
E_2^{uu,(1)} &\equiv \left(\bar{q}\gamma^{\mu_1}\gamma^{\mu_2}\gamma^{\mu_3}P_L u\right)\left(\bar{u}\gamma_{\mu_1}\gamma_{\mu_2}\gamma_{\mu_3}P_L b\right) - 16Q_2^{uu}\,,\\
E_1^{cu,(1)} &\equiv \left(\bar{q}\gamma^{\mu_1}\gamma^{\mu_2}\gamma^{\mu_3}T^a P_L u\right)\left(\bar{c}\gamma_{\mu_1}\gamma_{\mu_2}\gamma_{\mu_3}T^a P_L b\right) - 16Q_1^{cu}\,,\\
E_2^{cu,(1)} &\equiv \left(\bar{q}\gamma^{\mu_1}\gamma^{\mu_2}\gamma^{\mu_3}P_L u\right)\left(\bar{c}\gamma_{\mu_1}\gamma_{\mu_2}\gamma_{\mu_3}P_L b\right) - 16Q_2^{cu}\,,\\
E_1^{uc,(1)} &\equiv \left(\bar{q}\gamma^{\mu_1}\gamma^{\mu_2}\gamma^{\mu_3}T^a P_L c\right)\left(\bar{u}\gamma_{\mu_1}\gamma_{\mu_2}\gamma_{\mu_3}T^a P_L b\right) - 16Q_1^{uc}\,,\\
E_2^{uc,(1)} &\equiv \left(\bar{q}\gamma^{\mu_1}\gamma^{\mu_2}\gamma^{\mu_3}P_L c\right)\left(\bar{u}\gamma_{\mu_1}\gamma_{\mu_2}\gamma_{\mu_3}P_L b\right) - 16Q_2^{uc}\,.
\end{aligned}
\tag{2.67}
$$

At $\mathcal{O}(\alpha_s^2)$, the second generation of evanescent operators is required, which reads [101]

$$
\begin{aligned}
E_1^{(2)} &\equiv (\bar{q}\gamma^{\mu_1}\ldots\gamma^{\mu_5}P_L T^a c)\left(\bar{c}\gamma_{\mu_1}\ldots\gamma_{\mu_5}P_L T^a b\right) - 20E_1^{(1)} - 256Q_1\,,\\
E_2^{(2)} &\equiv (\bar{q}\gamma^{\mu_1}\ldots\gamma^{\mu_5}P_L c)\left(\bar{c}\gamma_{\mu_1}\ldots\gamma_{\mu_5}P_L b\right) - 20E_2^{(1)} - 256Q_2\,,\\
E_3^{(2)} &\equiv (\bar{q}\gamma^{\mu_1}\ldots\gamma^{\mu_7}P_L b)\sum_f\left(\bar{f}\gamma_{\mu_1}\ldots\gamma_{\mu_7} f\right) - 336Q_5 + 1280Q_3\,,\\
E_4^{(2)} &\equiv (\bar{q}\gamma^{\mu_1}\ldots\gamma^{\mu_7}P_L T^a b)\sum_f\left(\bar{f}\gamma_{\mu_1}\ldots\gamma_{\mu_7} T^a f\right) - 336Q_6 + 1280Q_4\,.
\end{aligned}
\tag{2.68}
$$

As for the first generation, there are additional evanescent operators, $E_1^{q_1q_2,(2)}$ and $E_2^{q_1q_2,(2)}$, for the current-current operators of different flavour structures:

$$\begin{aligned}
E_1^{uu,(2)} &\equiv (\bar{q}\gamma^{\mu_1}\dots\gamma^{\mu_5}P_L T^a u)\left(\bar{u}\gamma_{\mu_1}\dots\gamma_{\mu_5}P_L T^a b\right) - 20E_1^{uu,(1)} - 256Q_1^{uu}\,,\\
E_2^{uu,(2)} &\equiv (\bar{q}\gamma^{\mu_1}\dots\gamma^{\mu_5}P_L u)\left(\bar{u}\gamma_{\mu_1}\dots\gamma_{\mu_5}P_L b\right) - 20E_2^{uu,(1)} - 256Q_2^{uu}\,,\\
E_1^{cu,(2)} &\equiv (\bar{q}\gamma^{\mu_1}\dots\gamma^{\mu_5}P_L T^a u)\left(\bar{c}\gamma_{\mu_1}\dots\gamma_{\mu_5}P_L T^a b\right) - 20E_1^{cu,(1)} - 256Q_1^{cu}\,,\\
E_2^{cu,(2)} &\equiv (\bar{q}\gamma^{\mu_1}\dots\gamma^{\mu_5}P_L u)\left(\bar{c}\gamma_{\mu_1}\dots\gamma_{\mu_5}P_L b\right) - 20E_2^{cu,(1)} - 256Q_2^{cu}\,,\\
E_1^{uc,(2)} &\equiv (\bar{q}\gamma^{\mu_1}\dots\gamma^{\mu_5}P_L T^a c)\left(\bar{u}\gamma_{\mu_1}\dots\gamma_{\mu_5}P_L T^a b\right) - 20E_1^{uc,(1)} - 256Q_1^{uc}\,,\\
E_2^{uc,(2)} &\equiv (\bar{q}\gamma^{\mu_1}\dots\gamma^{\mu_5}P_L c)\left(\bar{u}\gamma_{\mu_1}\dots\gamma_{\mu_5}P_L b\right) - 20E_2^{uc,(1)} - 256Q_2^{uc}\,. \qquad (2.69)
\end{aligned}$$

The renormalisation constants for the CMM basis are given in Appendix A.

2.3 Derivation of the Heavy Quark Expansion for the decay matrix

Before introducing the operator bases for the $|\Delta B| = 2$ and $|\Delta B| = 0$ transition operators, the derivation of the Heavy Quark Expansion (HQE) in the context of lifetimes and mixing of B mesons is discussed. The HQE appears when the physics of heavy quarks is described in terms of the Heavy Quark Effective Theory (HQET), which is a Type-II EFT in the terminology of Ref. [63]. This means that in contrast to the weak effective Hamiltonian, the heavy degrees of freedom are static, but other particles may still collide with them elastically.

The HQE is developed from the expansion of the momentum of the heavy quark, in our case a bottom quark,

$$p_b^\mu = m_b v^\mu + k^\mu\,, \qquad (2.70)$$

where v^μ is the velocity of the hadron [106]. This decomposition is useful because the bottom quark moves to a good approximation with the same velocity as the hadron and is only slightly off-shell such that $k^\mu \ll m_b v^\mu$. Scattering processes with the bottom quark can change its momentum k^μ by only a small amount, which also goes to zero as $\Lambda_{\text{QCD}}/m_b \to 0$.

After splitting the heavy quark field in large and small component fields h and H, the heavy small component field H can be integrated out to yield an expansion in Λ_{QCD}/m_b. The component fields are defined as

$$\begin{aligned}
h(x) &\equiv e^{im_b v\cdot x} P_+\, b(x)\,,\\
H(x) &\equiv e^{im_b v\cdot x} P_-\, b(x) \qquad (2.71)
\end{aligned}$$

where $P_\pm = (1 \pm \not{v})/2$ are the positive and negative energy projectors. These fields obey the identities

$$\begin{aligned} \not{v} h &= h\,, & P_+ h &= h\,, & P_- h &= 0\,, \\ \not{v} H &= -H\,, & P_+ H &= 0\,, & P_- H &= H\,. \end{aligned} \tag{2.72}$$

The quark field can hence be decomposed into the two components via

$$b(x) = e^{-im_b v\cdot x}\left[h(x) + H(x)\right]\,. \tag{2.73}$$

To show that the small component field $H(x)$ is suppressed by $\Lambda_{\mathrm{QCD}}/m_b$, we consider the equation of motion

$$0 = (i\not{D} - m_b)b(x) = \left[i\not{D}h + (i\not{D} - 2m_b)H\right] e^{-im_b v\cdot x}\,, \tag{2.74}$$

where the field decomposition from Eq. (2.73) was substituted in. Applying the projector P_- to the above equation yields

$$i(\not{D} - v\cdot D)h - (2m + iv\cdot D)H = 0\,, \tag{2.75}$$

and using $(v\cdot D)h = (v\cdot D)\not{v}h$, we can solve for the small component field,

$$H = \frac{1}{iv\cdot D + 2m_b} i\not{D}_\perp h\,, \tag{2.76}$$

where the covariant derivative orthogonal to the heavy quark velocity

$$D_\perp^\mu \equiv D^\mu - v^\mu v\cdot D \tag{2.77}$$

was defined [106].

Substituting Eq. (2.76) into Eq. (2.73), the full heavy quark field can be written as

$$\begin{aligned} b(x) &= e^{-im_b v\cdot x}\left[1 + \frac{i\not{D}_\perp}{iv\cdot D + 2m_b}\right] h(x) \\ &= e^{-im_b v\cdot x}\left[1 + \frac{i\not{D}_\perp}{2m_b} + \mathcal{O}\left(\frac{1}{m_b^2}\right)\right] h(x)\,. \end{aligned}$$

Using this relation, any operator containing the heavy quark field can be written as an expansion in the heavy quark mass. From this relation it is also apparent that the higher order corrections are suppressed by $\Lambda_{\mathrm{QCD}}/m_b$ as the residual perpendicular momentum in the hadron is $\mathcal{O}(\Lambda_{\mathrm{QCD}})$.

After motivating the HQE, we expand the decay matrix of a b hadron in $1/m_b$ as

$$\Gamma = \Gamma_3 + \Gamma_5\frac{\langle\mathcal{O}_5\rangle}{m_b^2} + \Gamma_6\frac{\langle\mathcal{O}_6\rangle}{m_b^3} + \cdots + 16\pi^2\left(\tilde{\Gamma}_6\frac{\langle\tilde{\mathcal{O}}_6\rangle}{m_b^3} + \tilde{\Gamma}_7\frac{\langle\tilde{\mathcal{O}}_7\rangle}{m_b^4} + \ldots\right)\,, \tag{2.78}$$

where the subscripts label the dimension of the transition operators contributing to the decay matrix [27]. All low-energy physics is captured by the operator matrix elements $\langle \mathcal{O}_i \rangle$. The terms Γ_i denote the high-energy contributions to the decays of the free b quark while the terms with $\tilde{\Gamma}_i$ encode the four-quark operator contributions. Therefore, the terms Γ_i do not contribute to the off-diagonal element of the decay matrix, and the leading term in the HQE is contained in $\tilde{\Gamma}_6$. The factor of $16\pi^2$ in Eq. (2.78) is a historical choice of normalisation because the contributions from $\tilde{\Gamma}_i$ have an additional loop as compared to the contributions from Γ_i at the same order in α_s.

For both the diagonal and off-diagonal decay matrix elements, the focus of this thesis is on $\tilde{\Gamma}_6$ as this describes the leading contribution in the HQE to the mixing of B mesons as well as the lifetime ratios. The current status of theoretical calculations of $\tilde{\Gamma}_6$ is presented in Section 1.5.1 and Section 1.5.3 for B meson mixing and lifetime ratios respectively. In the following sections, the respective operator bases for mixing and decays are outlined.

2.4 The $|\Delta B| = 2$ transition operator

The $|\Delta B| = 2$ transition operator to leading power in the HQE is defined via

$$\mathcal{T} \equiv \text{Abs}\left(i \int \mathrm{d}^4 x \, T \, \mathcal{H}^{|\Delta B|=1}(x) \, \mathcal{H}^{|\Delta B|=1}(0) \right) \equiv \frac{G_F^2 m_b^2}{12\pi} \Big[HQ + \tilde{H}_S \tilde{Q}_S \Big] , \qquad (2.79)$$

which can be used in conjunction with Eq. (1.35) to equate the amplitude of the $|\Delta B| = 1$ and $|\Delta B| = 2$ theories and obtain the matching coefficients H and $\tilde{H}_S$. These matching coefficients encode the high-energy effects that are calculated in this thesis. The operator matrix elements $\langle Q \rangle$ and $\langle \tilde{Q}_S \rangle$ contain the low-energy physics, and the matching condition for B meson mixing processes is discussed in more detail in Section 2.6. Here and in the following we use the shorthand notation for operator matrix elements $\langle O \rangle$ to denote $\langle B | O | \bar{B} \rangle$, and the external down-type quark $q \in \{d, s\}$ is left unspecified.

Using the generalised optical theorem from Eq. (1.3) for the off-diagonal decay matrix element, the transition operator can be used to calculate Γ_{12} through

$$\Gamma_{12} = \frac{1}{2M_B} \langle B | \mathcal{T} | \bar{B} \rangle = \frac{G_F^2 m_b^2}{24\pi M_B} \Big[H \langle Q \rangle + \tilde{H}_S \langle \tilde{Q}_S \rangle \Big] + \mathcal{O}(\Lambda_{\text{QCD}}/m_b) \, . \qquad (2.80)$$

2.4.1 Physical operators

Focusing on the dimension-six operators, i.e. the leading contribution to B meson mixing in the HQE, the basis of physical operators consists of two independent operators, but a careful treatment of higher order corrections in the HQE is required to obtain this basis.

In a first step, all amplitudes are mapped for convenience onto three physical operators, which we choose to be

$$\begin{aligned} Q &\equiv 4\left(\bar{q}^c\gamma^\mu P_L b^c\right)\left(\bar{q}^d\gamma_\mu P_L b^d\right), \\ \widetilde{Q}_S &\equiv 4\left(\bar{q}^c P_R b^d\right)\left(\bar{q}^d P_R b^c\right), \\ Q_S &\equiv 4\left(\bar{q}^c P_R b^c\right)\left(\bar{q}^d P_R b^d\right), \end{aligned} \tag{2.81}$$

where c, d are the colour indices of the quark fields. The evanescent operators which are required for the purpose of renormalisation are discussed in Section 2.4.3.

At leading order in the HQE and for the specific process under consideration, the above operators do not constitute a basis as a linear combination of them,

$$R_0 \equiv \frac{1}{2}Q + Q_S + \widetilde{Q}_S, \tag{2.82}$$

is part of the next order in the expansion since $\langle B|R_0|\bar{B}\rangle = \mathcal{O}(\Lambda_{\text{QCD}}/m_b)$ [47]. Eq. (2.82) is hence used to eliminate one of the three original operators. We choose to substitute Q_S for R_0. However, R_0 also contains an evanescent part which is not power-suppressed, meaning that $\langle B|R_0|\bar{B}\rangle^{(n)}$ requires finite renormalisation constants for its finite part to be $\mathcal{O}(\Lambda_{\text{QCD}}/m_b)$ [49]. The calculation of these constants is presented in Ref. [20], and the renormalisation with R_0 is discussed further in Section 2.4.4. Additionally, R_0 needs to be part of the matching calculation due to its evanescent contribution and can only be discarded after the matching procedure, see Section 2.6.1.

2.4.2 Using Fierz symmetry to obtain a basis of evanescent operators

In the following, we provide a detailed description of the steps necessary to pick a basis of evanescent operators which enables the evaluation of renormalised matrix elements that respect Fierz symmetry. The main motivation for setting up the $|\Delta B| = 2$ transition operator in this way is that the low-energy matrix elements, which need to be combined with the high-energy matching coefficients obtained in this thesis, are calculated within four-dimensional frameworks, e.g. lattice gauge theory. Therefore, they automatically obey Fierz symmetry and Fierz identities may be used in the calculation of low-energy matrix elements.

The property of Fierz symmetry and the definition of evanescent operators and hence the renormalisation scheme are closely linked [85, 87]. In the following we present the conditions we impose to preserve the Fierz symmetry of the renormalised matrix elements [20]:

1. The renormalised matrix elements of physical operators are equal to those of their Fierz-transformed counterparts: $\lim_{d\to 4}\langle O\rangle^{\text{ren}} = \lim_{d\to 4}\langle O^F\rangle^{\text{ren}}$.

2. The evanescent operator definitions must be independent of the number of quark flavours N_f.

3. The $\mathcal{O}(\epsilon)$ contributions of physical operators to the evanescent operators must be at most $\mathcal{O}(N_c^0)$ as $N_c \to \infty$. This is because the large-N_c limit of the renormalised physical operator matrix elements fixes the leading term of the NNLO matrix element to be of order N_c^2, and the definition of evanescent operators must not affect this term.

It can be checked that these conditions lead to a unique definition of the leading $\mathcal{O}(N_c^2)$ term of the renormalised physical matrix elements. Also note that in enforcing condition 1, it is convenient to work with off-shell kinematics such that no IR poles occur, but the equality must hold for any choice of IR regulator.

The third condition we impose is more subtle, and hence it is worth explaining its origin from the Vacuum Insertion Approximation (VIA), which also provides further motivation for enforcing Fierz symmetry of the renormalised matrix elements. The VIA is an approximation for the limit as $N_c \to \infty$, i.e. it can be used to calculate the leading term of the matrix elements as well as the first-order correction in $1/N_c$.

The large-N_c limit is implemented by factorising a four-quark operator into two current matrix elements after inserting the vacuum as we will illustrate for the operator $\widetilde{Q}_S$. Introducing the shorthand notation $\Gamma \equiv (1+\gamma_5)$, the matrix element in the VIA is

$$\langle B|\widetilde{Q}_S|\bar{B}\rangle \overset{\text{VIA}}{=} 2\Gamma_{\alpha\beta}\Gamma_{\gamma\delta}\left[\langle B|\bar{q}^c_\alpha b^d_\beta|0\rangle\langle 0|\bar{q}^d_\gamma b^c_\delta|\bar{B}\rangle - \langle B|\bar{q}^c_\alpha b^c_\delta|0\rangle\langle 0|\bar{q}^d_\gamma b^d_\beta|\bar{B}\rangle\right]. \quad (2.83)$$

Here, $\alpha, \beta, \gamma, \delta$ denote spinor indices while the colour indices are c and d. The vacuum insertion leads to four possible Wick contractions of the quark fields with the external fields, and each of the terms in Eq. (2.83) corresponds to two contractions. The relative minus sign is a result of anti-commuting the quark fields.

To compute the matrix element of the second term analytically, the spinor indices need to be swapped on the Dirac matrices by applying a Fierz identity,

$$\Gamma_{\alpha\beta}\Gamma_{\gamma\delta} \overset{\text{Fierz}}{=} \frac{1}{2}\Gamma_{\alpha\delta}\Gamma_{\gamma\beta} + \frac{1}{8}\Big[\sigma_{\mu\nu}(1+\gamma_5)\Big]_{\alpha\delta}\Big[\sigma^{\mu\nu}(1+\gamma_5)\Big]_{\gamma\beta}, \quad (2.84)$$

such that the VIA can be written as

$$\langle B|\widetilde{Q}_S|\bar{B}\rangle \overset{\text{VIA}}{=} 2\langle B|\bar{q}^c\Gamma b^d|0\rangle\langle 0|\bar{q}^d\Gamma b^c|\bar{B}\rangle - \langle B|\bar{q}^c\Gamma b^c|0\rangle\langle 0|\bar{q}^d\Gamma b^d|\bar{B}\rangle. \quad (2.85)$$

For a derivation of generic Fierz identities as well as their application to the specific example given in Eq. (2.84), see Appendix C. The antisymmetric terms with $\sigma^{\mu\nu}$ vanish in the case at hand because there is only one external momentum for the B meson, so we cannot construct any antisymmetric Lorentz tensors. As B mesons are parity odd, only terms with γ_5 will remain in Eq. (2.85). Note also that the mesons are colour singlets, so

$$\langle B|\bar{q}^c\gamma_5 b^d|0\rangle = \frac{1}{N_c}\delta^{cd}\langle B|\bar{q}\gamma_5 b|0\rangle. \quad (2.86)$$

With all of the above considerations, the VIA leads to the result

$$\begin{aligned}\langle B|\widetilde{Q}_S(\mu_2)|\bar{B}\rangle &\overset{\text{VIA}}{=} \left(\frac{2}{N_c}-1\right)\langle B|\bar{q}\gamma_5 b|0\rangle\langle 0|\bar{q}\gamma_5 b|\bar{B}\rangle \\ &= \left(1-\frac{2}{N_c}\right)\frac{f_B^2 M_B^4}{\Big[m_b(\mu_2)+m_q(\mu_2)\Big]^2}\,,\end{aligned} \tag{2.87}$$

where f_B denotes the decay constant of the B meson. This equation fixes the leading $1/N_c$ term. Moreover, it was necessary to apply a Fierz identity in obtaining the result, which further motivates our renormalisation conditions in that regard.

As the result in Eq. (2.87) shows the form of the VIA for the leading order matrix element, it is also instructive to see that the matrix elements go as N_c^n at the nth order in perturbation theory. In the VIA, gluons cannot connect across the two separated current insertions as they annihilate in the vacuum. Therefore, they can only connect across the same spin line as shown in Fig. 2.4. Diagrams where the gluons are attached to the same spin line yield

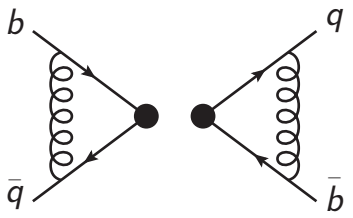

Figure 2.4: NNLO corrections to an operator matrix element in the VIA. The dots represent the factorised current insertions.

additional factors in N_c of the form

$$T^a T^a = \frac{N_c^2-1}{N_c} \sim N_c\,, \tag{2.88}$$

so each order in perturbation theory comes with an additional factor of N_c for the leading term of the VIA.

2.4.3 Definition of evanescent operators

The definitions of all evanescent operators required for the NNLO calculation of Γ_{12} are presented below following a description of the practical implementation of the conditions 1, 2 and 3 from Section 2.4.2.

Before constructing the basis, it is worth discussing the required number of operators. It is sufficient to include only a finite number of evanescent operators to renormalise a given set of operators to a fixed order in perturbation theory even though there is in

principle an infinite number of evanescent operators. Up to order $\mathcal{O}(\alpha_s^2)$, the generations of evanescent operators to be inserted at LO, NLO and NNLO are given in Tab. 2.1 for evanescent operators up to third generation. This is the highest generation which needs to be considered to carry out the matching as described in Section 2.6 since the matrix elements of the third generation appear at LO on the $|\Delta B| = 1$ side. However, only the evanescent operators contributing to the renormalisation of the physical operators, i.e. those up to second generation, need to be fully determined with their correct $\mathcal{O}(\epsilon)$ and $\mathcal{O}(\epsilon^2)$ parts.

To evaluate the Fierz-transformed matrix elements, the basis for those operators is defined first, starting with the physical operators. These are given by

$$\begin{aligned} \widetilde{Q} = Q^F &\equiv 4\left(\bar{q}^c\gamma_\mu P_L b^d\right)\left(\bar{q}^d\gamma^\mu P_L b^c\right), \\ Q_S^F &\equiv \frac{1}{12}Q_T - \frac{1}{6}\widetilde{Q}_T, \\ \widetilde{Q}_S^F &\equiv \frac{1}{12}\widetilde{Q}_T - \frac{1}{6}Q_T, \end{aligned} \tag{2.89}$$

where

$$\begin{aligned} Q_T &\equiv 4\left(\bar{q}^c\sigma^{\mu\nu}P_R b^c\right)\left(\bar{q}^d\sigma_{\mu\nu}P_R b^d\right), \\ \widetilde{Q}_T &\equiv 4\left(\bar{q}^c\sigma^{\mu\nu}P_R b^d\right)\left(\bar{q}^d\sigma_{\mu\nu}P_R b^c\right). \end{aligned} \tag{2.90}$$

This is a result of applying the familiar Fierz identity

$$(P_R)_{\alpha\beta}(P_R)_{\gamma\delta} = \frac{1}{8}(\sigma^{\mu\nu}P_R)_{\alpha\delta}(\sigma_{\mu\nu}P_R)_{\gamma\beta} + \frac{1}{2}(P_R)_{\alpha\delta}(P_R)_{\gamma\beta}. \tag{2.91}$$

It is worth noting that Q and the corresponding evanescent operators renormalise separately from Q_S and $\widetilde{Q}_S$ and their respective evanescent operators because the odd and even numbers of γ matrices do not mix. This also holds true for the Fierz-transformed basis.

The first generation evanescent operators with an odd number of γ matrices are defined as

$$\begin{aligned} E_1^{(1)}[Q] &\equiv Q - \widetilde{Q}, \\ E_2^{(1)}[Q] &\equiv 4\left(\bar{q}^c\gamma_{\mu_1}\gamma_{\mu_2}\gamma_{\mu_3}P_L b^d\right)\left(\bar{q}^d\gamma^{\mu_3}\gamma^{\mu_2}\gamma^{\mu_1}P_L b^c\right) - \left(4 + \tilde{f}\epsilon + \tilde{g}\epsilon^2\right)\widetilde{Q}, \\ E_3^{(1)}[Q] &\equiv 4\left(\bar{q}^c\gamma_{\mu_1}\gamma_{\mu_2}\gamma_{\mu_3}P_L b^c\right)\left(\bar{q}^d\gamma^{\mu_3}\gamma^{\mu_2}\gamma^{\mu_1}P_L b^d\right) - \left(4 + f\epsilon + g\epsilon^2\right)Q. \end{aligned} \tag{2.92}$$

The operator $E_1^{(1)}[Q]$ appears because the colour-flipped version of Q, i.e. $\widetilde{Q}$, is also the Fierz-transformed operator and not part of the regular basis. Therefore, an additional evanescent operator is introduced as compared to the case of an even number of γ matrices, corresponding to the renormalisation of $\{Q_S, \widetilde{Q}_S\}$, where the evanescent operators of the

first generation are

$$\begin{aligned}
E^{(1)}[Q_S] \equiv\, & 4\left(\bar{q}^c\gamma_{\mu_1}\gamma_{\mu_2}P_R b^c\right)\left(\bar{q}^d\gamma^{\mu_2}\gamma^{\mu_1}P_R b^d\right) + \left(8+\tilde{a}\epsilon+\tilde{b}\epsilon^2\right)\widetilde{Q}_S \\
& - \left(a\epsilon+b\epsilon^2\right)Q_S\,, \\
E^{(1)}[\widetilde{Q}_S] \equiv\, & 4\left(\bar{q}^c\gamma_{\mu_1}\gamma_{\mu_2}P_R b^d\right)\left(\bar{q}^d\gamma^{\mu_2}\gamma^{\mu_1}P_R b^c\right) + \left(8+\tilde{a}_2\epsilon+\tilde{b}_2\epsilon^2\right)Q_S \\
& - \left(a_2\epsilon+b_2\epsilon^2\right)\widetilde{Q}_S\,.
\end{aligned} \tag{2.93}$$

These operators first appear in the NLO diagrams of the $|\Delta B| = 2$ theory, and for the renormalisation of physical operators to $\mathcal{O}(\alpha_s)$, the ϵ^2 terms are not required.

For the Fierz-transformed basis, the first generation evanescent operators with an odd number of γ matrices are defined similarly as

$$\begin{aligned}
E_1^{(1)}[Q^F] &\equiv E_1^{(1)}[Q]\,, \\
E_2^{(1)}[Q^F] &\equiv E_2^{(1)}[Q]\,, \\
E_3^{(1)}[Q^F] &\equiv E_3^{(1)}[Q]\,.
\end{aligned} \tag{2.94}$$

Note that this choice implies that the ϵ and ϵ^2 coefficients are identical for Q and Q^F, which is permissible because the relation between the Fierz-transformed operators is relatively simple. For the operators with an even number of γ matrices, the Fierz-transformed operators have slightly more complicated definitions, see Eq. (2.89), and it is not possible to choose the same definition for the regular and Fierz-transformed basis beyond NLO. In anticipation of this and to be completely exhaustive, we allow for more freedom in the definitions of the first generation evanescent operators:

$$\begin{aligned}
E^{(1)}[Q_S^F] \equiv\, & -\frac{2}{3}\left(\bar{q}^c\gamma_{\mu_1}\gamma_{\mu_2}\sigma^{\mu\nu}\gamma^{\mu_2}\gamma^{\mu_1}P_R b^d\right)\left(\bar{q}^d\sigma_{\mu\nu}P_R b^c\right) \\
& + \frac{1}{3}\left(\bar{q}^c\gamma_{\mu_1}\gamma_{\mu_2}\sigma^{\mu\nu}P_R b^c\right)\left(\bar{q}^d\sigma_{\mu\nu}P_R\gamma^{\mu_2}\gamma^{\mu_1}b^d\right) \\
& + \left(8+\tilde{a}^F\epsilon+\tilde{b}^F\epsilon^2\right)\widetilde{Q}_S^F - \left(a^F\epsilon+b^F\epsilon^2\right)Q_S^F\,, \\
E^{(1)}[\widetilde{Q}_S^F] \equiv\, & -\frac{2}{3}\left(\bar{q}^c\gamma_{\mu_1}\gamma_{\mu_2}\sigma^{\mu\nu}\gamma^{\mu_2}\gamma^{\mu_1}P_R b^c\right)\left(\bar{q}^d\sigma_{\mu\nu}P_R b^d\right) \\
& + \frac{1}{3}\left(\bar{q}^c\gamma_{\mu_1}\gamma_{\mu_2}\sigma^{\mu\nu}P_R b^d\right)\left(\bar{q}^d\sigma_{\mu\nu}P_R\gamma^{\mu_2}\gamma^{\mu_1}b^c\right) \\
& + \left(8+\tilde{a}_2^F\epsilon+\tilde{b}_2^F\epsilon^2\right)Q_S^F - \left(a_2^F\epsilon+b_2^F\epsilon^2\right)\widetilde{Q}_S^F\,.
\end{aligned} \tag{2.95}$$

Note that the definition of the evanescent operators for calculations up to a finite order in α_s, in our case up to α_s^2, can only be fixed to the same order in ϵ, i.e. to ϵ^2 here. Therefore, even after determining the constants in front of the physical operators in Eq. (2.95), the definitions have arbitrary $\mathcal{O}(\epsilon^3)$ terms, and a choice of evanescent operators which differs in those terms is equally valid. The particular choice of evanescent operators here is

convenient for manual calculations on the $|\Delta B| = 2$ side at NLO as the spinor structures appearing in diagrams can be directly identified with the evanescent operators.

In order to impose condition 1 from Section 2.4.2, the amplitudes $\langle Q\rangle^{(1),\text{ren}}$, $\langle Q_S\rangle^{(1),\text{ren}}$ and $\langle \widetilde{Q}_S\rangle^{(1),\text{ren}}$ and $\langle \widetilde{Q}\rangle^{(1),\text{ren}}$, $\langle Q_S^F\rangle^{(1),\text{ren}}$ and $\langle \widetilde{Q}_S^F\rangle^{(1),\text{ren}}$ are calculated in the standard and Fierz-transformed basis respectively. The standard basis amplitudes are obtained from tree-level and one-loop diagrams of the operators in Eqs. (2.81), (2.92) and (2.93) together with the corresponding renormalisation constants, which need to be computed too. Similarly, the calculation in the Fierz-transformed basis proceeds with the operators in Eqs. (2.89), (2.94) and (2.95) and their renormalisation constants. For a discussion of the setup of amplitudes for the determination of renormalisation constants see Section 3.2, where the regularisation of IR divergences in those amplitudes is explained.

When comparing the renormalised amplitudes of a standard operator $\langle O\rangle^{\text{ren}}$ with its Fierz-transformed counterpart $\langle O^F\rangle^{\text{ren}}$, the amplitudes should be expressed in a basis of operator matrix elements, which could be either the standard or Fierz-transformed operators. However, at this point the amplitudes are finite, and the tree-level matrix elements of the Fierz-transformed operators can be identified with the standard operators, dropping an evanescent difference in the process. In practice, one sets the coefficient of e.g. $\langle Q_S\rangle^{(0)}$ in a renormalised amplitude like $\langle Q_S\rangle^{(1),\text{ren}}$ equal to the coefficient of $\langle Q_S^F\rangle^{(0)}$ in the renormalised amplitude $\langle Q_S^F\rangle^{(1),\text{ren}}$.

Hence, the definition of the evanescent operators of the first generation,

$$\begin{aligned} a = a_2 &= 0\,, & \tilde{a} = \tilde{a}_2 &= -8\,,\\ a^F = a_2^F &= 0\,, & \tilde{a}^F = \tilde{a}_2^F &= -8\,,\\ f = \tilde{f} &= -8\,. \end{aligned} \tag{2.96}$$

is obtained. This agrees with the results given in the literature, see e.g. Refs. [49, 54, 87, 107].

At $\mathcal{O}(\alpha_s^2)$, the second generation of evanescent operators needs to be considered, and the ϵ^2 terms in the first generation operators in Eqs. (2.92) through (2.95) appear in the physical amplitudes. The second generation evanescent operators with an odd number of γ matrices are

$$\begin{aligned} E_1^{(2)}[Q] \equiv\ & 4\Big(\bar{q}^c\gamma_{\mu_1}\gamma_{\mu_2}\gamma_{\mu_3}\gamma_{\mu_4}\gamma_{\mu_5}P_L b^d\Big)\Big(\bar{q}^d\gamma^{\mu_5}\gamma^{\mu_4}\gamma^{\mu_3}\gamma^{\mu_2}\gamma^{\mu_1}P_L b^c\Big)\\ & -\Big(16+\tilde{h}\epsilon+\tilde{k}\epsilon^2\Big)\widetilde{Q},\\ E_2^{(2)}[Q] \equiv\ & 4\Big(\bar{q}^c\gamma_{\mu_1}\gamma_{\mu_2}\gamma_{\mu_3}\gamma_{\mu_4}\gamma_{\mu_5}P_L b^c\Big)\Big(\bar{q}^d\gamma^{\mu_5}\gamma^{\mu_4}\gamma^{\mu_3}\gamma^{\mu_2}\gamma^{\mu_1}P_L b^d\Big)\\ & -\Big(16+h\epsilon+k\epsilon^2\Big)Q\,. \end{aligned} \tag{2.97}$$

Analogous to the first generation, we define the second generation evanescent operators with an even number of γ matrices as

$$\begin{aligned}
E^{(2)}[Q_S] \equiv\, & 4\left(\bar{q}^c\gamma_{\mu_1}\gamma_{\mu_2}\gamma_{\mu_3}\gamma_{\mu_4}P_R b^c\right)\left(\bar{q}^d\gamma^{\mu_4}\gamma^{\mu_3}\gamma^{\mu_2}\gamma^{\mu_1}P_R b^d\right) \\
& + \left(128 + \tilde{c}\epsilon + \tilde{d}\epsilon^2\right)\widetilde{Q}_S - \left(c\epsilon + d\epsilon^2\right)Q_S\,, \\
E^{(2)}[\widetilde{Q}_S] \equiv\, & 4\left(\bar{q}^c\gamma_{\mu_1}\gamma_{\mu_2}\gamma_{\mu_3}\gamma_{\mu_4}P_R b^d\right)\left(\bar{q}^d\gamma^{\mu_4}\gamma^{\mu_3}\gamma^{\mu_2}\gamma^{\mu_1}P_R b^c\right) \\
& + \left(128 + \tilde{c}_2\epsilon + \tilde{d}_2\epsilon^2\right)Q_S - \left(c_2\epsilon + d_2\epsilon^2\right)\widetilde{Q}_S\,.
\end{aligned} \tag{2.98}$$

On the Fierz-transformed side, the evanescent operators with an odd number of γ matrices are again chosen to be identical to those of the standard basis,

$$\begin{aligned}
E_1^{(2)}[Q^F] &\equiv E_1^{(2)}[Q]\,, \\
E_2^{(2)}[Q^F] &\equiv E_2^{(2)}[Q]\,,
\end{aligned} \tag{2.99}$$

and for the evanescent operators with an even number of γ matrices, we define

$$\begin{aligned}
E^{(2)}[Q_S^F] \equiv\, & -\frac{2}{3}\left(\bar{q}^c\gamma_{\mu_1}\gamma_{\mu_2}\gamma_{\mu_3}\gamma_{\mu_4}\sigma^{\mu\nu}\gamma^{\mu_4}\gamma^{\mu_3}\gamma^{\mu_2}\gamma^{\mu_1}P_R b^d\right)\left(\bar{q}^d\sigma_{\mu\nu}P_R b^c\right) \\
& + \frac{1}{3}\left(\bar{q}^c\gamma_{\mu_1}\gamma_{\mu_2}\gamma_{\mu_3}\gamma_{\mu_4}\sigma^{\mu\nu}P_R b^c\right)\left(\bar{q}^d\sigma_{\mu\nu}P_R\gamma^{\mu_4}\gamma^{\mu_3}\gamma^{\mu_2}\gamma^{\mu_1}b^d\right) \\
& + \left(128 + \tilde{c}^F\epsilon + \tilde{d}^F\epsilon^2\right)\widetilde{Q}_S^F - \left(c^F\epsilon + d^F\epsilon^2\right)Q_S^F\,, \\
E^{(2)}[\widetilde{Q}_S^F] \equiv\, & -\frac{2}{3}\left(\bar{q}^c\gamma_{\mu_1}\gamma_{\mu_2}\gamma_{\mu_3}\gamma_{\mu_4}\sigma^{\mu\nu}\gamma^{\mu_4}\gamma^{\mu_3}\gamma^{\mu_2}\gamma^{\mu_1}P_R b^c\right)\left(\bar{q}^d\sigma_{\mu\nu}P_R b^d\right) \\
& + \frac{1}{3}\left(\bar{q}^c\gamma_{\mu_1}\gamma_{\mu_2}\gamma_{\mu_3}\gamma_{\mu_4}\sigma^{\mu\nu}P_R b^d\right)\left(\bar{q}^d\sigma_{\mu\nu}P_R\gamma^{\mu_4}\gamma^{\mu_3}\gamma^{\mu_2}\gamma^{\mu_1}b^c\right) \\
& + \left(128 + \tilde{c}_2^F\epsilon + \tilde{d}_2^F\epsilon^2\right)Q_S^F - \left(c_2^F\epsilon + d_2^F\epsilon^2\right)\widetilde{Q}_S^F\,.
\end{aligned} \tag{2.100}$$

Equating the renormalised amplitudes in the standard and Fierz-transformed bases proceeds in a similar fashion as for the NLO definitions. After imposing condition 1, we can further examine the N_f terms only and impose condition 2 to yield the ϵ^2 terms of the first generation evanescent operators,

$$\begin{aligned}
b = b_2 &= 4\,, & \tilde{b} = \tilde{b}_2 &= 0\,, \\
b^F = b_2^F &= 4\,, & \tilde{b}^F = \tilde{b}_2^F &= 0\,, \\
g = \tilde{g} &= 4\,.
\end{aligned} \tag{2.101}$$

This is consistent with the definitions used in the literature, see for example Ref. [51].

For the c, d, h and k coefficients of the second generation evanescent operators, we obtain a solution space. The coefficients of all tree-level matrix elements must agree individually for condition 1, so we obtain a number of equations for the aforementioned constants. We solve the equations for $\{c, \tilde{c}, d, \tilde{d}, h, \tilde{h}\}$, leaving the rest of the constants undetermined.

Imposing condition 3, the coefficients of N_c and N_c^2 in the solutions of the evanescent constants must vanish, so another set of equations can be obtained to further reduce the dimensionality of the solution space. Note that in imposing condition 3 on the solutions for $\{c, \tilde{c}, d, \tilde{d}, h, \tilde{h}\}$, we have chosen a particular subset of the solution space. This particular solution sub-space consistent with all physical conditions from Section 2.4.2 is given in Ref. [20].

In practice, it is useful to pick a unique solution from the full set of allowed definitions, which simplifies the intermediate steps. We find it convenient to choose as many of the constants appearing in the standard operator basis as possible to be equal to zero. Therefore, we choose the simplest version of the second generation evanescent operators with an even number of γ matrices,

$$c = c_2 = \tilde{c} = d = d_2 = \tilde{d} = \tilde{d}_2 = 0\,, \tag{2.102}$$

and discard the ϵ^2 terms of the second generation evanescent operators of Q and $\widetilde{Q}$,

$$k = \tilde{k} = 0\,. \tag{2.103}$$

The unique solution for the second generation which results from this choice is given by

$$\begin{aligned}
\tilde{c}_2 &= -1024\,,\\
c^F &= \frac{-256(534 - 344\,N_c - 119\,N_c^2 - 366\,N_c^3 - 116\,N_c^4 + 163\,N_c^5)}{15(8 - 16\,N_c^2 + 2\,N_c^3 + 2\,N_c^4 + N_c^5)}\,,\\
c_2^F &= \frac{256(92 + 46\,N_c + 164\,N_c^2 + 104\,N_c^3 + 141\,N_c^4 + 17\,N_c^5)}{15(8 - 16\,N_c^2 + 2\,N_c^3 + 2\,N_c^4 + N_c^5)}\,,\\
\tilde{c}^F &= \frac{-128(196 - 220\,N_c + 26\,N_c^2 - 445\,N_c^3 + 256\,N_c^4 + 226\,N_c^5)}{15(8 - 16\,N_c^2 + 2\,N_c^3 + 2\,N_c^4 + N_c^5)}\,,\\
\tilde{c}_2^F &= \frac{128(172 - 608\,N_c - 138\,N_c^2 - 730\,N_c^3 + 120\,N_c^4 + 25\,N_c^5)}{15(8 - 16\,N_c^2 + 2\,N_c^3 + 2\,N_c^4 + N_c^5)}\,,\\
d^F &= \frac{-32(1958 - 2608\,N_c + 6957\,N_c^2 - 3572\,N_c^3 - 2697\,N_c^4 + 1391\,N_c^5)}{15(8 - 16\,N_c^2 + 2\,N_c^3 + 2\,N_c^4 + N_c^5)}\,,\\
d_2^F &= \frac{64(92 + 46\,N_c + 164\,N_c^2 + 104\,N_c^3 + 141\,N_c^4 + 17\,N_c^5)}{15(8 - 16\,N_c^2 + 2\,N_c^3 + 2\,N_c^4 + N_c^5)}\,,\\
\tilde{d}^F &= \frac{-32(-964 - 1550\,N_c + 2696\,N_c^2 - 3610\,N_c^3 + 411\,N_c^4 + 1061\,N_c^5)}{15(8 - 16\,N_c^2 + 2\,N_c^3 + 2\,N_c^4 + N_c^5)}\,,\\
\tilde{d}_2^F &= \frac{32(1132 - 608\,N_c - 2058\,N_c^2 - 490\,N_c^3 + 360\,N_c^4 + 145\,N_c^5)}{15(8 - 16\,N_c^2 + 2\,N_c^3 + 2\,N_c^4 + N_c^5)}\,,\\
h &= \frac{-64(-98 - 158\,N_c + 23\,N_c^2 + 30\,N_c^3)}{-14 - 14\,N_c - 7\,N_c^2 + 6\,N_c^3}\,,\\
\tilde{h} &= -448\,.
\end{aligned} \tag{2.104}$$

The particular solution for the second generation provided here is useful because the evanescent operators for Q_S and $\widetilde{Q}_S$ have only one non-vanishing constant, $\tilde{c}_2$, which is also N_c-independent. The evanescent operators for Q and $\widetilde{Q}$ are also simple and have no ϵ^2 terms. The trade-off is that the Fierz-transformed basis is more complicated, but this is not relevant as it is not used in any calculations.

An interesting feature that appears for the first time at NNLO is that the definitions of the evanescent operators are now QCD-specific as they depend on N_c. This is because condition 1 is applied to the renormalised amplitudes which contain QCD corrections and an explicit dependence on N_c.

The operator definitions introduced so far are sufficient to renormalise physical matrix elements at NNLO, but they need to be supplemented by the definitions of all evanescent operators that appear in the matching, see Section 2.6. The evanescent operators up to second generation have been defined above, and we will give the corresponding definitions of the third to fifth generation below.

For the additional generations of evanescent operators, it is sufficient to only determine the correct vanishing ϵ-finite part, so all $\mathcal{O}(\epsilon)$ constants in front of physical operators can be left undetermined and drop out of the matching. When working with penguin operators, the highest generation of evanescent operators that appears at LO is the third generation. These operators need to be renormalised to NNLO, so we will also require the fourth and fifth generation. We define the third generation generically as

$$\begin{aligned}
E_1^{(3)} &\equiv 4\big(\bar{q}^c\gamma_{\mu_1}\cdots\gamma_{\mu_7}P_L b^d\big)\big(\bar{q}^d\gamma^{\mu_7}\cdots\gamma^{\mu_1}P_L b^c\big) - \big(64+\mathcal{O}(\epsilon)\big)\widetilde{Q}\,,\\
E_2^{(3)} &\equiv 4\big(\bar{q}^c\gamma_{\mu_1}\cdots\gamma_{\mu_7}P_L b^c\big)\big(\bar{q}^d\gamma^{\mu_7}\cdots\gamma^{\mu_1}P_L b^d\big) - \big(64+\mathcal{O}(\epsilon)\big)Q\,,\\
E^{(3)}[Q_S] &\equiv 4\big(\bar{q}^c\gamma_{\mu_1}\cdots\gamma_{\mu_6}P_R b^c\big)\big(\bar{q}^d\gamma^{\mu_6}\cdots\gamma^{\mu_1}P_R b^d\big)\\
&\quad + \big(2048+\mathcal{O}(\epsilon)\big)\widetilde{Q}_S + \mathcal{O}(\epsilon)Q_S\,,\\
E^{(3)}[\widetilde{Q}_S] &\equiv 4\big(\bar{q}^c\gamma_{\mu_1}\cdots\gamma_{\mu_6}P_R b^d\big)\big(\bar{q}^d\gamma^{\mu_6}\cdots\gamma^{\mu_1}P_R b^c\big)\\
&\quad + \big(2048+\mathcal{O}(\epsilon)\big)Q_S + \mathcal{O}(\epsilon)\widetilde{Q}_S\,,
\end{aligned} \tag{2.105}$$

and the fourth generation as

$$\begin{aligned}
E_1^{(4)} &\equiv 4\big(\bar{q}^c\gamma_{\mu_1}\cdots\gamma_{\mu_9}P_L b^d\big)\big(\bar{q}^d\gamma^{\mu_9}\cdots\gamma^{\mu_1}P_L b^c\big) - \big(256+\mathcal{O}(\epsilon)\big)\widetilde{Q}\,,\\
E_2^{(4)} &\equiv 4\big(\bar{q}^c\gamma_{\mu_1}\cdots\gamma_{\mu_9}P_L b^c\big)\big(\bar{q}^d\gamma^{\mu_9}\cdots\gamma^{\mu_1}P_L b^d\big) - \big(256+\mathcal{O}(\epsilon)\big)Q\,,\\
E^{(4)}[Q_S] &\equiv 4\big(\bar{q}^c\gamma_{\mu_1}\cdots\gamma_{\mu_8}P_R b^c\big)\big(\bar{q}^d\gamma^{\mu_8}\cdots\gamma^{\mu_1}P_R b^d\big)\\
&\quad + \big(32768+\mathcal{O}(\epsilon)\big)\widetilde{Q}_S + \mathcal{O}(\epsilon)Q_S\,,\\
E^{(4)}[\widetilde{Q}_S] &\equiv 4\big(\bar{q}^c\gamma_{\mu_1}\cdots\gamma_{\mu_8}P_R b^d\big)\big(\bar{q}^d\gamma^{\mu_8}\cdots\gamma^{\mu_1}P_R b^c\big)\\
&\quad + \big(32768+\mathcal{O}(\epsilon)\big)Q_S + \mathcal{O}(\epsilon)\widetilde{Q}_S\,,
\end{aligned} \tag{2.106}$$

and finally the fifth generation as

$$\begin{aligned}
E_1^{(5)} &\equiv 4\Big(\bar{q}^c\gamma_{\mu_1}\cdots\gamma_{\mu_{11}}P_L b^d\Big)\Big(\bar{q}^d\gamma^{\mu_{11}}\cdots\gamma^{\mu_1}P_L b^c\Big) - \Big(1024+\mathcal{O}(\epsilon)\Big)\widetilde{Q}\,,\\
E_2^{(5)} &\equiv 4\Big(\bar{q}^c\gamma_{\mu_1}\cdots\gamma_{\mu_{11}}P_L b^c\Big)\Big(\bar{q}^d\gamma^{\mu_{11}}\cdots\gamma^{\mu_1}P_L b^d\Big) - \Big(1024+\mathcal{O}(\epsilon)\Big)Q\,,\\
E^{(5)}[Q_S] &\equiv 4\Big(\bar{q}^c\gamma_{\mu_1}\cdots\gamma_{\mu_{10}}P_R b^c\Big)\Big(\bar{q}^d\gamma^{\mu_{10}}\cdots\gamma^{\mu_1}P_R b^d\Big)\\
&\quad + \Big(524288+\mathcal{O}(\epsilon)\Big)\widetilde{Q}_S + \mathcal{O}(\epsilon)Q_S\,,\\
E^{(5)}[\widetilde{Q}_S] &\equiv 4\Big(\bar{q}^c\gamma_{\mu_1}\cdots\gamma_{\mu_{10}}P_R b^d\Big)\Big(\bar{q}^d\gamma^{\mu_{10}}\cdots\gamma^{\mu_1}P_R b^c\Big)\\
&\quad + \Big(524288+\mathcal{O}(\epsilon)\Big)Q_S + \mathcal{O}(\epsilon)\widetilde{Q}_S\,.
\end{aligned} \tag{2.107}$$

2.4.4 Renormalisation with the R_0 operator

The renormalisation procedure of the $|\Delta B| = 2$ theory follows for the most part the steps described in Section 2.1.3, but the $\Lambda_{\mathrm{QCD}}/m_b$ suppression of $\langle B|R_0|\bar{B}\rangle$ requires a special treatment, which will be discussed in the following. As the renormalisation procedure is process-independent, one may choose to renormalise the amplitude with a basis of physical operators like $\{Q, Q_S, \widetilde{Q}_S\}$ or $\{Q, \widetilde{Q}_S, R_0\}$. The power-suppression of R_0 is a result of the particular process that is being considered. To preserve it at higher loop orders, a finite counterterm is introduced, but the UV divergences are unaffected.

It is convenient to calculate the renormalisation constants first in the basis of physical operators $\{Q, Q_S, \widetilde{Q}_S\}$ as the operator Q does not mix with the other two. Note that switching one of the operators for R_0 does not simplify the calculation because the power-suppression of its matrix element is an on-shell phenomenon. Therefore, it is not applicable to the renormalisation, which encodes the off-shell properties of the transition operator. The renormalisation matrix for general N_c obtained in this way is given in Ref. [20], and for illustration purposes we list the $\overline{\mathrm{MS}}$ renormalisation constants of the physical operators here:

$$\begin{aligned}
Z_Q^{(1,1)} &= 2\,, \qquad Z_Q^{(2,2)} = -9+\frac{2}{3}N_f\,, \qquad Z_Q^{(2,1)} = -\frac{45815}{516}+\frac{1}{9}N_f\,,\\
Z_{Q_S\widetilde{Q}_S}^{(1,1)} &= \begin{pmatrix} -\frac{14}{3} & \frac{2}{3} \\ \frac{8}{3} & \frac{16}{3}\end{pmatrix}, \qquad Z_{Q_S\widetilde{Q}_S}^{(2,2)} = \begin{pmatrix} \frac{337}{9}-\frac{14N_f}{9} & -\frac{31}{9}+\frac{2N_f}{9} \\ -\frac{124}{9}+\frac{8N_f}{9} & -\frac{128}{9}+\frac{16N_f}{9}\end{pmatrix},\\
Z_{Q_S\widetilde{Q}_S}^{(2,1)} &= \begin{pmatrix} \frac{547}{9}+\frac{22N_f}{27} & -\frac{227}{9}+\frac{2N_f}{27} \\ \frac{1235}{6}-\frac{19N_f}{27} & \frac{641}{18}-\frac{83N_f}{27}\end{pmatrix},
\end{aligned} \tag{2.108}$$

where $N_c = 3$, and the basis of evanescent operators defined via Eqs. (2.101) to (2.104) was chosen. The renormalised operators are hence given by

$$Q = Z_Q\, Q^{\text{bare}} + Z_{QE}\, \vec{E}^{\text{bare}}\,, \qquad \begin{pmatrix} Q_S \\ \widetilde{Q}_S \end{pmatrix} = Z_{Q_S\widetilde{Q}_S} \begin{pmatrix} Q_S^{\text{bare}} \\ \widetilde{Q}_S^{\text{bare}} \end{pmatrix} + Z_{Q_SE}\, \vec{E}^{\text{bare}}\,, \tag{2.109}$$

where the mixing with the evanescent operators is shown schematically.

After obtaining the renormalisation matrix in the basis without R_0, the matrix is then transformed through a change of basis. In the following, we will consider bases which are extended by a vector of all relevant evanescent operators $\vec{E}$ to demonstrate the effect on the renormalisation constants of evanescent operators too. The basis transformation can be naively carried out by equating the renormalised operators,

$$\begin{pmatrix} Q \\ \widetilde{Q}_S \\ \frac{1}{2}Q + \widetilde{Q}_S + Q_S \\ \vec{E} \end{pmatrix}_{\{Q,Q_S,\widetilde{Q}_S\}} = \begin{pmatrix} Q \\ \widetilde{Q}_S \\ R_0 \\ \vec{E} \end{pmatrix}^{\text{naive}}_{\{Q,\widetilde{Q}_S,R_0\}}\,, \tag{2.110}$$

where the renormalised operators are related to the bare operators through $\mathcal{O}_i = Z_{ij}\mathcal{O}_j^{\text{bare}}$. In order to solve for the new renormalisation matrix, the bare operators are substituted using Eq. (2.82), which leads to the "naive" renormalisation matrix

$$Z^{\text{naive}} = (Z_1^{\text{naive}}, Z_2^{\text{naive}}, Z_3^{\text{naive}}, Z_4^{\text{naive}}) \tag{2.111}$$

for the $\{Q, \widetilde{Q}_S, R_0, \vec{E}\}$ basis. The individual components are given by

$$Z_1^{\text{naive}} = \begin{pmatrix} Z_Q \\ -\frac{1}{2}\left(Z_{Q_S\widetilde{Q}_S}\right)_{21} \\ \frac{1}{2}\left[Z_Q - \left(Z_{Q_S\widetilde{Q}_S}\right)_{11} - \left(Z_{Q_S\widetilde{Q}_S}\right)_{21}\right] \\ Z_{EQ} - \frac{1}{2}Z_{EQ_S} \end{pmatrix},$$

$$Z_2^{\text{naive}} = \begin{pmatrix} 0 \\ -\left(Z_{Q_S\widetilde{Q}_S}\right)_{21} + \left(Z_{Q_S\widetilde{Q}_S}\right)_{22} \\ -\left(Z_{Q_S\widetilde{Q}_S}\right)_{11} + \left(Z_{Q_S\widetilde{Q}_S}\right)_{12} - \left(Z_{Q_S\widetilde{Q}_S}\right)_{21} + \left(Z_{Q_S\widetilde{Q}_S}\right)_{22} \\ Z_{E\widetilde{Q}_S} - Z_{EQ_S} \end{pmatrix},$$

$$Z_3^{\text{naive}} = \begin{pmatrix} 0 \\ \left(Z_{Q_S\widetilde{Q}_S}\right)_{21} \\ \left(Z_{Q_S\widetilde{Q}_S}\right)_{11} + \left(Z_{Q_S\widetilde{Q}_S}\right)_{21} \\ Z_{EQ_S} \end{pmatrix},$$

$$Z_4^{\text{naive}} = \begin{pmatrix} Z_{QE} \\ Z_{\widetilde{Q}_S E} \\ \frac{1}{2}Z_{QE} + Z_{Q_S E} + Z_{\widetilde{Q}_S E} \\ Z_{EE} \end{pmatrix}. \tag{2.112}$$

However, as previously mentioned, the power-suppression of the matrix element of R_0 requires finite renormalisation constants, which are not contained in Eq. (2.112). These renormalisation constants are necessary to cancel terms proportional to $\langle Q\rangle^{(0)}$ and $\langle\widetilde{Q}_S\rangle^{(0)}$ in the renormalised $\langle R_0\rangle$ matrix element in the physical basis $\{Q, \widetilde{Q}_S, R_0\}$. As R_0 contains a leading-power evanescent part, it needs to be renormalised with a finite piece similar to other evanescent operators. Otherwise, it may be multiplied with IR divergences, leading to finite contributions in dimensional regularisation [54].

The finite renormalisation constants can be constructed from considering the linear combination of the renormalised Q, $\widetilde{Q}_S$ and Q_S matrix elements,

$$\langle R_0\rangle = \frac{1}{2}\alpha_1\langle Q\rangle + \alpha_2\langle\widetilde{Q}_S\rangle + \langle Q_S\rangle\,, \tag{2.113}$$

which we require to be suppressed by Λ_{QCD}/m_b. The coefficients α_1 and α_2 are perturbative quantities with the expansions

$$\alpha_i = 1 + \frac{\alpha_s}{4\pi}\alpha_i^{(1)} + \left(\frac{\alpha_s}{4\pi}\right)^2\alpha_i^{(2)} + \mathcal{O}(\alpha_s^3)\,. \tag{2.114}$$

The coefficient of Q_S in Eq. (2.113) was chosen to be equal to one. This eliminates a degree of freedom stemming from a perturbative redefinition of R_0. For a discussion of the calculation of the constants α_i, in particular the regularisation of IR divergences with a massive gluon, see Refs. [20, 28].

Equipped with the constants α_i, the renormalisation matrix including the finite renormalisation for R_0 is obtained by amending Eq. (2.110) as

$$\begin{pmatrix} Q \\ \widetilde{Q}_S \\ \frac{1}{2}\alpha_1 Q + \alpha_2\widetilde{Q}_S + Q_S \\ E \end{pmatrix}_{\{Q,Q_S,\widetilde{Q}_S\}} = \begin{pmatrix} Q \\ \widetilde{Q}_S \\ R_0 \\ E \end{pmatrix}_{\{Q,\widetilde{Q}_S,R_0\}}. \tag{2.115}$$

This set of equations can be solved to yield the renormalisation matrix

$$Z = (Z_1, Z_2, Z_3, Z_4), \tag{2.116}$$

where

$$Z_1 = \begin{pmatrix} Z_Q \\ -\frac{1}{2}\left(Z_{Q_S\widetilde{Q}_S}\right)_{21} \\ \frac{1}{2}\left[\alpha_1 Z_Q - \left(Z_{Q_S\widetilde{Q}_S}\right)_{11} - \alpha_2\left(Z_{Q_S\widetilde{Q}_S}\right)_{21}\right] \\ Z_{EQ} - \frac{1}{2}Z_{EQ_S} \end{pmatrix},$$

$$Z_2 = \begin{pmatrix} 0 \\ -\left(Z_{Q_S\widetilde{Q}_S}\right)_{21} + \left(Z_{Q_S\widetilde{Q}_S}\right)_{22} \\ -\left(Z_{Q_S\widetilde{Q}_S}\right)_{11} + \left(Z_{Q_S\widetilde{Q}_S}\right)_{12} - \alpha_2\left(Z_{Q_S\widetilde{Q}_S}\right)_{21} + \alpha_2\left(Z_{Q_S\widetilde{Q}_S}\right)_{22} \\ Z_{E\widetilde{Q}_S} - Z_{EQ_S} \end{pmatrix},$$

$$Z_3 = \begin{pmatrix} 0 \\ \left(Z_{Q_S\widetilde{Q}_S}\right)_{21} \\ \left(Z_{Q_S\widetilde{Q}_S}\right)_{11} + \alpha_2\left(Z_{Q_S\widetilde{Q}_S}\right)_{21} \\ Z_{EQ_S} \end{pmatrix},$$

$$Z_4 = \begin{pmatrix} Z_{QE} \\ Z_{\widetilde{Q}_S E} \\ \frac{1}{2}\alpha_1 Z_{QE} + Z_{Q_S E} + \alpha_2 Z_{\widetilde{Q}_S E} \\ Z_{EE} \end{pmatrix}. \tag{2.117}$$

The interpretation of α_1 and α_2 as finite renormalisation constants materialises here because they multiply the diagonal elements Z_Q and $(Z_{Q_S\widetilde{Q}_S})_{22}$ and therefore lead to an ϵ-finite contribution.

The full renormalisation matrix is provided in computer-readable format with Ref. [20]. As many generations of evanescent operators need to be included, the resulting matrices are large and hence not shown here.

2.5 The $|\Delta B| = 0$ transition operator

In this section, the relevant $|\Delta B| = 0$ transition operator for the calculation of lifetime ratios is developed by considering the leading term in the HQE that results in a non-zero lifetime difference. Referring to Eq. (2.78), the leading contribution to b decays in the HQE stems from the decay of the free bottom quark, and the corrections due to the different spectator quark flavours, e.g. up or down quarks, start with $\tilde{\Gamma}_6$. We can therefore write the decay width $\Gamma(H_b)$ of any bottom-flavoured hadron with light quarks H_b as the sum of a leading contribution $\Gamma(b)$ from the decay of the free bottom quark and corrections $\delta\Gamma(H_b)$,

$$\Gamma(H_b) = \Gamma(b) + \delta\Gamma(H_b)\,, \tag{2.118}$$

where the corrections $\delta\Gamma(H_b)$ are specific to the b hadron under consideration and suppressed by at least two powers of Λ_{QCD}/m_b. A lifetime ratio can thus be written as

$$\frac{\tau(H_b)}{\tau(H_b')} \approx 1 + \left[\delta\Gamma(H_b') - \delta\Gamma(H_b)\right] \times \tau(H_b)\,, \tag{2.119}$$

up to higher-order terms in Λ_{QCD}/m_b that were omitted in $\delta\Gamma(H_b^{(\prime)})$. Here, the decay width of the free bottom quark drops out, and the experimental value for $\tau(H_b)$ is used, such that only the calculations of $\delta\Gamma(H_b)$ and $\delta\Gamma(H_b')$ are required to predict the lifetime ratio [32]. Due to isospin symmetry, the two-quark operator contributions Γ_i from Eq. (2.78) drop out in the lifetime ratio of B^+ and B_d as well as the corresponding baryons. Therefore, the leading contribution stems from $\tilde{\Gamma}_6$.

The $|\Delta B| = 0$ transition operator for the lifetimes is defined as

$$\mathcal{T} \equiv \text{Im}\left(i \int \mathrm{d}^4x\, T\, \mathcal{H}^{|\Delta B|=1}(x)\, \mathcal{H}^{|\Delta B|=1}(0)\right), \tag{2.120}$$

and it is related to the decay width via the optical theorem, see Eq. (1.41),

$$\delta\Gamma(H_b) = \frac{1}{2M_{H_b}} \langle H_b|\mathcal{T}|H_b\rangle\,. \tag{2.121}$$

For the leading-power corrections, the relevant transition operator is further decomposed as

$$\mathcal{T} = \mathcal{T}_u + \mathcal{T}_d + \mathcal{T}_{\text{sing}}\,, \tag{2.122}$$

where the subscript refers to the quark flavour in the intermediate state of the LO CKM-leading process. The SU(3)_F singlet operator $\mathcal{T}_{\text{sing}}$ contains contributions which cancel in the difference of lifetime corrections [58]. These singlet contributions stem from gluon exchanges with the spectator quark, which is why they are flavour-independent and cancel in the lifetime ratio, see Fig. 2.5. In the following, only $\mathcal{T}_u$ and $\mathcal{T}_d$ will be considered.

For mesons at leading order, the operator $\mathcal{T}_u$ corresponds to the weak annihilation (WA) while $\mathcal{T}_d$ mediates Pauli interference (PI), see Fig. 2.6. In the case of baryons, $\mathcal{T}_u$ leads to

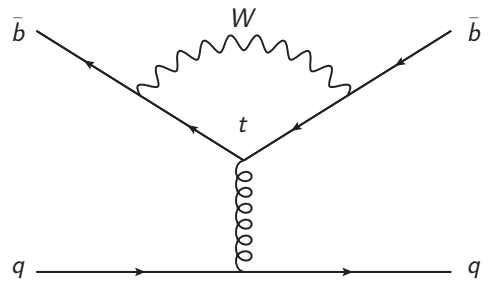

(a) Full theory

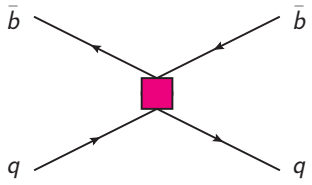

(b) Operator in $\mathcal{T}_{\text{sing}}$

Figure 2.5: Singlet operator with the underlying penguin topology in the full theory. These operators couple to all active quark flavours, which is why they are singlets under $\text{SU}(3)_\text{F}$.

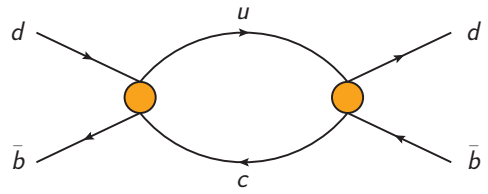

(a) Weak annihilation

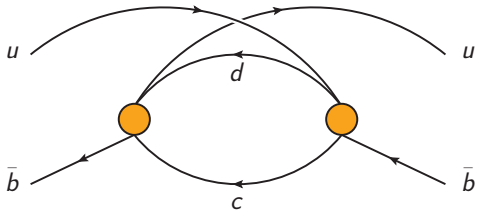

(b) Pauli interference

Figure 2.6: Leading-CKM one-loop diagrams of the WA and PI topologies for mesons. The orange dots represent current-current operator insertions.

the weak scattering (WS) process while the insertion of $\mathcal{T}_d$ again corresponds to PI, see Fig. 2.7.

The non-singlet parts of the transition operator can be further written as [58]

$$\begin{aligned}\mathcal{T}_u \equiv \frac{G_F^2 m_b^2 |V_{cb}|^2}{6\pi}\Big[&|V_{ud}|^2\left(F^u Q^d + F_S^u Q_S^d + G^u T^d + G_S^u T_S^d\right)\\ &+ |V_{cd}|^2\left(F^c Q^d + F_S^c Q_S^d + G^c T^d + G_S^c T_S^d\right)\Big],\\ \mathcal{T}_d \equiv \frac{G_F^2 m_b^2 |V_{cb}|^2}{6\pi}\Big[&F^d Q^u + F_S^d Q_S^u + G^d T^u + G_S^d T_S^u\Big]. \end{aligned} \tag{2.123}$$

Note that the WA operator for B_s mesons is identical to $\mathcal{T}_u$ above after swapping the down-type quark $d \to s$. The superscripts on the matching coefficients F^q, F_S^q, G^q and G_S^q refer to the quark flavour q in the cq pair of quarks in the loop. To be explicit, the u matching coefficients stem from the WA and WS diagrams shown in Fig. 2.6a and Fig. 2.7a while the d matching coefficients correspond to the PI diagrams in Fig. 2.6b and

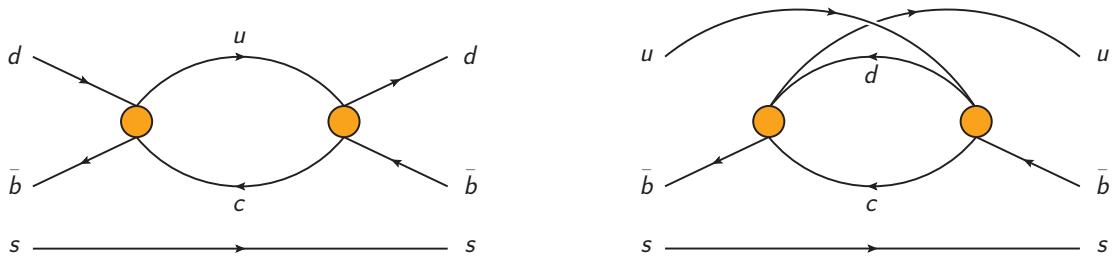

(a) Weak scattering

(b) Pauli interference

Figure 2.7: Leading-CKM one-loop diagrams of the WS and PI topologies for baryons. The orange dots represent current-current operator insertions.

Fig. 2.6b. Finally, the c contributions match onto WA and WS diagrams in the $|\Delta B| = 1$ calculations with two charm quarks in the internal loop. Doubly CKM-suppressed operators have been ignored, and the relation $|V_{ud}|^2 + |V_{us}|^2 \approx 1$ together with $C^d = C^s$ for all matching coefficients C was used to simplify the PI transition operator. The equality of the matching coefficients holds under the assumption that the down and strange quarks have the same mass, in particular $m_d = m_s = 0$.

The physical $|\Delta B| = 0$ operators are defined as

$$\begin{aligned} Q^q &\equiv 4\big(\bar{b}\gamma_\mu P_L q\big)\big(\bar{q}\gamma^\mu P_L b\big), & Q_S^q &\equiv 4\big(\bar{b}P_L q\big)\big(\bar{q}P_R b\big), \\ T^q &\equiv 4\big(\bar{b}\gamma_\mu P_L T^a q\big)\big(\bar{q}\gamma^\mu P_L T^a b\big), & T_S^q &\equiv 4\big(\bar{b}P_L T^a q\big)\big(\bar{q}P_R T^a b\big). \end{aligned} \tag{2.124}$$

We also need to define the first and second generation evanescent operators to renormalise the physical operators at NNLO. The first generation is

$$\begin{aligned} E^{(1)}[Q^q] &\equiv 4\big(\bar{b}\gamma^{\mu_1}\gamma^{\mu_2}\gamma^{\mu_3}P_L q\big)\big(\bar{q}\gamma_{\mu_3}\gamma_{\mu_2}\gamma_{\mu_1}P_L b\big) - \big(4 - 8\epsilon + a\epsilon^2\big)Q^q, \\ E^{(1)}[Q_S^q] &\equiv 4\big(\bar{b}\gamma^{\mu_1}\gamma^{\mu_2}P_L q\big)\big(\bar{q}\gamma_{\mu_2}\gamma_{\mu_1}P_R b\big) - \big(4 - 8\epsilon + a_S\epsilon^2\big)Q_S^q, \end{aligned} \tag{2.125}$$

with analogous definitions for the $E[T^q_{(S)}]$ operators, which have the generators T^a of $\mathrm{SU}(3)_C$ inserted. The second generation is given by

$$\begin{aligned} E[Q^q]^{(2)} &\equiv 4\big(\bar{b}\gamma^{\mu_1}\gamma^{\mu_2}\gamma^{\mu_3}\gamma^{\mu_4}\gamma^{\mu_5}P_L q\big)\big(\bar{q}\gamma_{\mu_5}\gamma_{\mu_4}\gamma_{\mu_3}\gamma_{\mu_2}\gamma_{\mu_1}P_L b\big) \\ &\quad - \big(16 + b\epsilon + c\epsilon^2\big)Q^q, \\ E[Q_S^q]^{(2)} &\equiv 4\big(\bar{b}\gamma^{\mu_1}\gamma^{\mu_2}\gamma^{\mu_3}\gamma^{\mu_4}P_L q\big)\big(\bar{q}\gamma_{\mu_4}\gamma_{\mu_3}\gamma_{\mu_2}\gamma_{\mu_1}P_R b\big) \\ &\quad - \big(16 + b_S\epsilon + c_S\epsilon^2\big)Q_S^q, \end{aligned} \tag{2.126}$$

and similar evanescent operators for the colour octet structures. The constants $a_{(S)}$, $b_{(S)}$ and $c_{(S)}$ appear in renormalised amplitudes at NNLO; however, they do not appear in

physical results when the perturbative matching coefficients are combined with the low energy matrix elements. Since the lattice calculations do not make use of Fierz identities for the $|\Delta B| = 0$ matrix elements, we are free to choose the constants as we wish. As a check, the dependence of the physical results on the aforementioned constants must disappear when matching the lattice results to the perturbative matching coefficients, e.g. with the gradient flow formalism [108–110]. This is in contrast with the $|\Delta B| = 2$ transition operator, where the definitions of the evanescent operators are determined by the requirement of Fierz symmetry.

In intermediate steps before the matching, we also encounter the third generation evanescent operators, which we define as

$$\begin{aligned} E^{(3)}[Q^q] &\equiv 4\left(\bar{b}\gamma^{\mu_1}\cdots\gamma^{\mu_7}P_L q\right)\left(\bar{q}\gamma_{\mu_7}\cdots\gamma_{\mu_1}P_L b\right) - \left(64 + e\epsilon + f\epsilon^2\right)Q^q, \\ E^{(3)}[Q_S^q] &\equiv 4\left(\bar{b}\gamma^{\mu_1}\cdots\gamma^{\mu_6}P_L q\right)\left(\bar{q}\gamma_{\mu_6}\cdots\gamma_{\mu_1}P_R b\right) - \left(64 + e_S\epsilon + f_S\epsilon^2\right)Q_S^q\,, \end{aligned} \quad (2.127)$$

and similarly for the corresponding operators $E[T^q_{(S)}]$. The constants $e_{(S)}$ and $f_{(S)}$ drop out of the matching coefficients and do not need to be considered in the matching to low-energy matrix elements. The reason that only the third generation is required for the decays whereas up to five generations appear in the mixing calculation is the inclusion of different operators on the $|\Delta B| = 1$ sides. In Section 2.6, the number of generations necessary for the matching calculation is discussed in detail.

The renormalisation constants for the $|\Delta B| = 0$ transition operator are given in Appendix B.

2.6 Matching procedure

2.6.1 Matching to the $|\Delta B| = 2$ transition operator

In the following, the matching of the amplitudes calculated with the weak effective Hamiltonian to the $|\Delta B| = 2$ transition operators is discussed. Most of the steps presented can be easily transferred to the matching to the $|\Delta B| = 0$ transition operator, and some key differences are explained in Section 2.6.2.

The matching condition from Eq. (1.35) reads

$$\Gamma_{12}^{ij} = \frac{1}{M_B}\mathrm{Im}\left(\mathcal{M}^{ij}\right)\,, \quad (2.128)$$

and recalling that the off-diagonal decay matrix element is calculated from the absorptive part of a bi-local matrix element in Eq. (2.80), we write

$$\Gamma_{12}^{ij} = \frac{G_F^2 m_b^2}{24\pi M_{B_q}}\left[H^{ij}(z)\langle B_q|Q|\bar{B}_q\rangle + \widetilde{H}_S^{ij}(z)\langle B_q|\widetilde{Q}_S|\bar{B}_q\rangle\right] + \mathcal{O}(\Lambda_{\mathrm{QCD}}/m_b)\,, \quad (2.129)$$

where the factorisation of the CKM matrix elements from Eq. (1.34) was used. The matching coefficients are determined in this thesis as an expansion in $z = m_c^2/m_b^2$ up to $\mathcal{O}(z^{10})$.

The matching coefficients can be evaluated from the bottom up, order by order in α_s, i.e. calculating the matching coefficients first at LO, then NLO and so on. Here, it is crucial to also note the order in ϵ to which the matching coefficients are computed. This is important because both the amplitude $\mathcal{M}$ evaluated with the effective $|\Delta B| = 1$ Hamiltonian and the matrix elements of the $|\Delta B| = 2$ transition operator have IR poles beyond LO. Since the IR and UV divergences are regulated with the same regulator ϵ, it is important to carry out lower-order matching calculations beyond the ϵ-finite order. This way, the poles in ϵ cancel, and we recover the correct finite contributions which arise from divergences multiplying matching coefficients vanishing in the limit $d \to 4$. The power of ϵ to which the matching coefficients need to be evaluated is hence determined by the IR poles appearing in front of those matching coefficients. It turns out that the LO and NLO matching coefficients need to be expanded up to ϵ^2 and ϵ^1 respectively.

Another issue that deserves special consideration is the number of generations of evanescent operators to be renormalised at each order on the $|\Delta B| = 2$ side for the matching. This is determined by the loop order of the $|\Delta B| = 1$ calculation at which the tree-level matrix elements of the corresponding evanescent operators first appear, as is illustrated below.

The matching equation Eq. (2.128) can be expanded in α_s and ϵ. For this purpose, we define the expansion of the matching coefficients

$$H^{ij} = H^{(0),ij} + \frac{\alpha_s}{4\pi} H^{(1),ij} + \left(\frac{\alpha_s}{4\pi}\right)^2 H^{(2),ij} + \mathcal{O}(\alpha_s^3)\,, \tag{2.130}$$

as well as similar expansions for Γ_{12}^{ij}, $\mathcal{M}^{ij}$ and the renormalised matrix elements $\langle O\rangle \equiv \langle B|O|\bar{B}\rangle$. The LO matching equation reads

$$(\Gamma_{12}^{ij})^{(0)} = \frac{G_F^2 m_b^2}{24\pi M_{B_q}} \left[H_P^{(0),ij}\langle P\rangle^{(0)} + H_E^{(0),ij}\langle E\rangle^{(0)}\right], \tag{2.131}$$

where the operators P and E stand for any physical and evanescent operator respectively. Note that for the purpose of this discussion, R_0 is treated like an evanescent operator, i.e. $P \in \{Q, \widetilde{Q}_S\}$. This is because after carrying out the renormalisation as outlined in Section 2.4.4, including the finite renormalisation constants from α_1 and α_2, the physical piece of $\langle R_0\rangle$ is suppressed by Λ_{QCD}/m_b, but the evanescent part is unsuppressed, see Ref. [54].

The LO amplitude in the $|\Delta B| = 1$ effective theory is also expanded in ϵ,

$$\begin{aligned}\text{Im}(\mathcal{M}^{ij})^{(0)} = \frac{G_F^2 m_b^2}{24\pi}\Big[&\left(a^{(0,0)} + \epsilon a^{(0,1)} + \epsilon^2 a^{(0,2)} + \mathcal{O}(\epsilon^3)\right)\langle P\rangle^{(0)} \\ &+ \left(b^{(0,0)} + \epsilon b^{(0,1)} + \epsilon^2 b^{(0,2)} + \mathcal{O}(\epsilon^3)\right)\langle E\rangle^{(0)}\Big]\,,\end{aligned} \tag{2.132}$$

so by equating Eq. (2.131) and Eq. (2.132), the LO matching coefficients

$$\begin{aligned} H_P^{(0),ij} &= a^{(0,0)} + \epsilon a^{(0,1)} + \epsilon^2 a^{(0,2)} + \mathcal{O}(\epsilon^3)\,, \\ H_E^{(0),ij} &= b^{(0,0)} + \epsilon b^{(0,1)} + \epsilon^2 b^{(0,2)} + \mathcal{O}(\epsilon^3) \end{aligned} \tag{2.133}$$

are obtained.

At NLO, the matching proceeds analogously, but IR poles appear for the first time, so it is interesting to observe their impact on the computation of the matching coefficients. The transition operator contribution to the decay matrix element is decomposed as

$$\begin{aligned} (\Gamma_{12}^{ij})^{(1)} = \frac{G_F^2 m_b^2}{24\pi M_{B_q}} \Big[& H_P^{(0),ij} \langle P \rangle^{(1)} + H_P^{(1),ij} \langle P \rangle^{(0)} \\ & + H_E^{(0),ij} \langle E \rangle^{(1)} + H_E^{(1),ij} \langle E \rangle^{(0)} \Big]\,, \end{aligned} \tag{2.134}$$

where the operator matrix elements are further expanded as a series in ϵ,

$$\begin{aligned} \langle P \rangle^{(1)} &= \left(\frac{c^{(1,-1)}}{\epsilon} + c^{(1,0)} + \epsilon c^{(1,1)} + \mathcal{O}(\epsilon^2) \right) \langle P \rangle^{(0)} \\ &\quad + \left(\frac{d^{(1,-1)}}{\epsilon} + d^{(1,0)} + \epsilon d^{(1,1)} + \mathcal{O}(\epsilon^2) \right) \langle E \rangle^{(0)}\,, \\ \langle E \rangle^{(1)} &= \left(e^{(1,0)} + \epsilon e^{(1,1)} + \mathcal{O}(\epsilon^2) \right) \langle P \rangle^{(0)} \\ &\quad + \left(\frac{f^{(1,-1)}}{\epsilon} + f^{(1,0)} + \epsilon f^{(1,1)} + \mathcal{O}(\epsilon^2) \right) \langle E \rangle^{(0)}\,. \end{aligned} \tag{2.135}$$

The evanescent operators are of order ϵ, so the renormalised NLO matrix element has at most a finite $\mathcal{O}(\epsilon^0)$ part stemming from IR poles. This means, however, that there are no poles multiplying the physical matrix elements $\langle P \rangle^{(0)}$. The amplitude obtained from the weak effective Hamiltonian at NLO can be similarly expanded as

$$\begin{aligned} \mathrm{Im}(\mathcal{M}^{ij})^{(1)} = \frac{G_F^2 m_b^2}{24\pi} \Bigg[& \left(\frac{a^{(1,-1)}}{\epsilon} + a^{(1,0)} + \epsilon a^{(1,1)} + \mathcal{O}(\epsilon^2) \right) \langle P \rangle^{(0)} \\ & + \left(\frac{b^{(1,-1)}}{\epsilon} + b^{(1,0)} + \epsilon b^{(1,1)} + \mathcal{O}(\epsilon^2) \right) \langle E \rangle^{(0)} \Bigg]\,. \end{aligned} \tag{2.136}$$

The NLO matching coefficients are obtained by inserting Eq. (2.135) into Eq. (2.134) and then equating with Eq. (2.136). They have the following expansion in ϵ:

$$\begin{aligned} H_P^{(1),ij} &= \frac{a^{(1,-1)}}{\epsilon} + a^{(1,0)} + \epsilon a^{(1,1)} - \left(\frac{c^{(1,-1)}}{\epsilon} + c^{(1,0)} + \epsilon c^{(1,1)} \right) H_P^{(0),ij} \\ &\quad - \left(e^{(1,0)} + \epsilon e^{(1,1)} \right) H_E^{(0),ij} + \mathcal{O}(\epsilon^2) \,, \\ H_E^{(1),ij} &= \frac{b^{(1,-1)}}{\epsilon} + b^{(1,0)} + \epsilon b^{(1,1)} - \left(\frac{f^{(1,-1)}}{\epsilon} + f^{(1,0)} + \epsilon f^{(1,1)} \right) H_E^{(0),ij} \\ &\quad - \left(\frac{d^{(1,-1)}}{\epsilon} + d^{(1,0)} + \epsilon d^{(1,1)} \right) H_P^{(0),ij} + \mathcal{O}(\epsilon^2) \,. \end{aligned} \tag{2.137}$$

These matching coefficients show two key mechanisms in the matching of IR-divergent amplitudes: the cancellation of the IR poles in the matching coefficients and the contribution of $\mathcal{O}(\epsilon)$ terms from lower-order matching coefficients to physical results. For the NLO matching coefficients to be finite, we require that

$$a^{(1,-1)} - c^{(1,-1)} H_P^{(0),ab} = \mathcal{O}(\epsilon) \,, \tag{2.138}$$

which serves as a cross-check for the matching calculation. Furthermore, since the pole $c^{(1,-1)}/\epsilon$ multiplies the LO matching coefficient $H_P^{(0),ij}$, the term $a^{(0,1)}$ from Eq. (2.133) contributes to the physical NLO matching coefficient $H_P^{(1),ij}$, which demonstrates that lower-order matching coefficients require deeper expansions in ϵ.

At NNLO, no new features arise, but the expressions become more involved. For the transition operator, the expansion is

$$\begin{aligned} (\Gamma_{12}^{ij})^{(2)} = \frac{G_F^2 m_b^2}{24\pi M_{B_q}} \Big[& H_P^{(0),ij} \langle P \rangle^{(2)} + H_P^{(1),ij} \langle P \rangle^{(1)} + H_P^{(2),ij} \langle P \rangle^{(0)} \\ & + H_E^{(0),ij} \langle E \rangle^{(2)} + H_E^{(1),ij} \langle E \rangle^{(1)} + H_E^{(2),ij} \langle E \rangle^{(0)} \Big] \,, \end{aligned} \tag{2.139}$$

where the renormalised matrix elements are parametrised in a similar way as for the NLO calculation:

$$\begin{aligned} \langle P \rangle^{(2)} &= \left(\frac{c^{(2,-2)}}{\epsilon^2} + \frac{c^{(2,-1)}}{\epsilon} + c^{(2,0)} \right) \langle P \rangle^{(0)} + \left(\frac{d^{(2,-2)}}{\epsilon^2} + \frac{d^{(2,-1)}}{\epsilon} + d^{(2,0)} \right) \langle E \rangle^{(0)} \,, \\ \langle E \rangle^{(2)} &= \left(\frac{e^{(2,-1)}}{\epsilon} + e^{(2,0)} \right) \langle P \rangle^{(0)} + \left(\frac{f^{(2,-2)}}{\epsilon^2} + \frac{f^{(2,-1)}}{\epsilon} + f^{(2,0)} \right) \langle E \rangle^{(0)} \,. \end{aligned} \tag{2.140}$$

On the $|\Delta B| = 1$ side, the amplitude is written as

$$\mathrm{Im}(\mathcal{M}^{ij})^{(2)} = \frac{G_F^2 m_b^2}{24\pi}\Bigg[\left(\frac{a^{(2,-2)}}{\epsilon^2} + \frac{a^{(2,-1)}}{\epsilon} + a^{(2,0)} + \mathcal{O}(\epsilon)\right)\langle P\rangle^{(0)} + \left(\frac{b^{(2,-2)}}{\epsilon^2} + \frac{b^{(2,-1)}}{\epsilon} + b^{(2,0)} + \mathcal{O}(\epsilon)\right)\langle E\rangle^{(0)}\Bigg]. \tag{2.141}$$

As before, Eq. (2.140) is inserted into Eq. (2.139) and equated with Eq. (2.141) to obtain the NNLO matching coefficients, which have the expansions

$$\begin{aligned}
H_P^{(2),ab} &= \frac{a^{(2,-2)}}{\epsilon^2} + \frac{a^{(2,-1)}}{\epsilon} + a^{(2,0)} - e^{(1,0)} H_E^{(1),ab} - \left(\frac{c^{(1,-1)}}{\epsilon} + c^{(1,0)}\right) H_P^{(1),ab} \\
&\quad - \left(\frac{e^{(2,-1)}}{\epsilon} + e^{(2,0)}\right) H_E^{(0),ab} - \left(\frac{c^{(2,-2)}}{\epsilon^2} + \frac{c^{(2,-1)}}{\epsilon} + c^{(2,0)}\right) H_P^{(0),ab} + \mathcal{O}(\epsilon)\,, \\
H_E^{(2),ab} &= \frac{b^{(2,-2)}}{\epsilon^2} + \frac{b^{(2,-1)}}{\epsilon} + b^{(2,0)} - \left(\frac{f^{(1,-1)}}{\epsilon} + f^{(1,0)}\right) H_E^{(1),ab} \\
&\quad - \left(\frac{d^{(1,-1)}}{\epsilon} + d^{(1,0)}\right) H_P^{(1),ab} - \left(\frac{f^{(2,-2)}}{\epsilon^2} + \frac{f^{(2,-1)}}{\epsilon} + f^{(2,0)}\right) H_E^{(0),ab} \\
&\quad - \left(\frac{d^{(2,-2)}}{\epsilon^2} + \frac{d^{(2,-1)}}{\epsilon} + d^{(2,0)}\right) H_P^{(0),ab} + \mathcal{O}(\epsilon).
\end{aligned} \tag{2.142}$$

The cancellation of all IR poles in ϵ provides yet another cross-check of the matching calculation, leading to similar conditions as the one given in Eq. (2.138). We also observe that the LO and NLO matching coefficients are multiplied by poles in ϵ such that their $\mathcal{O}(\epsilon^2)$ and $\mathcal{O}(\epsilon)$ parts respectively contribute to the finite parts of the NNLO matching coefficients.

The matching procedure provides another powerful cross-check on our calculation as the gauge parameter dependence must cancel in the process. The amplitudes calculated with the weak effective Hamiltonian and the $|\Delta B| = 2$ transition operator depend on the gauge parameter ξ of the strong interaction. The gauge parameter stems from the gluon propagator,

$$\Delta_{\mu\nu}^{ab} = \frac{i\delta^{ab}}{k^2}\left(g^{\mu\nu} - (1-\xi)\frac{k^\mu k^\nu}{k^2}\right), \tag{2.143}$$

where the gauge $\xi = 1$ corresponds to Feynman-t'Hooft gauge. Since physical observables must not depend on the choice of gauge, the matching coefficients must be independent of ξ. Working in the general R_ξ gauge, one can check that the gauge parameter cancels in the matching.

Using the above results, we return to the issue of the number of generations of evanescent operators to include in the matching. From Eq. (2.142), we can see that the LO and NLO matching coefficients of evanescent operators, $H_E^{(0)}$ and $H_E^{(1)}$, contribute to the matching coefficients of physical operators. The way that the evanescent matching coefficients enter the physical result is through the renormalised matrix elements of evanescent operators, as is evident from Eq. (2.139). Therefore, evanescent operators whose tree-level matrix elements appear in the LO calculation on the $|\Delta B| = 1$ side, i.e. in Eq. (2.132), must be renormalised to NNLO. The evanescent operators for which the matrix elements are encountered at NLO for the first time, i.e. in Eq. (2.136), need to be renormalised to NLO.

In general terms, the highest generation k_{max} of evanescent operators for which there are tree-level matrix elements in the amplitude calculated from the $|\Delta B| = 1$ Hamiltonian needs to be renormalised to the highest order n in α_s. The matrix elements of all $k \leq k_{\text{max}}$ generations are renormalised to the same order in α_s while higher generations $k > k_{\text{max}}$ are renormalised to the order α_s^m given by

$$m = n - (k - k_{\text{max}}) \,. \tag{2.144}$$

To illustrate the above, we will consider two cases: the contribution from two current-current and two penguin operators respectively at NNLO, which are presented in Tab. 2.2. For the first case with two current-current operators, the matrix elements of the first generation evanescent operators appear in the LO calculation of the $|\Delta B| = 1$ side, so they need to be renormalised to NNLO. At NLO, the tree-level matrix elements of the second generation appear, meaning they have to be renormalised to NLO. The renormalised amplitude of the $|\Delta B| = 2$ transition operator hence includes the third, second and first generation of evanescent operators to LO, NLO and NNLO respectively. For the case with two penguin operator insertions, the tree-level matrix elements of the third, fourth and fifth generation evanescent operators appear respectively at LO, NLO and NNLO in the calculation of the $|\Delta B| = 1$ side. Therefore, they are renormalised on the $|\Delta B| = 2$ side to NNLO and NLO for evanescent operators belonging to the third and fourth generation respectively. For the fifth generation, no renormalisation is required.

An exhaustive list of $|\Delta B| = 2$ operator matrix elements that appear in calculations of Γ_{12} using the $|\Delta B| = 1$ effective Hamiltonian is given in Tab. 2.3. In principle, it is sufficient to identify the highest generation evanescent operators whose matrix elements appear at the lowest order in α_s and then determine the orders to which all other generations need to be renormalised using Eq. (2.144). With Tab. 2.3 this can be confirmed for all considered operators.

Operators	LO diagram on $\lvert\Delta B\rvert = 1$ side	Highest evanescent generation at LO	Required renormalised $\lvert\Delta B\rvert = 2$ matrix elements
$Q_{1,2} \times Q_{1,2}$	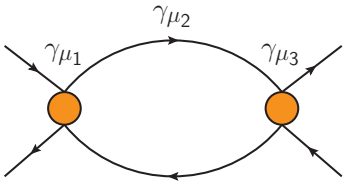	$\langle E_i^{(1)} \rangle^{(0)}$	$\langle E_i^{(1)} \rangle^{(2)}$, $\langle E_i^{(2)} \rangle^{(1)}$
$Q_{3\text{–}6} \times Q_{3\text{–}6}$	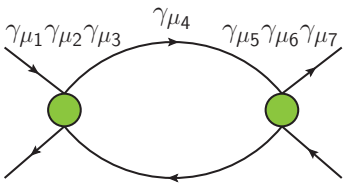	$\langle E_i^{(3)} \rangle^{(0)}$	$\langle E_i^{(3)} \rangle^{(2)}$, $\langle E_i^{(2)} \rangle^{(2)}$, $\langle E_i^{(1)} \rangle^{(2)}$, $\langle E_i^{(4)} \rangle^{(1)}$

Table 2.2: The evanescent operators required on the $\lvert\Delta B\rvert = 2$ side for a NNLO matching calculation depend on the physical operators included on the $\lvert\Delta B\rvert = 1$ side.

Order	$\lvert\Delta B\rvert = 1$ operators	Highest generation evanescent $\lvert\Delta B\rvert = 2$ operator matrix elements
α_s^0	$Q_{1,2} \times Q_{1,2}$	$\langle E_i^{(1)} \rangle^{(0)}$
	$Q_{1,2} \times Q_{3\text{–}6}$	$\langle E_i^{(1)} \rangle^{(0)}$
	$Q_{3\text{–}6} \times Q_{3\text{–}6}$	$\langle E_i^{(3)} \rangle^{(0)}$
α_s^1	$Q_{1,2} \times Q_{1,2}$	$\langle E_i^{(2)} \rangle^{(0)}$
	$Q_{1,2} \times Q_{3\text{–}6}$	$\langle E_i^{(2)} \rangle^{(0)}$
	$Q_{3\text{–}6} \times Q_{3\text{–}6}$	$\langle E_i^{(4)} \rangle^{(0)}$
	$Q_8 \times Q_{1\text{–}6}$	$\langle E_i^{(1)} \rangle^{(0)}$
α_s^2	$Q_{1,2} \times Q_{1,2}$	$\langle E_i^{(3)} \rangle^{(0)}$
	$Q_{1,2} \times Q_{3\text{–}6}$	$\langle E_i^{(3)} \rangle^{(0)}$
	$Q_{3\text{–}6} \times Q_{3\text{–}6}$	$\langle E_i^{(5)} \rangle^{(0)}$
	$Q_8 \times Q_{1\text{–}6}$	$\langle E_i^{(2)} \rangle^{(0)}$
	$Q_8 \times Q_8$	$\langle E_i^{(2)} \rangle^{(0)}$
α_s^3	$Q_8 \times Q_8$	$\langle E_i^{(3)} \rangle^{(0)}$

Table 2.3: Tree-level $\lvert\Delta B\rvert = 2$ operator matrix elements which appear in the amplitude on the $\lvert\Delta B\rvert = 1$ side at each order in α_s.

2.6.2 Matching to the $|\Delta B| = 0$ transition operator

The procedure for the B meson decays is similar to the one outlined in Section 2.6.1, so the focus of this section is on highlighting the steps that are specific to the $|\Delta B| = 0$ calculation. The key aspect of the $|\Delta B| = 0$ matching is that we are only interested in the difference of the decay widths since we are calculating the lifetime ratio, see Eq. (2.119). As the matching procedure is the same for the meson and baryon lifetime ratios, only the mesonic case is discussed in the following. There is, however, a difference in the treatment of the hadronic matrix elements, which is discussed in Section 6.2.

Both $\mathcal{T}_u$ and $\mathcal{T}_d$ contribute to both $\delta\Gamma(B_d)$ and $\delta\Gamma(B^+)$, and in evaluating the difference, we can use the isospin symmetry relations

$$\begin{aligned}
&\langle B_d|Q^{d,u}|B_d\rangle = \langle B^+|Q^{u,d}|B^+\rangle\,, \qquad \langle B_d|T^{d,u}|B_d\rangle = \langle B^+|T^{u,d}|B^+\rangle\,,\\
&\langle B_d|Q_S^{d,u}|B_d\rangle = \langle B^+|Q_S^{u,d}|B^+\rangle\,, \qquad \langle B_d|T_S^{d,u}|B_d\rangle = \langle B^+|T_S^{u,d}|B^+\rangle\,.
\end{aligned} \tag{2.145}$$

The lifetime ratio for B_d and B^+ mesons can hence be written in a compact form with the matching coefficients in Eq. (2.123) and the expansion of the lifetime ratio to the first non-trivial order in the HQE from Eq. (2.119):

$$\begin{aligned}
\frac{\tau(B^+)}{\tau(B_d)} &= 1 + \Big[\delta\Gamma(B_d) - \delta\Gamma(B^+)\Big] \times \tau(B^+)\\
&= 1 + \left[\frac{G_F^2 m_b^2 |V_{cb}|^2}{12\pi} f_B^2 M_B \left(|V_{ud}|^2 \vec{F}^u + |V_{cd}|^2 \vec{F}^c - \vec{F}^d\right)\cdot \vec{B}\right] \times \tau(B^+)\,,
\end{aligned} \tag{2.146}$$

where the vector notation

$$\vec{F}^q = \begin{pmatrix} F^q \\ F_S^q \\ G^q \\ G_S^q \end{pmatrix}\,, \qquad \vec{B} = \begin{pmatrix} B_1 \\ B_2 \\ \epsilon_1 \\ \epsilon_2 \end{pmatrix} \tag{2.147}$$

was introduced following Ref. [58]. The constants in $\vec{B}$ contain the low-energy physics and are related to the matrix elements via

$$\begin{aligned}
\left\langle B^+ \left| \left(Q^u - Q^d\right) \right| B^+ \right\rangle &= f_B^2\, M_B^2\, B_1\,,\\
\left\langle B^+ \left| \left(Q_S^u - Q_S^d\right) \right| B^+ \right\rangle &= f_B^2\, M_B^2\, B_2\,,\\
\left\langle B^+ \left| \left(T^u - T^d\right) \right| B^+ \right\rangle &= f_B^2\, M_B^2\, \epsilon_1\,,\\
\left\langle B^+ \left| \left(T_S^u - T_S^d\right) \right| B^+ \right\rangle &= f_B^2\, M_B^2\, \epsilon_2\,.
\end{aligned} \tag{2.148}$$

It is worth noting that the matrix elements $\langle B^+|\mathcal{O}^d|B^+\rangle$ for $\mathcal{O} \in \{Q, Q_S, T, T_S\}$ drop out of the lifetime ratios to good approximation but yield small contributions to the total decay rates [111, 112].

Since both the calculation of $\delta\Gamma(B_d)$ and $\delta\Gamma(B^+)$ leads to the matching coefficients $\vec{F}^u$, $\vec{F}^c$ and $\vec{F}^d$, we can simplify the calculation by ignoring redundant information. The path we choose is to calculate $\delta\Gamma(B_d)$ and $\delta\Gamma(B^+)$ separately, and to match only onto the $|\Delta B| = 0$ matrix elements which start at LO, i.e. $\langle B_d|\mathcal{O}^d|B_d\rangle$ and $\langle B^+|\mathcal{O}^u|B^+\rangle$ respectively. This means the matching of $\delta\Gamma(B_d)$ yields $\vec{F}^u$ and $\vec{F}^c$ while we extract $\vec{F}^d$ from $\delta\Gamma(B_u)$. Therefore, the calculation needs to be carried out to NNLO on both sides of the matching in order to obtain the NNLO matching coefficients. Moreover, the $|\Delta B| = 0$ calculation is only carried out for the flavour combination where the external states have the same light quark as the inserted $|\Delta B| = 0$ operators. Due to isospin symmetry, only one of B_d or B^+ needs to be considered here to calculate the renormalised matrix elements of either $\langle B_d|\mathcal{O}^d|B_d\rangle$ or $\langle B^+|\mathcal{O}^u|B^+\rangle$ for the matching.

The other strategy that does not calculate any redundant diagrams focuses only on one of the decay width corrections, either $\delta\Gamma(B_d)$ or $\delta\Gamma(B^+)$, but it is slightly more involved overall. One can extract all matching coefficients by computing e.g. only $\delta\Gamma(B_d)$. This requires a calculation of the $|\Delta B| = 0$ transition operator that includes both $\langle B_d|\mathcal{O}^d|B_d\rangle$ and $\langle B_d|\mathcal{O}^u|B_d\rangle$. However, since the matrix elements of the opposite light flavour $\langle B_d|\mathcal{O}^u|B_d\rangle$ vanish to LO, both sides of the matching would need to be calculated to N3LO in order to extract the NNLO matching coefficients. Therefore, we do not pursue this path.

Care must also be taken to calculate only the $\mathrm{SU}(3)_\mathrm{F}$-breaking diagrams which contribute to the corrections $\delta\Gamma(B_d)$ and $\delta\Gamma(B^+)$ since the matching coefficients are only extracted from one of the two corrections, with the difference being implicit. The types of diagrams which must hence be discarded on both sides of the matching are the penguin contractions shown in Fig. 2.8, which appear at NLO and NNLO. These diagrams contribute to $\delta\Gamma(B_d)$ and $\delta\Gamma(B^+)$ and cancel in the difference.

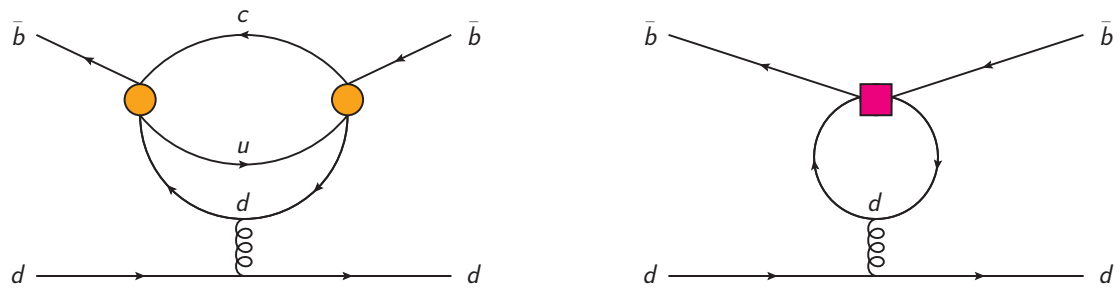

(a) Penguin contraction from $\mathcal{H}^{|\Delta B|=1}$

(b) Penguin contraction from $\mathcal{T}^d$

Figure 2.8: Penguin contraction diagrams for the $|\Delta B| = 1$ and $|\Delta B| = 0$ sides of the matching calculation with B_d external states. The orange dots represent current-current operator insertions while the ruby square is an insertion of the $|\Delta B| = 0$ transition operator.

The remainder of the matching procedure for the individual matching coefficients follows similar steps as outlined for the B meson mixing in Section 2.6.1. In particular, the cancellation of the IR poles occurs in the same way across orders, so evanescent operators need to be included at lower orders in α_s, and $\mathcal{O}(\epsilon)$ matching coefficients at LO and NLO affect the NNLO matching coefficients. For the current-current contributions to the lifetime difference, the tree-level matrix elements of only the first generation of evanescent operators appear at LO in the PI diagrams, so the $E^{(1)}$ operators are renormalised to NNLO while the $E^{(2)}$ operators are renormalised to NLO, as summarised in Tab. 2.4. Since one of the $|\Delta B| = 1$ operators is Fierz-transformed, all but one of the γ matrices of the WA diagrams have contracted Lorentz indices, and no $|\Delta B| = 0$ evanescent operators need to be renormalised to NNLO, and the $E^{(1)}$ operators are renormalised only to NLO.

Decay width	LO diagram on $\|\Delta B\| = 1$ side	Highest evanescent generation at LO	Required renormalised $\|\Delta B\| = 0$ matrix elements
$\delta\Gamma(B_d) \sim$ WA	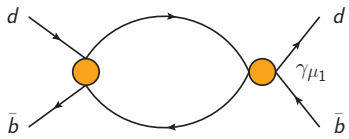	None	$\langle E_i^{(1)} \rangle^{(1)}$
$\delta\Gamma(B^+) \sim$ PI	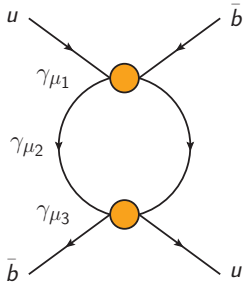	$\langle E_i^{(1)} \rangle^{(0)}$	$\langle E_i^{(1)} \rangle^{(2)}$, $\langle E_i^{(2)} \rangle^{(1)}$

Table 2.4: The evanescent operators required on the $|\Delta B| = 0$ side for a NNLO matching calculation depend on the physical operators included on the $|\Delta B| = 1$ side.

Order	Decay width	Highest generation evanescent $\lvert\Delta B\rvert = 0$ operator matrix elements
α_s^0	$\delta\Gamma(B_d) \sim$ WA	None
	$\delta\Gamma(B^+) \sim$ PI	$\langle E_i^{(1)} \rangle^{(0)}$
α_s^1	$\delta\Gamma(B_d) \sim$ WA	$\langle E_i^{(1)} \rangle^{(0)}$
	$\delta\Gamma(B^+) \sim$ PI	$\langle E_i^{(2)} \rangle^{(0)}$
α_s^2	$\delta\Gamma(B_d) \sim$ WA	$\langle E_i^{(2)} \rangle^{(0)}$
	$\delta\Gamma(B^+) \sim$ PI	$\langle E_i^{(3)} \rangle^{(0)}$

Table 2.5: Tree-level $|\Delta B| = 0$ operator matrix elements which appear in the amplitude on the $|\Delta B| = 1$ side at each order in α_s.

3 Calculation of Amplitudes

This chapter provides a detailed description of the methods used to calculate amplitudes for B meson mixing and decay processes based on the theories outlined in Chapter 2. Therefore, the theoretical models are linked to the desired phenomenological output for the key observables. Using the methods described here, amplitudes of $\mathcal{O}(10^6)$ diagrams are computed efficiently and in such a way that the matching coefficients for the applications in Chapters 4 and 6 are easily extracted following the matching procedure from Section 2.6.

The structure of this chapter is as follows: The overall workflow of the automated evaluation of amplitudes is presented first, followed by a discussion of the specific setup and kinematics employed for mixing and decay processes. Two particularly challenging aspects of the computation, the spinor projectors and the evaluation of master integrals, are then explained in more detail. For the projectors, an efficient algorithm applicable to generic four-fermion scattering is developed, which has been published in Ref. [113]. The chapter closes with a presentation of the semi-analytic evaluation of master integrals.

3.1 Overview of workflow

3.1.1 Calculation of individual diagrams

Due to the large number of diagrams, of which there are $\mathcal{O}(10^6)$ at NNLO for the B mixing amplitude on the $|\Delta B| = 1$ side, an automated toolchain is constructed based on well-tested and cutting-edge software packages. A graphical overview of the toolchain up to the computation of individual diagrams in terms of scalar integrals is shown in Fig. 3.1. At this point, the outputs are passed on to the second half of the toolchain, shown in Fig. 3.4 which evaluates the scalar integrals and produces our final results for the bare amplitudes.

The first half of the toolchain handles most of the process-specific steps, starting with the generation of Feynman diagrams, see Fig. 3.1. For the diagram generation, we use `QGRAF` [114], which generates a list of all allowed diagrams based on the external states and the propagator and vertex combinations permitted by the Lagrangian of the problem. It is possible to employ simple topology-based filters, e.g. to limit the number of certain propagators or vertices. `QGRAF` can also be used to differentiate between so-called on-shell

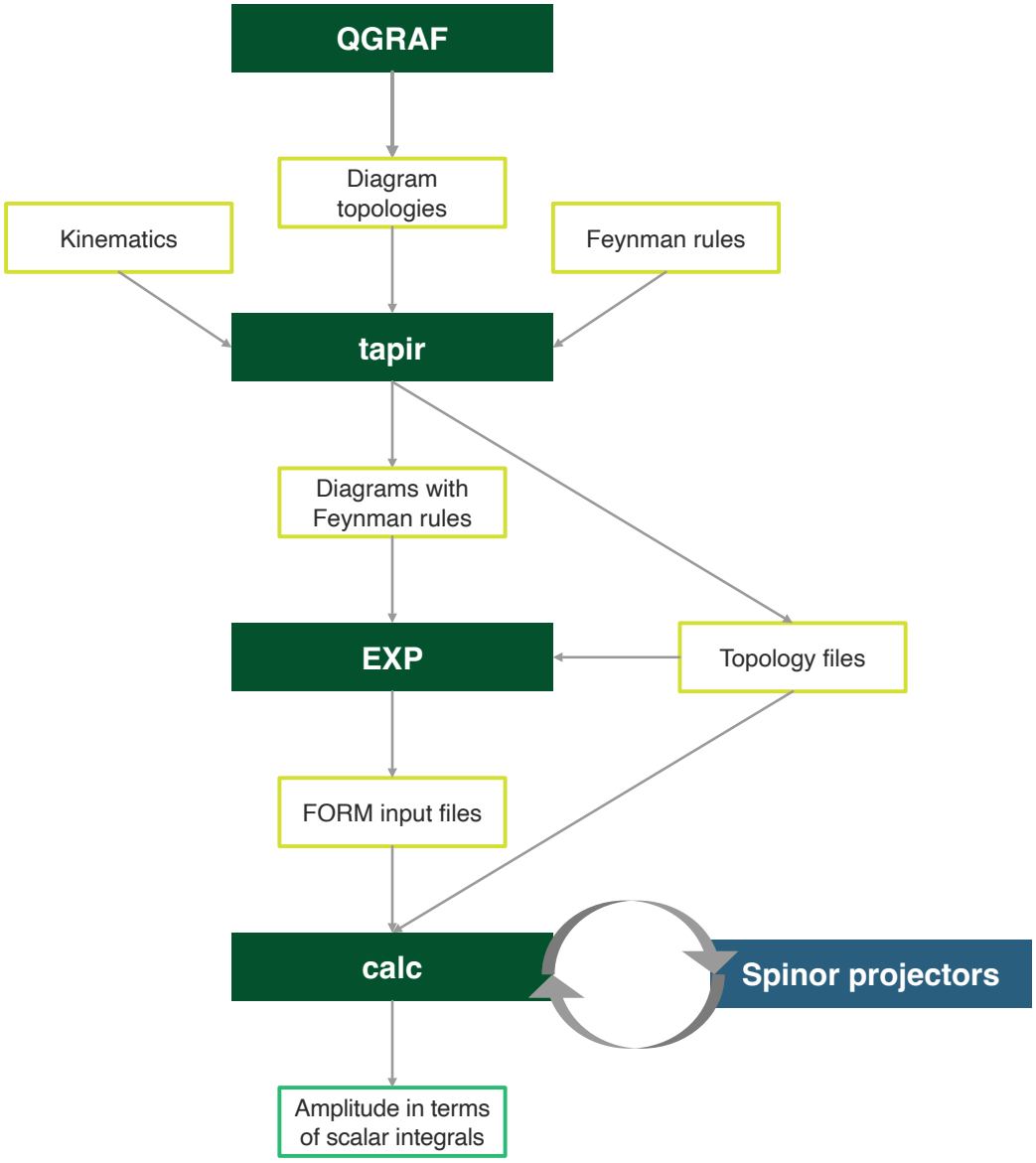

Figure 3.1: Workflow for the generation of amplitudes in terms of scalar integrals. The program in dark blue was developed as part of this thesis.

and off-shell topologies, where off-shell topologies are those that have a one-particle irreducible (1PI) propagator connected via a bridge to the rest of the diagram, see Fig. 3.2. This is useful for filtering out QCD self-energies on the legs of the diagram, which need to be amputated; however, it is not possible to distinguish between flavour-changing self-energies and QCD self-energies with this option. Therefore, `QGRAF` filters cannot be employed in some cases, see Section 3.2.2.

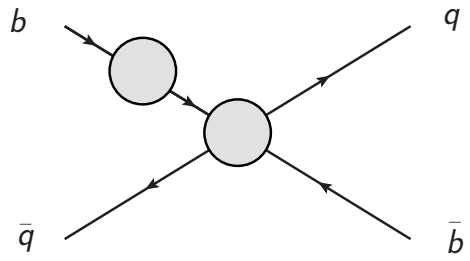

Figure 3.2: Off-shell topology as identified by `QGRAF`.

Since most of the effective operators that we use in our calculation have four-fermion vertices, the implementation of these vertices deserves special attention. The main complication is that we need to determine the correct sign of the diagram. This sign is determined by crossing symmetry, i.e. the anti-commutative property of the Grassmann-valued fermion fields. `QGRAF` can account for this sign change, and the most practical way of implementing such four-fermion vertices is by introducing a so-called σ particle. These auxiliary particles are used to split the four-fermion vertex into two separate three-particle interactions connected by the scalar σ particle, see Fig. 3.3. The propagator of the σ particle is the product of the identity matrix in colour space and metric tensors, contracting the Lorentz indices across the two spin lines. The Wilson coefficient can be split across the two vertices, e.g. each vertex can be chosen to have the square root of the original coupling. For each effective operator, a distinct σ-particle is introduced, with the penguin operators having special sigma particles that couple to quark pairs $q\bar{q}$ of all active flavours.

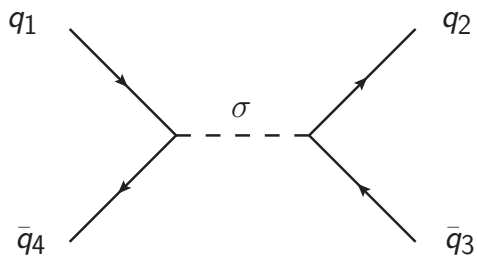

Figure 3.3: Four-fermion vertex decomposed as two separate three-particle vertices connected by an auxiliary σ particle.

The next step in the toolchain is the insertion of the Feynman rules for all propagators and vertices in the topologies generated in the previous step. For this step we use `tapir` [115]. This program offers a very convenient interface from `QGRAF` output to `FORM` [116–119] expressions, which can the be used for further manipulations. Therefore, `tapir` requires Feynman rules in `FORM` code format as additional input. The kinematics of the problem are also specified here, and additional filters on propagators, vertices and special topologies can be applied. Most notably, `tapir` differentiates between flavour-changing and non-flavour-changing self-energies. Thus, we use it in this step to filter out any QCD self-energies, which are always of the non-flavour-changing type. In addition to the diagram output, `tapir` also generates various topology files that can be used in later steps of the calculation.

To generate `FORM` code that can be readily executed in an automated and parallelised manner, and to map the diagram files generated by `tapir` to the corresponding topologies, we use `EXP` [120, 121]. This program has additional capabilities in performing asymptotic expansions of diagrams in terms of sub-diagrams, but for our calculation, we mainly use it to identify the topologies corresponding to individual diagrams. Note that this is not completed in the previous step as `tapir` generates one topology for each diagram, with some redundancies removed in a separate step. `EXP` is able to identify the minimal set of topologies needed out of those provided by `tapir`. Moreover, the output files include `make` files that can be used in the final step of manipulations on the diagram level.

The diagram evaluation is done with `calc`, an implementation written in `FORM` that efficiently handles diagram manipulations and colour factor evaluation based on the program `color` [122]. This last step simplifies the expressions obtained for each Feynman diagram as much as possible, reducing each to a linear combination of scalar integrals that are multiplied with the corresponding colour factor, and a rational polynomial of the occurring quark masses and the dimensional regulator ϵ. Additionally, the spinor structures of the diagrams need to be identified with basis elements, which are tree-level matrix elements of the transition operator that the matching is done with. For this purpose, dedicated spinor projectors were developed as part of this thesis, which are described in more detail in Section 3.3. These are also written as standalone modules in `FORM` and can be readily integrated within `calc`, see the dark blue box in Fig. 3.1.

3.1.2 Evaluation of the full amplitude

In the second half of the toolchain, the scalar integrals are evaluated and inserted into the amplitude, with some of the intermediate results used across different processes. As shown in Fig. 3.4, the amplitude expressed in terms of scalar integrals together with the topology files from `tapir` are the starting point for the reduction to master integrals (MIs). The first step is the extraction of all scalar integrals, called seeds, which can be reduced to a minimal set of integrals using integration-by-parts (IBP) [123, 124] and Lorentz invariance

(LI) [125] identities as well as symmetries of the integrals, e.g. under momentum shifts. The IBP identities can be derived from considering integrals of total derivatives like

$$\int_{k_1,\ldots,k_n} \mathrm{d}^d k_1 \ldots \mathrm{d}^d k_n \frac{\partial}{\partial k_j^\mu} \left(k_l^\mu \prod_i \frac{(p\cdot k)_i^{b_i}}{(q_i^2+m_i^2)^{a_i}} \right) = 0 \tag{3.1}$$

where the original Feynman integrand, i.e. the product of propagators in parentheses, vanishes on the integration surface [124]. Here, the momenta labelled p are external, k are loop momenta and q are linear combinations of different momenta. The second type of identities, the LI identities, require asymmetric combinations of external momenta and are hence not relevant for the processes considered here with one external momentum. The package `Kira` [126–128] offers an efficient implementation of all aforementioned identities, generating and solving the necessary equations with `Fermat` [129] or `FireFly` [130, 131] to reduce either a list of integrals or an entire sector.

In an intermediate step, we use the script `ImproveMasters.m` [132] to refine the basis of MIs for which `Kira` finds linear relations with all seed integrals. A good basis of master integrals has the feature that the dependence on any kinematic variables and on the dimensional regulator ϵ factorise in the denominators of the IBP relations. This is desirable as it leads to more compact IBP relations with simpler rational coefficients, which also facilitates the evaluation of MIs in the next step. Since we first require a list of IBP reductions to find a good basis of masters, `Kira` is run three times; first, for the sector in which we expect to find our master integrals, and then once more for the list of seed integrals and the preferred masters as provided by `ImproveMasters.m`. A third and final run of `Kira` is then used to find symmetry relations among the MIs across different families. Here, the list of all previously determined masters is taken as the set of seed integrals for the reduction.

Next, the IBP reductions are used to reduce the amplitude to a minimal basis of MIs. This is done with a few custom `FORM` routines, and requires a careful treatment of the dimensional regulator ϵ as the expressions should be Taylor-expanded in ϵ, but at the same time, poles in ϵ may appear in IBP identities and symmetry relations. Therefore, expansions in ϵ are done as soon as all reductions and symmetries are inserted, and up to the minimum order as required for the matching and taking into account potential poles from the MIs.

The IBP tables are also required for the evaluation of the master integrals in a semi-analytic expansion using the "expand and match" approach [133–136]. The method is described in more detail in Section 3.4, and we note here that further input for the numerical boundary conditions of integrals is required, for which we use `AMFlow` [137].

In the final step, the MIs are inserted into the amplitude and the expression is saved as a series expansion in ϵ and the mass ratio m_c/m_b. These expressions are then further treated

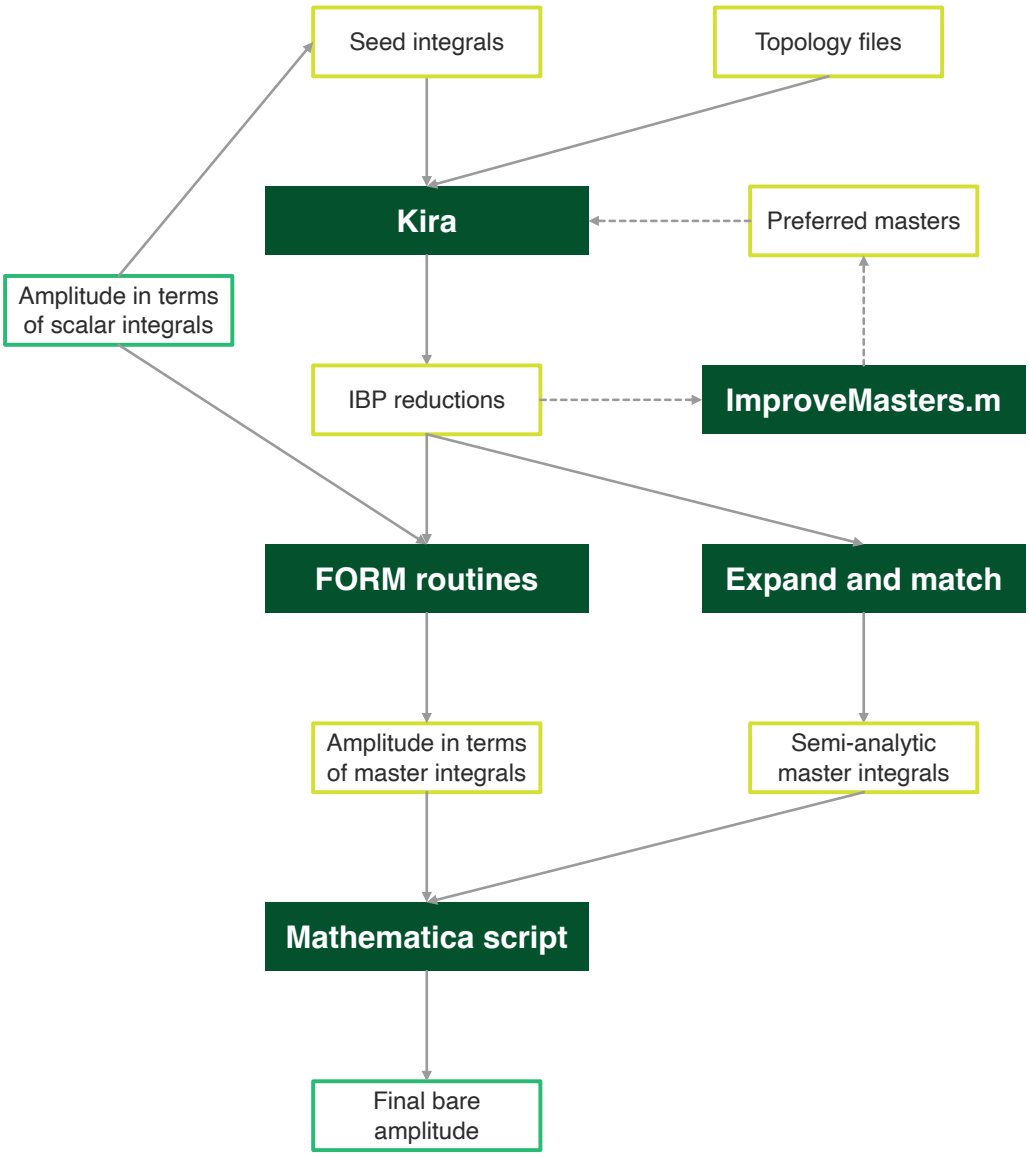

Figure 3.4: Workflow for the reduction to master integrals and evaluation of those integrals for the bare amplitude.

in the renormalisation and matching procedures, see Sections 2.1.3 and 2.6 respectively. These last computations are all carried out in `Mathematica` [138].

The key steps in setting up and executing the workflow outlined here are discussed in the following sections.

3.2 Setup and kinematics

3.2.1 General considerations for four-point interactions

In the following, the setup of the amplitude calculations for the mixing and decay processes is outlined. First, general considerations applicable to all mixing and decay amplitudes are discussed, with the specifics of the individual processes presented in Sections 3.2.2 and 3.2.4.

For the calculations presented in this thesis, we work with five active quark flavours, namely up, down, charm, strange and bottom quarks. The masses of the light quarks are set to zero, i.e. $m_u = m_d = m_s = 0$, while for the charm and bottom quarks we work with the non-zero masses m_c and m_b respectively. For the calculation of matching coefficients, we take the external quarks to be on-shell as we are interested in the physical observables. Choosing a reference frame where the three-momentum of the light external quark vanishes, there is only one non-zero external momentum q. The on-shell condition for the bottom quark implies that $q^2 = m_b^2$.

The topologies that are filtered for in the diagram generation differ slightly across the two sides of the matching. On the $|\Delta B| = 1$ side, calculations in general may include one-particle reducible contributions while the transition operators only require 1PI topologies since we amputate all QCD corrections on the legs. The allowed topologies of the amplitudes from two insertions of the $|\Delta B| = 1$ Hamiltonian depend on the pairs of operators inserted.

To determine the renormalisation constants of the $|\Delta B| = 2$ and $|\Delta B| = 0$ transition operators, off-shell amplitudes may be calculated since the UV divergences are the same as for the physical on-shell amplitudes. However, care must be taken to differentiate between IR and UV divergences. The way we regularise IR divergences is by introducing a finite mass for the light external quark, setting it equal to the bottom mass m_b. In this way, the amplitudes are IR-finite, and by working with vanishing external momenta, all integrals reduce to tadpoles. These can be evaluated with the `MATAD` package [139].

3.2.2 Setup of the B meson mixing amplitudes

The B mixing amplitudes are generated following the general considerations above with the exception that flavour-changing self-energies (FCSE) require a careful filtering of topologies. In this thesis, the contributions to the $|\Delta B| = 2$ matching coefficient from both current-current and penguin operators are calculated to NNLO, so there is a wide range of topologies that can appear in the amplitude generated from the $|\Delta B| = 1$ Hamiltonian. The most interesting class of topologies is those of FCSEs, which give non-vanishing contributions from NLO onwards, see Fig. 3.5. It is worth noting that these diagram classes do not appear when considering only current-current operators. Therefore, they were first considered in Ref. [140], where the mixed contributions from one current-current and one penguin operator were calculated. At NNLO and beyond, the FCSE topologies appear also with only current-current operator insertions.

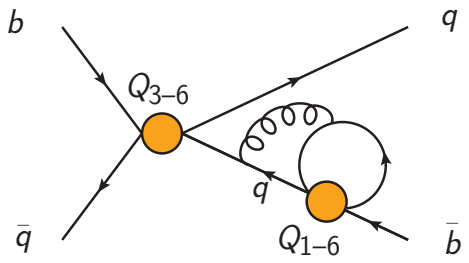

Figure 3.5: Flavour-changing self-energy diagrams at NLO.

For this thesis, the current-current and penguin operator contributions are calculated up to NNLO, i.e. diagrams of up to three-loops on the $|\Delta B| = 1$ side are generated with any two of the operators Q_{1-6}. The contributions from the chromomagnetic operator Q_8 are computed up to two loops, corresponding to NNLO for the mixed contributions with Q_{1-6} and to N3LO for the contributions proportional to C_8^2 since this operator comes with an additional factor of the strong coupling g_s. For the $|\Delta B| = 2$ transition operator, two-loop diagrams with a single $|\Delta B| = 2$ operator insertion are computed.

3.2.3 Linear charm mass dependence in B meson mixing

The NNLO contributions to the matching coefficients are special because they give rise to $\sqrt{z} = m_c/m_b$ terms, and it is instructive to show how they appear. The square root terms stem from diagrams like the one shown in Fig. 3.6a, which can be reduced to a linear combination of master integrals that includes the integral in Fig. 3.6b. Odd powers in m_c/m_b arise from the integral

$$I = \int\int\int \mathrm{d}^d k\, \mathrm{d}^d \ell\, \mathrm{d}^d p\, \frac{1}{k^2} \frac{1}{(\ell^2 - m_c^2)^3} \frac{1}{p^2 - m_c^2} \frac{1}{(\ell - p + q)^2 - m_b^2} \frac{1}{(k+q)^2} (k+p)^4 \tag{3.2}$$

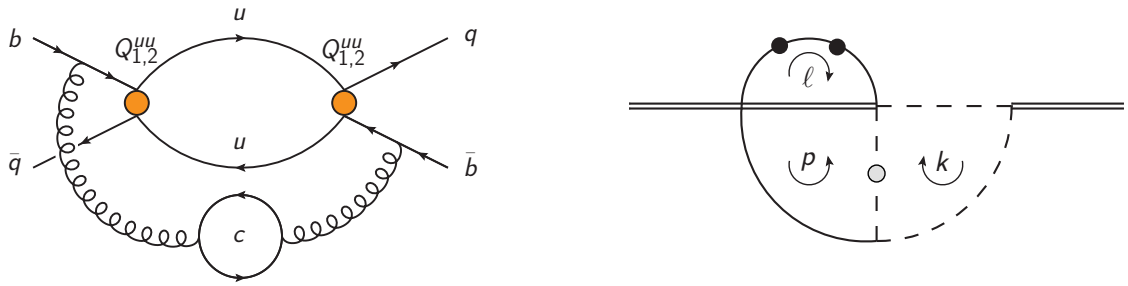

(a) Diagram with $\sqrt{z}$ terms

(b) MI with $\sqrt{z}$ terms

Figure 3.6: Diagram with the relevant master integral which gives rise to $\sqrt{z}$ terms. The dashed, single and double lines of the MI are massless, charm and bottom propagators respectively. The filled dots denote additional powers of the propagator while the grey dot denotes an inverted dot, i.e. a propagator raised to the power of $+2$.

in the limit $m_c \to 0$ and can be obtained by carrying out an asymptotic expansion with the method of regions [141, 142]. In the following, we explicitly show the source of the linear m_c/m_b contribution. There are two scalings of squared loop momenta to consider, the hard ($\sim q^2 = m_b^2$) and the soft ($\sim m_c^2$) regime. The only region which contributes to the $\sqrt{z}$ terms is

$$k^2 \sim q^2\,, \qquad \ell^2 \sim m_c^2\,, \qquad p^2 \sim m_c^2\,. \tag{3.3}$$

This is because the bottom propagator for soft ℓ and p has a simplified leading term, $2q \cdot (\ell - p)$, which leads to a linear term in m_c. The third loop momentum k needs to be hard because the integral otherwise contains a massless tadpole and vanishes. The leading term of the integral from Eq. (3.2) in the relevant region is

$$I_{hss} = \int\int\int \mathrm{d}^d k\, \mathrm{d}^d \ell\, \mathrm{d}^d p\, \frac{1}{(\ell^2 - m_c^2)^3}\, \frac{1}{p^2 - m_c^2}\, \frac{1}{2q \cdot (\ell - p)}\, \frac{k^2}{(k+q)^2} + \mathcal{O}\left(\frac{m_c^2}{m_b^2}\right)\,, \tag{3.4}$$

where the integral over k can be carried out, and the remaining two-loop integral is found in Ref. [143] such that

$$I_{hss} \sim m_b^2 \left(\frac{m_c}{m_b} + \mathcal{O}(m_c^2/m_b^2)\right)\,, \tag{3.5}$$

from which it becomes apparent that the discussed diagrams will lead to $\sqrt{z}$ terms in the matching coefficients at NNLO.

3.2.4 Setup of the B meson decay amplitudes

For the decay amplitudes, the diagram generation on the $|\Delta B| = 1$ side is special because one of the current-current operators is Fierz-transformed. This is necessary because we

want to be able to match onto $|\Delta B| = 0$ operators which have exactly one bottom quark per spin line without introducing evanescent operators on the $|\Delta B| = 0$ side that vanish under a Fierz transformation. Fierz-transforming a $|\Delta B| = 1$ operator instead is possible through the correct choice of evanescent operators in the historical basis as shown in Section 2.2.2. The diagrams are then generated by inserting one regular and one Fierz-transformed current-current operator, leading to topologies as shown in Fig. 3.7. The advantage here is that there are no closed fermion lines, so no difficulties with γ_5 arise.

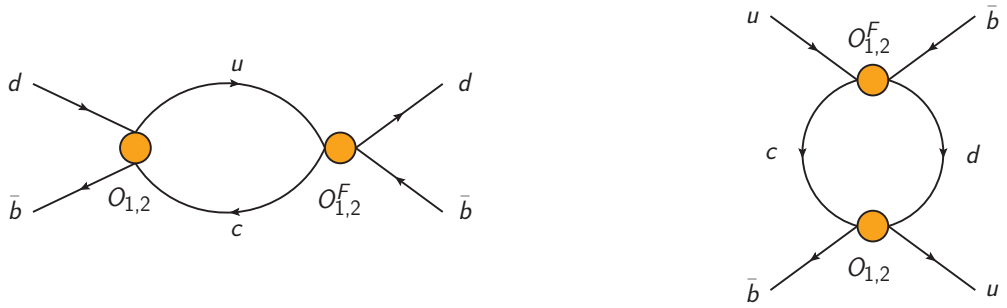

(a) Fierz-transformed WA

(b) Fier-transformed PI

Figure 3.7: Leading-order diagrams with one regular and one Fierz-transformed current-current operator.

We calculate the leading-CKM contributions, i.e. $\vec{F}^{u,d}$, to NNLO and the sub-leading-CKM contributions, i.e. $\vec{F}^{c}$, to NLO, see Eq. (2.146). Therefore, the diagrams we compute on the $|\Delta B| = 1$ side are generated by inserting only $Q_{1,2}$ at NLO and NNLO, while at LO we also need the penguin operators. The differentiation between leading and sub-leading contributions in terms of the CKM factors is relevant for the Weak Annihilation diagrams, i.e. those with B_d external states. The leading terms have a u and a c quark in the internal loop, while the sub-leading terms have two c quarks. Referring to Eq. (2.123), the sub-leading contributions are those that give rise to the matching coefficients with the superscript c. The suppression factor relative to the leading terms is $|V_{ud}|^2/|V_{cd}|^2$, which is roughly 5%. The leading contribution is given by only the current-current operators because the penguin operators have the CKM factor

$$V^*_{tb}V_{td} = -V^*_{cb}V_{cd} - V^*_{ub}V_{ud}\,, \tag{3.6}$$

where we have used the unitarity of the CKM matrix. Therefore, all penguin contributions are suppressed, and we choose to discard the doubly Cabibbo-suppressed second term above. For the sub-leading CKM contribution, which we calculate to NLO from current-current operators, penguin operators are needed to LO and as counterterm contributions to the current-current amplitude. In these LO diagrams with one penguin and one current-current operator as shown in Fig. 3.8a, the current-current operator should not be

Fierz-transformed to avoid closed fermion lines. This is consistent, since we are always free to choose either $O^F_{1,2}$ or $O_{1,2}$ when inserting a current-current operator. Moreover, the corresponding current-current NLO diagrams in Fig. 3.8b that receive counterterm contributions from the mixed one-loop diagrams do not involve Fierz-transformed operators either, as is necessary to avoid issues with γ_5.

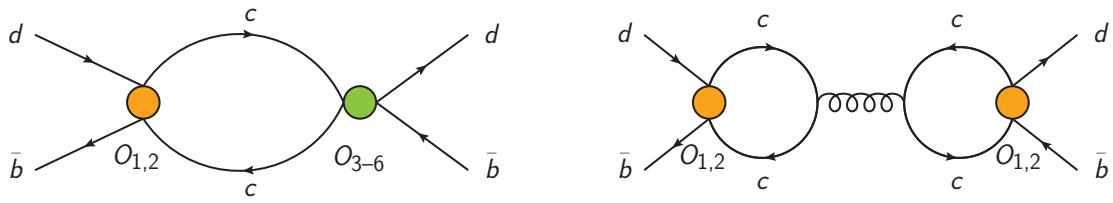

(a) LO current-current × penguin

(b) NLO current-current

Figure 3.8: Penguin topologies contributing to the CKM-suppressed $\vec{F}^c$ matching coefficients.

As discussed in Section 2.6.2, the matching coefficients are only extracted for the $SU(3)_F$-breaking contributions; therefore, all diagrams that lead to $SU(3)_F$ singlet matrix elements should be filtered out. This is achieved by discarding all diagrams on both sides of the matching where two b quarks sit on the same spin line. Sample diagrams of those contributions that are discarded are shown in Fig. 2.8 on page 64.

Similar to the B meson mixing calculation, the $|\Delta B| = 1$ side involves diagrams with two effective operator insertions and up to three loops while for the transition operator two-loop diagrams with a single $|\Delta B| = 0$ operator insertion are computed.

3.3 Spinor projector algorithm

The projection of spinor structures that appear in dimensional regularisation poses a particular challenge, which is efficiently treated using the algorithm presented here. The general idea is to reduce the Dirac chains in the diagrams with computationally inexpensive manipulations before applying two tables of pre-computed identification statements, see Fig. 3.9. The use of lookup tables reduces the need for carrying out expensive calculations multiple times since they are only done for a minimal set of spinor structures. Moreover, through the successive application of two tables, one for the γ matrices and one for the momentum insertions, the computation time in setting up the projectors is reduced significantly. The individual steps of the algorithm, including the generation of the lookup tables are explained in the following.

The implementation of the algorithm was written in `FORM` as this language offers an efficient implementation of the d-dimensional trace over a product of γ matrices and is

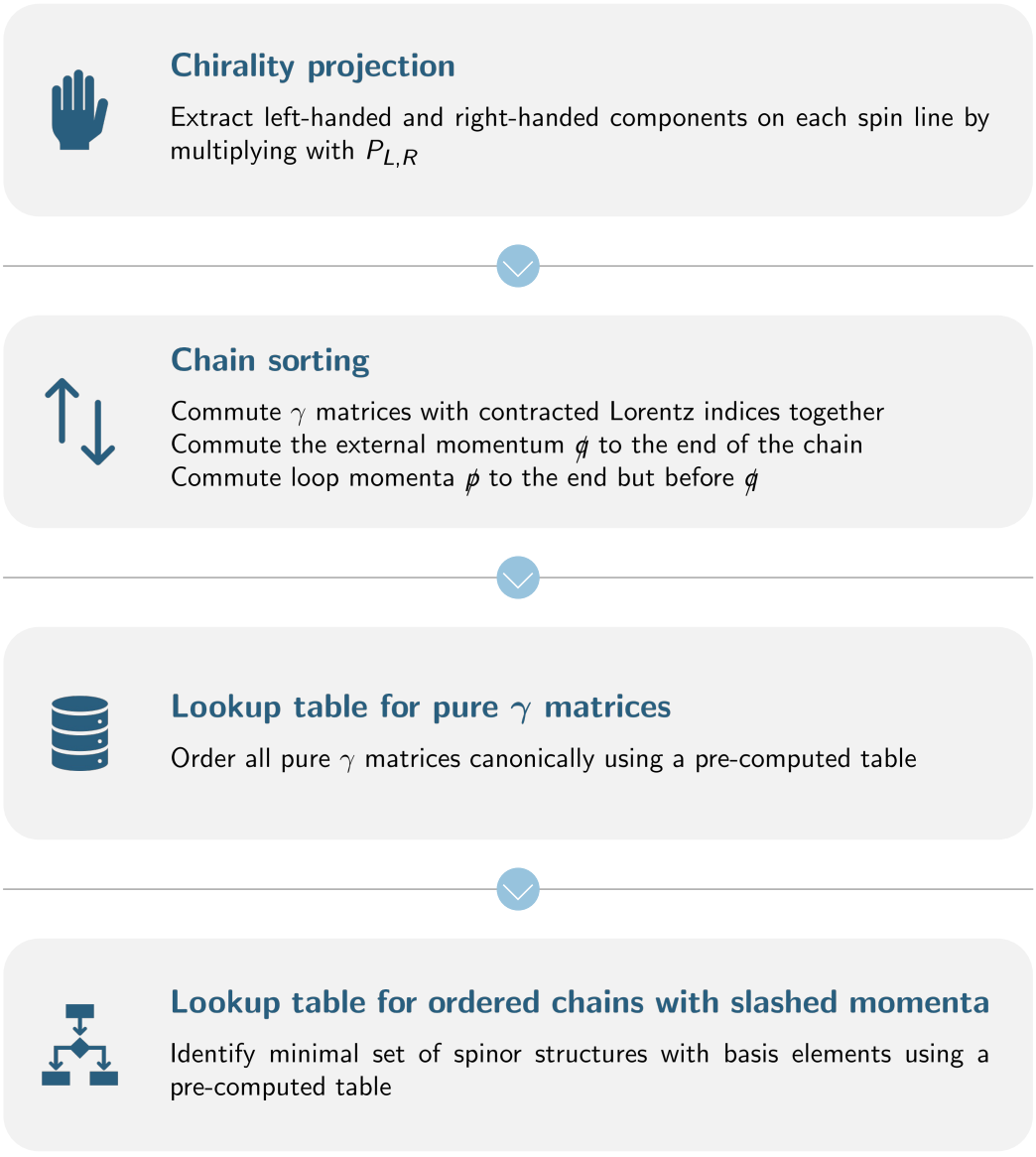

Figure 3.9: Overview of the spinor projector algorithm.

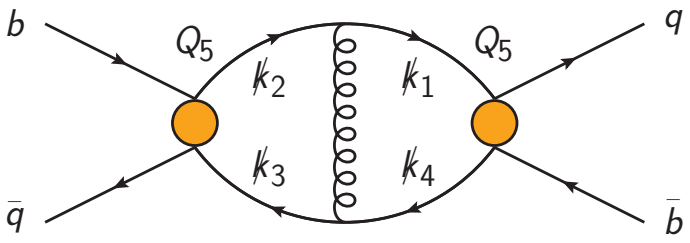

Figure 3.10: B mixing at NLO with two Q_5 penguin operators inserted.

able to handle large expressions of hundreds of GB. We primarily discuss the projectors for two spin lines with one external momentum.

For the computation of the renormalisation constants, we also have to consider diagrams without an external momentum. The corresponding projectors do not include elements with a slashed external momentum and are hence simpler.

In the following, the problem is first defined in terms of the spinor structures that appear in the amplitudes. After a discussion of the mathematical tools and the construction of projectors over special vector spaces, the details of the spinor projector algorithm, which has been published in Ref. [113], are presented.

3.3.1 Dirac chains in amplitudes

The purpose of applying spinor projectors to a scattering amplitude between Dirac spinors is to decompose the appearing tensor integrals in terms of linear combinations of scalar integrals. Those linear combinations should only depend a minimal set of spinor structures independent of the loop momenta. The spinor structures of four-fermion amplitudes consist of two matrices in spinor space, each of which is a product of Dirac γ matrices. These products are called spin lines or equivalently Dirac chains. The Lorentz indices on the γ matrices can be contracted with other γ matrices, loop momenta or the external momentum. To illustrate this point, the most complicated spinor structure of the diagram shown in Fig. 3.10 is given by

$$P_R\,\gamma^{\mu_1}\gamma^{\mu_2}\gamma^{\mu_3}\,\not{k}_1\,\gamma^{\sigma}\,\not{k}_2\,\gamma^{\nu_1}\gamma^{\nu_2}\gamma^{\nu_3} \otimes P_R\,\gamma_{\nu_1}\gamma_{\nu_2}\gamma_{\nu_3}\,\not{k}_3\,\gamma_{\sigma}\,\not{k}_4\,\gamma_{\mu_1}\gamma_{\mu_2}\gamma_{\mu_3}\,. \tag{3.7}$$

Since γ_5 never appears in closed fermion loops, the chirality projectors can always be commuted to the end of the spin line as has been done here. The momenta k_i are the propagator momenta of the fermion lines and therefore linear combinations of the loop momenta and the external momentum q. In the following, γ matrices which do not have their Lorentz indices contracted with a momentum vector are called "pure" γ matrices, and their products are referred to as "pure" spin lines.

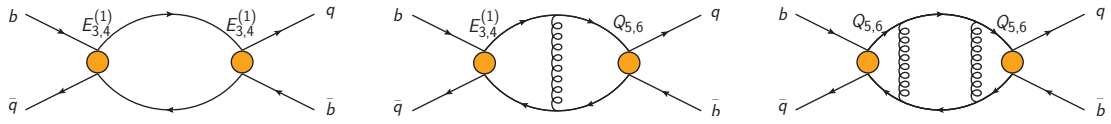

(a) One-loop (b) Two-loop (c) Three-loop

Figure 3.11: Sample diagrams with the maximum number of eleven γ matrices in B mixing on the $|\Delta B| = 1$ side.

Like the number of generations of evanescent operators to be considered, the number of γ matrices per spin line is also limited by the most complicated three-loop structure that appears in the amplitude calculations. The maximum number of γ matrices on a single spin line after contracting repeated Lorentz indices on the same spin line is eleven, which appears in the B meson mixing amplitudes. The most complicated diagrams on the $|\Delta B| = 1$ side with eleven γ matrices on each spin line are, by loop order:

- LO diagrams with second generation penguin evanescent operators $E^{(2)}_{3,4}$ and a penguin operator $Q_{5,6}$ or equivalently two first generation penguin evanescent operators $E^{(1)}_{3,4}$. In either case, there are ten pure γ matrices and only one slashed momentum per spin line.
- NLO diagrams with a first generation penguin evanescent operator $E^{(1)}_{3,4}$ and a penguin operator. Here, we have two slashed momenta and nine pure γ matrices one each spin line.
- NNLO diagrams with two penguin operators $Q_{5,6}$, which have three slashed momenta and eight pure γ matrices per spin line.

These topologies have all gluons connecting across the spin lines, so the number of slashed momenta is given by the number of loops. Sample diagrams for each of the above categories are shown in Fig. 3.11.

3.3.2 Vector spaces over γ matrices

Pure γ matrices

To be able to define an inner product and hence projectors, we need to discuss the vector spaces we are dealing with. The construction of vector spaces is done first over spin lines with only pure γ matrices to illustrate the basic concepts. A generic element of the vector space over pure spin lines can be written as

$$\Xi = \Gamma^{\mu_1,\ldots,\mu_n} \otimes \Gamma_{\mu_{\sigma(1)},\ldots,\mu_{\sigma(n)}}\,, \tag{3.8}$$

where $\sigma(x)$ is a permutation of the n Lorentz indices. Note that the Clifford algebra

$$\{\gamma^\mu, \gamma^\nu\} = 2g^{\mu\nu} \tag{3.9}$$

should be used to commute γ matrices with repeated Lorentz indices together to reduce a degree of redundancy from inserting an identity on either spin line using

$$\mathbb{1} = \frac{1}{d}\gamma^{\mu}\gamma_{\mu}\,. \tag{3.10}$$

In setting up Eq. (3.9), we specify the NDR scheme, which is used throughout the calculation of amplitudes. We further define the trace of the unit matrix in spinor space to be equal to four. With these definitions, spinor structures like the one given in Eq. (3.8) are elements of

$$\mathrm{Cl}_{p,q}(\mathbb{C}) \otimes \mathrm{Cl}_{p,q}(\mathbb{C})\,, \tag{3.11}$$

where $\mathrm{Cl}_{p,q}$ is the Clifford algebra over the spacetime $\mathbb{R}^{p,q}$. In our case we have $p = 1$ time and $q = d - 1$ space dimensions. However, the Clifford algebra is not closed in d dimensions, so we can further simplify the mathematical description of our problem by building a vector space from the finite number of spinor structures that actually appear in the scattering amplitudes at hand.

In practice, any diagram can be written as the sum of Dirac chains of different lengths, so the actual spinor structure of the diagram is fully encoded by the n-tuple

$$x = \left(c^{(0)}\mathbb{1}\otimes\mathbb{1},\; c^{(1)}\gamma^{\mu}\otimes\gamma_{\mu},\; \sum_i c_i^{(2)}\Gamma^{(2)}\otimes\Gamma_i^{(2)},\; \ldots \right)\,, \tag{3.12}$$

where the γ matrices in a spin line $\Gamma_i^{(k)}$ of length k have not been ordered. That is, the index i labels a particular permutation of the Lorentz indices on the second spin line; the first spin line can always be canonically labelled with indices $\mu_1, \ldots, \mu_k$. The elements x live in the vector space

$$\tilde{V}_n \equiv \tilde{V}^{(0)} \oplus \tilde{V}^{(1)} \oplus \ldots \oplus \tilde{V}^{(n)}\,, \tag{3.13}$$

which is the direct sum of the vector spaces of unordered γ matrices of length k, $\tilde{V}^{(k)}$. The diagram limits the maximum number of γ matrices to be at most n, which for the most complicated diagrams is eleven.

This description still has too many degrees of freedom since the Clifford algebra from Eq. (3.9) can be used to order the γ matrices canonically. Therefore, there exists a linear map $\phi_{\mathrm{Cliff}} : \tilde{V}_n \to V_n$, where we define the vector space over ordered spin lines up to length n as

$$V_n \equiv \mathrm{span}_{\mathbb{C}}\left(\{\mathbb{1}\otimes\mathbb{1}, \gamma^{\mu}\otimes\gamma_{\mu}, \ldots, \gamma^{\mu_1}\ldots\gamma^{\mu_n}\otimes\gamma_{\mu_n}\ldots\gamma_{\mu_1}\}\right)\,, \tag{3.14}$$

or equivalently

$$V_n \equiv V^{(0)} \oplus V^{(1)} \oplus \ldots \oplus V^{(n)} \tag{3.15}$$

where $V^{(k)} \cong \mathbb{C}$ is the vector space of ordered γ matrices of length k. Hence, V_n is isomorphic to $\mathbb{C}^{n+1}$. This vector space is much smaller compared to $\tilde{V}_n$, where each of

the sub-spaces $\tilde{V}^{(k)}$ has $k!$ complex dimensions. The definition of the vector space in Eq. (3.14) is only meaningful in d dimensions, where we cannot apply four-dimensional identities like the Chisholm identities or Fierz-transform the spinor structures.

For pure γ matrices, we hence need to implement the map ϕ_{Cliff} in an efficient manner in order to reduce any spinor structure in terms of the basis elements of V_n as defined in Eq. (3.14).

Adding complexity with slashed momenta

The challenge in working with actual amplitudes is that we need to treat spinor structures that also contain slashed momenta. Assuming that all momenta have been commuted to the left and γ matrices with repeated Lorentz indices on the same spin line have been contracted, we are left with spinor structures like

$$\Xi = \not{p}_1 \dots \not{p}_m \gamma^{\mu_1} \dots \gamma^{\mu_k} \otimes \not{p}_{m+1} \dots \not{p}_r \gamma_{\mu_{\sigma(1)}} \dots \gamma_{\mu_{\sigma(k)}}, \tag{3.16}$$

where $\sigma(x)$ is a permutation of the Lorentz indices. The number of slashed momentum insertions r is at most equal to the number of fermion propagators.

We now proceed to construct the vector space for spinor structures of the form given in Eq. (3.16) from the bottom up by starting from the observation that

$$\Xi \in \mathbb{C}^d \oplus \dots \oplus \mathbb{C}^d \oplus \tilde{V}^{(k)} \cong (\mathbb{C}^d)^r \oplus \tilde{V}^{(k)} \equiv W_{r,k}, \tag{3.17}$$

since the slashed momenta live in $\mathbb{C}^d$. Eventually, the final result is written in terms of physical Lorentz tensors appearing in the process, i.e. the external momentum q^μ and the metric tensor $g^{\mu\nu}$. Therefore, we are interested in finding a map onto the vector space

$$\begin{aligned} W_k \equiv \text{span}_{\mathbb{C}}\Big(\{&\mathbb{1} \otimes \mathbb{1},\ \not{e}_q \otimes \mathbb{1},\ \mathbb{1} \otimes \not{e}_q,\ \not{e}_q \otimes \not{e}_q, \\ &\gamma^\mu \otimes \gamma_\mu,\ \dots,\ \gamma^{\mu_1} \dots \gamma^{\mu_k} \not{e}_q \otimes \gamma_{\mu_k} \dots \gamma_{\mu_1} \not{e}_q\}\Big), \end{aligned} \tag{3.18}$$

where we have defined

$$\not{e}_q \equiv \frac{\not{q}}{\sqrt{q^2}}. \tag{3.19}$$

Note that W_k is isomorphic to $\mathbb{C}^{4k+4}$.

In the following, we will also make reference to the vector space

$$\widetilde{W}_{r,n} \equiv (\mathbb{C}^d)^r \oplus \tilde{V}_n, \tag{3.20}$$

which has elements of the form

$$\begin{aligned} x = \Big(&c^{(0)} \not{p}_1 \dots \not{p}_m \otimes \not{p}_{m+1} \dots \not{p}_r,\ c^{(1)} \not{p}_1 \dots \not{p}_m \gamma^\mu \otimes \not{p}_{m+1} \dots \not{p}_r \gamma_\mu, \\ &\sum_i c_i^{(2)} \not{p}_1 \dots \not{p}_m \Gamma_i^{(2)} \otimes \not{p}_{m+1} \dots \not{p}_r \Gamma_i^{(2)}, \dots\Big). \end{aligned} \tag{3.21}$$

This extends $W_{r,k}$ in a similar fashion as $\tilde{V}_n$ in Eq. (3.13) extends $\tilde{V}^{(k)}$. The vector space which covers all possible spinor structures, accounting for different numbers of slashed momenta, is the direct sum

$$\widetilde{U}_{R,n} \equiv \bigoplus_{r \leq R} \widetilde{W}_{r,n} \tag{3.22}$$

with up to R slashed momenta.

3.3.3 Constructing projectors with inner products

Projections in vector spaces are carried out with the help of an appropriately defined inner product $\langle \cdot\,, \cdot \rangle$. For example, the projectors P_i can be applied to an element x of a vector space to obtain the projection onto a subspace,

$$P(x) = \sum_i e_i P_i(x) = \sum_{i,j} e_i \lambda_{ij} \langle e_j, x \rangle\,, \tag{3.23}$$

where e_i are the basis elements of that subspace. Since a projection of any basis element should yield that same basis element,

$$P_i(e_k) = \sum_j \lambda_{ij} \langle e_j, e_k \rangle = \sum_j \lambda_{ij} G_{jk} \stackrel{!}{=} \delta_{ik}\,, \tag{3.24}$$

the coefficients λ_{ij} can be determined from the above equality. The matrix G is called the Gram matrix, which is defined via

$$\mathrm{G}_{ij} \equiv \langle e_i, e_j \rangle\,, \tag{3.25}$$

such that the coefficient matrix λ_{ij} is given by its inverse. In order to construct a set of projectors, the Gram matrix must be invertible, which is the case when the vectors e_i form a proper basis because in that case they are linearly independent.

The problem of defining a set of projectors can hence be reduced to defining an inner product $\langle \cdot\,, \cdot \rangle : V \times V \to \mathbb{C}$. An inner product has the following properties:

(i) Conjugation symmetry: $\overline{\langle x, y \rangle} = \langle y, x \rangle$

(ii) Linearity: $\langle ax + by, z \rangle = a\langle x, z \rangle + b\langle y, z \rangle \; \forall\, a, b \in \mathbb{C}$

(iii) Positive-definiteness: $\langle x, x \rangle > 0$

However, one can also compromise on property (iii) if the resulting Gram matrix is nevertheless invertible.

The traditional choice of inner product

The inner product on the vector space $W_{r,k}$ for $x, y \in W_{r,k}$ is usually defined as

$$\begin{aligned}\langle x, y\rangle \equiv \mathrm{Tr}\Big[\left(\not{p}_1 \dots \not{p}_{m_x} \gamma^{\mu_1} \dots \gamma^{\mu_{k_x}}\right)^\dagger \not{q}_1 \dots \not{q}_{m_y} \gamma^{\nu_1} \dots \gamma^{\nu_{k_y}}\Big] \times \\ \mathrm{Tr}\Big[\left(\not{p}_{m_x+1} \dots \not{p}_{r_x} \gamma_{\mu_{\sigma(1)}} \dots \gamma_{\mu_{\sigma(k_x)}}\right)^\dagger \not{q}_{m_y+1} \dots \not{q}_{r_y} \gamma^{\nu_{\sigma'(1)}} \dots \gamma^{\nu_{\sigma'(k_y)}}\Big],\end{aligned} \tag{3.26}$$

see for example Refs. [144, 145]. In the inner product above, the indices μ_i and ν_i with the permutations σ and σ' belong to x and y with the momenta p_i and q_i.

It can be checked that this is a proper inner product, fulfilling the three conditions above. For Eq. (3.26), property (i) is obeyed for either complex conjugation or the interchange of the two spin lines. Although the traditional inner product uses complex conjugation, the more natural choice is the interchange of spin lines. The latter conjugation symmetry is also more easily obeyed.

Showing that property (ii) is fulfilled by Eq. (3.26) is slightly more involved as the definition needs to be extended to $\widetilde{W}_{r,n}$ to handle spinor structures with more than one term, e.g. $x = \gamma^\mu \otimes \gamma_\mu + \gamma^\mu\gamma^\nu \otimes \gamma_\mu\gamma_\nu$. To ensure the correct contraction of Lorentz indices, the scalar product should be applied to all pairs of vector components in Eq. (3.21) individually,

$$\begin{aligned}\langle \cdot, \cdot \rangle : \left(\left(x^{(0)}, x^{(1)}, \dots, x_m^{(n)}\right), \left(y^{(0)}, y^{(1)}, \dots, y_m^{(n)}\right)\right) \mapsto \\ \phi(x^{(0)}, y^{(0)}) + \phi(x^{(0)}, y^{(1)}) + \dots + \phi(x_m^{(n)}, y_m^{(n)})\,.\end{aligned} \tag{3.27}$$

We can thus see that the scalar map from Eq. (3.26) that is an inner product on $W_{r,k}$ is a special case of the scalar map ϕ,

$$\begin{aligned}\phi_t : (\mathbb{C}^d)^r \oplus \tilde{V}^{(k)} \times (\mathbb{C}^d)^r \oplus \tilde{V}^{(k)} \to \mathbb{C} \\ (x_1 \otimes x_2,\, y_1 \otimes y_2) \mapsto \mathrm{Tr}\left[x_1^\dagger y_1\right] \times \mathrm{Tr}\left[x_2^\dagger y_2\right]\,,\end{aligned} \tag{3.28}$$

which we use in the definition of the inner product on the bigger vector space $\widetilde{W}_{r,n}$. With the definition of the inner product on $\widetilde{W}_{r,n}$ from Eq. (3.27), we can now see that the linearity condition (ii) is fulfilled for any linear map ϕ.

It is therefore important to differentiate between the scalar map ϕ which maps elements from $(\mathbb{C}^d)^r \oplus \tilde{V}^{(k)} \times (\mathbb{C}^d)^r \oplus \tilde{V}^{(k)}$ to $\mathbb{C}$ and the inner product $\langle \cdot, \cdot \rangle$ which maps elements from $\widetilde{W}_{r,n} \times \widetilde{W}_{r,n} = (\mathbb{C}^d)^r \oplus \tilde{V}_n \times (\mathbb{C}^d)^r \oplus \tilde{V}_n$ to $\mathbb{C}$. Note that the extension to $\widetilde{W}_{R,n}$ proceeds analogously with the inner product being defined component-wise for each number of slashed momenta, and applying the map to all pairs of vector components as in Eq. (3.27).

Choosing $\phi = \phi_t$, the traditional inner product is also positive definite, fulfilling property (iii). However, this requirement can be relaxed for the purpose of defining projectors as long as the Gram matrix is invertible.

Choosing a new scalar map

For long spin lines, especially those with many pure γ matrices, the traditional map ϕ_t is not the most efficient, and we may choose a different map instead. This is because in the traditional map the Lorentz indices on the γ matrices are contracted across the two traces. Therefore, the intermediate expressions after taking one of the traces become quite large, and the computation cannot easily be parallelised. For example, each individual trace product that appears in the projection of spin lines with nine γ matrices requires several days of single-core computation with `FORM`.

The alternative that we choose for the map ϕ is

$$\begin{aligned} \phi_p : (\mathbb{C}^d)^r \oplus \tilde{V}^{(k)} \times (\mathbb{C}^d)^r \oplus \tilde{V}^{(k)} &\to \mathbb{C} \\ (x_1 \otimes x_2,\, y_1 \otimes y_2) &\mapsto \mathrm{Tr}\left[x_1 y_1 x_2 y_2\right] . \end{aligned} \tag{3.29}$$

The main advantage of ϕ_p is that there is only one single trace, and all Lorentz indices of the pure γ matrices are contracted within the same trace. Therefore, γ matrices with pairwise contracted Lorentz indices can be commuted together and eliminated, reducing the length of the trace. As a trade-off, commuting the γ matrices through the spin line will generate additional terms, but each of them will have fewer γ matrices, and they can be evaluated in parallel on multiple cores. Since the map ϕ_p is particularly powerful for spinor structures with many pure γ matrices, it carries the subscript "p".

The properties (i) to (iii) need to be checked for this new definition of ϕ_p. Linearity still holds, and with the interchange of the spin lines, conjugation symmetry is also obeyed. However, property (iii) does not hold since the map is not positive-definite as can be checked for $x = \gamma^\mu \otimes \gamma_\mu$. Since we still want to use this map ϕ_p to construct projectors, the Gram matrix must be checked for invertibility.

With a proper inner product, the invertibility condition for the Gram matrix is automatically fulfilled. For example, for the vector space V_n of pure ordered γ matrices,

$$\langle x, x\rangle > 0 \;\forall\; x \in V_n : x \neq 0 \iff \vec{v}^\dagger G \vec{v} > 0 \;\forall\; \vec{v} \in \mathbb{C}^{n+1} \cong V_n : \vec{v} \neq 0\,, \tag{3.30}$$

where $\vec{v}$ is the coefficient vector of the $(n+1)$-tupel of basis elements up to length n. Conversely, if the bilinear map $\langle \cdot\,, \cdot \rangle$ is not positive-definite, the Gram matrix becomes non-invertible in case there are eigenvectors with zero eigenvalue,

$$\langle x, x\rangle > 0 \implies \forall \vec{v} \neq 0 : G\vec{v} \neq 0, \tag{3.31}$$

$$\exists \vec{v} \neq 0 : G\vec{v} = 0 \iff G \text{ non-invertible.} \tag{3.32}$$

For the vector space V_n, there are no such eigenvectors; however, for W_n such eigenvectors exist when the basis is not chosen with care.

Construction of a spinor basis

We now outline the construction of the Dirac basis and the strategy used to ensure that the associated Gram matrix remains invertible. Since we are considering amplitudes with one external momentum, the basis elements contain at most one slashed momentum per spin line. For the projection of tadpole amplitudes, all basis elements with slashed momenta are removed. The full list of basis elements is given in Appendix D.

In projecting the Dirac structures appearing in the amplitude with one external momentum, we first determine the number n of γ matrices on the shorter spin line. The projector basis is then built to include all combinations containing up to n total γ matrices, as well as an additional slashed momentum on the longer spin line. This upper bound reflects the most complicated Dirac structure that can arise in the amplitude. Whenever the longer spin line contains more γ matrices, index contractions must occur, effectively reducing the number of γ matrices. If both spin lines have the same length, we still add a further basis element as the Gram matrix would otherwise become non-invertible for odd numbers of γ matrices.

A special treatment is required when both spin lines contain eleven γ matrices. In this symmetric configuration, each spin line features ten pure γ matrices and one slashed momentum. The standard approach would be to add an additional basis element with an additional slashed momentum on one of the spin lines. However, since enlarging the basis to twelve γ matrices would entail a substantial computational overhead, we instead employ a slightly modified basis. For this case, we retain all structures containing up to eleven γ matrices on each spin line, including slashed momenta, but we omit a single asymmetric element. The element that is removed has ten γ matrices on both lines and a slashed momentum on only one of them. This adjustment ensures that the Gram matrix remains invertible. The asymmetric basis element is not required because it is impossible to reduce the number of γ matrices by exactly one since the length of the spin lines can only be reduced as a result of a Lorentz index contraction via $\gamma^\mu\gamma_\mu = d$.

3.3.4 A different view on pure γ matrix chains

As alluded to earlier, the problem of mapping an unordered chain of pure γ matrices onto a linear combination of ordered basis elements hinges on the efficient implementation of the Clifford algebra, but we can find a simpler description of the problem without making reference to the underlying algebra. In essence, what needs to be determined are the

functions

$$f_k : S_k \to \mathbb{R}^{k+1} \tag{3.33}$$
$$\sigma \mapsto \vec{a}\,, \tag{3.34}$$

where S_k denotes the permutation group of k elements. Here, the elements $\sigma \in S_k$ are the permutations of the Lorentz indices of the spin line which is not labelled canonically, and $\vec{a} \in \mathbb{R}^{k+1}$ are the coefficients of the linear combination of ordered spinor structures. The ordering of the coefficients is chosen such that a_1 is the coefficient of the longest Dirac chain, while the a_{k+1} for each f_k is the coefficient of the identity. If the full set of functions f_k up to the maximum length of Dirac chains is known, all spinor structures of pure γ matrices can be resolved in terms of the basis that spans V_n as defined in Eq. (3.14).

The functions f_k can be explicitly constructed by applying the Dirac algebra, and they read for the first few elements:

$$\begin{aligned}
&f_1 : S_1 \to \mathbb{R}^2\,, && (1) \mapsto (1,0)\\
&f_2 : S_2 \to \mathbb{R}^3\,, && \begin{cases} (12) \mapsto (1,0,0) \\ (21) \mapsto (-1,0,2d) \end{cases}\\
&f_3 : S_3 \to \mathbb{R}^4, && \begin{cases} (123) \mapsto (1,0,0,0) \\ (132) \mapsto (-1,0,2d,0) \\ (231) \mapsto (1,0,4-4d,0) \\ \quad\vdots \end{cases}
\end{aligned} \tag{3.35}$$

The permutations $(\dots)$ denote the ordering of the Lorentz indices μ_i on the spin which is not labelled canonically, back to front. That is, the permutation which has all Lorentz indices in the correct order directly corresponds to a basis elements of V_n. As an example, consider $f_2((21))$, which is given by

$$\gamma^{\mu_1}\gamma^{\mu_2} \otimes \gamma_{\mu_1}\gamma_{\mu_2} = -\gamma^{\mu_1}\gamma^{\mu_2} \otimes \gamma_{\mu_2}\gamma_{\mu_1} + 2d(\mathbb{1} \otimes \mathbb{1})\,. \tag{3.36}$$

From the discussion above, a clear pattern can be observed. The first coefficient, corresponding to the contribution from the longest basis element of length k, is always given by the sign of the permutation, i.e. $a_1 = \mathrm{sgn}(\sigma)$. Furthermore, all even coefficients a_{2n} vanish, since any contraction on the Lorentz indices necessarily reduces the number of γ matrices on a spin line by two. Although deriving closed analytic expressions for the coefficients is rather involved, constructing a lookup table for all permutations of Dirac chains up to length $k = 11$ is straightforward and required $\mathcal{O}(10^6)$ single-core CPU minutes.

When computing the lookup table, the computational efforts can be reduced significantly by recognising that for the function f_{k+1} one only needs to commute the γ matrix with

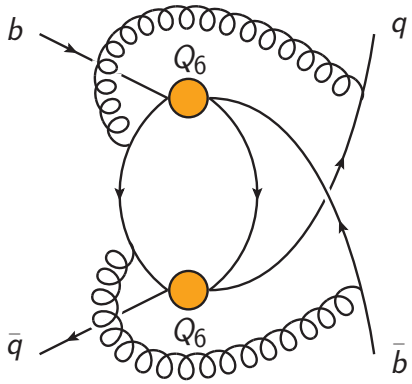

Figure 3.12: Sample diagram appearing in the NNLO B mixing calculation used to illustrate the spinor projector algorithm with the most complicated topologies. The Lorentz indices associated with the penguin operators Q_6 are denoted by μ_i and ν_i, whereas the gluon vertices carry Lorentz indices α_i.

the Lorentz index μ_{k+1} into position. After that, the map f_k is applied to all generated terms, and the maps can be generated from the bottom up in an efficient manner.

Using this method, the basis mapping of pure γ matrices can be resolved and the computational effort for projecting spinor amplitudes is significantly reduced. Consequently, only a limited number of spinor structures needs to be projected because the pure γ matrices are easily brought in order.

3.3.5 A practical algorithm for generic Dirac chains

With the general framework established in the preceding sections, we now describe the algorithm employed to handle the γ matrices appearing in our amplitude. The objective is to express each diagram as a linear combination of operator matrix elements in the $|\Delta B| = 2$ theory. This is achieved in two stages: first, the pure γ matrices are brought into canonical order, and subsequently the projectors are applied to resolve the slashed momentum insertions. The complete procedure is summarised below, and for illustration we show the intermediate structures encountered in the evaluation of the diagram shown in Fig. 3.12.

(i) Project onto the left- and right-handed spinor structures. This can be accomplished by multiplying with the chirality projectors $P_{R/L} = (1 \pm \gamma_5)/2$ and subsequently discarding all remaining terms containing γ_5. Such terms do not contribute to the amplitude, since the chiral projectors can always be commuted through to the end of each spin line, ensuring that no overall γ_5 factor remains. For the sample diagram

shown in Fig. 3.12 we obtain

$$\begin{aligned}&\gamma^{\mu_1}\gamma^{\mu_2}\gamma^{\mu_3}\not{k}_1\gamma^{\alpha_1}\not{k}_2\gamma^{\alpha_2}\not{k}_3\gamma^{\nu_1}\gamma^{\nu_2}\gamma^{\nu_3}\otimes\\&\quad\gamma_{\alpha_2}\not{k}_4\gamma_{\mu_1}\gamma_{\mu_2}\gamma_{\mu_3}\not{k}_5\gamma_{\nu_1}\gamma_{\nu_2}\gamma_{\nu_3}\not{k}_6\gamma_{\alpha_1}+3\text{ terms}\,.\end{aligned}\tag{3.37}$$

Here, the k_i are the line momenta of the propagators.

(ii) Rewrite all line momenta in terms of the loop momenta and the external momentum. This substitution reduces the number of possible slashed γ matrices that can appear. For instance, in the case of the sample diagram we have

$$\begin{aligned}&\gamma^{\mu_1}\gamma^{\mu_2}\gamma^{\mu_3}\not{p}_3\gamma^{\alpha_1}\not{p}_3\gamma^{\alpha_2}\not{p}_2\gamma^{\nu_1}\gamma^{\nu_2}\gamma^{\nu_3}\otimes\\&\quad\gamma_{\alpha_2}\not{p}_3\gamma_{\mu_1}\gamma_{\mu_2}\gamma_{\mu_3}\not{p}_1\gamma_{\nu_1}\gamma_{\nu_2}\gamma_{\nu_3}\not{p}_2\gamma_{\alpha_1}+95\text{ terms}\,.\end{aligned}\tag{3.38}$$

(iii) Canonically order the slashed momenta:

a) Replace any repeated momenta on the same spin line by corresponding scalar products. This step increases the number of terms by at most an order of magnitude; for the example considered here, the expression expands to 419 terms after this transformation.

b) Move all slashed momenta to the left along each spin line by commuting them through the pure γ matrices. This operation can increase the number of terms by up to a factor of 10^3.

c) Bring all instances of the external momentum to the far left, followed by the loop momenta. Arranging the external momentum in this position is advantageous, as several basis elements contain a slashed external momentum situated on the right. Applying a projector element with an external momentum immediately leads to a scalar product q^2, which shortens the trace. For the sample diagram, this step results in a total of 318 808 terms.

d) Resolve all permutations of the loop momenta, e.g. with the indices in descending order.

At the end of these steps to reorder the slashed momenta, the sample diagram has the following structure:

$$\not{p}_3\not{p}_2\not{p}_1\gamma^{\mu_2}\gamma^{\mu_3}\gamma^{\alpha_2}\gamma^{\nu_1}\gamma^{\nu_2}\gamma^{\nu_3}\otimes\not{p}_3\gamma_{\alpha_2}\gamma_{\mu_2}\gamma_{\mu_3}\gamma_{\nu_1}\gamma_{\nu_2}\gamma_{\nu_3}+181\,510\,\text{terms}\,.\tag{3.39}$$

(iv) Contract repeated Lorentz indices appearing on the same spin line by commuting the corresponding γ matrices together.

(v) Arrange all pure γ matrices in canonical order. This is accomplished using a precomputed lookup table that resolves the permutations of pure γ matrices. The

table provides all mappings of permutations involving up to ten γ matrices on each spin line into linear combinations of canonically ordered structures. The biggest such table has a size of 1.5 GB and contains all 10! permutations of up to ten pure gamma matrices. To minimise the number of terms generated when applying the map ϕ_p from Eq. (3.29) during the projection, it is advantageous to adopt a canonical ordering in which the γ matrices on the two spin lines appear in reversed order relative to one another. In this configuration, the maximum number of required commutations equals the length of the projector element inserted between the spin lines. For the sample diagram, this yields

$$\not{p}_3\not{p}_2\not{p}_1\gamma^{\rho_1}\gamma^{\rho_2}\gamma^{\rho_3}\gamma^{\rho_4}\gamma^{\rho_5}\gamma^{\rho_6} \otimes \not{p}_3\gamma_{\rho_6}\gamma_{\rho_5}\gamma_{\rho_4}\gamma_{\rho_3}\gamma_{\rho_2}\gamma_{\rho_1} + 40\,134\,\text{terms}\,, \tag{3.40}$$

which is usually a significant reduction by a factor of five in the number of terms compared to the previous step. Note that this step is the most expensive of the algorithm, taking up more than 90% of the computation time.

(vi) Map the expressions containing ordered pure γ matrices and isolated slashed momenta directly onto the basis elements given in Appendix D. This is accomplished using a pre-computed lookup table generated by applying projectors to the ordered γ structures. Since the procedure is symmetric under the interchange of the spin lines, it suffices to evaluate only one of the two configurations whenever the distribution of loop momenta is asymmetric under such an exchange. The lookup table is relatively compact with a total size of 1.3 MB and around 150 lines. For vacuum integrals, the table is even smaller with around 50 kB.

In constructing the lookup table, different projectors, in particular different inner products, may be employed depending on the specific spinor structure to be resolved. For most cases, we employ the bilinear map ϕ_p defined in Eq. (3.29). However, for the projection of spinor structures involving eleven γ matrices and slashed momenta on both spin lines, this map becomes inefficient as the slashed momenta effectively represent open Lorentz indices within the trace. In these instances, we instead use the linear map ϕ_t, which performs the traces over both spin lines separately, as defined in Eq. (3.26).[1]

For the representative diagram, this procedure yields

$$\frac{(p_1 \cdot p_3)^2 p_2^2}{d^3 - 6d^2 + 11d - 6} \times B_{45} + 104\,335\,\text{terms}\,, \tag{3.41}$$

where the dimension is $d = 4 - 2\epsilon$. For the definition of B_{45} see Appendix D.

[1] To optimise the computation of the lookup table entry for ϕ_t, the inner products are divided into separate files, each containing up to 10^5 terms after the first trace has been taken. Parallelising the second trace renders this calculation feasible, although the large intermediate file sizes of up to 2 TB remain a practical challenge.

(vii) Map the spinor basis elements onto the corresponding operator matrix elements, such as $\langle Q \rangle$, $\langle \widetilde{Q}_S \rangle$, $\langle E_1^{(1)} \rangle$, and so on. This step is efficiently implemented through the use of another lookup table.

The main advantage of the above algorithm is that it avoids the three main bottlenecks of a traditional spinor projector, namely:

- The hybrid approach of ordering the pure γ matrices before applying projectors minimises the number of spinor structures for which $\phi_{p,t}$ need to be calculated.
- The lookup tables cover all cases of up to eleven γ matrices and for the kinematics of a two-point function without having the need to recompute new traces on the fly.
- Applying the projectors only when generating lookup tables avoids inflating the amplitude by a few orders of magnitude in intermediate steps.

3.3.6 Future improvements to the spinor projector algorithm

To conclude the discussion of the spinor projector algorithm, two possible improvements which have not been implemented in this thesis are highlighted as possible areas for future research. The first concerns a modification of the implementation of ϕ_t, especially with slashed momenta in the diagram, while the second focuses on the basis mapping of pure gamma matrices.

The map ϕ_t, as defined in Eq. (3.26), is the most efficient treatment of long spinor structures with many slashed momenta, e.g. for seven pure γ matrices and four slashed momenta on each spin line, but minor improvements of the implementation are possible. The limiting step in the calculation is taking the first of the two traces on a single core and generating all of the terms from multiplying out the index contractions with the second spin line. However, this step may be parallelised as shown in Ref. [146]. We define a Dirac chain of length n as

$$\Gamma_n \equiv \gamma_{\mu_1} \dots \gamma_{\mu_n} \,, \tag{3.42}$$

and the same Dirac chain with the k th and l th matrices deleted as

$$\Gamma_n^{k,l} \equiv \gamma_{\mu_1} \dots \gamma_{\mu_{k-1}} \gamma_{\mu_{k+1}} \dots \gamma_{\mu_{l-1}} \gamma_{\mu_{l+1}} \dots \gamma_{\mu_n} \,. \tag{3.43}$$

For an even length n, we have the identity [146]

$$\mathrm{Tr}(\Gamma_n) = \sum_{k=2}^{n} (-1)^k g_{\mu_1 \mu_k} \mathrm{Tr}(\Gamma_n^{1,k}) \,, \tag{3.44}$$

which can be used to split a trace into multiple terms with shorter traces. While this does not reduce the overall complexity or the number of terms generated, it allows for the limiting step to be parallelised.

Another projector algorithm for pure γ matrices is presented in Ref. [147], where the γ matrices are treated as fermionic operators in a non-interacting field theory. This allows for the derivation of various identities for antisymmetric products of γ matrices, which correspond to normal ordered products in the free field theory. The main idea is to identify each γ matrix with a fermionic operator

$$\gamma_\mu \to \psi_\mu \equiv a_\mu + a_\mu^\dagger \,, \tag{3.45}$$

where a_μ and $a_\mu^\dagger$ correspond to the annihilation and creation operators. Since these obey the usual anti-commutation relations

$$\{a_\mu, a_\nu\} = 0 \,, \qquad \{a_\mu^\dagger, a_\nu^\dagger\} = 0 \,, \qquad \{a_\mu, a_\nu^\dagger\} = g_{\mu\nu} \,, \tag{3.46}$$

the fields ψ_μ fulfil the Clifford algebra, see Eq. (3.9). Crucially, the antisymmetric product of ψ fields is equal to the normal ordered product,

$$\mathrm{As}\left(\psi_{\mu_1} \dots \psi_{\mu_n}\right) = :\psi_{\mu_1} \dots \psi_{\mu_n}: \,, \tag{3.47}$$

where the antisymmetric product is defined as

$$\mathrm{As}\left(\psi_{\mu_1} \dots \psi_{\mu_n}\right) \equiv \frac{1}{n!}\left(\psi_{\mu_1}\psi_{\mu_2} \dots \psi_{\mu_n} - \psi_{\mu_2}\psi_{\mu_1} \dots \psi_{\mu_n} \pm \dots\right) . \tag{3.48}$$

Therefore, a convenient basis for a single spin line in this formalism is given by the antisymmetric products of γ matrices. Finding a mapping onto the basis elements of one spin line is hence equivalent to computing the normal ordered products. Moreover, the trace operation on γ matrices translates to taking the vacuum expectation value $\langle 0| \dots |0\rangle$ of a product of ψ fields. These calculations are simplified by the fact that Wick's theorem can be used in the free field theory.

The application of the field-theoretic approach to the case of two Dirac chains lies in the determination of the coefficients R_m in

$$\Gamma \otimes \Gamma' = \sum_{m=0}^{\infty} \frac{1}{m!} R_m \, \gamma_C^{(m)} \otimes \gamma_C^{(m)} \tag{3.49}$$

using functional methods. In the equation above Γ and Γ' are Dirac chains with all Lorentz indices contracted between them. In this sense they are products of pure γ matrices. The symbol $\gamma_C^{(m)}$ stands for the antisymmetric product of γ matrices, containing m matrices with the set of Lorentz indices C contracted across the two spin lines. For a formula for the calculation of R_m, see Ref. [147].

While this approach provides an efficient mechanism to order the pure γ matrices, it is not directly applicable to the most difficult problem at hand. First of all, the problem of treating slashed momenta has not been solved in this formalism. Secondly, the antisymmetric

ordering of the γ matrices in the result, i.e. on the right-hand side of Eq. (3.49), is not a convenient basis to work with in order to map to evanescent operators, which do not have antisymmetric products of γ matrices in their definition. An implementation of this formalism for the processes considered here should treat the case of slashed momenta or, equivalently, open Lorentz indices on Γ' and map to a more convenient basis of γ matrices.

3.4 Calculation of scalar integrals

After reducing the amplitude to a linear combination of a minimal set of scalar integrals, the so-called master integrals (MIs), those integrals need to be evaluated in order to extract the final results from the amplitudes. The methods employed in calculating the MIs are described in this section. Since the one- and two-loop integrals are available in the literature [142, 148], the focus is on the three-loop integrals. As only the imaginary part of the three-loop amplitudes is required, all purely real MIs can be discarded, and only 610 complex integrals need to be calculated. Here, we obtain semi-analytic expansions for the MIs, which can be used to cover the entire range of the charm to bottom mass ratio relevant for phenomenological applications, $[0.17, 0.35]$. The lower bound of this interval is given by the smallest possible charm mass, i.e. $\overline{m}_c(8.4\,\text{GeV})$, and the largest possible bottom mass, i.e. $\overline{m}_b(2.1\,\text{GeV})$. The upper bound of the interval is obtained from the largest possible charm mass, i.e. m_c^{OS}, and the smallest possible bottom mass, i.e. $\overline{m}_b(8.4\,\text{GeV})$.

The semi-analytic "expand and match" approach [133–136] starts from a differential equation of the master integrals in a kinematic variable, which is then solved using an appropriate ansatz that captures the structure of the expected divergences in ϵ and the kinematic variable. In the following, we describe the three main steps in calculating master integrals: setting up a differential equation, solving it using an expansion ansatz and finally matching to numerical boundary conditions.

3.4.1 Differential equations for master integrals

In a first step, the differential equation for a set of MIs is obtained by differentiating a vector of integrals with respect to the kinematic variable. In the B mixing and decay amplitudes, there are two scales, and an appropriate kinematic variable is $x \equiv m_c/m_b$. The differential equation

$$\frac{\mathrm{d}}{\mathrm{d}x}\,\vec{J} = A\,\vec{J} \tag{3.50}$$

is then set up with the help of the IBP relations obtained earlier for the reduction of the seed scalar integrals in the amplitude. Considering a master integral of the form

$$J_i = \iiint \mathrm{d}^d p_1\,\mathrm{d}^d p_2\,\mathrm{d}^d p_3\,D_1^{-n_1}\ldots D_k^{-n_k} \equiv J(n_1,\ldots,n_k)\,, \tag{3.51}$$

where the denominators D_i are functions of the loop momenta and the masses, we can see that the derivative simply raises the index, i.e. the power, of a charm propagator. Normalising all momenta to the bottom mass, a massive charm propagator is written as

$$D_c = p^2 - x^2\,, \tag{3.52}$$

and the derivative of J_i is hence given as

$$\frac{\mathrm{d}}{\mathrm{d}x} J_i = \sum_{D_j = D_c} 2\,x\,n_j\,J_i(n_1, \ldots, n_j + 1, \ldots, n_k)\,, \tag{3.53}$$

where the sum is over all massive charm propagators. The resulting integrals on the right-hand side are not necessarily in the set of master integrals, so the IBP relations need to be applied to obtain the differential equation for $\vec{J}$. It is possible, however, that the MIs appearing in an amplitude are not sufficient to write down a closed differential equation, i.e. that new masters appear in the reduction of the derivatives. In this case, the vector of MIs is extended by the new masters, which are then part of the differential equation. This procedure is iterated until a closed form of Eq. (3.50) is obtained.

The computation time for the expand and match approach depends on the form of the matrix A, so it is important to choose a good basis of masters for $\vec{J}$. A necessary condition for the expansion to converge is that there are no poles in ϵ on the diagonal of A. Additionally, the calculation is more efficient if the denominators of the IBP relations factorise in polynomials in x and ϵ, which can be achieved with the program `ImproveMasters.m` [132]. A basis that fulfils these conditions is called "good". Overall, the expand and match approach offers more flexibility than traditional analytic expansion methods which require the differential equation to be transformed to ϵ-form where $A = \epsilon B(x)$, see e.g. Refs. [149–151].

In order to bring the matrix A into the required form and facilitate the expansion, we use a simple trick to remove ϵ poles on the diagonals by hand. The strategy is to choose a new master integral J' from the left-hand side of the IBP reduction table to replace the old master integral J_1 which has a pole on the diagonal in A. It turns out that the new MI should have a factor of ϵ in front of the old master in the IBP relation of the form

$$J' = k_1 J_1 + k_2 J_2 + \ldots\,. \tag{3.54}$$

Considering the derivative of the new MI,

$$\begin{aligned}\frac{\mathrm{d}}{\mathrm{d}x} J' &= \frac{\mathrm{d}}{\mathrm{d}x}\left(k_1 J_1 + k_2 J_2 \ldots\right) \\ &= k_1\left(A_{11} J_1 + A_{12} J_2 + \ldots\right) + k_2\left(A_{21} J_1 + A_{22} J_2 + \ldots\right) + \ldots\,,\end{aligned} \tag{3.55}$$

and inserting the definition of J' to replace J_1, we obtain

$$\frac{\mathrm{d}}{\mathrm{d}x} J' = \left(A_{11} + \frac{k_2}{k_1} A_{21} + \ldots\right) J' + \ldots\,, \tag{3.56}$$

where the elements of A were inserted explicitly. The terms proportional to the master integrals J_i with $i > 1$ have been omitted here as they are not relevant to the discussion of the poles on the diagonal of A. The objective is to find an integral J' such that there is no pole multiplying that same integral on the right-hand side above, given that A_{11} has a pole in ϵ. We therefore require

$$A_{11} + \sum_{i=2}^{n} \frac{k_i}{k_1} A_{i1} \stackrel{!}{=} \mathcal{O}(\epsilon^0)\,. \tag{3.57}$$

Choosing an integral J' where k_1 starts at $\mathcal{O}(\epsilon)$ is hence a good candidate to remove the pole in A_{11} from the diagonal. However, not all such candidates will work, so we try out possible substitutions until we find one for which the pole disappears.

3.4.2 Solving the differential equations with "expand and match"

The expand and match algorithm from Refs. [133–136] was not implemented anew as part of this thesis. An existing setup within our collaboration was employed for this part of the calculation, and the theoretical foundations are summarised here for completeness. To set up the expand and match framework, we first need to choose the correct ansatz for the expansion and then match it to boundary conditions. It is necessary to choose the expansion points to be at the thresholds of the integrals, i.e. at points where the integrals have additional cuts, because the intermediate state charm quarks can be on shell. Otherwise, expansions around regular points are only valid in a small interval up to the next threshold. Since there are cuts through $0, 1, 2, 3$ and 4 charm quarks, there are threshold expansions around $x \in \{0, 1/4, 1/3, 1/2, 1\}$. To cover the range of physical charm masses, we expand around the points

$$x_E \in \{0, 1/10, 1/4, 1/3\}\,, \tag{3.58}$$

where the regular point $x_E = 1/10$ was added for additional coverage. The generic ansatz used in the expansion around x_E is

$$J_i = \sum_{k=-2}^{\epsilon_{\max}} \sum_{m=0}^{k+2} \sum_{n=n_{\min}}^{n_{\max}} c_{i,k,m,n}\, \epsilon^k\, (x - x_E)^{n/2}\, \log^m (x - x_E)\,. \tag{3.59}$$

The highest ϵ pole appearing in the imaginary part of the three-loop integrals is $1/\epsilon^2$ as is reflected in the expansion above. Each integral is expanded up to at least ϵ^0 if there are no spurious poles in the amplitude multiplying that integral. Otherwise, $\epsilon_{\max}$ is chosen to match the power of the spurious pole such that after the integral is inserted, the amplitude is correct up to and including $\mathcal{O}(\epsilon^0)$. The power of the logarithms has an upper limit as those terms stem from expansions of $x^{a\epsilon}/\epsilon^2$. The summation over n starts at $n_{\min} < 0$ as some of the integrals have poles which will cancel in the bare amplitude. The upper

limit is chosen to be $n_{\max} = 100$, which is sufficient to achieve a precision of 20 digits or more at each physical value separately for all MIs, see Ref. [113]. The regular point $x_E = 1/10$ has no expansion terms with logarithms as there is no divergence at that point. The expansion terms also vanish for odd values of n in the expansions around $x_E = 0, 1/10$ and $1/3$, but for $x_E = 1/4$ there are square roots stemming from cuts through an even number of massive charm quarks [152–154].

For the boundary conditions, we use numerical evaluations of the MIs obtained at a matching point x_M from `AMFlow` [137]. The matching points are chosen to be

$$x_M \in \left\{ \frac{1}{100}, \frac{1}{10}, \frac{6}{25}, \frac{29}{100} \right\} \tag{3.60}$$

for the expansions around $0, 1/10, 1/4$ and $1/3$ respectively. At each point, the integrals are evaluated to a precision of 100 digits, allowing for an accurate determination of the undetermined coefficients $c_{i,k,m,n}$ when matching to the expansion.

4 Phenomenology of B Meson Mixing

In this chapter, the results of the novel, precise determination of Γ_{12} are presented. Using the ratio Γ_{12}/M_{12}, the two mixing observables $\Delta\Gamma$ and a_{fs} are calculated, and the achieved precision of the perturbative calculation is discussed in detail. Moreover, the double ratio of the off-diagonal matrix elements across the B_d and B_s systems is calculated to obtain the most accurate prediction of $\Delta\Gamma_d$ to date. The chapter concludes with a discussion of the constraints on new physics and the CKM unitarity triangle, in particular from a_{fs}^d and $\Delta\Gamma_d/\Delta\Gamma_s$. The results for Γ_{12}/M_{12} are also given with the explicit dependence on hadronic matrix elements and CKM input values to enable more precise calculations in the future. The phenomenological outcomes presented in this chapter have been published in Refs. [20, 155].

4.1 Included matching coefficients and comparison with previous calculations

Before discussing the phenomenological results, the included matching coefficients are listed and compared to previous calculations. The results presented here are obtained using the matching coefficients for Γ_{12} computed in this thesis together with literature results for M_{12} as published in Ref. [55]. The matching coefficients for M_{12} are only known to NLO. However, as the expansion is in $\alpha_s(\mu_t)$ with $\mu_t \sim m_t$ as opposed to $\alpha_s(m_b)$, this accuracy is sufficient. The leading-power contributions to Γ_{12} from different $|\Delta B| = 1$ operators are discussed in the following. For the power-suppressed Λ_{QCD}/m_b matching coefficients of Γ_{12}, LO literature results from Refs. [34, 47] were used. For the $|\Delta B| = 1$ matching coefficients, the NLO [85, 156, 157] and NNLO [103, 105, 158] literature results were used.

For the matching coefficients of Γ_{12}, we reproduce literature results for the current-current operator contributions at LO and NLO, which can be found in Refs. [34, 36, 49, 159], where Ref. [34] provides the exact $z = m_c^2/m_b^2$ dependence in the $\{Q, \widetilde{Q}_S\}$ basis. Furthermore, we calculate the NNLO current-current matching coefficients in an expansion up to z^{10}, extending the results of Ref. [28], which were computed up to z^1. Note that in Ref. [28]

the terms stemming from closed charm loops at NNLO were taken from Refs. [51–53] and converted to a different operator basis. In doing so, Ref. [28] missed a numerically small term. To clarify the source of this error, the transformation is shown here. Going from the basis of Ref. [51] to the basis employed by Ref. [28] and this thesis, we rewrite the renormalised operator matrix elements using the definition of the renormalised matrix element of the $\Lambda_{\mathrm{QCD}}/m_b$-suppressed operator R_0 from Eq. (2.113):

$$\begin{aligned}\Gamma_{12} &\propto (F+P)\langle Q\rangle + (F_S+P_S)\langle Q_S\rangle + \mathcal{O}\left(\frac{\Lambda_{\mathrm{QCD}}}{m_b}\right)\\ &\propto \left(F+P-\frac{\alpha_1}{2}F_S-\frac{\alpha_1}{2}P_S\right)\langle Q\rangle - \alpha_2\left(F_S+P_S\right)\langle \widetilde{Q}_S\rangle + \mathcal{O}\left(\frac{\Lambda_{\mathrm{QCD}}}{m_b}\right). \end{aligned} \tag{4.1}$$

The matching coefficients in the $\{Q, \widetilde{Q}_S\}$ basis can hence be read off from the above equation. The results presented in Ref. [160] do not include the cross-terms that stem from α_s^2 contributions of the decoupling constants $\alpha_{1,2}$ and α_s^0 parts of the matching coefficients $F_{(S)}$ and $P_{(S)}$:

$$\Gamma_{12,\,\mathrm{missing}} \propto -\frac{1}{2}\alpha_1^{(2)}\left(F_S^{(0)}+P_S^{(0)}\right)\langle Q\rangle - \alpha_2^{(2)}\left(F_S^{(0)}+P_S^{(0)}\right)\langle \widetilde{Q}_S\rangle\,. \tag{4.2}$$

If these are included in the basis transformation, the $\sqrt{z} = m_c/m_b$ terms of this thesis can be reproduced, see Section 3.2.3 for a discussion of their origin. The terms are numerically small, resulting in a relative contribution of less than 10^{-5} for the central value of Γ_{12} up to NNLO.

The z^1 terms from diagrams with closed charm loops which are reconstructed from Ref. [51] are only correct for the up-up contribution, i.e. the contribution that arises from current-current operators which do not couple to charm quarks. This is because the charm mass was only kept for the closed fermion loops in Ref. [51], see e.g. Fig. 3.6a on page 75. The matching coefficients of this thesis extend these results, obtaining the correct z^1 terms for all $|\Delta B| = 1$ operator contributions, and further increasing the expansion depth to z^{10}.

The penguin operator contributions were calculated to LO in Refs. [36, 47] with their exact z-dependence and to NLO in Ref. [140] in an expansion up to z^1. The results presented here agree with the aforementioned literature results and advance the NLO calculation to a deeper expansion up to z^{10} together with the entirely new NNLO matching coefficients up to z^{10}. Moreover, we find agreement with the chromomagnetic operator contributions published in Ref. [54], which presents the matching coefficients as an expansion up to z^1. The results of this thesis are calculated as a deeper expansion up to z^{10} for this operator as well.

In addition to comparing with the literature, internal checks have been carried out to ensure the robustness of the novel results. In particular, the matching coefficients with

penguin operators at NNLO had not been considered in any work before and were checked most thoroughly. For the subset of diagrams with the operator combination $Q_1 \times Q_6$ and only massless charm quarks $m_c = 0$, we calculated the bare amplitude using the projector method presented in Ref. [160] and found agreement with the results produced with the more efficient method presented in Section 3.3. We also carried out a completely separate calculation of the contributions from $Q_{1,2} \times Q_{3\text{–}6}$ with $m_c = 0$ using tensor reduction as presented in Ref. [113], where we also found agreement.

4.2 Input values and renormalisation schemes

In order to predict physical observables from the high-energy matching coefficients calculated in this thesis, we need to combine our results with low-energy matrix elements and other input parameters, which are given in this section. Our main focus is the determination of $\Delta\Gamma$, which can be calculated either from

$$\frac{\Delta\Gamma}{\Delta M} = -\,\mathrm{Re}\,\frac{\Gamma_{12}}{M_{12}} \tag{4.3}$$

with the experimental value of ΔM or from a direct determination

$$\Delta\Gamma = 2|\Gamma_{12}|\cos\phi \approx 2|\Gamma_{12}|\,. \tag{4.4}$$

The dispersive part of the off-diagonal decay matrix is given by

$$M_{12} = \frac{G_\mathrm{F}^2 M_W^2}{32\pi^2 M_{B_q}} \lambda_t^2 C_Q \langle B_q|Q|\bar{B}_q\rangle\,, \tag{4.5}$$

where the matching coefficient C_Q has been calculated to NLO in Ref. [55]. To leading order, it is given by

$$C_Q(\mu = M_W) = S_0(x_t) \equiv \frac{4x_t - 11x_t^2 + x_t^3}{4(1-x_t)^2} - \frac{3x_t^3\ln(x_t)}{2(1-x_t)^3}\,, \tag{4.6}$$

where $x_t \equiv m_t^2/M_W^2$ and S_0 is the Inami-Lim function [161]. The contributions from virtual up and charm quarks in the full theory diagrams are neglected here since they are suppressed by the Glashow-Iliopoulos-Maiani (GIM) mechanism [24].

In Tab. 4.1, all input parameters apart from the Λ_QCD/m_b-suppressed matrix elements and the CKM factors are listed. For the bag parameters, we quote the values $B_{B_q} = B_{B_q}(\mu_2)$ and $\widetilde{B}_{S,B_q} = \widetilde{B}_{S,B_q}(\mu_2)$ at the scale $\mu_2 = m_b^\mathrm{OS}$. With the value of $\overline{m}_b(\overline{m}_b)$ and the two-loop relation for the on-shell mass, we obtain $m_b^\mathrm{OS} = 4.758\,\mathrm{GeV}$. For the PS mass, we use the four-loop relation to the $\overline{\mathrm{MS}}$ mass, which yields $m_b^\mathrm{PS} = 4.480\,\mathrm{GeV}$ with the factorisation scale $\mu_f = 2\,\mathrm{GeV}$.

$\alpha_s(M_Z)$	=	0.1180 ± 0.0009	[162]	G_F	=	$1.166\,378\,7 \times 10^{-5}\,\text{GeV}^{-2}$	[162]
M_W	=	$(80.3629 \pm 0.0133)\,\text{GeV}$	[162]	M_Z	=	$(91.1880 \pm 0.0020)\,\text{GeV}$	[162]
m_t^{OS}	=	$(172.4 \pm 0.7)\,\text{GeV}$	[162]	$\overline{m}_b(\overline{m}_b)$	=	$(4.163 \pm 0.016)\,\text{GeV}$	[163]
$\overline{m}_c(3\,\text{GeV})$	=	$(0.993 \pm 0.008)\,\text{GeV}$	[164]	f_{B_s}/f_{B_d}	=	1.2109 ± 0.0039	[41]
M_{B_s}	=	$(5366.91 \pm 0.11)\,\text{MeV}$	[162]	M_{B_d}	=	$(5279.41 \pm 0.07)\,\text{MeV}$	[162]
B_{B_s}	=	0.813 ± 0.034	[40]	B_{B_d}	=	0.806 ± 0.041	[40]
$\widetilde{B}_{S,B_s}$	=	1.31 ± 0.09	[40]	$\widetilde{B}_{S,B_d}$	=	1.20 ± 0.09	[40]
f_{B_s}	=	$(0.2303 \pm 0.0013)\,\text{GeV}$	[41–44]	f_{B_d}	=	$(0.1905 \pm 0.0013)\,\text{GeV}$	[41–44]
ξ	=	1.216 ± 0.016	[40]	ξ_S	=	1.263 ± 0.020	[40, 41]

Table 4.1: Input parameters for the phenomenological analysis. The mass m_t^{OS} corresponds to $\overline{m}_t(\overline{m}_t) = (162.6 \pm 0.7)\,\text{GeV}$ in the $\overline{\text{MS}}$ scheme. The value of ξ_S was computed using results from the quoted references, see Eq. (4.9).

For the low-energy matrix elements, we implement two different parametrisations, which are explained below. When calculating observables in the B_s and B_d systems separately, we use the bag parameters as calculated on the lattice for each of the mesons. The respective input values for the leading-power matrix elements

$$\begin{aligned}\langle B_q|Q|\bar{B}_q\rangle &= \frac{8}{3}M_{B_q}^2 f_{B_q}^2 B_{B_q}\,,\\ \langle B_q|\widetilde{Q}_S|\bar{B}_q\rangle &= \frac{1}{3}M_{B_q}^2 f_{B_q}^2 \widetilde{B}_{S,B_q}\end{aligned} \tag{4.7}$$

are given in Tab. 4.1. In ratios of observables across the two systems, e.g. r_{ds} as discussed in Section 4.5, treating the bag parameters as independent input variables would overestimate the uncertainty of the observable. Therefore, we use the bag parameters for the B_s system and relate them to those of the B_d system using the ratio

$$\xi^2 \equiv \frac{f_{B_s}^2 B_{B_s}}{f_{B_d}^2 B_{B_d}} \tag{4.8}$$

as well as the equivalent for the $\widetilde{B}_S$ bag parameters,

$$\xi_S^2 \equiv \frac{f_{B_s}^2 \widetilde{B}_{S,B_s}}{f_{B_d}^2 \widetilde{B}_{S,B_d}}\,. \tag{4.9}$$

While ξ has been determined in Ref. [40], the ratio ξ_S is not commonly quoted in the literature. We calculate ξ_S using the ratio of decay constants f_{B_s}/f_{B_d} as given in Tab. 4.1 together with the ratio of the bag parameters $\widetilde{B}_S$, which can be calculated from the results of Ref. [40]. Here, we note that the bag parameters are defined differently as compared to this thesis,

$$\widetilde{B}_S \equiv \eta_3 B^{(3)}\,, \tag{4.10}$$

so we combine the result from Ref. [40],

$$\frac{B^{(3)}_{B_s}}{B^{(3)}_{B_d}} = 1.092 \pm 0.034\,, \tag{4.11}$$

with the ratio of the conversion factors

$$\frac{\eta_3^s}{\eta_3^d} = 0.996\,51 \pm 0.000\,39\,, \tag{4.12}$$

which was calculated using the input parameters in Tab. I of Ref. [40]. We obtain as an intermediate result

$$\frac{\widetilde{B}_{S,B_s}}{\widetilde{B}_{S,B_s}} = 1.088 \pm 0.034\,, \tag{4.13}$$

which yields together with f_{B_s}/f_{B_d} the value for ξ_S as given in Tab. 4.1. Note that using this parametrisation, the decay constants drop out completely from a ratio of B_d to B_s observables.

For the Λ_{QCD}/m_b-suppressed matrix elements, the lattice QCD results for the B_s system from Refs. [40, 165] read

$$\begin{aligned}
\langle B_s|R_0|\bar{B}_s\rangle &= (-0.43 \pm 0.18)\ f_{B_s}^2 M_{B_s}^2\,,\\
\langle B_s|R_1|\bar{B}_s\rangle &= (0.07 \pm 0.00)\ f_{B_s}^2 M_{B_s}^2\,,\\
\langle B_s|\widetilde{R}_1|\bar{B}_s\rangle &= (0.04 \pm 0.00)\ f_{B_s}^2 M_{B_s}^2\,,\\
\langle B_s|R_2|\bar{B}_s\rangle &= (-0.18 \pm 0.07)\ f_{B_s}^2 M_{B_s}^2\,,\\
\langle B_s|\widetilde{R}_2|\bar{B}_s\rangle &= (0.18 \pm 0.07)\ f_{B_s}^2 M_{B_s}^2\,,\\
\langle B_s|R_3|\bar{B}_s\rangle &= (0.38 \pm 0.13)\ f_{B_s}^2 M_{B_s}^2\,,\\
\langle B_s|\widetilde{R}_3|\bar{B}_s\rangle &= (0.29 \pm 0.10)\ f_{B_s}^2 M_{B_s}^2\,.
\end{aligned} \tag{4.14}$$

For the B_d system, we use the value

$$\langle B_d|R_0|\bar{B}_d\rangle = (-0.35 \pm 0.19)\ f_{B_d}^2 M_{B_d}^2 \tag{4.15}$$

from Ref. [40]. For the remaining matrix elements we neglect $\text{SU}(3)_\text{F}$-breaking effects beyond factorisation and write

$$\langle B_d|R_i|\bar{B}_d\rangle = \frac{f_{B_d}^2 M_{B_d}^2}{f_{B_s}^2 M_{B_s}^2}\langle B_s|R_i|\bar{B}_s\rangle\,, \tag{4.16}$$

where $R_i \in \{R_2, \widetilde{R}_2, R_3, \widetilde{R}_3\}$. The matrix elements of R_1 and $\widetilde{R}_1$ are suppressed by the ratio $m_d/m_s \approx 0.03$, so they are set to zero. For ratios of observables across the B_s and B_d systems, we use

$$\langle B_q|R_i|\bar{B}_q\rangle \equiv f_{B_q}^2 M_{B_q}^2 B_{R_i,B_q}\,, \qquad\qquad B_{R_i,B_d} \equiv \frac{B_{R_i,B_s}}{\zeta}\,, \tag{4.17}$$

where the parameter

$$\zeta = 1.0 \pm 0.1 \tag{4.18}$$

encodes the $SU(3)_F$-breaking effects. We choose to set the symmetry breaking effects at the central value to zero and introduce a 10% uncertainty as these effects have not been determined on the lattice yet. Using the ratio f_{B_s}/f_{B_d}, the decay constants drop out of the ratio of the Λ_{QCD}/m_b-suppressed corrections too.

As the last set of input parameters, we present the CKM elements used in the phenomenological analysis. We use the results from Ref. [166]:

$$\begin{aligned}\frac{\lambda_u^d}{\lambda_t^d} &= (0.0105 \pm 0.0107) + i\,(-0.4259 \pm 0.0091)\ , \\ \frac{\lambda_u^s}{\lambda_t^s} &= (-0.008\,77 \pm 0.000\,43) + i\,(0.018\,58 \pm 0.000\,38)\ .\end{aligned} \tag{4.19}$$

For a direct calculation of $\Delta\Gamma$, the absolute values $|\lambda_t^d|$ and $|\lambda_t^s|$ are required too. These depend on the value of $|V_{cb}|$, which is obtained from either inclusive or exclusive decays as [167]

$$|V_{cb}^{\text{incl}}| = (42.16 \pm 0.51) \times 10^{-3}\,, \quad \text{[168]}, \tag{4.20}$$

$$|V_{cb}^{\text{excl}}| = (39.45 \pm 0.56) \times 10^{-3}\,, \quad [B \to (D, D^*)\ell\nu]\,, \quad \text{FLAG avg.,} \quad \text{[30, 169–177]}, \tag{4.21}$$

where for the inclusive $|V_{cb}|$ the result from Ref. [178] may also be used and yields a similar value. Alternatively, we can also use the current SM fit which excludes measurements of $|V_{cb}|$ [166],

$$|V_{cb}^{\text{SM fit}}| = (41.78^{+0.61}_{-0.78}) \times 10^{-3}\,. \tag{4.22}$$

Note that the value cited in Ref. [20] contains a typo and uses the value of $|V_{cb}| = 0.0416$ from the full fit. This has been corrected here together with the corresponding plots shown below. Using these results, we calculate for λ_t^q:

$$\begin{aligned}|\lambda_t^{d,\text{SM fit}}| &= (8.56^{+0.08}_{-0.34}) \times 10^{-3}\,, & |\lambda_t^{d,\text{excl}}| &= (8.08^{+0.18}_{-0.37}) \times 10^{-3}\,, \\ |\lambda_t^{s,\text{incl}}| &= (41.39 \pm 0.50) \times 10^{-3}\,, & |\lambda_t^{s,\text{excl}}| &= (38.73 \pm 0.55) \times 10^{-3}\,.\end{aligned} \tag{4.23}$$

The value for $|\lambda_t^{d,\text{SM fit}}|$ above is obtained from the 1σ best-fit results for $|V_{td}|$ and $|V_{tb}|$ as calculated by Ref. [166] from a global fit of the CKM parameters. The value for $|\lambda_t^{d,\text{excl}}|$ is obtained by rescaling $|\lambda_t^{d,\text{SM fit}}|$ with the ratio of the two $|V_{cb}|$ values from Eq. (4.21) and Eq. (4.22) since fixing the value of $|V_{cb}|$ to the result from exclusive semileptonic B decays would yield a result with a poor p-value [20]. The CKM values in the B_s system are determined directly from $|V_{cb}^{\text{incl/excl}}|$ since $|V_{ts}| = (0.983 \pm 0.001)|V_{cb}|$ due to unitarity of the CKM matrix, and the value of $|V_{tb}| = 0.9991$ does not depend on the choice of $|V_{cb}|$.

Finally, it is worth remarking on the choice of renormalisation scales and schemes that will be referenced in the rest of the chapter. After the matching calculation as presented in Section 2.6, the charm and bottom masses are in the OS scheme. For phenomenological applications, we transform the squared mass ratio z to the $\overline{\text{MS}}$ scheme, which leads to the additional scales μ_c and μ_b from the renormalisation of the $\overline{\text{MS}}$ masses $\overline{m}_c$ and $\overline{m}_b$ respectively. For this purpose, we also transform the charm quark mass to the case of five active quarks, so we obtain $\overline{z}(4.2\,\text{GeV}) = 0.049540$. The overall factor $(m_b^{\text{OS}})^2$ of Γ_{12} in Eq. (2.80) can be calculated from different input values of the bottom mass. We consider three different approaches, which we call schemes. For the pole scheme, the on-shell bottom mass is substituted directly. In the $\overline{\text{MS}}$ scheme, we use the conversion of the OS to $\overline{\text{MS}}$ scheme to express the factor in terms of the $\overline{\text{MS}}$ mass. Lastly, the OS mass is converted to the PS mass, see Section 2.1.2, which we call the PS scheme. The conversions of different mass schemes are implemented as expansions in α_s, and we truncate the perturbation series after the conversion to the same order in α_s as the original expression obtained in the matching calculation, i.e. to α_s^3 for the contributions from Q_8 and to α_s^2 otherwise.

The results in the pole scheme, which use the m_b^{OS} mass directly as an input for the overall factor of $(m_b^{\text{OS}})^2$, are shown for comparison in the following sections, but we do not use them to calculate our final averages of the observables. This is because of the renormalon ambiguity of order Λ_{QCD}, which appears in the definition of the pole mass and leads to a poor convergence of the perturbative expansion in α_s.

Since the matching coefficients of the Λ_{QCD}/m_b-suppressed matrix elements are only known to LO, the conversion between different masses in the overall factor is of higher orders in α_s, i.e. any mass scheme may be used for the bottom mass in the overall factor. We choose this to be m_b^{PS} in all schemes mentioned above. The LO matching coefficients have a strong scale dependence; therefore, the perturbative uncertainty stemming from these matching coefficients is calculated separately.

The observables depend on a number of renormalisation scales for which there is some freedom of choice, as is explained below. The highest scale we encounter is μ_0, the scale of matching of the $|\Delta B| = 1$ Hamiltonian to the Standard Model, which we choose to be $\mu_0 = 165\,\text{GeV} \approx \overline{m}_t(\overline{m}_t)$. Next, we have the scale μ_1 of the matching to the $|\Delta B| = 2$ transition operator together with the mass renormalisation scales μ_c and μ_b. We choose these scales to be equal to each other and vary them simultaneously between 2.1 GeV and 8.4 GeV to estimate the perturbative uncertainty around the central value of $\mu_1 = 4.2\,\text{GeV}$. Lastly, the lowest scale of the problem is the scale μ_2 at which the matrix elements are defined. We chose $\mu_2 = m_b^{\text{OS}} = 4.758\,\text{GeV}$.

When results are presented at different orders in perturbation theory, those orders refer to the matching coefficients H and $\widetilde{H}_S$ only. The coefficients of the Λ_{QCD}/m_b-suppressed

matrix elements are always inserted to LO. Moreover, M_{12} is always inserted up to NLO to independently test the convergence of the perturbative series for Γ_{12}.

4.3 The width difference $\Delta\Gamma$ from $\Delta\Gamma/\Delta M$

We first present the results for the real part of Γ_{12}, i.e. for the observable $\Delta\Gamma$. The most accurate determinations of $\Delta\Gamma$ without using experimental values for ΔM as well as the ratio $\Delta\Gamma/\Delta M$ are shown in Fig. 4.1 for the B_s system and in Fig. 4.2 for the B_d system.

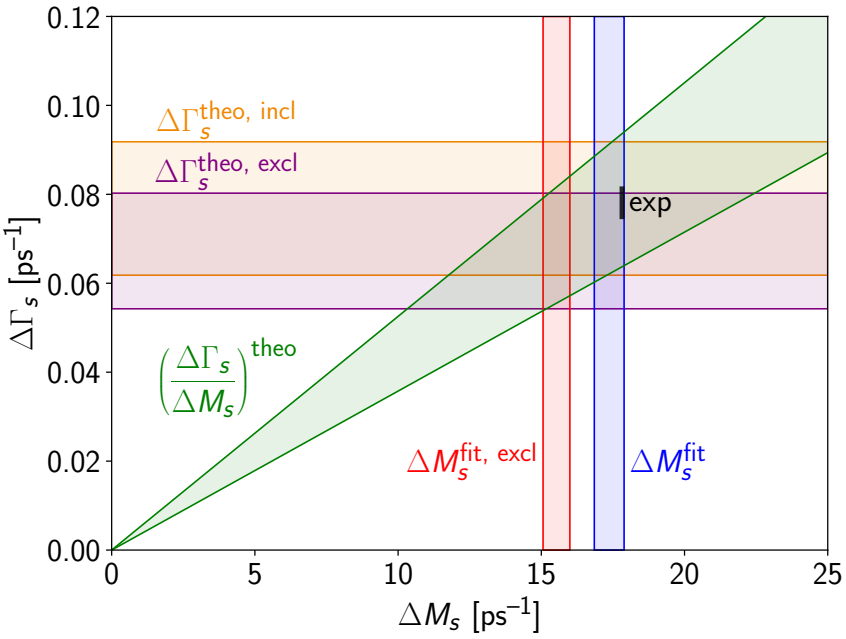

Figure 4.1: Comparison of theoretical determinations for $\Delta\Gamma_s$ and ΔM_s with their measurements for different values of $|V_{cb}|$ according to Eq. (4.23). The band for ΔM_s^{fit} corresponds to the 1σ-result given in Ref. [166] where ΔM_s was excluded from the fit. For $\Delta M_s^{\text{fit,excl}}$, the band was rescaled by $|V_{cb}^{\text{excl}}|^2/|V_{cb}^{\text{SM fit}}|^2$. The experimental values are as quoted in Eq. (1.43) and Eq. (1.44) except that the uncertainty on ΔM_s was increased by a factor of ten.

In order to identify new physics contributions, the theoretical and experimental bands in the two plots can be compared. However, there is a sizeable difference in the $|V_{cb}|$ measurements, see Eq. (4.21), which impacts our ability to make conclusive statements about potential disagreement between Standard Model theory and experiment from the $\Delta\Gamma$ or ΔM bands alone. The ratio $\Delta\Gamma/\Delta M$ does not have the same ambiguity since the CKM factor $\lambda_t \propto |V_{cb}|^2$ cancels. This underscores the importance of $\Delta\Gamma/\Delta M$ as

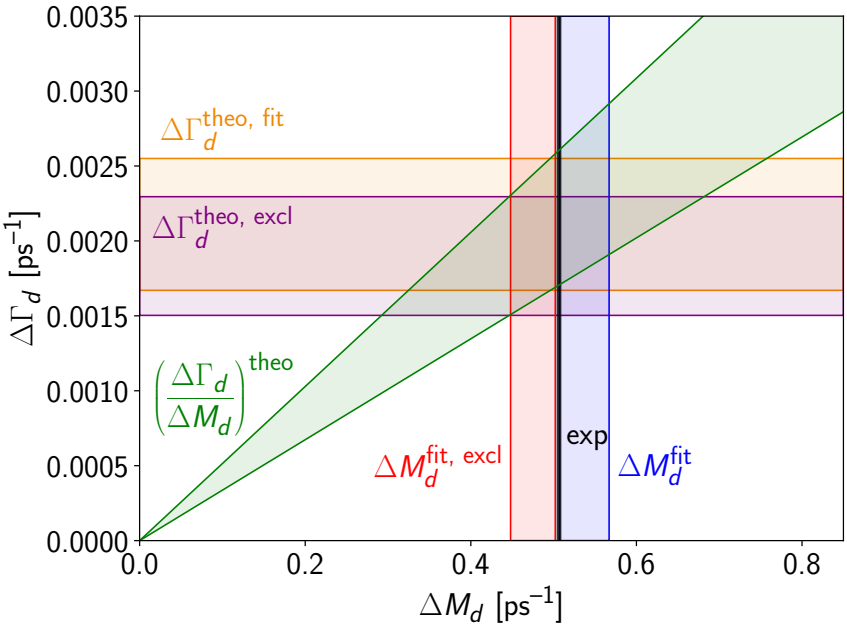

Figure 4.2: Comparison of theoretical determinations $\Delta\Gamma_d$ and ΔM_d with their measured values. The bands were determined in a similar fashion as for Fig. 4.1 except for $\Delta\Gamma_d^{\text{theo,fit}}$. In this case, the value of $|\lambda_t^{d,\text{SM fit}}|$ was used. The experimental values shown are as quoted in Eq. (1.46) and Eq. (1.47).

an observable where new physics contributions can be investigated independently of the $|V_{cb}|$ controversy.

In the following sections, the results for $\Delta\Gamma$ as obtained from the ratio $\Delta\Gamma/\Delta M$ are discussed in detail, including the uncertainty sources and the size of the novel contributions calculated in this thesis. The results for the deep expansion of only the current-current operators at NNLO have been published in Ref. [20] while the updated observables including penguin operators at NNLO can be found in Ref. [155].

4.3.1 B_s system

Before presenting the results for the ratio $\Delta\Gamma_s/\Delta M_s$, the uncertainty analysis is explained in brief. For the central value, the input values as given in Section 4.2 are used, and the scales are chosen as explained in that section. We set the matching and mass scales to $\mu_1 = \mu_c = \mu_b = 4.2\,\text{GeV}$. For the other scales, we choose $\mu_0 = 165\,\text{GeV}$ and $\mu_2 = 4.758\,\text{GeV}$, which are kept fixed for the central value and the uncertainty analysis.

To determine the contributions to the total uncertainty from each of the input parameters, they are varied within the given uncertainty, and the symmetrised results are shown below.

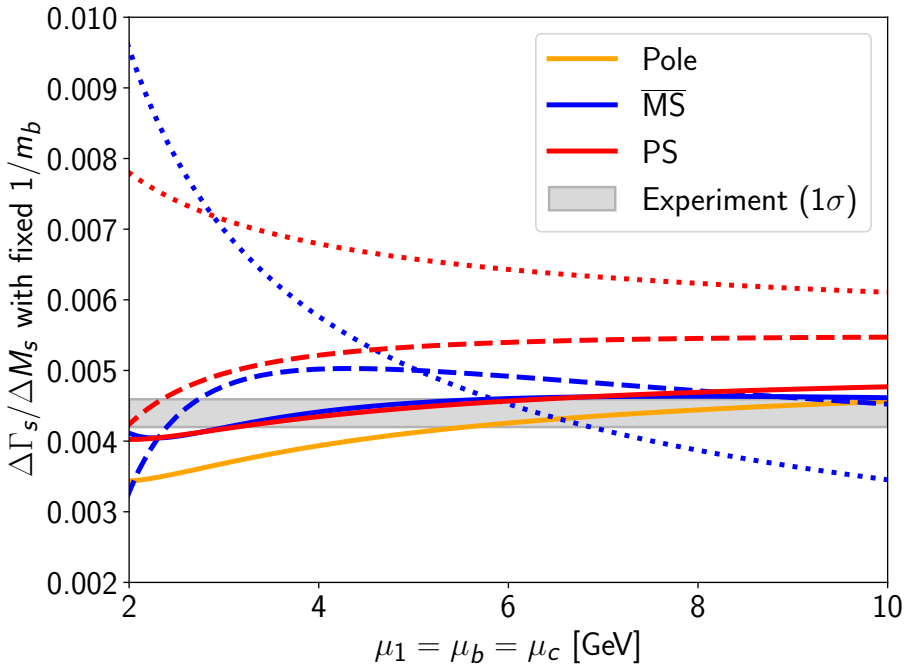

Figure 4.3: Renormalisation scale dependence of $\Delta\Gamma_s/\Delta M_s$ at LO (short dashes), NLO (long dashes) and NNLO (solid). The Λ_{QCD}/m_b-suppressed contributions are kept fixed at the central scale.

We group the input parameter uncertainties into three groups for which the individual contributions have been added in quadrature. The first, labelled "$B\widetilde{B}_S$", contains only the uncertainty stemming from the leading-power bag parameters. The Λ_{QCD}/m_b-suppressed matrix elements have their uncertainties combined in the term "$1/m_b$", where the correlation between the matrix elements of R_2, $\widetilde{R}_2$, R_3 and $\widetilde{R}_3$ has been accounted for, see Eq. (4.59) in Section 4.7. All remaining input parameter uncertainties are combined in the "input" term.

The individual contributions to the total uncertainty from the hadronic matrix elements as well as all other input parameters are shown in Appendix E for all observables discussed in this chapter, i.e. $\Delta\Gamma/\Delta M$ and a_{fs} in the B_s and B_d systems as well as the double ratio $(\Delta\Gamma_d/\Delta M_d)/(\Delta\Gamma_s/\Delta M_s)$.

The perturbative uncertainty, which results from the remaining scale dependence after truncating the perturbation series, is split into an uncertainty stemming from the leading ("scale") and power-suppressed ("scale, $1/m_b$") matching coefficients. To determine the scale uncertainty, we simultaneously vary $\mu_1 = \mu_c = \mu_b$ between 2.1 GeV and 8.4 GeV. The scale variation of the matching coefficients for the leading-power matrix elements is shown in Fig. 4.3. For comparison, the full scale variation including the scale dependence of the power-suppressed matching coefficients is presented in Fig. 4.4.

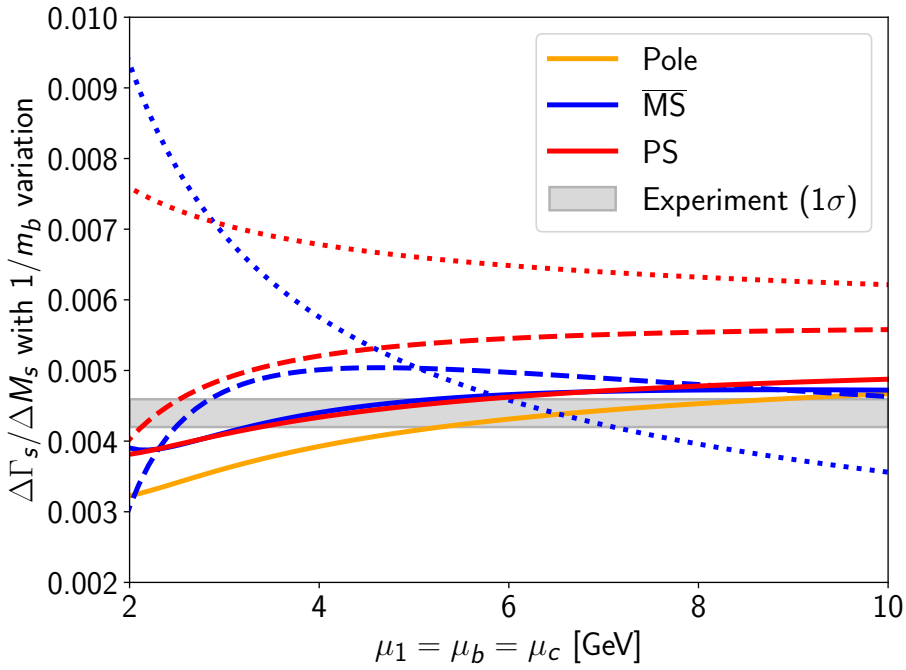

Figure 4.4: Renormalisation scale dependence of $\Delta\Gamma_s/\Delta M_s$ at LO (short dashes), NLO (long dashes) and NNLO (solid) for the leading-power and Λ_{QCD}/m_b-suppressed matching coefficients.

The results obtained at NNLO are

$$\begin{aligned}
\frac{\Delta\Gamma_s}{\Delta M_s} &= \left(3.98^{+0.49}_{-0.53\text{scale}}\ {}^{+0.09}_{-0.19\text{scale, }1/m_b} \pm 0.11_{B\widetilde{B}_S} \pm 0.78_{1/m_b} \pm 0.06_{\text{input}}\right) \times 10^{-3}\ (\text{pole})\,, \\
\frac{\Delta\Gamma_s}{\Delta M_s} &= \left(4.45^{+0.19}_{-0.40\text{scale}}\ {}^{+0.09}_{-0.19\text{scale, }1/m_b} \pm 0.12_{B\widetilde{B}_S} \pm 0.78_{1/m_b} \pm 0.05_{\text{input}}\right) \times 10^{-3}\ (\overline{\text{MS}})\,, \\
\frac{\Delta\Gamma_s}{\Delta M_s} &= \left(4.38^{+0.33}_{-0.35\text{scale}}\ {}^{+0.09}_{-0.19\text{scale, }1/m_b} \pm 0.12_{B\widetilde{B}_S} \pm 0.78_{1/m_b} \pm 0.05_{\text{input}}\right) \times 10^{-3}\ (\text{PS})\,.
\end{aligned} \tag{4.24}$$

We observe that the uncertainty from the Λ_{QCD}/m_b-suppressed matrix elements has the biggest impact, followed by the perturbative uncertainty of the leading-power matching coefficients, which are the focus of this thesis. The other sources of uncertainty are less important. For the perturbative uncertainty at leading power, we can confirm that successive orders in α_s reduce the remaining scale uncertainty, as shown in Fig. 4.3 for the $\overline{\text{MS}}$ and PS schemes. The variation of the $\overline{\text{MS}}$ results decreases from 121% at LO to 33% at NLO and then to 13% at NNLO, all computed over the interval of $2.1\,\text{GeV} \leq \mu_1 \leq 8.4\,\text{GeV}$. In the PS scheme, the variation at LO is much smaller at 34%, and it is further reduced to 25% at NLO and 16% at NNLO. At NNLO, the $\overline{\text{MS}}$ and PS schemes lead to very similar results over the entire renormalisation scale interval considered, which illustrates the stability of the perturbative expansion.

At the central scale, the size of the successive orders in the perturbative series gives an indication of the accuracy and convergence of the series. In the PS scheme, the NLO corrections reduce the LO result by about 22%, and the NNLO corrections are smaller than those at NLO by about 40%. This shows that successive terms in the series are indeed decreasing in magnitude. For the $\overline{\text{MS}}$ scheme, the NLO corrections reduce the LO result by about 10%, but the NNLO corrections are of a similar size. However, at values of μ_1 larger or smaller than the central scale, the NNLO corrections are much smaller, demonstrating the good convergence of the perturbative expansion. The central scale is special because the NLO corrections vanish at 5 GeV in the $\overline{\text{MS}}$ scheme.

The agreement with the experimental value is very good at the central scale at NNLO. Both the $\overline{\text{MS}}$ and PS scheme calculations are within the 1σ uncertainty of the experiment for a range of about ± 1 GeV around the central value. Remarkably, the LO and NLO determinations do not agree well with the experiment for most of the considered scale range, underscoring the importance of the NNLO corrections. However, the pole scheme calculation underestimates the true value of the observable, and the renormalisation scale dependence is worse as well due to the renormalon uncertainty.

Since the inclusion of the penguin operators at NNLO and as a deeper expansion in z at NLO is a novel result, the size of these corrections and their impact on the scale uncertainty in comparison with the results from Ref. [20] is worth commenting on. A direct comparison of the scale uncertainty as visualised in Fig. 4.5 shows that the symmetrised uncertainty is reduced by about 8%, which is true for both the $\overline{\text{MS}}$ and PS schemes. In the $\overline{\text{MS}}$ scheme at the central scale, the NLO penguin contributions receive corrections of about 70% from higher terms in the z expansion, and at NNLO the new penguin operators contributions make up about 12% of the total NNLO term. Overall, the central value differs by about 2% between the results in Ref. [20] and the full NNLO calculation.

Before calculating $\Delta\Gamma$, it is interesting to see how the dependence on the hadronic elements is reduced when considering the ratio $\Delta\Gamma/\Delta M$. The leading term in the ratio does not depend on any low-energy matrix elements as ΔM is proportional to $\langle B_q|Q|\bar{B}_q\rangle$, which subsequently cancels. The ratio therefore only depends on the ratios of the matrix elements of $\widetilde{Q}_S$ and R_i to the leading term matrix element. Writing the result in the $\overline{\text{MS}}$ scheme as

$$\frac{\Delta\Gamma_s}{\Delta M_s} = 4.45 \times 10^{-3} \approx \left(4.27 + 1.70_{\widetilde{Q}_S/Q} - 1.53_{1/m_b}\right) \times 10^{-3}\ (\overline{\text{MS}})\,, \tag{4.25}$$

it becomes apparent that the sub-leading terms cancel almost entirely. In the decomposition above, the first term is independent of any hadronic matrix elements while $\widetilde{Q}_S/Q$ depends on the ratio of the leading-power matrix elements. The final term contains all contributions from Λ_{QCD}/m_b-suppressed matrix elements. The corrections from the sub-leading terms are less than 4%.

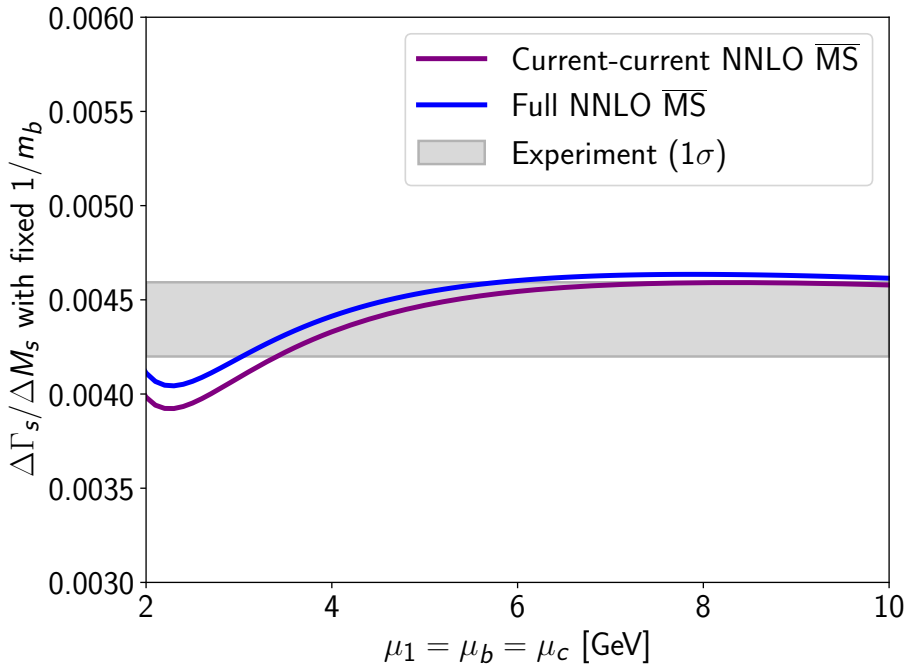

Figure 4.5: Renormalisation scale dependence of $\Delta\Gamma_s/\Delta M_s$ in the $\overline{\text{MS}}$ scheme for the leading-power terms with $\mu_1 = \mu_b = \mu_c$. The NNLO current-current result includes the penguin operator contributions at NLO in an expansion up to z^1. The full NNLO result including penguin operators uses a more accurate expansion of the penguin contributions up to z^{10}.

The current state-of-the-art prediction for $\Delta\Gamma_s$ is obtained by multiplying the theoretical value of $\Delta\Gamma_s/\Delta M_s$ by the experimental value for ΔM_s, which is [25]

$$\Delta M_s^{\text{exp}} = (17.7656 \pm 0.0057)\,\text{ps}^{-1}\,. \tag{4.26}$$

Hence, our results read

$$\begin{aligned}
\Delta\Gamma_s &= \left(7.06^{+0.88}_{-0.94\text{scale}}\ {}^{+0.16}_{-0.34\text{scale, }1/m_b} \pm 0.19_{B\widetilde{B}_S} \pm 1.39_{1/m_b} \pm 0.10_{\text{input}}\right) \times 10^{-2}\,\text{ps}^{-1}\ (\text{pole})\,,\\
\Delta\Gamma_s &= \left(7.90^{+0.34}_{-0.71\text{scale}}\ {}^{+0.16}_{-0.34\text{scale, }1/m_b} \pm 0.21_{B\widetilde{B}_S} \pm 1.39_{1/m_b} \pm 0.09_{\text{input}}\right) \times 10^{-2}\,\text{ps}^{-1}\ (\overline{\text{MS}})\,,\\
\Delta\Gamma_s &= \left(7.77^{+0.59}_{-0.62\text{scale}}\ {}^{+0.16}_{-0.34\text{scale, }1/m_b} \pm 0.20_{B\widetilde{B}_S} \pm 1.39_{1/m_b} \pm 0.09_{\text{input}}\right) \times 10^{-2}\,\text{ps}^{-1}\ (\text{PS})\,.
\end{aligned} \tag{4.27}$$

To obtain the final result for $\Delta\Gamma_s$, the values from the $\overline{\text{MS}}$ and PS schemes are averaged. The uncertainties are first added in quadrature separately for the upper and lower bounds, then symmetrised and finally averaged across the renormalisation schemes. The most accurate prediction for $\Delta\Gamma_s$ is hence

$$\Delta\Gamma_s = (0.078 \pm 0.015)\,\text{ps}^{-1}\,. \tag{4.28}$$

In comparison with the experimental value [26]

$$\Delta\Gamma_s^{\text{exp}} = (0.0781 \pm 0.0035)\,\text{ps}^{-1}\,, \tag{4.29}$$

we observe that the theoretical uncertainty is about four times as large as that of the measured value. However, with the perturbative corrections calculated in this thesis, the theoretical uncertainty is dominated by the Λ_{QCD}/m_b-suppressed contributions, more specifically the corresponding hadronic matrix elements. The perturbative uncertainty of the leading-power matching coefficients on the other hand is only slightly larger than the experimental uncertainty.

Finally, it is worth comparing the result obtained in this work with that of Refs. [27, 179], which calculate $\Delta\Gamma_s = (0.091 \pm 0.015)\,\text{ps}^{-1}$ to NLO. Our corresponding NLO prediction is $\Delta\Gamma_s = (0.091 \pm 0.020)\,\text{ps}^{-1}$, which agrees within the given uncertainties. It is perhaps unexpected that the central values are identical given that the penguin operators were only considered to LO in Refs. [27, 179]; however, the authors also use different hadronic matrix elements obtained from QCD sum rules as calculated in Refs. [45, 46]. We note that the renormalisation scale dependence in Refs. [27, 179] is constructed to be much smaller, and the same is true for the power-suppressed matrix elements.

4.3.2 B_d system

The phenomenological analysis for the B_d system proceeds in the same way as for the B_s system discussed in the preceding section. The ratio as calculated in the three renormalisation schemes by analogy with $\Delta\Gamma_s/\Delta M_s$ is

$$\begin{aligned}
\frac{\Delta\Gamma_d}{\Delta M_d} &= \left(3.83^{+0.49}_{-0.53\text{scale}}\,{}^{+0.12}_{-0.20\text{scale, }1/m_b} \pm 0.11_{B\widetilde{B}_S} \pm 0.79_{1/m_b} \pm 0.06_{\text{input}}\right) \times 10^{-3}\ (\text{pole})\,,\\
\frac{\Delta\Gamma_d}{\Delta M_d} &= \left(4.29^{+0.19}_{-0.40\text{scale}}\,{}^{+0.12}_{-0.20\text{scale, }1/m_b} \pm 0.12_{B\widetilde{B}_S} \pm 0.79_{1/m_b} \pm 0.05_{\text{input}}\right) \times 10^{-3}\ (\overline{\text{MS}})\,,\\
\frac{\Delta\Gamma_d}{\Delta M_d} &= \left(4.22^{+0.33}_{-0.35\text{scale}}\,{}^{+0.12}_{-0.20\text{scale, }1/m_b} \pm 0.12_{B\widetilde{B}_S} \pm 0.79_{1/m_b} \pm 0.05_{\text{input}}\right) \times 10^{-3}\ (\text{PS})\,,
\end{aligned} \tag{4.30}$$

where the uncertainty sources are clustered in the same categories as in Eq. (4.24), and the individual contributions are given in Appendix E. The variation of the renormalisation scale for the leading-power matching coefficients is shown in Fig. 4.6. For comparison, the variation of both the leading-power and Λ_{QCD}/m_b-suppressed contributions is presented in Fig. 4.7. The uncertainties are very similar to what is observed for the B_s system, see the discussion following Eq. (4.24). Moreover, the impact of the novel contributions from a deeper expansion in z for the penguin operators at NLO and the inclusion of the penguin operators at NNLO leads to the same improvements as observed for the B_s system.

Besides the cancellation of the hadronic matrix elements in the ratio $\Delta\Gamma_d/\Delta M_d$, we also observe a similar cancellation among the linear and quadratic terms in λ_u^d/λ_t^d for the B_d

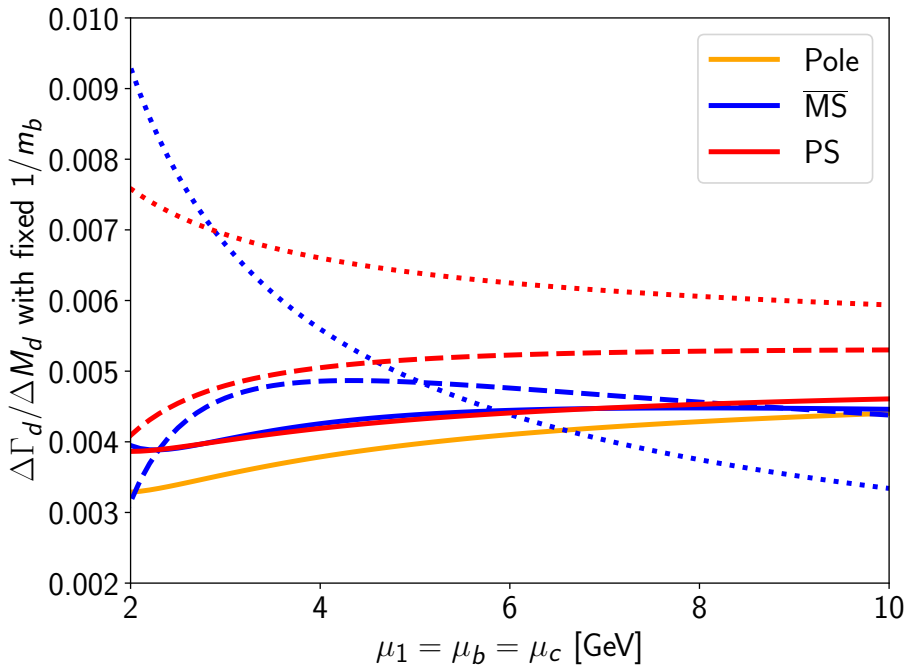

Figure 4.6: Renormalisation scale dependence of $\Delta\Gamma_d/\Delta M_d$ at LO (short dashes), NLO (long dashes) and NNLO (solid). The Λ_{QCD}/m_b-suppressed contributions are kept fixed at the central scale.

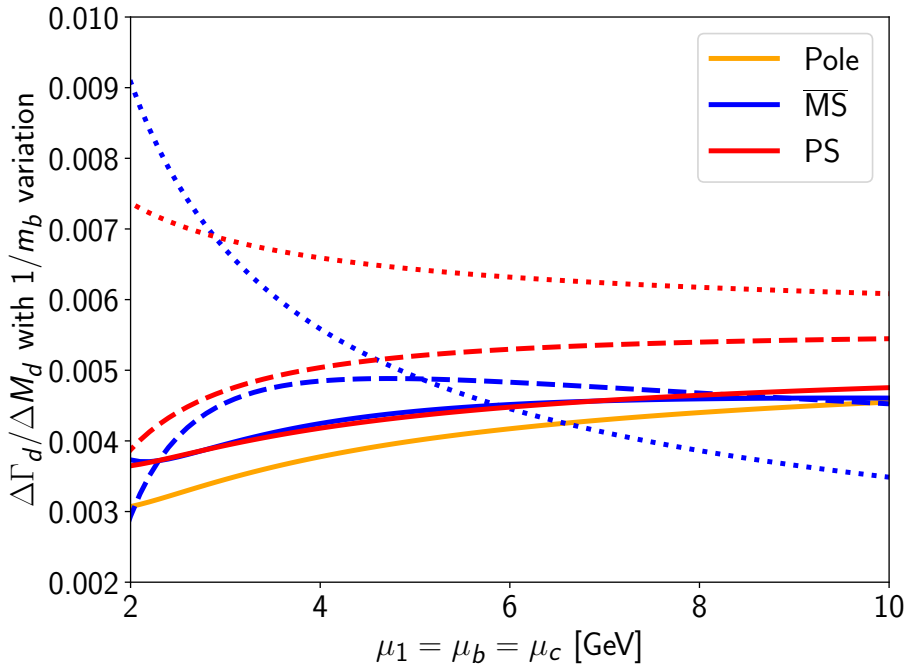

Figure 4.7: Renormalisation scale dependence of $\Delta\Gamma_d/\Delta M_d$ at LO (short dashes), NLO (long dashes) and NNLO (solid) for the leading-power and Λ_{QCD}/m_b-suppressed matching coefficients.

system, see Eq. (1.61) on page 12. We confirm the results of Ref. [36], where it was found that the sum of the aforementioned terms leads to a correction of about 2% at NLO. With the complete NNLO results presented here, the correction from λ_u^d/λ_t^d has a size of about 1.9%. As the terms proportional to λ_u^s/λ_t^s are numerically small too, leading to corrections of about 0.2%, the ratio $\Delta\Gamma/\Delta M$ agrees within the uncertainties across the B_s and B_d systems, see Section 4.5.

Multiplying $\Delta\Gamma_d/\Delta M_d$ by the experimentally measured value for ΔM_d [26],

$$\Delta M_d^{\text{exp}} = (0.5065 \pm 0.0019)\,\text{ps}^{-1}\,, \tag{4.31}$$

we obtain $\Delta\Gamma_d$ in the respective schemes,

$$\begin{aligned}
\Delta\Gamma_d &= \left(1.94^{+0.25}_{-0.27\text{scale}}\,{}^{+0.06}_{-0.10\text{scale, }1/m_b} \pm 0.06_{B\widetilde{B}_S} \pm 0.40_{1/m_b} \pm 0.03_{\text{input}}\right) \times 10^{-3}\,\text{ps}^{-1}\ (\text{pole})\,,\\
\Delta\Gamma_d &= \left(2.17^{+0.10}_{-0.20\text{scale}}\,{}^{+0.06}_{-0.10\text{scale, }1/m_b} \pm 0.06_{B\widetilde{B}_S} \pm 0.40_{1/m_b} \pm 0.03_{\text{input}}\right) \times 10^{-3}\,\text{ps}^{-1}\ (\overline{\text{MS}})\,,\\
\Delta\Gamma_d &= \left(2.14^{+0.17}_{-0.18\text{scale}}\,{}^{+0.06}_{-0.10\text{scale, }1/m_b} \pm 0.06_{B\widetilde{B}_S} \pm 0.40_{1/m_b} \pm 0.03_{\text{input}}\right) \times 10^{-3}\,\text{ps}^{-1}\ (\text{PS})\,.
\end{aligned} \tag{4.32}$$

As for the B_s system, we average the results from the $\overline{\text{MS}}$ and PS schemes together with the symmetrised uncertainties. These are obtained by first adding the upper and lower bounds separately in quadrature and then symmetrising for each scheme. The averaged result is

$$\Delta\Gamma_d = (0.002\,15 \pm 0.000\,45)\,\text{ps}^{-1}\,. \tag{4.33}$$

Since $\Delta\Gamma_d$ is not measured to a high enough precision, the comparison with the theoretical prediction does not allow us to draw any conclusions. To further reduce the theoretical uncertainty from this calculation, a more accurate determination of the Λ_{QCD}/m_b-suppressed matrix elements is necessary, similar to what is observed in the B_s system. However, $\Delta\Gamma_d$ may also be computed from the double ratio discussed in Section 4.5, where the dependence on the hadronic matrix elements largely cancels and which leads to a more accurate prediction.

4.4 The flavour-specific CP asymmetry a_{fs}

The results of the flavour-specific CP asymmetry for B_s mesons in the three schemes as defined in Section 4.2 are

$$\begin{aligned}
a_{\text{fs}}^s &= \left(2.27^{+0.00}_{-0.03\text{scale}}\,{}^{+0.01}_{-0.00\text{scale, }1/m_b} \pm 0.01_{B\widetilde{B}_S} \pm 0.04_{1/m_b} \pm 0.07_{\text{input}}\right) \times 10^{-5}\ (\text{pole})\,,\\
a_{\text{fs}}^s &= \left(2.24^{+0.10}_{-0.18\text{scale}}\,{}^{+0.01}_{-0.00\text{scale, }1/m_b} \pm 0.01_{B\widetilde{B}_S} \pm 0.04_{1/m_b} \pm 0.07_{\text{input}}\right) \times 10^{-5}\ (\overline{\text{MS}})\,,\\
a_{\text{fs}}^s &= \left(2.30^{+0.03}_{-0.07\text{scale}}\,{}^{+0.01}_{-0.00\text{scale, }1/m_b} \pm 0.01_{B\widetilde{B}_S} \pm 0.04_{1/m_b} \pm 0.07_{\text{input}}\right) \times 10^{-5}\ (\text{PS})\,.
\end{aligned} \tag{4.34}$$

The uncertainties are clustered in the same way as for $\Delta\Gamma/\Delta M$, and the contributions from each individual parameter are presented in Appendix E. For a_{fs}, the inclusion of the penguin operators has a smaller impact on the final result when comparing with the results from Ref. [20], where only the current-current operators are included to NNLO. In the $\overline{\text{MS}}$ scheme, the overall result changes by about 0.5%. This is because the NNLO penguin terms only contribute 1% to the NNLO result, mainly since the contributions stemming from two penguin operators are proportional to λ_t, so they do not affect the imaginary part of Γ_{12}. At NLO, the behaviour is the same, and the deeper expansion for the penguins beyond z^1 changes the total NLO contribution by about 3%.

Similarly, for the B_d system, we obtain

$$\begin{aligned}
a_{\text{fs}}^d &= -\left(5.18^{+0.00}_{-0.08\text{scale}}{}^{+0.03}_{-0.01\text{scale, }1/m_b} \pm 0.03_{B\widetilde{B}_S} \pm 0.09_{1/m_b} \pm 0.16_{\text{input}}\right) \times 10^{-4}\ (\text{pole})\,, \\
a_{\text{fs}}^d &= -\left(5.12^{+0.23}_{-0.41\text{scale}}{}^{+0.03}_{-0.01\text{scale, }1/m_b} \pm 0.03_{B\widetilde{B}_S} \pm 0.09_{1/m_b} \pm 0.16_{\text{input}}\right) \times 10^{-4}\ (\overline{\text{MS}})\,, \\
a_{\text{fs}}^d &= -\left(5.26^{+0.07}_{-0.15\text{scale}}{}^{+0.03}_{-0.01\text{scale, }1/m_b} \pm 0.03_{B\widetilde{B}_S} \pm 0.09_{1/m_b} \pm 0.16_{\text{input}}\right) \times 10^{-4}\ (\text{PS})\,.
\end{aligned} \tag{4.35}$$

Also in this case, the inclusion of the penguin operators does not significantly impact the final result, with the central value in the $\overline{\text{MS}}$ scheme shifting by 0.5% as compared to the NNLO current-current results from Ref. [20]. This is because of the same reason as for the B_s system: The contributions from two penguin operator insertions to Γ_{12}/M_{12} are purely real.

The scale variation of the leading-power terms is shown in Figs. 4.8 and 4.9 for the B_s and B_d systems respectively. As for $\Delta\Gamma$, we add the uncertainties of the upper and lower bounds in quadrature in the $\overline{\text{MS}}$ and PS scheme, symmetrise the total uncertainty and then average the results across the schemes to yield

$$\begin{aligned}
a_{\text{fs}}^s &= (2.27 \pm 0.13) \times 10^{-5}\,, \\
a_{\text{fs}}^d &= -(5.19 \pm 0.30) \times 10^{-4}\,.
\end{aligned} \tag{4.36}$$

The uncertainties of a_{fs} are comparable for B_s and B_d, and the relative size of them is similar to $\Delta\Gamma/\Delta M$ apart from the parameter uncertainty. The variation of the parameters leads to a larger uncertainty for the CP asymmetry since the leading term of a_{fs} is proportional to m_c and λ_u/λ_t. The uncertainty of the two respective input parameters is of comparable magnitude, and the total "input" uncertainty is of similar size as that of the Λ_{QCD}/m_b-suppressed matrix elements.

The CP asymmetry vanishes in the limit $m_c \to 0$, so it is interesting to see the size of the contributions from higher-order terms in the $z = m_c^2/m_b^2$ expansion. The size of those contributions in the PS and $\overline{\text{MS}}$ schemes is only 13% for both a_{fs}^s and a_{fs}^d. Therefore, the results obtained in this thesis agree within the uncertainty with those of Ref. [29].

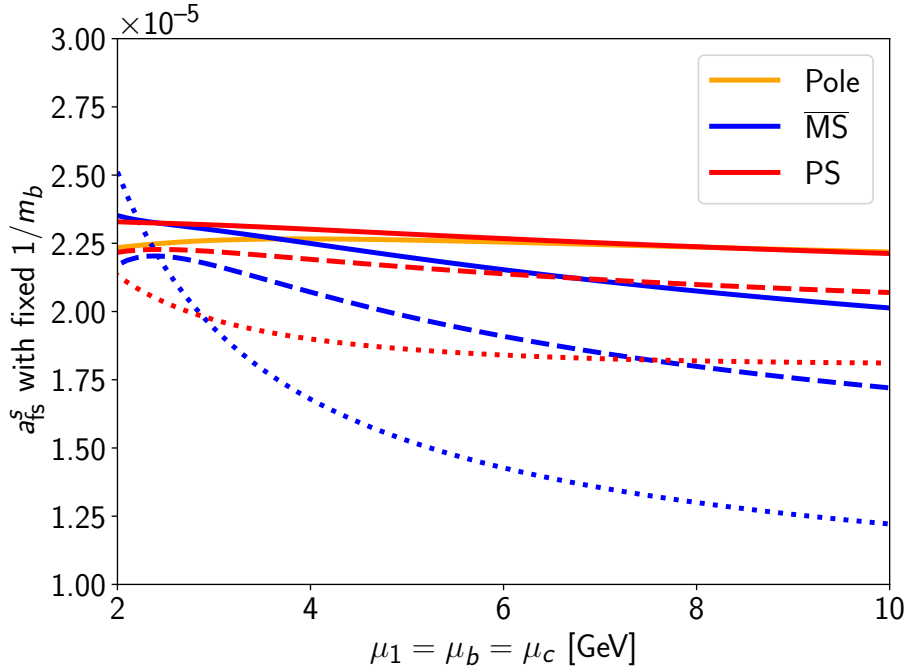

Figure 4.8: Renormalisation scale dependence of $a_{\rm fs}^s$ at LO (short dashes), NLO (long dashes) and NNLO (solid) for the simultaneous scale variation of $\mu_1 = \mu_b = \mu_c$. The matching coefficients of the $\Lambda_{\rm QCD}/m_b$-suppressed matrix elements are kept fixed at the central scale.

Referring to the scale variation plots in Fig. 4.8 and Fig. 4.9, we observe that the dependence on the renormalisation scale is reduced when higher orders in the perturbative series are included. In the PS scheme, the size of the NNLO corrections at the central scale is a factor of three smaller than the NLO corrections, indicating a good convergence of the perturbative series. The ranges of the scale variation of successive orders also overlap, which also shows that the perturbative corrections are decreasing and converging asymptotically. We also note that the pole scheme result, which is shown for comparison, exhibits a very flat scale dependence and is close to the curve for the PS scheme.

The comparison of the theoretical predictions with experiments is limited by the availability of accurate measurements. For $a_{\rm fs}^d$, however, the NNLO predictions agree with the 1σ uncertainty of the experimental value. Once more accurate measurements become available, the theoretical results presented here will serve as a benchmark, enabling inferences about BSM physics. In particular, any non-zero measurement of $a_{\rm fs}^s$ will likely point towards new physics effects due to its small SM value. The measurement of the CP asymmetry in the B_d system on the other hand can be used in combination with the theoretical prediction to constrain the apex of the CKM unitarity triangle, see Section 4.6.

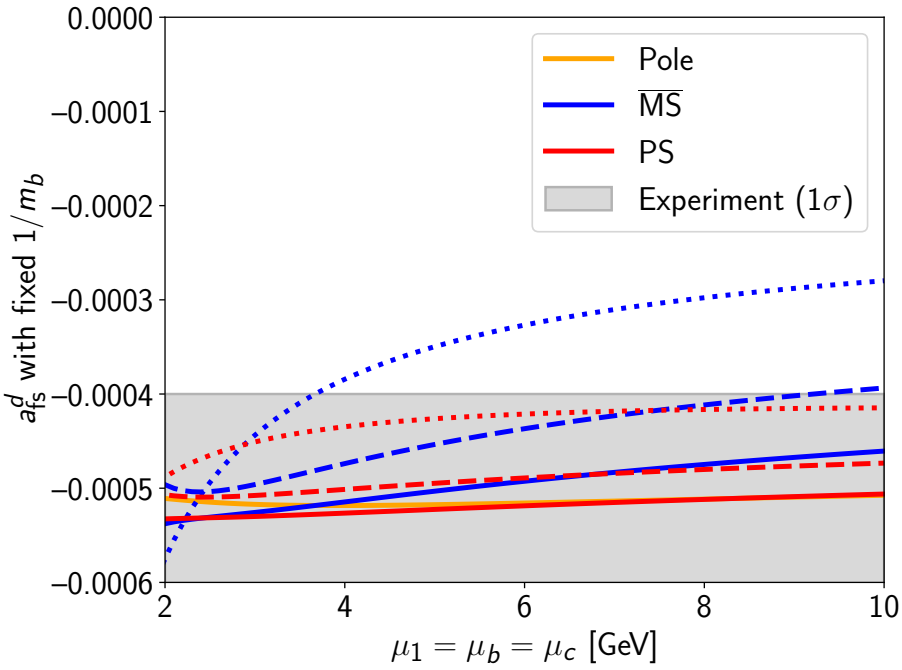

Figure 4.9: Renormalisation scale dependence of $a_{\rm fs}^d$ at LO (short dashes), NLO (long dashes) and NNLO (solid) for the simultaneous scale variation of $\mu_1 = \mu_b = \mu_c$. The matching coefficients of the $\Lambda_{\rm QCD}/m_b$-suppressed matrix elements are kept fixed at the central scale.

4.5 The double ratio $(\Delta\Gamma_d/\Delta M_d)/(\Delta\Gamma_s/\Delta M_s)$

In this section, another observable is discussed, which is a ratio of four observables taken across the B_s and B_d system,

$$r_{ds} \equiv \frac{\Delta\Gamma_d}{\Delta M_d} \times \frac{\Delta M_s}{\Delta\Gamma_s}\,. \tag{4.37}$$

The advantage of calculating this quantity is that many of the uncertainties that impact accurate predictions of $\Delta\Gamma_d$ cancel in the ratio. Moreover, $\Delta\Gamma_s$, ΔM_s and ΔM_d have been measured precisely, so r_{ds} can be combined with those measurements to yield a very accurate prediction of $\Delta\Gamma_d$.

The cancellation of uncertainties in the double ratio r_{ds} is due to the fact that the hadronic matrix elements can be expressed in terms of their ratios in the B_s and B_d systems, which are more accurately determined. For example, the leading-power matrix elements can be expressed entirely in terms of the constants ξ and ξ_S as given in Tab. 4.1 as well as the corresponding bag parameters B_{B_s} and $\widetilde{B}_{B_s}$ in the B_s system. For the power-suppressed matrix elements, we used the parametrisation of Eq. (4.17) and manually fix the SU(3)$_F$ breaking beyond factorisation to zero, i.e. we choose $\zeta = 1$. With this and the accurately

determined ratio of the decay constants f_{B_s}/f_{B_d}, the quantity r_{ds} has a reduced uncertainty stemming from the bag parameters, which are only needed for the B_s system.

Using this parametrisation, the results for the double ratio in the three different renormalisation schemes are

$$\begin{aligned}
r_{ds} &= 0.962^{+0.003}_{-0.008\text{scale, comb.}} \pm 0.012_{B\widetilde{B}_S} \pm 0.040_{1/m_b} \pm 0.003_{\text{input}}\ (\text{pole})\,,\\
r_{ds} &= 0.965^{+0.002}_{-0.007\text{scale, comb.}} \pm 0.011_{B\widetilde{B}_S} \pm 0.036_{1/m_b} \pm 0.003_{\text{input}}\ (\overline{\text{MS}})\,,\\
r_{ds} &= 0.964^{+0.003}_{-0.008\text{scale, comb.}} \pm 0.012_{B\widetilde{B}_S} \pm 0.036_{1/m_b} \pm 0.003_{\text{input}}\ (\text{PS})\,. \qquad (4.38)
\end{aligned}$$

Note that the perturbative uncertainty for the leading-power and Λ_{QCD}/m_b-suppressed terms has been combined here as both are minor sources of uncertainty. The biggest source of uncertainty in the above observable stems from the Λ_{QCD}/m_b-suppressed matrix elements in the B_s system and the uncertainty of 10% that was assumed on the symmetry-breaking effects in ζ. However, this term is actually dominated by ζ, and the uncertainty from the bag parameters alone is just ± 0.008. With a future determination of the ratio similar to ξ and ξ_S, we expect this uncertainty to shrink. The other dominant source of uncertainty is from the leading-power bag parameters in the B_s system. For a detailed breakdown of the uncertainties, see Appendix E.

In Appendix F, we also present the results for r_{ds} without making use of the parametrisation of the matrix elements in terms of ξ, ξ_S, f_{B_s}/f_{B_d} and ζ, using the same input values as for the separate calculations of the observables in the B_s and B_d systems. This leads to an increased uncertainty from the matrix elements by about a factor of two.

The remaining scale dependence of r_{ds} is shown in Fig. 4.10. The scale dependence from the truncation of the perturbation series increases at higher orders, which is the opposite of what one would expect for a converging series. However, this is because the scale variation of $\Delta\Gamma/\Delta M$ is almost identical for the B_s and B_d system, see Figs. 4.3 and 4.6. Therefore, small variations at higher orders lead to a seemingly bad convergence of the perturbation series. However, we note that the perturbative uncertainty is small compared to all other sources, and the NNLO predictions are very accurate.

As for the other observables, we average the results from the $\overline{\text{MS}}$ and PS schemes to obtain the overall result

$$r_{ds} = 0.965 \pm 0.038\,. \qquad (4.39)$$

The value of r_{ds} is close to one because the dependence on the ratio of the matrix elements of Q and $\widetilde{Q}_S$ cancels with the power-suppressed matrix elements, see Eq. (4.25). Additionally, the dependence on the CKM parameters λ_u/λ_t is small for B_s and B_d. Referring to the parametrisation from Eq. (1.61),

$$\frac{\Gamma_{12}^q}{M_{12}^q} \equiv \left[c^q + a^q\,\frac{\lambda_u^q}{\lambda_t^q} + b^q\,\frac{(\lambda_u^q)^2}{(\lambda_t^q)^2}\right] \times 10^{-4}\,, \qquad (4.40)$$

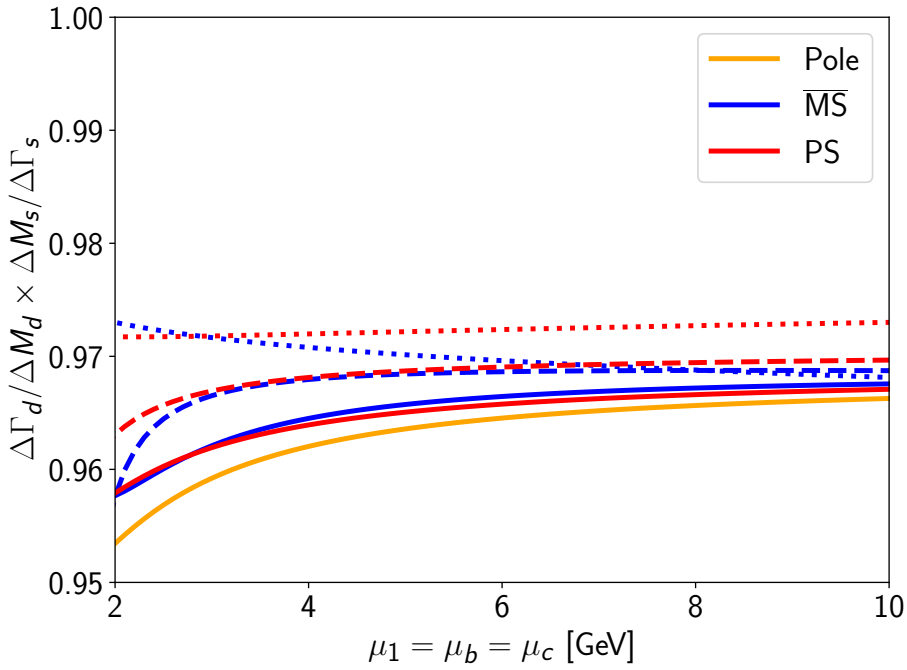

Figure 4.10: Renormalisation scale dependence of r_{ds} at LO (short dashes), NLO (long dashes) and NNLO (solid) for the simultaneous scale variation of $\mu_1 = \mu_b = \mu_c$. The matching coefficients of the leading-power and Λ_{QCD}/m_b-suppressed matrix elements are varied together.

this means that the ratio mostly depends on c^d/c^s, and the values for c^d and c^s are very similar due to the cancellation of the sub-leading matrix elements in each constant.

Finally, r_{ds} can be combined with the experimental values for the mass differences from Eqs. (4.26) and (4.31) and $\Delta\Gamma_s$ from Eq. (4.29) to obtain

$$\Delta\Gamma_d = (0.002\,15 \pm 0.000\,13)\,\text{ps}^{-1}\,. \tag{4.41}$$

This is the most accurate prediction of $\Delta\Gamma_d$ to date, where we note that the uncertainty has been reduced by about 70% as compared to Eq. (4.33) due to the use of r_{ds}, which suppresses the impact of the hadronic uncertainties on the final result.

4.6 Constraints on the CKM triangle from B meson observables

The apex of the CKM unitarity triangle can be constrained using B meson mixing observables to identify sectors with new physics, as presented in this section. The general strategy for new physics searches in the B meson sector using the mixing observables starts with the most accurate observable, which is the double ratio r_{ds}. Once a deviation from

the Standard Model is observed here, one can then investigate the ratios $\Delta\Gamma_d/\Delta\Gamma_s$ and $\Delta M_d/\Delta M_s$ to further narrow down the effective operators in which new physics enters.

Since the measurement of $\Delta\Gamma_d$ is not accurate enough yet, we cannot fully implement this approach. However, we can examine the effect that precise measurements would have on the apex of the CKM triangle. For this purpose, both $\Delta\Gamma_d/\Delta\Gamma_s$ and a_{fs}^d are investigated to yield constraints in the $(\bar{\rho},\bar{\eta})$-plane, which can be combined with other measurements and constraints to draw conclusions about BSM physics. This graphical representation is hence a convenient tool to compare the constraints from B mixing observables with those from other measurements.

The apex of the CKM unitarity triangle is precisely determined from other B meson mixing observables, so the constraints from $\Delta\Gamma_d/\Delta\Gamma_s$ and a_{fs}^d provide a way to test the Standard Model using exclusively B meson mixing observables. The length of one of the sides of the unitarity triangle $R_t = \sqrt{\bar{\rho}^2+\bar{\eta}^2}$ is obtained from measurements of $\Delta M_d/\Delta M_s$ while the angle β at the origin is determined by $a_{CP}(B_d(t)\to J/\psi K_S)\propto \sin(2\beta)$.

Before presenting the constraints, the CKM unitarity triangle is defined in terms of the CKM matrix elements that appear in the B meson mixing. In general, the unitarity of the CKM matrix implies

$$\sum_k V_{ik}V_{jk}^* = 0\,, \tag{4.42}$$

where $i\neq j$ denote two different up-type quark flavours. There are six relations of this type, giving rise to six unitarity triangles. The most commonly considered is the one stemming from

$$V_{ud}V_{ub}^* + V_{cd}V_{cb}^* + V_{td}V_{tb}^* = 0\,, \tag{4.43}$$

which is the CKM unitarity triangle that is referred to in the following. We can also write the equation above in terms of the constants λ_i^d, normalising to λ_c^d:

$$1 + \frac{\lambda_u^d}{\lambda_c^d} + \frac{\lambda_t^d}{\lambda_c^d} = 0\,. \tag{4.44}$$

The triangle constructed in this way has the vertices $(0,0)$, $(1,0)$ and $(\bar{\rho},\bar{\eta})$ in the Wolfenstein parametrisation [35, 180, 181]. This is because $\lambda_u^d/\lambda_c^d = -\bar{\rho}+i\bar{\eta}$.

The parametrisation of a_{fs}^d that can be used to constrain the CKM triangle is discussed first. With the definition of Eq. (4.40), we write

$$a_{\text{fs}}^d = \left[a^d\,\text{Im}\frac{\lambda_u^d}{\lambda_t^d} + b^d\,\text{Im}\frac{(\lambda_u^d)^2}{(\lambda_t^d)^2}\right]\times 10^{-4}\,, \tag{4.45}$$

so a_{fs}^d is expressed in terms of the constants a^d, b^d and the Wolfenstein parameters A, λ, $\bar{\rho}$ and $\bar{\eta}$. The ratio λ_u^d/λ_t^d is defined in terms of the Wolfenstein parameters as

$$\frac{\lambda_u^d}{\lambda_t^d} \equiv -\frac{R_u}{R_t}\,e^{i\alpha} = \frac{1-\bar{\rho}-i\bar{\eta}}{(1-\bar{\rho})^2+\bar{\eta}^2} - 1\,. \tag{4.46}$$

$\overline{\text{MS}}$	LO	NLO	NNLO	PS	LO	NLO	NNLO
a_0^d	$8.20^{+4.20}_{-1.94}$	$10.40^{+0.81}_{-1.45}$	$11.40^{+0.55}_{-0.95}$	a_0^d	$9.53^{+1.17}_{-0.39}$	$11.11^{+0.22}_{-0.50}$	$11.71^{+0.15}_{-0.35}$
b_0^d	$0.069^{+0.037}_{-0.020}$	$0.112^{+0.043}_{-0.020}$	$0.134^{+0.042}_{-0.022}$	b_0^d	$0.081^{+0.011}_{-0.009}$	$0.122^{+0.027}_{-0.008}$	$0.140^{+0.034}_{-0.015}$
c_0^d	$-69.7^{+17.7}_{-35.0}$	$-64.1^{+14.2}_{-0.0}$	$-58.3^{+4.0}_{-1.9}$	c_0^d	$-81.0^{+5.2}_{-9.4}$	$-66.2^{+8.7}_{-2.1}$	$-57.6^{+3.5}_{-3.3}$

Table 4.2: Results for a_0^d, b_0^d and c_0^d in the $\overline{\text{MS}}$ (left) and PS (right) schemes. The perturbative uncertainty is obtained by varying $\mu_1 = \mu_b = \mu_c$ simultaneously between 2.1 GeV and 8.4 GeV.

Therefore, a measurement of a_{fs}^d can be used to produce a curve on which the apex $(\bar{\rho}, \bar{\eta})$ of the CKM triangle must lie.

To construct the constraints, the values of a^d, b^d and c^d are calculated to LO, NLO and NNLO. We give their contributions from the leading-power and Λ_{QCD}/m_b-suppressed matrix elements separately,

$$\begin{aligned} a &= a_0 + a_1 \,, \\ b &= b_0 + b_1 \,, \\ c &= c_0 + c_1 \,, \end{aligned} \tag{4.47}$$

where the subscripts 0 and 1 denote the leading and Λ_{QCD}/m_b-suppressed contributions respectively. The power-suppressed contributions are

$$\begin{aligned} a_1^d &= 0.622^{+0.073}_{-0.020\,\text{scale, }1/m_b} \pm 0.35_{\text{param}} \,, \\ b_1^d &= 0.091^{+0.011}_{-0.003\,\text{scale, }1/m_b} \pm 0.031_{\text{param}} \,, \\ c_1^d &= 15.36^{+1.98}_{-1.22\,\text{scale, }1/m_b} \pm 8.03_{\text{param}} \,, \end{aligned} \tag{4.48}$$

where the uncertainty from varying all input parameters labelled "param" has been absorbed into the sub-leading contributions, i.e. the constants a_0^d, b_0^d and c_0^d carry only a perturbative uncertainty. For the perturbative uncertainties, the scales $\mu_1 = \mu_c = \mu_b$ are varied simultaneously in the interval [2.1 GeV, 8.4 GeV] around the central scale 4.2 GeV. The leading-power contributions are given in Tab. 4.2 in the $\overline{\text{MS}}$ and PS schemes with the perturbative uncertainties at each order.

The results for a_0^d and b_0^d can be compared to a previous determination in Ref. [20] using only the current-current contributions at NNLO. It is interesting to see that b_0^d is unchanged because the penguin operators do not contribute to the $(\lambda_u^d)^2/(\lambda_t^d)^2$ term. Only the mixed contributions from one penguin and one current-current operator insertion affect a_{fs}^d, and only at the linear λ_u^d/λ_t^d order, i.e. a_0^d.

$\overline{\text{MS}}$	LO	NLO	NNLO	PS	LO	NLO	NNLO
a_0^s	$8.23^{+4.21}_{-1.94}$	$10.43^{+0.82}_{-1.46}$	$11.44^{+0.56}_{-0.96}$	a_0^s	$9.56^{+1.17}_{-0.39}$	$11.15^{+0.23}_{-0.50}$	$11.76^{+0.16}_{-0.35}$
b_0^s	$0.072^{+0.038}_{-0.021}$	$0.115^{+0.043}_{-0.021}$	$0.137^{+0.042}_{-0.022}$	b_0^s	$0.083^{+0.011}_{-0.009}$	$0.125^{+0.026}_{-0.007}$	$0.143^{+0.034}_{-0.015}$
c_0^s	$-71.1^{+18.2}_{-35.8}$	$-65.4^{+14.5}_{-0.0}$	$-59.6^{+4.0}_{-1.9}$	c_0^s	$-82.6^{+5.4}_{-9.6}$	$-67.6^{+8.9}_{-2.1}$	$-58.9^{+3.5}_{-3.3}$

Table 4.3: Results for a_0^s, b_0^s and c_0^s in the $\overline{\text{MS}}$ (left) and PS (right) schemes. The perturbative uncertainty is obtained by varying $\mu_1 = \mu_b = \mu_c$ simultaneously between 2.1 GeV and 8.4 GeV.

The second constraint on the apex of the CKM triangle is constructed from the ratio $\Delta\Gamma_d/\Delta\Gamma_s$, which can be parametrised as

$$\frac{\Delta\Gamma_d}{\Delta\Gamma_s} = \frac{1}{\xi^2}\,\frac{M_{B_d}}{M_{B_s}}\left|\frac{\lambda_t^d}{\lambda_t^s}\right|^2 \frac{c^d + a^d\,\text{Re}\dfrac{\lambda_u^d}{\lambda_t^d} + b^d\,\text{Re}\dfrac{(\lambda_u^d)^2}{(\lambda_t^d)^2}}{c^s + a^s\,\text{Re}\dfrac{\lambda_u^s}{\lambda_t^s} + b^s\,\text{Re}\dfrac{(\lambda_u^s)^2}{(\lambda_t^s)^2}}\,, \tag{4.49}$$

using Eq. (4.5) and Eq. (4.40) . The values of a_0^s, b_0^s and c_0^s are given in Tab. 4.3, and the power-suppressed contributions are

$$\begin{aligned} a_1^s &= 0.616^{+0.074}_{-0.025\text{scale, }1/m_b} \pm 0.35_{\text{param}}\,, \\ b_1^s &= 0.090^{+0.011}_{-0.004\text{scale, }1/m_b} \pm 0.030_{\text{param}}\,, \\ c_1^s &= 15.28^{+1.90}_{-0.93\text{scale, }1/m_b} \pm 7.90_{\text{param}}\,, \end{aligned} \tag{4.50}$$

where the uncertainties are defined in the same way as for the B_d system above. Since the constants x^s and x^d agree within their perturbative uncertainties, the ratio in Eq. (4.49) can be simplified by identifying the constants of the B_s system with those of the B_d system, effectively ignoring SU(3)_F-breaking corrections to the hadronic matrix elements. The simplified ratio is hence given by

$$\frac{\Delta\Gamma_d}{\Delta\Gamma_s} = \frac{1}{\xi^2}\,\frac{M_{B_d}}{M_{B_s}}\left|\frac{\lambda_t^d}{\lambda_t^s}\right|^2 \frac{1 + \dfrac{a^d}{c^d}\,\text{Re}\dfrac{\lambda_u^d}{\lambda_t^d} + \dfrac{b^d}{c^d}\,\text{Re}\dfrac{(\lambda_u^d)^2}{(\lambda_t^d)^2}}{1 + \dfrac{a^d}{c^d}\,\text{Re}\dfrac{\lambda_u^s}{\lambda_t^s} + \dfrac{b^d}{c^d}\,\text{Re}\dfrac{(\lambda_u^s)^2}{(\lambda_t^s)^2}}\,. \tag{4.51}$$

In addition to the Wolfenstein parametrisation of λ_u^d/λ_t^d given in Eq. (4.46), we need similar expressions for the ratio in the B_s system as well as the absolute values of λ_t^q. These are given by

$$\frac{\lambda_u^s}{\lambda_t^s} = \lambda^2(-\bar\rho + i\bar\eta) + \lambda^4\left(-\bar\rho(1-\bar\rho) - \bar\eta^2 + i\bar\eta(1-2\bar\rho)\right) + \mathcal{O}(\lambda^6)\,, \tag{4.52}$$

and

$$\left|\lambda_t^d\right|^2 = A^2\lambda^4\left(\bar{\eta}^2 + (1-\bar{\rho})^2\right)\lambda^2 + \mathcal{O}\left(\lambda^{10}\right), \tag{4.53}$$

$$\left|\lambda_t^s\right|^2 = A^2\lambda^4\left(1 - \lambda^2(1-2\bar{\rho})\right) + \mathcal{O}\left(\lambda^8\right), \tag{4.54}$$

where the common factor $A^2\lambda^4 = |V_{cb}|^2$ drops out in the ratio, eliminating a large source of uncertainty. The ratio $|\lambda_t^d/\lambda_t^s|^2$ can hence be expanded as

$$\left|\frac{\lambda_t^d}{\lambda_t^s}\right|^2 = \lambda^2\left(\bar{\eta}^2 + (1-\bar{\rho})^2\right) \times \left(1 + \lambda^2(1-2\bar{\rho})\right) + \mathcal{O}\left(\lambda^6\right). \tag{4.55}$$

Therefore, only the Wolfenstein parameter λ is needed for $\Delta\Gamma_d/\Delta\Gamma_s$, and it is given by [166]

$$\lambda = 0.224\,98 \pm 0.000\,23\,. \tag{4.56}$$

Substituting Eqs. (4.46), (4.52) and (4.55) into Eq. (4.51) leads to the second constraint on the apex of the CKM triangle.

In Fig. 4.11, the constraints for the apex of the CKM triangle are shown for two hypothetical measurements of a_{fs}^d and $\Delta\Gamma_d$. The width of the bands is given by the perturbative uncertainty of the leading-power terms, illustrating the level of accuracy achieved by the calculations of this thesis. Here, only the PS scheme results are shown since we find agreement between the PS and $\overline{\text{MS}}$ schemes within the perturbative uncertainties, see Ref. [20]. The perturbative uncertainty given by the width of the bands in Fig. 4.11 is obtained from the simultaneous variation of the leading-power and Λ_{QCD}/m_b-suppressed terms, so it is smaller than the uncertainty that would be obtained from adding the scale variation of x_0^q and x_1^q. However, this difference is not visible in a plot of the constraints on the unitarity triangle.

Additionally, the constraints with all uncertainties combined are shown in Fig. 4.12. It is interesting to observe that the width of the bands does not change significantly for $\Delta\Gamma_d/\Delta\Gamma_s$. This is because the terms involving a^d/c^d and b^d/c^d are small and we have neglected the $\text{SU}(3)_\text{F}$-breaking effects in the hadronic matrix elements. This is a good approximation since those effects are negligible in the ratio and at any rate precisely determined in ξ and ξ_S for the leading-power matrix elements. Therefore, we do not significantly underestimate the uncertainty, as verified in Section 4.7.

Having shown the constraints implied by a_{fs}^d and $\Delta\Gamma_d/\Delta M_d$, the significance of the observables in the context of new physics searches should be stressed again. The flavour-specific CP asymmetry is an interesting probe of new physics since a small change in the phase ϕ_{12}^d in $\arg(M_{12}^d)$ will have a much bigger effect on a_{fs}^d than on β as determined from $a_{CP}(B_d(t) \to J/\psi K_S)$, see the discussion at the beginning of this section. This is because a_{fs}^d in the SM is suppressed by m_c^2/m_b^2 as the leading terms of M_{12}^d and Γ_{12}^d have the same phase. However, a new physics contribution affecting the phase leads

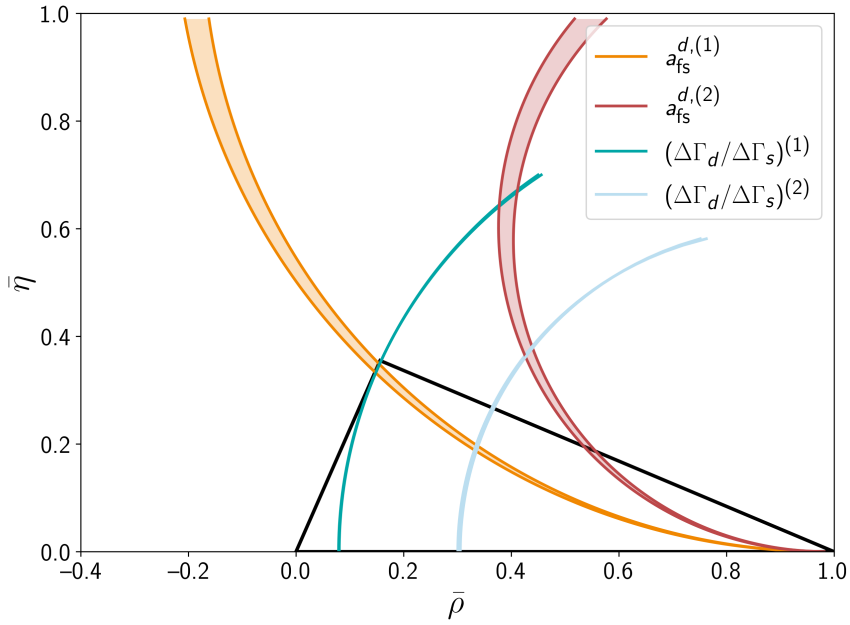

Figure 4.11: Constraints on the apex of the CKM triangle as obtained in the PS scheme. The width of the bands is given by the perturbative uncertainty of the leading-power term. The bands are plotted with $a_{\mathrm{fs}}^{d,(1)} = -5 \times 10^{-4}$, $a_{\mathrm{fs}}^{d,(2)} = -1 \times 10^{-3}$, $(\Delta\Gamma_d/\Delta\Gamma_s)^{(1)} = 0.029$ and $(\Delta\Gamma_d/\Delta\Gamma_s)^{(2)} = 0.0145$ for reference.

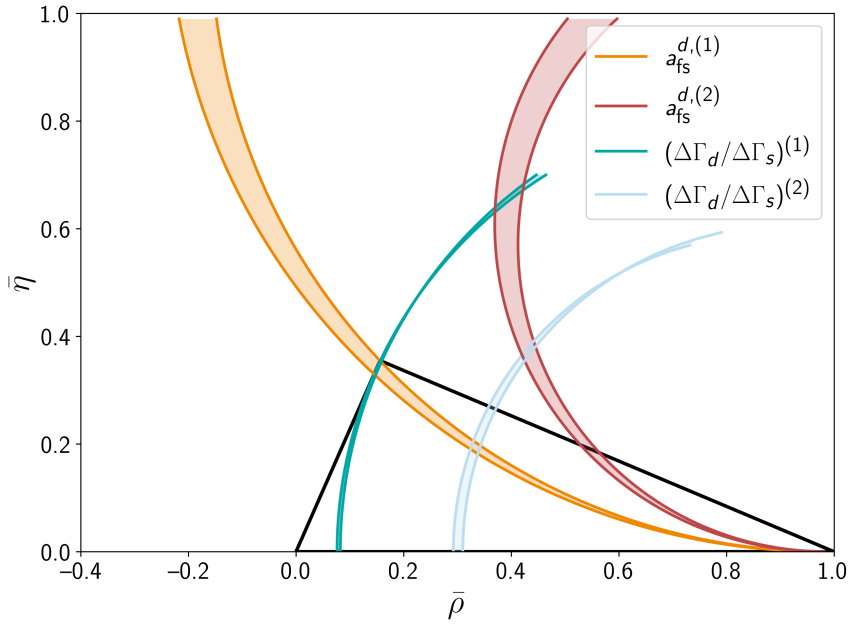

Figure 4.12: Constraints on the apex of the CKM triangle as obtained in the PS scheme. The width of the bands is given by the full uncertainty on the predictions, and the measurements are as given in Fig. 4.11.

to a correction of order $\sin\phi_{12}^d$ at $\mathcal{O}(m_c^0/m_b^0)$ [36, 182]. Meanwhile, the measurement $a_{CP}(B_d(t)\to J/\psi K_S)\propto\sin(2\beta+\phi_{12}^d)$ does not affect β significantly, so the constraints from the two different CP asymmetries would be incompatible in the presence of new physics.

Lastly, let us remark on the use of $\Delta\Gamma_d/\Delta\Gamma_s$ for constraining the CKM triangle. The ratio provides an accurate constraint because many input parameters that have large uncertainties cancel. Most importantly, $|V_{cb}|$ cancels in the ratio, so there is no ambiguity in whether the inclusive or exclusive measurement should be used. Additionally, there are cancellations in the bag parameters and the $\Lambda_{\rm QCD}/m_b$-suppressed corrections as discussed in Ref. [36] and shown in Eq. (4.25). Moreover, the CKM-suppressed contributions in $\Delta\Gamma_s$ are tiny due to the size of λ_u^s, and in $\Delta\Gamma_d$ the terms linear and quadratic in λ_u^d in Eq. (4.40) cancel by coincidence, see the discussion following Eq. (4.30). This makes it possible to determine $\Delta\Gamma_d/\Delta\Gamma_s$ to a very high accuracy and provide better constraints for the CKM triangle than would be possible with $\Delta\Gamma_d/\Delta M_d$. Note also that the overall factor $|\lambda_t^d|^2/|\lambda_t^s|^2$ is the same for the two ratios, so the constraints have a similar shape.

4.7 Results independent of hadronic matrix elements and CKM inputs

Since the phenomenological predictions in this chapter are dependent on many input parameters, which will be determined more accurately in the future, we present our results for Γ_{12}/M_{12} in a convenient format that can be used to update phenomenological predictions without implementing the matching coefficients for Γ_{12} first. For this purpose, Γ_{12}/M_{12} is parametrised as

$$\frac{\Gamma_{12}^q}{M_{12}^q}=\sum_O\left[c_O+a_O\frac{\lambda_u^q}{\lambda_t^q}+b_O\frac{(\lambda_u^q)^2}{(\lambda_t^q)^2}\right]\frac{\langle B_q|O|\bar B_q\rangle}{\langle B_q|Q|\bar B_q\rangle}\times 10^{-4}\,, \tag{4.57}$$

which generalises Eq. (4.40) by removing the dependence on hadronic matrix elements from the coefficients a_O, b_O and c_O. As a consequence, the three sets of coefficients are independent of the light quark flavour, i.e. they are the same for B_s and B_d. The sum in Eq. (4.57) is over the operators

$$O\in\{Q,\widetilde{Q}_S,R_0,R_1,\widetilde{R}_1,\widetilde{R}_2,\widetilde{R}_3\}\,, \tag{4.58}$$

where the operators R_2 and R_3 were removed from the ratio as they are collinear with the set above. Their matrix elements are expressed in terms of $\widetilde{R}_2$ and $\widetilde{R}_3$ as [47]

$$R_2=-\widetilde{R}_2\,,\qquad\qquad R_3=\widetilde{R}_3+\frac{1}{2}\widetilde{R}_2\,, \tag{4.59}$$

where higher orders in Λ_{QCD}/m_b have been discarded. Note that these relations also receive corrections in α_s when they are being applied to operator matrix elements. This is similar to the behaviour of $\langle R_0 \rangle$ at higher orders, see Section 2.4.4, but we can ignore these corrections since the power-suppressed matching coefficients are only determined to LO. The results for the leading-power coefficients in the $\overline{\text{MS}}$ and PS schemes are given in Tabs. 4.4 and 4.5 respectively. The coefficients of the Λ_{QCD}/m_b-suppressed matrix elements are the same across both schemes since they are only known to LO and are presented in Tab. 4.6.

The perturbative uncertainties are obtained from the variation of $\mu_1 = \mu_b = \mu_c$ between 2.1 GeV and 8.4 GeV with the central scale at 4.2 GeV. The uncertainties from the remaining input parameters,

$$\left\{\alpha_s(M_Z),\, m_b(m_b),\, m_c(3\,\text{GeV}),\, m_t^{\text{OS}},\, M_W,\, M_Z\right\}, \tag{4.60}$$

are added in quadrature and given separate from the perturbative uncertainty. The dominant contribution to the total uncertainty stems from the scale variation, so the values given in Tab. 4.4, Tab. 4.5 and Tab. 4.6 can be used for state-of-the-art predictions of $\Delta\Gamma$, a_{fs} and constraints on the CKM unitarity triangle until higher-order matching coefficients become available. We note that the constraints from $\Delta\Gamma_d/\Delta\Gamma_s$ shown in Fig. 4.12 were obtained from the simplified parametrisation given in Eq. (4.51); however, the values quoted here can be used in conjunction with ξ, ξ_S, f_{B_s}/f_{B_d} and ζ as explained in Section 4.5 to obtain almost identical bands when ζ is taken as exactly one.

$\overline{\text{MS}}$	c_O	a_O	b_O
Q	$-42.6^{+4.4}_{-1.8} \pm 0.5$	$10.9^{+0.46}_{-0.90} \pm 0.21$	$0.108^{+0.038}_{-0.023} \pm 0.005$
$\widetilde{Q}_S$	$-84.6^{+0.88}_{-2.90} \pm 0.99$	$2.66^{+0.48}_{-0.28} \pm 0.11$	$0.141^{+0.023}_{-0.000} \pm 0.011$

Table 4.4: Coefficients from Eq. (4.57) in the $\overline{\text{MS}}$ scheme for the leading-power matrix elements with the one-sided input and two-sided perturbative uncertainty.

PS	c_O	a_O	b_O
Q	$-41.9^{+3.7}_{-2.7} \pm 0.5$	$11.20^{+0.08}_{-0.32} \pm 0.23$	$0.115^{+0.030}_{-0.017} \pm 0.006$
$\widetilde{Q}_S$	$-84.4^{+0.8}_{-3.0} \pm 1.0$	$2.74^{+0.39}_{-0.16} \pm 0.11$	$0.139^{+0.022}_{-0.000} \pm 0.012$

Table 4.5: Coefficients from Eq. (4.57) in the PS scheme for the leading-power matrix elements with the one-sided input and two-sided perturbative uncertainty.

$1/m_b$	c_O	a_O	b_O
R_0	$27.9^{+4.3}_{-5.2} \pm 0.5$	$-0.493^{+0.093}_{-0.076} \pm 0.019$	$-0.0449^{+0.0084}_{-0.0069} \pm 0.0024$
R_1	$-55.8^{+10.5}_{-8.6} \pm 0.9$	$0.99^{+0.15}_{-0.19} \pm 0.04$	$0.090^{+0.014}_{-0.017} \pm 0.005$
$\widetilde{R}_1$	$172^{+22}_{-14} \pm 2$	$-3.05^{+0.25}_{-0.39} \pm 0.11$	$-0.277^{+0.023}_{-0.036} \pm 0.015$
$\widetilde{R}_2$	$231^{+31}_{-25} \pm 3$	$-0.73^{+0.16}_{--0.12} \pm 0.02$	$0.0615^{+0.0058}_{-0.0000} \pm 0.0036$
$\widetilde{R}_3$	$3.89^{+0.46}_{-0.12} \pm 0.14$	$4.47^{+0.53}_{-0.14} \pm 0.17$	$0.579^{+0.068}_{-0.018} \pm 0.032$

Table 4.6: Coefficients from Eq. (4.57) for the $\Lambda_{\rm QCD}/m_b$-suppressed matrix elements with the two-sided perturbative and one-sided input uncertainty.

5 BSM Effects in B Meson Mixing from the Chromoelectric Operator

In this chapter, a specific type of BSM models is investigated in the context of B meson mixing. The impact of an additional contribution to the effective coupling of gluons to $\bar{b}q$ currents is modelled for a generic BSM operator contribution to the chromoelectric vertex. For this purpose, the running of the $|\Delta B| = 1$ and $|\Delta B| = 2$ Hamiltonians is extended by right-handed operators, and the mixing between the two Hamiltonians is discussed. We find that the current experimental measurements of $\Delta\Gamma_s$ and a_{fs}^d provide the strongest constraint on new physics in the chromoelectric vertex. The chapter concludes with a presentation of a simple UV completion which highlights the model properties that are relevant for avoiding the exclusion due to measurements of ΔM. The analysis presented here will be published in Ref. [183].

5.1 The chromoelectric vertex and its relevance to BSM models

Before proceeding with the discussion of the Hamiltonians, the particular type of BSM models studied in this chapter is motivated. While Γ_{12} is generally considered to be a probe of light new physics, see e.g. Refs. [31, 184], it is also sensitive to heavy new coloured particles through the effective b-q-gluon vertex shown in Fig. 5.1. In the following, the generic case of the down-type quark $q \in \{d, s\}$ is discussed.

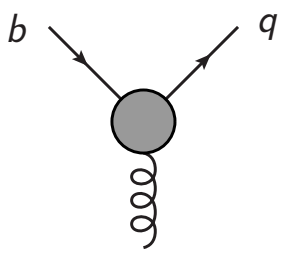

Figure 5.1: Effective b-q-gluon vertex with q denoting a down or strange quark.

The vertex has four form factors, which are the two pairs

$$m_b \bar{v}_q \sigma_{\mu\nu} P_{L,R} T^a u_b \, p^\mu \,, \qquad \bar{v}_q \gamma_\mu P_{L,R} T^a u_b \left(p^2 g^{\mu\nu} - p^\mu p^\nu \right) \,, \tag{5.1}$$

where the light quark mass has been set to zero so that no corresponding form factors proportional to m_q appear. The momentum p^μ is the momentum carried by the gluon while u_q and v_b are spinors of the quark fields. A full-theory contribution to the b-q-gluon vertex can hence be constructed from the four effective operators

$$\begin{aligned} Q_8 &\equiv -\frac{g_s}{16\pi^2} \, m_b \, (\bar{q} \sigma^{\mu\nu} T^a P_R b) \; G^a_{\mu\nu} \,, \qquad & Q^L_{\text{ce}} &\equiv (\bar{q} \gamma_\nu T_a P_L b) \; D^{ab}_\mu G^{\mu\nu}_b \,, \\ Q'_8 &\equiv -\frac{g_s}{16\pi^2} \, m_b \, (\bar{q} \sigma^{\mu\nu} T^a P_L b) \; G^a_{\mu\nu} \,, \qquad & Q^R_{\text{ce}} &\equiv (\bar{q} \gamma_\nu T_a P_R b) \; D^{ab}_\mu G^{\mu\nu}_b \,. \end{aligned} \tag{5.2}$$

The operator Q_{ce} is the chromoelectric operator, alternative terms are chromo-monopole operator or chromo-anapole moment [185]. Using the equations of motion, this operator can be replaced with the penguin operator Q_4 of the CMM basis,

$$\begin{aligned} Q_4 &\equiv \left(\bar{q} \gamma_\mu T^a P_L b \right) \sum_f \left(\bar{f} \gamma^\mu T^a f \right) , \\ Q'_4 &\equiv \left(\bar{q} \gamma_\mu T^a P_R b \right) \sum_f \left(\bar{f} \gamma^\mu T^a f \right) , \end{aligned} \tag{5.3}$$

where the operator Q'_4 with the opposite chirality as obtained from the Standard Model diagrams was introduced. The key relation with the chromoelectric operator is

$$Q^{L(R)}_{\text{ce}} = -g_s Q^{(\prime)}_4 + \text{unphysical operators only needed as counterterms} \,. \tag{5.4}$$

On the level of Feynman diagrams, the chromoelectric operator leads to the form factor on the right of Eq. (5.1), and the terms in the parentheses which depend on the gluon momentum p cancel with the gluon propagator when it is connected to a quark line. Therefore, $Q^{L(R)}_{\text{ce}}$ is absorbed into $Q^{(\prime)}_4$. For a discussion of this equivalence beyond leading order, see Ref. [186].

The chromoelectric vertex as a source of new physics is interesting because its contributions to M_{12} are suppressed as compared to the effect on the Wilson coefficient C'_4 of the corresponding $|\Delta B| = 1$ operator. The new physics effects appear as an effective chromoelectric operator after integrating out heavy new particles of mass M_{NP}, so the direct contribution to M_{12} from the diagram in Fig. 5.2 scale as m_b^2/M_{NP}^4. Interference diagrams with one chromoelectric operator and a loop involving a W boson, as discussed in Section 5.2, also contribute to M_{12}, and are suppressed by $m_b^2/(M_{\text{NP}}^2 M_W^2)$. On the other hand, the contribution to C_4 scales as $1/M_{\text{NP}}^2$, so it is enhanced compared to the direct effects in M_{12}, and Γ_{12} can serve as a probe of heavy new physics.

In the following sections, we will show the effective $|\Delta B| = 1$ and $|\Delta B| = 2$ Hamiltonians which result from generic new physics entering the chromoelectric vertex. The RGE running will also be discussed for two different cases of scale hierarchies: Either the new physics particles are much heavier than the scale of the W boson and top quark masses, $M_{\text{NP}} \gg \mu_t$, or the scales are comparable, $M_{\text{NP}} \sim \mu_t$.

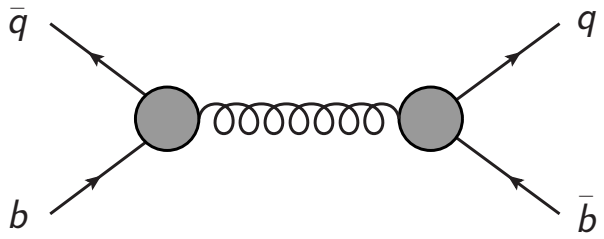

Figure 5.2: Direct contribution to M_{12} from new physics effects due to an effective chromoelectric vertex, which can be absorbed into a $|\Delta B| = 2$ operator.

5.2 Effective Hamiltonians with new physics in the chromoelectric operator

5.2.1 The $|\Delta B| = 1$ Hamiltonian with new physics contributions

To discuss generic heavy new physics in the b-q-gluon vertex using effective operators, we extend the effective $|\Delta B| = 1$ Hamiltonian in the CMM basis from Section 2.2.3 by additional chirality contributions. In the Standard Model, only the operators introduced before have non-vanishing Wilson coefficients; however, BSM models may give rise to non-zero Wilson coefficients for the opposite-chirality operators,

$$
\begin{aligned}
Q_1' &\equiv \left(\bar{q}\gamma_\mu T^a P_R c\right)\left(\bar{c}\gamma^\mu T^a P_R b\right), & Q_2' &\equiv \left(\bar{q}\gamma_\mu P_R c\right)\left(\bar{c}\gamma^\mu P_R b\right),\\
Q_1^{uu\prime} &\equiv \left(\bar{q}\gamma_\mu T^a P_R u\right)\left(\bar{u}\gamma^\mu T^a P_R b\right), & Q_2^{uu\prime} &\equiv \left(\bar{q}\gamma_\mu P_R u\right)\left(\bar{u}\gamma^\mu P_R b\right),\\
Q_3' &\equiv \left(\bar{q}\gamma_\mu P_R b\right)\sum_f\left(\bar{f}\gamma^\mu f\right),\\
Q_4' &\equiv \left(\bar{q}\gamma_\mu T^a P_R b\right)\sum_f\left(\bar{f}\gamma^\mu T^a f\right),\\
Q_5' &\equiv \left(\bar{q}\gamma_{\mu_1}\gamma_{\mu_2}\gamma_{\mu_3} P_R b\right)\sum_f\left(\bar{f}\gamma^{\mu_1}\gamma^{\mu_2}\gamma^{\mu_3} f\right),\\
Q_6' &\equiv \left(\bar{q}\gamma_{\mu_1}\gamma_{\mu_2}\gamma_{\mu_3} T^a P_R b\right)\sum_f\left(\bar{f}\gamma^{\mu_1}\gamma^{\mu_2}\gamma^{\mu_3} T^a f\right),
\end{aligned}
\tag{5.5}
$$

where $f \in \{u, d, c, s, b\}$. In addition to the primed chromomagnetic operator in Eq. (5.2), the electromagnetic penguin operator with quarks of opposite chirality is defined as

$$
Q_7' \equiv \frac{e}{16\pi^2}\, m_b\, (\bar{q}\sigma^{\mu\nu} P_L b)\, F_{\mu\nu}\,. \tag{5.6}
$$

The full $|\Delta B| = 1$ Hamiltonian is hence

$$
\mathcal{H}_{\text{SM+BSM}}^{|\Delta B|=1} \equiv \mathcal{H}_{\text{CMM}} + \frac{4G_F}{\sqrt{2}}\left[-\lambda_t \sum_{i=1}^{8} C_i' Q_i' - \lambda_u \sum_{i=1}^{2} C_i'(Q_i' - Q_i^{uu\prime})\right] + \text{h.c.}\,, \tag{5.7}
$$

where $\mathcal{H}_{\text{CMM}}$ is as given in Eq. (2.59) on page 34. At the high-energy scale M_{NP}, all Wilson coefficients belonging to the operators with the SM chirality are zero, and only the BSM coefficients appear. In Section 5.5, a model that generates C_4', C_7' and C_8' is presented, but in the following sections, we focus on models which generate a non-zero Wilson coefficient exclusively for Q_{ce}^R, i.e. contribute only to C_4'.

To make predictions regarding physical observables, the Wilson coefficients need to be calculated at the scale $\mu_b \sim m_b$ as the hadronic matrix elements are evaluated at that scale. Therefore, the solution of the RGE running is used to relate the Wilson coefficients at μ_b to those obtained at M_{NP}. This is done in two steps, first for the interval between M_{NP} and μ_t, and then for the interval between μ_t and μ_b. The running from M_{NP} down to μ_t involves six active quark flavours. At the scale μ_t, the top quark and the W boson are integrated out, generating the SM effective $|\Delta B| = 1$ operators. Finally, the Wilson coefficients at μ_b are related to those at μ_t through the RGE running with five active quark flavours.

For the scale evolution, Eq. (2.36) from page 28 is used to leading order, i.e.

$$\vec{C}(\mu_2) = \vec{C}(\mu_1)^T \exp\left[-\frac{\gamma_0}{2\beta_0} \ln\left(\frac{\alpha_s(\mu_2)}{\alpha_s(\mu_1)}\right)\right], \tag{5.8}$$

where γ_0 is the one-loop anomalous dimension matrix. The effective operators with different chiralities do not mix, and the anomalous dimension is the same for the primed and unprimed set of operators. At leading order, the anomalous dimension is given by

$$\gamma_0 = 2Z^{(1,1)}, \tag{5.9}$$

and is hence obtained from the renormalisation constants given in Appendix A.

There are two ways of treating the scale hierarchy, and we find agreement between the two approaches within the perturbative uncertainty. The first approach considers the scales $M_{\text{NP}} \sim \mu_t$ to be of similar magnitude, such that the top quark, W boson and all BSM particles are integrated out at the same scale. In this scenario, only C_4' is non-zero at the scale μ_t. All other primed Wilson coefficients vanish at that scale. In the second approach, the scale of new physics is assumed to be much larger than the scale of the W boson and top quark masses, $M_{\text{NP}} \gg \mu_t$. In this case, the RGE evolution from M_{NP} to μ_t generates all primed Wilson coefficients at the scale μ_t due to the operator mixing. The evolution between μ_t and μ_b is the same in both scenarios; only the starting conditions at μ_t differ. Finally, the amplitude can be matched onto a local $|\Delta B| = 2$ operator in order to determine the contribution to Γ_{12}, see Section 2.6.1.

5.2.2 The $|\Delta B| = 2$ Hamiltonian with new physics contributions

Since a BSM model contributing to the chromoelectric vertex also contributes to the effective $|\Delta B| = 2$ Hamiltonian, the effect on M_{12} needs to be considered when discussing

constraints from measurements of B meson mixing observables on the new physics effects. The $|\Delta B| = 2$ Hamiltonian is given by

$$\mathcal{H}^{|\Delta B|=2} = \frac{G_F^2}{16\pi^2} M_W^2 \lambda_t^2 \left(C_Q Q + C_1^{LR} Q_1^{LR} + C_2^{LR} Q_2^{LR} + C_Q^{RR} Q^{RR} \right) + \text{h.c.}\,, \quad (5.10)$$

where the operators are defined as [187]

$$\begin{aligned} Q &\equiv 4 \left(\bar{q} \gamma^\mu P_L b \right) \left(\bar{q} \gamma_\mu P_L b \right), \\ Q_1^{LR} &\equiv 4 \left(\bar{q} \gamma^\mu P_L b \right) \left(\bar{q} \gamma_\mu P_R b \right), \\ Q_2^{LR} &\equiv 4 \left(\bar{q} P_L b \right) \left(\bar{q} P_R b \right), \\ Q^{RR} &\equiv 4 \left(\bar{q} \gamma^\mu P_R b \right) \left(\bar{q} \gamma_\mu P_R b \right). \end{aligned} \quad (5.11)$$

The effective operator Q also appears in the $|\Delta B| = 2$ transition operator in Section 2.4; however, in the following discussion we are considering an effective Hamiltonian and not just a transition operator. In the definitions of the operators, the colour indices are contracted within each scalar product of spinors and hence suppressed. The operator Q receives a non-zero Wilson coefficient from Standard Model diagrams while $Q_{1,2}^{LR}$ stem from the interference of new physics with SM particles. The fourth operator in the basis, Q^{RR}, receives a Wilson coefficient from diagrams where the heavy new particles couple to two right-handed quark pairs.

There are two effects which give rise to $|\Delta B| = 2$ Wilson coefficients at the scale μ_t from new physics in the chromoelectric vertex. The first contribution arises from the mixing of the $|\Delta B| = 1$ and $|\Delta B| = 2$ operators under RGE running, and the second contribution results from the matching of interference diagrams containing an effective $|\Delta B| = 1$ operator from new physics and heavy SM particles to the $|\Delta B| = 2$ Hamiltonian. To show this, we consider the two scenarios of scale hierarchies, $M_{\text{NP}} \sim \mu_t$ and $M_{\text{NP}} \gg \mu_t$, similar to the discussion of the $|\Delta B| = 1$ Hamiltonian.

In the first scenario, $M_{\text{NP}} \sim \mu_t$, the SM and BSM particles are integrated out at the same scale. There are contributions to C_Q^{RR} from the diagram shown in Fig. 5.3, which are suppressed by m_b^2/m_t^2. There are also contributions to $C_{1,2}^{LR}$ from diagrams with one BSM and one SM loop, which are suppressed by a factor of m_b^2/M_W^2. The aforementioned contributions should be compared to the SM Wilson coefficient C_Q, which at the scale μ_t is not suppressed by a mass ratio. In conclusion, the contributions from generic new physics in the chromoelectric vertex to M_{12} are expected to be negligible when the scale of new physics is comparable to that of the W boson and top quark masses. However, in Section 5.5, it is shown that additional direct contributions from UV completions can give rise to larger effects.

For the second scenario with $M_{\text{NP}} \gg \mu_t$, there is a contribution to the $|\Delta B| = 2$ Wilson coefficients from the running of the $|\Delta B| = 1$ Wilson coefficient $C_4'(M_{\text{NP}})$ that is obtained

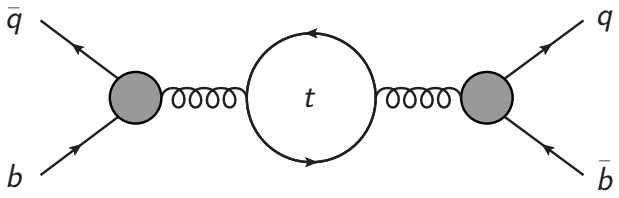

Figure 5.3: Contribution to C_Q^{RR} and hence M_{12} when integrating out heavy SM and BSM particles at the same scale. The shaded vertices are BSM loops that contribute to the chromoelectric vertex.

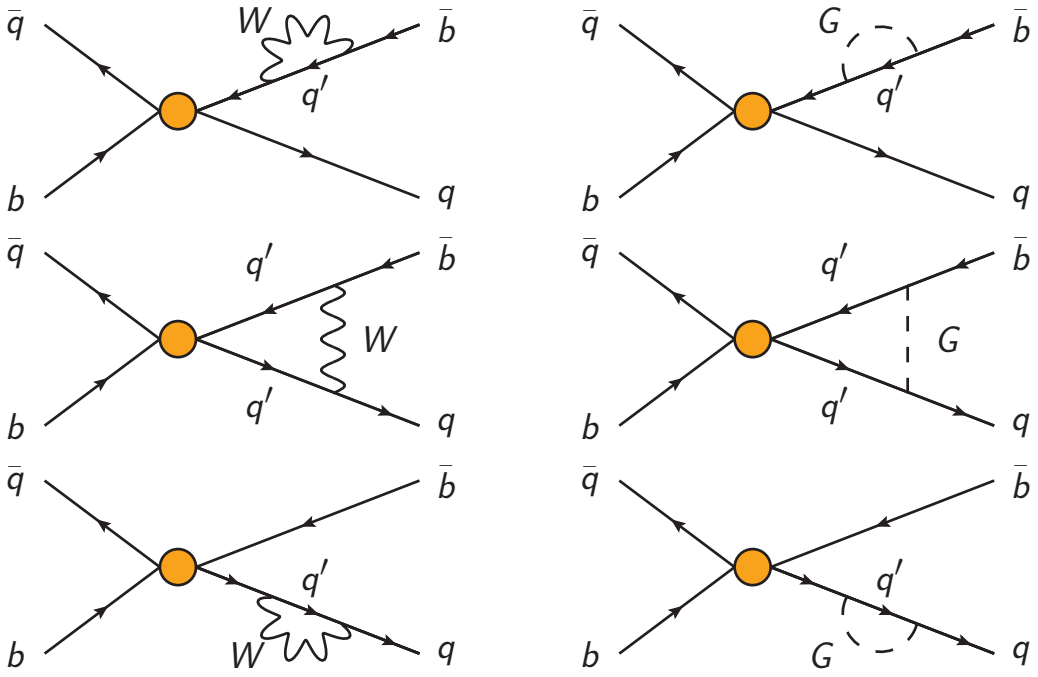

Figure 5.4: Diagrams which result in the mixing of the $|\Delta B| = 1$ and $|\Delta B| = 2$ operators. The orange dot corresponds to $Q'_{3\text{–}6}$.

after integrating out the heavy new particles. This operator mixing contribution stems from the interference of the primed BSM $|\Delta B| = 1$ operators with heavy Standard Model particles, see Fig. 5.4, which match onto $Q_{1,2}^{LR}$. Note that the diagrams with C'_4 give negligible contributions as they are suppressed by m_b^2/M_W^2, so the leading BSM effects in $C_{1,2}^{LR}$ come from the mixing into other $|\Delta B| = 1$ operators, which then mix into the $|\Delta B| = 2$ operators. This is formally NNLO in the full theory. Out of the primed BSM operators, only Q'_5 and Q'_6 need to be considered for the mixing since they have diagrams which are enhanced by m_t^2/m_W^2. The operators Q'_3, Q'_4, and Q'_8 lead to diagrams suppressed by m_b^2/M_W^2.

The mixing of the $|\Delta B| = 1$ and $|\Delta B| = 2$ operators is obtained from the LO anomalous dimension. For the diagrams in Fig. 5.4, counterterms proportional to $Q_{1,2}^{LR}$ are required

to render the contributions from Q_5' and Q_6' finite. The anomalous dimension matrix can hence be written as

$$\gamma^{(0)} = \begin{pmatrix} \gamma^{(0)}_{|\Delta B|=1} & \gamma^{(0)}_{\text{mix}} \\ 0 & \gamma^{(0)}_{|\Delta B|=2} \end{pmatrix} , \tag{5.12}$$

where the sub-matrix $\gamma^{(0)}_{\text{mix}}$ generates non-zero $|\Delta B| = 2$ Wilson coefficients through the running of the $|\Delta B| = 1$ Wilson coefficients.

To solve the RGE running to LO, the $|\Delta B| = 2$ operators that appear in the counterterms and receive non-zero Wilson coefficients in the running need to be rescaled. This is because the large logarithm $\ln(M_{\text{NP}}/\mu_t)$ appears in the combination $\alpha_s^n \ln^{n+1}(M_{\text{NP}}/\mu_t)$, i.e. the diagrams in Fig. 5.4 are $\mathcal{O}(\alpha_s^0)$, but the RGE is set up in an expansion in α_s. Therefore, the counterterms should appear with a factor of α_s, and the $|\Delta B| = 2$ Hamiltonian is redefined as [188, 189]

$$\mathcal{H}^{|\Delta B|=2} \supset \frac{G_F^2}{16\pi^2} M_W^2 \lambda_t^2 \left(C_1^{ct} Q_1^{ct} + C_2^{ct} Q_2^{ct} \right) + \text{h.c.} , \tag{5.13}$$

with

$$Q_{1,2}^{ct} = \frac{m_t^2}{M_W^2 g_s^2 \mu^{2\epsilon}} Q_{1,2}^{LR} . \tag{5.14}$$

The counterterm operator is rescaled with μ since $g_{s,\text{ bare}} = Z_{g_s} g_s \mu^{\epsilon}$ is substituted in the Hamiltonian. In order to obtain renormalisation constants independent of particle masses, the counterterm operator is further rescaled by m_t^2/M_W^2. The Wilson coefficients $C_{1,2}^{LR}$ are later obtained from the solution of the RGE by rescaling the Wilson coefficients of the counterterm operators with $g_s^2 M_W^2/m_t^2$.

From the poles of the diagrams in Fig. 5.4, we obtain the renormalisation constants

$$\begin{aligned} Z^{(1,1)}_{5,Q_1^{ct}} &= -24 , & Z^{(1,1)}_{5,Q_2^{ct}} &= 0 , \\ Z^{(1,1)}_{6,Q_1^{ct}} &= \frac{12}{N_c} = 4 & Z^{(1,1)}_{6,Q_2^{ct}} &= 24 , \end{aligned} \tag{5.15}$$

and all other renormalisation constants $Z_{i,Q_{1,2}^{ct}}$ with $i \neq 5, 6$ as well as $Z_{Q_{1,2}^{ct},i}$ with $i \in \{1, \ldots, 8\}$ vanish.

The anomalous dimension is obtained from the renormalisation constants where special attention needs to be paid to the sub-matrix of the counterterm operators. For all other operators, which do not receive any rescaling, the anomalous dimension is given by

$$\begin{aligned} \gamma = \frac{\alpha_s}{4\pi} \gamma^{(0)} + \mathcal{O}\left(\alpha_s^2\right) &= -\beta(\alpha_s, \epsilon) \left(\frac{\mathrm{d}}{\mathrm{d}\alpha_s} Z \right) Z^{-1} \\ &= \left(2\epsilon + \mathcal{O}(\alpha_s)\right) \left(\frac{\alpha_s}{4\pi} Z^{(1)} + \mathcal{O}\left(\alpha_s^2\right) \right) \left(\mathbb{1} + \mathcal{O}(\alpha_s)\right) \\ &= 2\frac{\alpha_s}{4\pi} Z^{(1,1)} + \mathcal{O}\left(\alpha_s^2\right) , \end{aligned} \tag{5.16}$$

such that $\gamma^{(0)} = 2Z^{(1,1)}$. However, for the sub-matrix of the anomalous dimension $\gamma^{(0)}_{|\Delta B|=2} = \gamma^{(0)}_{Q_i^{ct},Q_j^{ct}}$, it is easier to directly calculate it through the scale variation

$$\begin{aligned}
\mu\frac{\mathrm{d}Q_j^{ct}}{\mathrm{d}\mu} &= \mu\frac{\mathrm{d}}{\mathrm{d}\mu}\left(Z_{Q_j^{ct},i}O_i^{\text{bare}}\right)\\
\mu\frac{\mathrm{d}}{\mathrm{d}\mu}\left(\frac{m_t^2}{g^2\mu^{2\epsilon}}Q_j\right) &= \mu\frac{\mathrm{d}Z_{Q_j^{ct},Q_i^{ct}}}{\mathrm{d}\mu}Q_i^{ct,\text{bare}}\\
\mu\frac{\mathrm{d}}{\mathrm{d}\mu}\left(\frac{m_t^2}{g^2\mu^{2\epsilon}}\right)Q_j + \frac{m_t^2}{g^2\mu^{2\epsilon}}\mu\frac{\mathrm{d}Q_j}{\mathrm{d}\mu} &= \mu\frac{\mathrm{d}Z_{Q_j^{ct},Q_i^{ct}}}{\mathrm{d}\mu}Q_i^{ct,\text{bare}}\\
\left(2\gamma_m - 2\frac{\mu}{g}\frac{\mathrm{d}g}{\mathrm{d}\mu} - 2\epsilon\right)\frac{m_t^2}{g^2\mu^{2\epsilon}}Q_j + \frac{m_t^2}{g^2\mu^{2\epsilon}}\frac{\mathrm{d}Z_{Q_j,Q_i}}{\mathrm{d}\mu}Q_i^{\text{bare}} &= \mu\frac{\mathrm{d}Z_{Q_j^{ct},Q_i^{ct}}}{\mathrm{d}\mu}Q_i^{ct,\text{bare}}\\
\left(2\gamma_m - \frac{1}{\alpha_s}\beta - 2\epsilon\right)Z_{Q_j^{ct},Q_i^{ct}}Q_i^{ct,\text{bare}} - \gamma_{Q_j,Q_k}Z_{Q_k,Q_i}Q_i^{\text{bare}}\frac{m_t^2}{g^2\mu^{2\epsilon}} &= \mu\frac{\mathrm{d}Z_{Q_j^{ct},Q_i^{ct}}}{\mathrm{d}\mu}Q_i^{ct,\text{bare}}\\
\left(2\gamma_m\,\delta_{jk} - \frac{1}{\alpha_s}\beta\,\delta_{jk} - 2\epsilon\,\delta_{jk} - \gamma_{Q_j,Q_k}\right)Z_{Q_k^{ct},Q_i^{ct}}Q_i^{ct,\text{bare}} &= \mu\frac{\mathrm{d}Z_{Q_j^{ct},Q_i^{ct}}}{\mathrm{d}\mu}Q_i^{ct,\text{bare}}\,,
\end{aligned} \tag{5.17}$$

where we used the fact that $Z_{Q_{(ct)},i}$ is only non-zero when $i = Q_{(ct)}$. Therefore, the sub-matrix is given by

$$\gamma_{Q_i^{ct},Q_j^{ct}} = \gamma_{Q_i,Q_j} - 2\gamma_m\,\delta_{ij} + \frac{1}{\alpha_s}\beta\,\delta_{ij} + 2\epsilon\,\delta_{ij}\,, \tag{5.18}$$

where $\gamma_m \equiv \mathrm{d}\ln m/\mathrm{d}\ln\mu$, and the relevant one-loop anomalous dimension is

$$\gamma^{(0)}_{Q_i^{ct},Q_j^{ct}} = \begin{pmatrix} -4+\frac{4}{3}N_f & 6+\frac{4}{3}N_f \\ -6+\frac{4}{3}N_f & -22+\frac{4}{3}N_f \end{pmatrix}. \tag{5.19}$$

For the original operators operators $Q_{1,2}^{LR}$, the anomalous dimension is given by

$$\gamma^{(0)}_{Q_i,Q_j} = \begin{pmatrix} 2 & 12 \\ 0 & -16 \end{pmatrix}, \tag{5.20}$$

which is in agreement with Ref. [187]. Combining the results from Eqs. (5.15) and (5.19) with the CMM renormalisation constants from Section A.2, the complete one-loop anomalous dimension for $\{Q_1', \ldots, Q_8', Q_1^{ct}, Q_2^{ct}\}$ can be reconstructed.

The contribution to the Wilson coefficients of the operators $Q_{1,2}^{LR}$ at the scale μ_t is obtained from the running of the Wilson coefficients together with the matching contribution after integrating out the heavy SM particles. For the running, Eq. (5.8) is used and the Wilson coefficients of the counterterm operators $Q_{1,2}^{ct}$ rescaled to obtain $C_{1,2}^{LR}$. The matching contribution to the Wilson coefficients is obtained from the renormalised contributions of the diagrams in Fig. 5.4, where only $C_{5,6}'$ give sizeable contributions since $C_{3,4,8}'$ are suppressed by m_b^2/m_t^2.

5.3 Calculating Γ_{12} and M_{12} with new physics

In order to constrain new physics in the chromoelectric vertex, observables need to be calculated from Γ_{12} and M_{12} with the effects from $C_4'(M_{\rm NP})$ included. For Γ_{12}, we use the HQE to match the amplitude obtained from the effective $|\Delta B| = 1$ Hamiltonian $\mathcal{H}_{\rm SM+BSM}^{|\Delta B|=1}$ onto a $|\Delta B| = 2$ transition operator, similar to the procedure described in Section 2.6.1. Compared to the SM case, the operator basis needs to be extended to

$$\left\{Q, Q_1^{LR}, Q_2^{LR}, Q^{RR}, \widetilde{Q}_S, \widetilde{Q}_S^{RR}\right\}, \tag{5.21}$$

where the operators are as defined in Eq. (5.11) and

$$\begin{aligned}\widetilde{Q}_S &\equiv 4\left(\bar{q}^c P_R b^d\right)\left(\bar{q}^d P_R b^c\right),\\ \widetilde{Q}_S^{RR} &\equiv 4\left(\bar{q}^c P_L b^d\right)\left(\bar{q}^d P_L b^c\right).\end{aligned} \tag{5.22}$$

Hence, Γ_{12} is expressed in terms of the matching coefficients and the hadronic matrix elements as

$$\begin{aligned}\Gamma_{12} = \frac{G_F^2 m_b^2}{24\pi M_{B_q}}\Bigg[&H\langle Q\rangle + \widetilde{H}_S\langle\widetilde{Q}_S\rangle + H_1^{LR}\langle Q_1^{LR}\rangle\\ &+ H_2^{LR}\langle Q_2^{LR}\rangle + H^{RR}\langle Q^{RR}\rangle + \widetilde{H}_S^{RR}\langle\widetilde{Q}_S^{RR}\rangle + \mathcal{O}\left(\frac{\Lambda_{\rm QCD}}{m_b}\right)\Bigg],\end{aligned} \tag{5.23}$$

which extends Eq. (2.80) to include all possible chirality combinations to leading-power in $\Lambda_{\rm QCD}/m_b$. Here, the shorthand notation $\langle B_q|O|\bar{B}_q\rangle \equiv \langle O\rangle$ was used. Note that the contributions to the different chirality matching coefficients depend on the $|\Delta B| = 1$ Wilson coefficients through

$$\begin{aligned}H &= \sum_{i,j=1,\ldots,6,8} C_i C_j p_{ij},\\ H_i^{LR}(z) &= \sum_{i,j=1,\ldots,6,8} C_i C_j' p_{ij,LR},\\ H^{RR}(z) &= \sum_{i=1,\ldots,6,8} C_i' C_j' p_{ij,RR},\end{aligned} \tag{5.24}$$

and analogous expressions hold for $\widetilde{H}_S$. The matching coefficients H and $\widetilde{H}_S$ are those obtained from the Standard Model chiralities, which have been discussed in the phenomenological analysis of Chapter 4. The matching coefficients H_i^{LR} and H^{RR} can be obtained from the ones appearing in the Standard Model as the coefficient functions p_{ij} do not depend on the chirality of the external quarks. Therefore, the matching coefficients for Q^{RR} and Q_1^{LR} are identical to those of Q while those of Q_2^{LR} are obtained from $\widetilde{Q}_S$ after a basis transformation. Since the matrix elements are evaluated at a scale $\mu \sim m_b$, the $|\Delta B| = 1$ Wilson coefficients are evolved down to that scale.

	$B^1_{B_q}(\overline{m}_b)$	$B^2_{B_q}(\overline{m}_b)$	$B^3_{B_q}(\overline{m}_b)$	$B^4_{B_q}(\overline{m}_b)$	$B^5_{B_q}(\overline{m}_b)$
B_s	2.168(93)	-2.18(10)	0.436(29)	3.65(15)	1.945(76)
B_d	2.15(11)	-2.06(11)	0.400(30)	3.82(18)	2.015(92)

Table 5.1: Bag parameters in the SUSY operator basis obtained from lattice QCD in Ref. [40]. The operators in Ref. [40] are transformed using Fierz identities to obtain the operator basis defined here.

The contributions to M_{12} follow directly from the $|\Delta B| = 2$ Hamiltonian discussed in Section 5.2.2. The dispersive part of the off-diagonal decay matrix is given by

$$\begin{aligned} M_{12} &= \frac{G_F^2 M_W^2 \lambda_t^2}{32\pi^2 M_{B_q}} \left[C_Q \langle Q \rangle + C_1^{LR} \langle Q_1^{LR} \rangle + C_2^{LR} \langle Q_2^{LR} \rangle + C_Q^{RR} \langle Q^{RR} \rangle \right] \\ &= M_{12,\mathrm{SM}}^q + \frac{G_F^2 M_W^2 \lambda_t^2}{32\pi^2 M_{B_q}} \left[C_1^{LR} \langle Q_1^{LR} \rangle + C_2^{LR}(\mu_t) \langle Q_2^{LR} \rangle + C_Q^{RR} \langle Q^{RR} \rangle \right] . \end{aligned} \tag{5.25}$$

The matrix element $\langle Q^{RR} \rangle$ is equal to $\langle Q^{LL} \rangle$ because QCD does not affect the parity of the particles involved. As numerical input, we use the values computed in Ref. [40] using lattice QCD, where the bag parameters $B^i_{B_q}(\mu)$ in

$$\langle B_q | O_i | \bar{B}_q \rangle (\mu) \equiv f^2_{B_q} M^2_{B_q} B^i_{B_q}(\mu) \tag{5.26}$$

are given, see Tab. 5.1

5.4 Constraints on generic new physics models

In this section, the constraints on the allowed values of $C_4'(M_{\mathrm{NP}})$ from the current experimental status of B meson mixing are discussed. Generic new physics that contributes to $C_4'(M_{\mathrm{NP}})$ only, with no direct contribution from the UV theory to observables, is considered. For this purpose, we separately investigate the B_d and B_s systems, adding a further constraint from the lifetime ratio at the end.

5.4.1 Constraints from the B_d system

The observables which we consider are ΔM_d, $\arg M_{12}^d$, $\Delta\Gamma_d$ and a_{fs}^d. For the observables related to the mass difference, we use the values determined in Ref. [166],

$$\Delta M_d = (0.5065 \pm 0.0019)\,\mathrm{ps}^{-1} , \tag{5.27}$$

$$\sin 2\beta = 0.708 \pm 0.011 , \tag{5.28}$$

which give a small allowed region in the complex M_{12}^d plane. The Standard Model contributions are taken from Ref. [166] as well, using the values where the observables have not been included in the fit,

$$\Delta M_d^{\mathrm{SM}} = \left(0.534^{+0.082}_{-0.078}\right)\ \mathrm{ps}^{-1}\,, \tag{5.29}$$

$$\sin 2\beta_{\mathrm{SM}} = 0.742^{+0.047}_{-0.050}\,, \tag{5.30}$$

where the quoted uncertainty is the 3σ interval. Comparing these values to the full fit given in Eqs. (5.27) and (5.28), the uncertainties of the full fit can be neglected. The constraint on the new physics part of M_{12}^d, and consequently on $C_4'(M_{\mathrm{NP}})$, is obtained by requiring that

$$M_{12,\mathrm{SM}}^d + M_{12,\mathrm{NP}}^d = M_{12}^d\,, \tag{5.31}$$

where the right-hand side is given by the experimental results of the full fit.

The constraint from $\Delta\Gamma_d$ is obtained in a similar manner, using the experimental values [26]

$$x_d = \frac{\Delta\Gamma^d}{\Gamma_d} = 0.001 \pm 0.010\,, \tag{5.32}$$

$$\tau_{B_d} = (1.517 \pm 0.004)\,\mathrm{ps}\,, \tag{5.33}$$

which can be combined to obtain $\Delta\Gamma_d$. For the CP asymmetry we use the measurement [26]

$$a_{\mathrm{fs}}^d = (-21 \pm 17) \times 10^{-4}\,. \tag{5.34}$$

The Standard Model predictions for $\Delta\Gamma_d$ and a_{fs}^d are given in Eqs. (4.33) and (4.36) respectively, i.e.

$$\Delta\Gamma_d^{\mathrm{SM}} = (0.002\,15 \pm 0.000\,45)\,\mathrm{ps}^{-1}\,, \tag{5.35}$$

$$a_{\mathrm{fs}}^{d,\mathrm{SM}} = -(5.19 \pm 0.32) \times 10^{-4}\,. \tag{5.36}$$

With the condition that

$$\Gamma_{12,\mathrm{SM}}^d + \Gamma_{12,\mathrm{NP}}^d = \Gamma_{12}^d\,, \tag{5.37}$$

we obtain another constraint for $C_4'(M_{\mathrm{NP}})$.

5.4.2 Constraints from the B_s system

Similar to the B_d system, we obtain constraints from ΔM_s, $\arg M_{12}^s$, $\Delta\Gamma_s$ and a_{fs}^s. For ΔM_s^{SM}, the value

$$\Delta M_s^{\mathrm{SM}} = 18.19\,\mathrm{ps}^{-1} \tag{5.38}$$

is used, where the uncertainty in the literature is quoted as either 3.5% [27] or 6.5% [46], and the result was calculated with the value for $|V_{cb}|$ as obtained from inclusive measurements.

For our analysis, we allow for a relative uncertainty of 5% as well as either inclusive or exclusive $|V_{cb}|$ values; therefore,

$$\frac{\Delta M_s}{\Delta M_s^{\mathrm{SM}}} \in [0.95, 1.25] \ . \tag{5.39}$$

From the discussion of the combined constraints in Section 5.4.4, it can be seen that the constraints from M_{12}^s are less stringent than from the other observables, so the precise interval has no consequence for the allowed values of $C_4'(M_{\mathrm{NP}})$. For the SM prediction of $\Delta\Gamma_s$ and a_{fs}^s, we use the results from Eqs. (4.28) and (4.36) respectively, which read

$$\begin{aligned} \Delta\Gamma_s^{\mathrm{SM}} &= (0.078 \pm 0.015)\,\mathrm{ps}^{-1} \ , \\ a_{\mathrm{fs}}^{s,\mathrm{SM}} &= (2.27 \pm 0.14) \times 10^{-5} \ . \end{aligned} \tag{5.40}$$

We also require the experimental measurements of all observables. For M_{12}^s, these are given by [26, 35]

$$\Delta M_s = (17.766 \pm 0.006)\,\mathrm{ps}^{-1} \ , \tag{5.41}$$

$$\sin 2\beta_s = 0.03757^{+0.00057}_{-0.00054} \ , \tag{5.42}$$

and for $\Delta\Gamma_s$ we use [26]

$$\Delta\Gamma^s = (0.0781 \pm 0.0035)\,\mathrm{ps}^{-1} \ . \tag{5.43}$$

Lastly, the flavour-specific CP asymmetry is measured to be [26]

$$a_{\mathrm{fs}}^s = (-60 \pm 280) \times 10^{-5} \ . \tag{5.44}$$

5.4.3 Constraints from the lifetime ratio $\tau(B_s)/\tau(B_d)$

An additional constraint on the new physics contributions from the chromoelectric vertex stems from the lifetime ratio $\tau(B_s)/\tau(B_d)$, which depends on the $|\Delta B| = 1$ Wilson coefficients at the hadronic scale $\mu \sim m_b$, see Ref. [190]. We include interference terms of the right-handed Wilson coefficient C_4' with Standard Model Wilson coefficients as well as quadratic terms proportional to $|C_4'|^2$. The LO matching coefficients for the mixed contributions are obtained from Ref. [190]. Additionally, the part of the matching coefficients stemming from two insertions of the BSM operator Q_4' are computed from diagrams shown in Fig. 5.5, which is consistent with the LO matching calculation for B meson mixing.

The constraint on C_4' is obtained by setting the LO Standard Model prediction [62]

$$\left.\frac{\tau(B_s)}{\tau(B_d)} - 1\right|_{\mathrm{SM}} = 0.0132^{+0.0070}_{-0.0072} \tag{5.45}$$

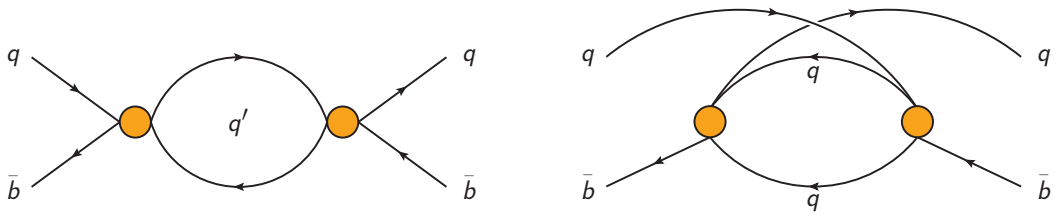

Figure 5.5: The two Feynman diagrams that need to be computed to obtain the matching contribution from $|C_4'|$ to the lifetime ratio $\tau(B_s)/\tau(B_d)$. As discussed in Section 2.5, the diagram on the left corresponds to WA while the one on the right is the PI part. The orange dot denotes Q_4' with $q' \in \{u, d, c, s\}$.

with additional BSM contributions equal to the experimental value [26]

$$\frac{\tau(B_s)}{\tau(B_d)} - 1 = 0.0017 \pm 0.0034\,. \tag{5.46}$$

Note that only one of the two Wilson coefficients $C_4^{\prime,d}$ and $C_4^{\prime,s}$ was taken to be non-zero at the same time when computing the constraints from $\tau(B_s)/\tau(B_d)$ on the corresponding Wilson coefficient.

5.4.4 Exclusion plots for the chromoelectric Wilson coefficients

BSM models that generate a contribution to the chromoelectric vertex only are not strongly constrained by current measurements and may lead to a significant modification of the decay width $\Delta\Gamma$ with respect to the Standard Model predictions, see Figs. 5.6 and 5.7 for the B_d and B_s system respectively. The precisely measured mass difference ΔM does not yield stringent constraints, and it is hence more impactful to focus on the other observables to exclude BSM models that enter through the chromoelectric vertex. In the following, we will use the shorthand notation $C_4^{q,\prime} \equiv C_4^{q,\prime}(M_{\text{NP}})$. In the plots shown here, the 2σ experimental uncertainties are used. The two B_q systems are discussed separately below.

For B_d mesons, we find that the strongest constraints are given by measurements of a_{fs}^d, see Fig. 5.6, while $\Delta\Gamma_d$ can vary by a factor of about six. The bounds from $\Delta\Gamma_d$ limit the absolute value of $C_4^{d,\prime}$ for purely real or purely imaginary contributions. We observe that the constraints from the lifetime ratio $\tau(B_s)/\tau(B_d)$ are of the same order of magnitude as those from $\Delta\Gamma_d$ and hence do not limit the allowed region further. The impact on ΔM^d is of the sub-percent level, and the constraints from M_{12}^d are therefore outside of the plot region. It is interesting to note that at the exclusion limits, the new physics contributions are dominated by the quadratic effects in $C_4^{d,\prime}$. For example, the term proportional to $|C_4^{q,\prime}|^2$ in the lifetime ratio leads to the circular constraint. For the

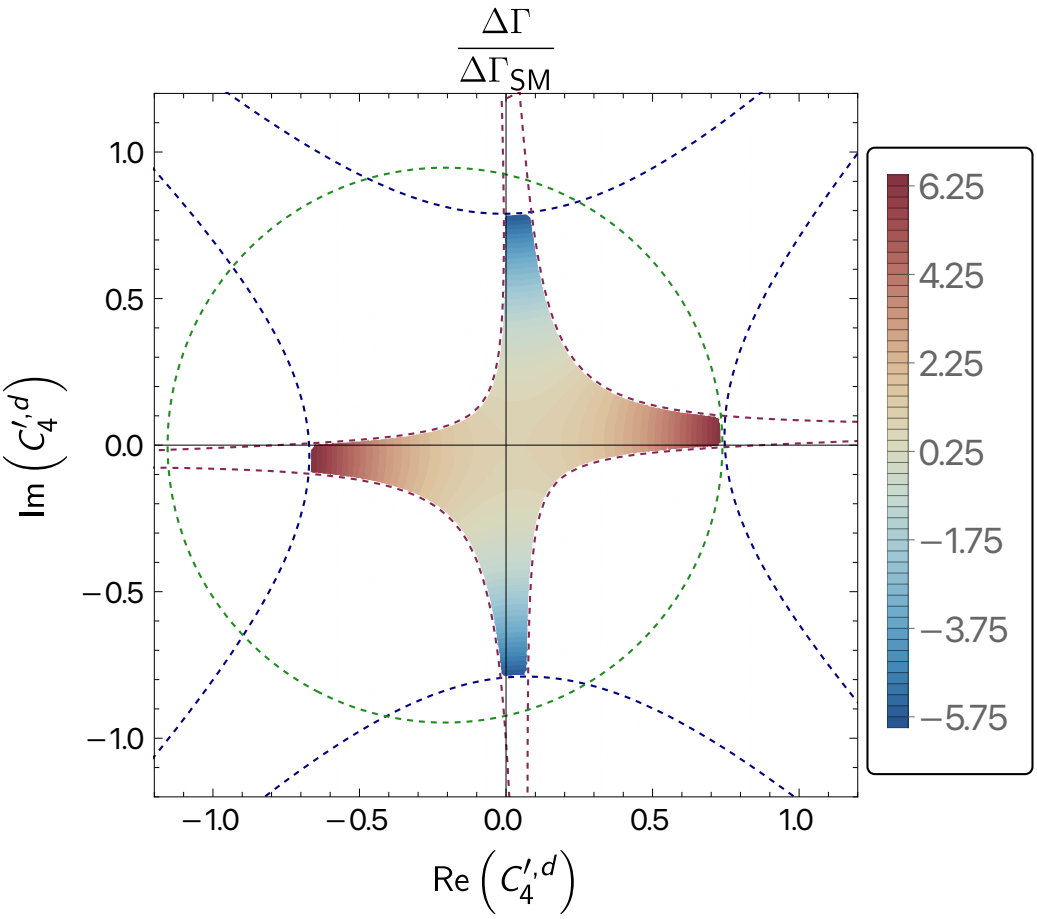

Figure 5.6: Constraints on $C_4^{\prime,d}$ from generic new physics in the chromoelectric vertex. The colour gradient corresponds to the value of $\Delta\Gamma/\Delta\Gamma_{\mathrm{SM}}$, and white regions are excluded through measurements. The experimental bounds are shown as dashed lines, with constraints from M_{12}^d in orange (outside the plot region), $\Delta\Gamma_d$ in blue, a_{fs}^d in red and $\tau(B_s)/\tau(B_d)$ in green. The scale of new physics has been chosen as $M_{\mathrm{NP}} = 490\,\mathrm{GeV}$. This value is not excluded from bounds shown in Fig. 8a of Ref. [191], where the masses in axial-vector models have been constrained.

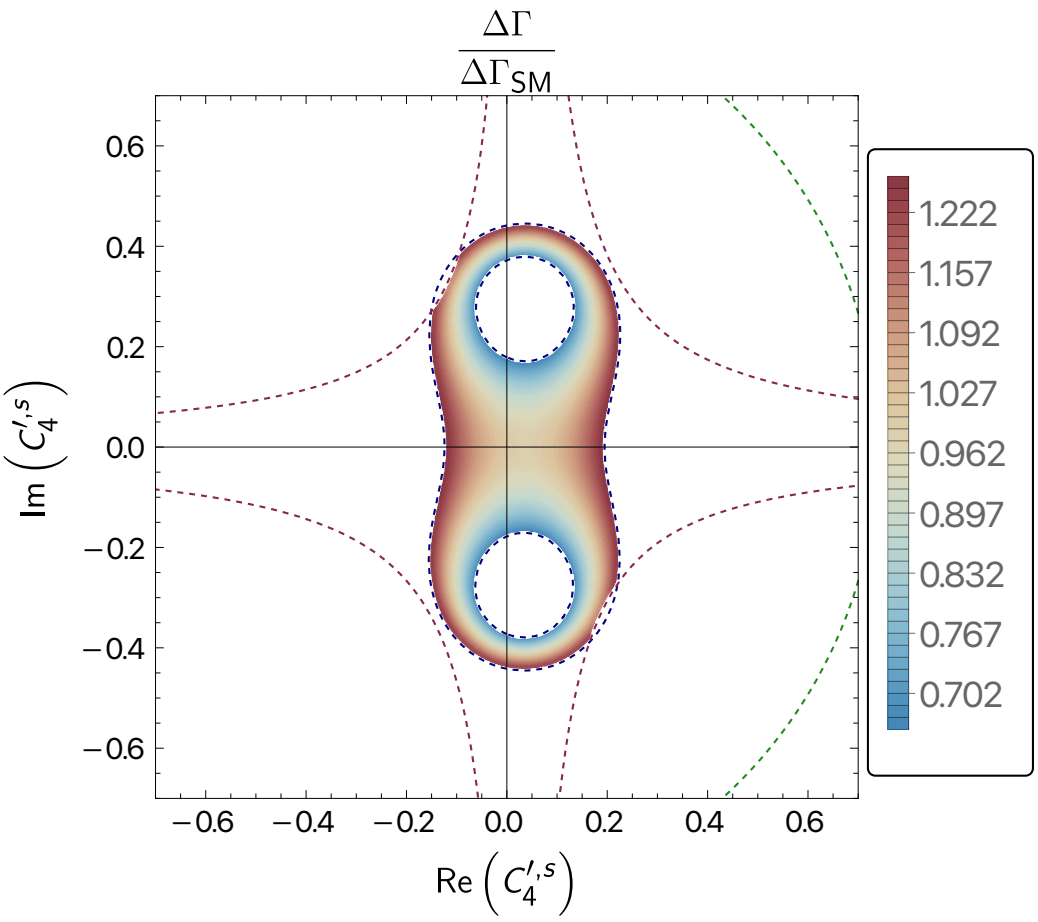

Figure 5.7: Constraints on $C_4^{\prime,s}$ from generic new physics in the chromoelectric vertex. The colour gradient corresponds to the value of $\Delta\Gamma/\Delta\Gamma_{\mathrm{SM}}$, and white regions are excluded through measurements. The experimental bounds are shown as dashed lines, with constraints from M_{12}^s in orange (outside the plot region), $\Delta\Gamma_s$ in blue, a_{fs}^s in red and $\tau\left(B_s\right)/\tau\left(B_d\right)$ in green. The scale of new physics has been chosen as $M_{\mathrm{NP}} = 490\,\mathrm{GeV}$. This value is not excluded from bounds shown in Fig. 8a of Ref. [191], where the masses in axial-vector models have been constrained.

lifetime difference and the CP asymmetry in flavour-specific decays, the quadratic terms are

$$\Delta\Gamma_d^{\text{BSM}} \propto \text{Re}\left(\left(C_4^{d,\prime}\right)^2\right) = \text{Re}\left(C_4^{d,\prime}\right)^2 - \text{Im}\left(C_4^{d,\prime}\right)^2 ,$$
$$a_{\text{fs}}^{d,\text{BSM}} \propto \text{Im}\left(\left(C_4^{d,\prime}\right)^2\right) = 2\,\text{Re}\left(C_4^{d,\prime}\right) \times \text{Im}\left(C_4^{d,\prime}\right) . \tag{5.47}$$

Thus, we obtain the two cross-shaped allowed regions, one aligned with the plot axes, and one rotated by 45°.

Overall, we observe that ΔM_d is not a good probe for BSM models that contribute exclusively to the chromoelectric vertex. On the other hand, $\Delta\Gamma_d$ can be used very effectively to constrain the new physics contributions in $C_4^{d,\prime}$, which motivates more accurate measurements of this observable.

In the B_s system, the constraints from $\Delta\Gamma_s$ are the strongest, with a_{fs}^s only impacting a small region of the allowed values for $C_4^{s,\prime}$, see Fig. 5.7. The constraints from the lifetime ratio are less stringent than those from the mixing observables, except for ΔM_s. The corresponding constraints from M_{12}^s are outside of the plot region and the variation of ΔM_s is below the percent level in the allowed parameter space. We find that the experimental bounds on $\Delta\Gamma_s$ are saturated, and the new physics contributions are dominated by the terms linear in $C_4^{\prime,s}$ throughout the allowed region.

5.5 Ultraviolet completions with an effective chromoelectric operator

It is necessary to investigate UV completions that give rise to an effective chromoelectric operator since they will yield a direct contribution to M_{12} from box diagrams. Therefore, the constraint from M_{12} on the new physics models is usually more stringent than the constraints obtained from only considering an effective $|\Delta B| = 1$ operator as shown in Section 5.4.4. In general, the BSM contributions to M_{12} and Γ_{12} scale as

$$\frac{M_{12}^{\text{NP}}}{M_{12}^{\text{SM}}} \sim \frac{M_{\text{NP}}^2}{M_W^2}, \qquad \frac{\Gamma_{12}^{\text{NP}}}{\Gamma_{12}^{\text{SM}}} \sim \frac{M_W^4}{M_{\text{NP}}^4}, \tag{5.48}$$

which means that M_{12} receives an enhanced contribution while the corresponding term for Γ_{12} is suppressed. This behaviour is demonstrated for a class of BSM models in the following sections.

5.5.1 A generic model with heavy vector-like quarks

In this section, we introduce a class of theories which produce the desired effective chromoelectric vertex as well as an effective $|\Delta B| = 2$ operator. The model contains

heavy vector-like quarks D_j, $j = 1, 2, 3$, which have the same quantum numbers as SM down-type quarks, i.e. $(3, 1, -1/3)$ for $\mathrm{SU(3)_C} \times \mathrm{SU(2)_L} \times \mathrm{U(1)_Y}$. The BSM quarks couple to a BSM Higgs field ϕ^0, which is a singlet under all symmetry groups, as well as to right-handed SM quarks. The complete Lagrangian is

$$\mathcal{L}_{\mathrm{BSM}} = \bar{D}_j(i\not{\partial} - M_j)D_j + \partial_\mu\phi^{0\dagger}\partial^\mu\phi^0 - M_\phi^2|\phi^0|^2 + \mathcal{L}_{Dd} + \mathcal{L}_{\mathrm{SM}}, \tag{5.49}$$

$$\mathcal{L}_{Dd} = -\sum_{j=1}^{3}\left(y\phi^0\bar{D}_j d_{R,j} + y^*\phi^{0\dagger}\bar{d}_{R,j}D_j\right). \tag{5.50}$$

The Yukawa coupling in $\mathcal{L}_{Dd}$ is flavour-blind and preserves the SU(3) flavour symmetry of simultaneous unitary rotations of D_j and $d_{R,j}$. Without loss of generality, we can take $y > 0$ because its phase can be absorbed into D_j. In order to suppress flavour-changing neutral current (FCNC) processes of kaons, we assume that $M \equiv M_1 = M_2 \neq M_3$. For a realistic theory, this Lagrangian would have to be extended by additional interactions because the lightest particle of the new theory would otherwise be stable; however, this is not relevant for our discussion.

The UV model is constructed in a way that GIM cancellations in FCNC processes appear. In the Standard Model, the mass eigenstates $d_{R,i}$ are related to the flavour eigenstates through a unitary rotation,

$$\begin{pmatrix} d_{R,1} \\ d_{R,2} \\ d_{R,3} \end{pmatrix} = U \begin{pmatrix} d_R \\ s_R \\ b_R \end{pmatrix}, \tag{5.51}$$

where the matrix U is unphysical in the Standard Model. However, it appears in the Feynman rules of the BSM Lagrangian:

$$\mathcal{L}_{Dd} = -y\phi^0\sum_{j=1}^{3}\bar{D}_j\left(U_{j1}d_R + U_{j2}s_R + U_{j3}b_R\right) + \mathrm{h.c.} \tag{5.52}$$

The unitarity of U gives rise to the aforementioned GIM suppression. For illustration purposes, consider for example a one-loop FCNC $b \to q$ transition as shown in Fig. 5.8. The corresponding amplitude for $q = s$ will be of the form

$$\sum_j U_{j2}U_{j3}^* f(M_j) = U_{32}U_{33}^*\left[f(M_3) - f(M)\right], \tag{5.53}$$

where we have used the unitarity of U,

$$\sum_j U_{jk}U_{jl}^* = \delta_{kl}. \tag{5.54}$$

Similar cancellations are present in the diagrams we will consider later.

After integrating out the heavy new particles at the scale of new physics M_{NP}, the UV model gives rise to effective operators. One of these will give a direct contribution to M_{12}^q because

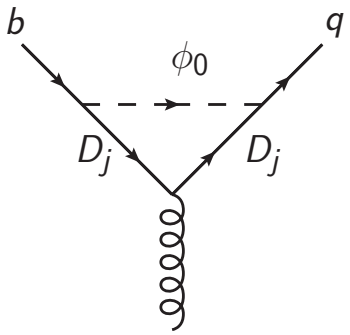

Figure 5.8: Sample diagram for a FCNC process in the generic BSM model.

there is a non-zero matching coefficient $C_Q^{RR}(M_{\text{NP}})$ for the $|\Delta B| = 2$ operator Q^{RR}. The second contribution is to the matching coefficients C_{ce}^R of the chromoelectric operator Q_{ce}^R, C_7' of the electromagnetic penguin operator Q_7', and C_8' of the chromomagnetic operator Q_8'. One would expect the contribution to M_{12}^q to be more strongly suppressed:

$$M_{12} \propto \frac{|M_3 - M|^2}{M^4} \propto x^2\,, \tag{5.55}$$

$$\left\{C_{\text{ce}}^R, C_7', C_8'\right\} \propto \frac{1}{M_\phi^2} \ln \frac{M_3}{M} \propto x\,, \tag{5.56}$$

where the dimensionless parameter

$$x \equiv \frac{M_3^2 - M^2}{M^2} \tag{5.57}$$

was introduced. However, M_{12} is proportional to y^4 while the $|\Delta B| = 1$ operators are proportional to y^2. Hence the GIM mechanism does not offer an additional lever on the relative size of the contributions since new physics contributions in both Γ_{12} and M_{12} are governed by the product xy^2.

In the following sections, the contributions to the $|\Delta B| = 2$ and $|\Delta B| = 1$ Hamiltonian are computed and their implications discussed.

5.5.2 Contributions to the $|\Delta B| = 2$ Hamiltonian

The contribution to the $|\Delta B| = 2$ operator Q^{RR} stems from the box diagrams shown in Fig. 5.9. Summing the diagrams in the limit $M_2 \to M_1 \equiv M$ and employing unitarity of the matrix U yields the total amplitude, which is most conveniently expressed in terms of x and r,

$$\tilde{\mathcal{M}} = \frac{\lambda_3^2 y^4\, r}{96\pi^2 M_\phi^2 (r-1)^5} x^2 \left[-1 - 9r + 9r^2 + r^3 - 6r\,(1+r)\ln(r)\right] + \mathcal{O}\left(x^3\right), \tag{5.58}$$

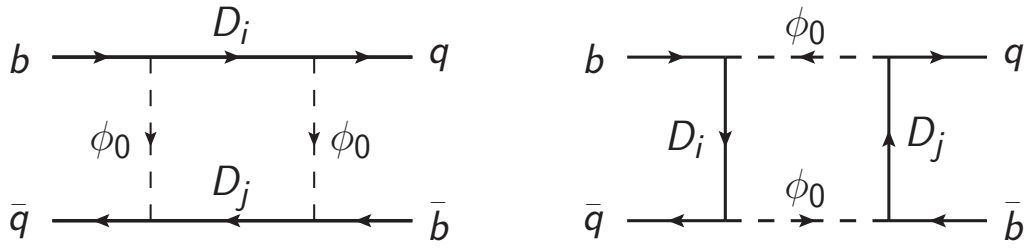

Figure 5.9: Two types of box diagrams in the UV theory contribute to the effective $|\Delta B| = 2$ operator.

where $r = M^2/M_\phi^2$ and the dimensionless parameter x defined in Eq. (5.57) were used to make the GIM-violating terms explicit. Note that the spinor structure $[\bar{b}\gamma_\mu P_R q]\otimes[\bar{b}\gamma^\mu P_R q]$ has been factored out here, so the contribution of the UV model to the matching coefficient is given by

$$C_Q^{RR} = -\frac{2\pi^2}{G_F^2 m_W^2 \lambda_t^2}\tilde{\mathcal{M}}\,. \tag{5.59}$$

We can also write down the contribution to M_{12}^q directly:

$$\begin{aligned} M_{12}^q(M_{NP}) = \frac{r\,y^4\left(U_{32}U_{33}^*\right)^2}{1536\,M_\phi^2\,(1-r)^5\,\pi^2}\,\langle\bar{B}_q|Q^{RR}|B_q\rangle \times \Big\{ & x^2\left[r^3+9\,r^2-9\,r-1\right] \\ & + x^2\ln r\,[-6\,r\,(1+r)] + \mathcal{O}\left(x^3\right)\Big\}\,. \end{aligned} \tag{5.60}$$

Note that M_{12}^q shows the expected "hard" quadratic GIM suppression, i.e. its leading term scales as x^2, as suggested in Eq. (5.55).

5.5.3 Contributions to the $|\Delta B| = 1$ Hamiltonian

In addition to the effective $|\Delta B| = 2$ operator, there are contributions to the matching coefficients C_{ce}^R, C_7' and C_8' from the diagrams shown in Fig. 5.10. The diagrams need to be expanded in the gluon momentum, which means that we naively expand in the external quark momenta and retain the quark masses m_b and m_s in intermediate steps.

In order to perform the calculation in an efficient manner, we first calculate the flavour-changing self-energies separately before attaching the gluon vertex and summing up all contributing diagrams. If we consider a general self-energy as shown in Fig. 5.11, the amplitude will have the form

$$\mathcal{M} = \bar{q}'\left(\Sigma_{RR}\,\not{p}\,P_R + \Sigma_{LL}\,\not{p}\,P_L + \Sigma_{LR}\,P_R + \Sigma_{RL}\,P_L\right)q\,, \tag{5.61}$$

but since the UV model couples to right-handed quarks, the only non-zero component of the self-energy is Σ_{RR}.

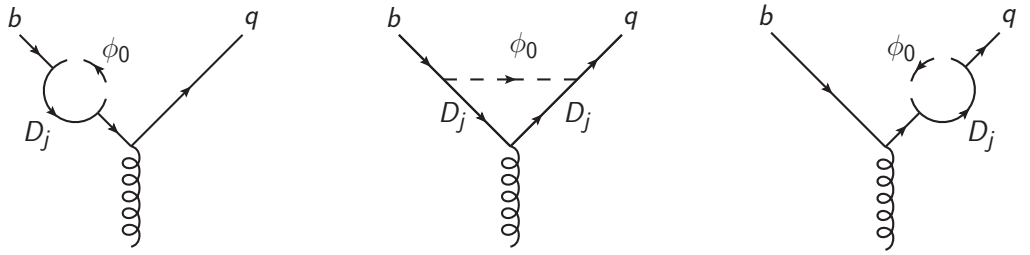

Figure 5.10: A vertex diagram and two types of flavour-changing self-energies in the UV model contribute to the effective $|\Delta B| = 1$ operators.

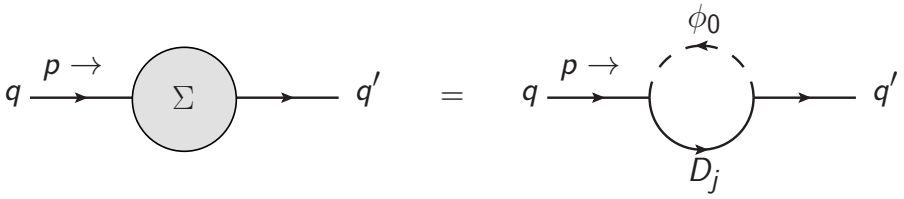

Figure 5.11: The general flavour-changing self-energy insertion for down-type quarks q and q', which has one type of one-loop diagram in the considered UV model.

The general flavour-changing self-energy can be used to calculate the combined contributions from the diagrams on the left and right in Fig. 5.10. The momentum p of the FCSE diagrams becomes the momentum of the external quark such that $p^2 = m_{q,b}$ and $\not{p} = \not{p}_{q,b}$, where we have picked the convention for the outgoing gluon momentum $q = p_q - p_b$. As only the right-handed quarks contribute, we drop the subscript RR on the self-energy component Σ_{RR} and write for the sum of the two diagrams

$$\begin{aligned}\left(V_{j,\text{se}}\right)^{\mu}_{a} &= \bar{b}\left[-g_s\, T_a\, \gamma^{\mu}\, \frac{\not{p}_q + m_b}{p_q^2 - m_b^2}\, \Sigma(m_q)\, \not{p}_q\, P_R - \Sigma(m_b)\, \not{p}_b\, P_R\, \frac{\not{p}_b + m_q}{p_b^2 - m_q^2}\, g_s\, T_a\, \gamma^{\mu}\right] q \\ &= -g_s\, \bar{b}\, T_a\, \left[\left(\Sigma^{(0)} + \left(m_b^2 + m_q^2\right)\, \Sigma^{(1)}\right)\, \gamma^{\mu}\, P_R + m_q\, m_b\, \Sigma^{(1)}\, \gamma^{\mu}\, P_L\right] q \\ &\quad + \mathcal{O}\left(m_b^4, m_q^4\right)\,, \end{aligned} \tag{5.62}$$

where we have expanded the flavour-changing self-energies in the quark masses

$$\Sigma(m) = \Sigma^{(0)} + m^2\, \Sigma^{(1)} + \mathcal{O}\left(m^4\right)\,. \tag{5.63}$$

Lastly, we calculate the middle diagram of Fig. 5.10. After naively expanding in the external momenta $p_{q,b}$, the remaining integrals are one-loop tadpoles and can be readily evaluated. To treat the spinor structures, we use an extension of the projector method shown in Ref. [136] to two different external masses, writing the amplitude in terms of form factors,

$$\left(V_j\right)^{\mu}_{a} = \bar{b}\Big[A\, \gamma^{\mu}\, P_R + B\, \gamma^{\mu}\, P_L + C\, \sigma^{\mu\nu}\, P_R + D\, \sigma^{\mu\nu}\, P_L\, q_{\nu} + E\, q^{\mu}\, P_R + F\, q^{\mu} P_L\Big] q\,. \tag{5.64}$$

Note that at this point the amplitude is explicitly finite in ϵ and multiplying with a gluon propagator does not lead to any poles in q^2. The q^μ components, i.e. coefficients E and F, can be discarded because we attach a gluon-quark-antiquark vertex to the gluon, which means that q^μ will be contracted with a γ^μ on the quark-antiquark line. This will vanish by the equation of motion of the quark and antiquark. The coefficient B also vanishes when we take the quark masses to zero and can hence be discarded.

For the chromoelectric operator, only the form factor A is relevant because the chromoelectric vertex is proportional to $\gamma_\nu(q^\nu q^\mu - q^2\eta^{\nu\mu})P_R$, and the first term contains q^μ, which vanishes as outlined above. Therefore, the Wilson coefficient is simply given by the coefficient of $-T_a q^2 \gamma^\mu P_R$. Discarding terms with higher powers of the quark masses and absorbing the chromoelectric operator into the matching coefficient of the penguin operator Q_4', we obtain

$$C_4' = x\,\frac{-\sqrt{2}g_s^2 y^2 U_{32}U_{33}^*}{2304\,\lambda_t G_F \pi^2 M_\phi^2 (r-1)^5}\Big\{-7\,r^4+51\,r^3-45\,r^2-11\,r+12 + \left(30r-54\,r^2\right)\ln r\Big\} + \mathcal{O}\left(x^2\right)\,. \tag{5.65}$$

This makes the linear GIM suppression from Eq. (5.56) explicit.

We can determine the Wilson coefficient for the chromomagnetic operator in a similar fashion from the coefficient C as it is proportional to $\sigma^{\mu\nu} P_R$. Note that the D coefficient would contribute to the other chromomagnetic operator that scales with m_s, but it vanishes because we take $m_s \to 0$. The matching coefficient for the chromomagnetic operator has the same linear GIM suppression as the chromoelectric operator and reads

$$C_8' = x\,\frac{y^2 U_{32}U_{33}^*}{48\sqrt{2}G_F \lambda_t M_\phi^2 (r-1)^5}\Big\{-5\,r^4+33\,r^3-63\,r^2+23\,r+12 + \left(42\,r-18\,r^2\right)\ln r\Big\} + \mathcal{O}\left(x^2\right)\,. \tag{5.66}$$

The matching coefficient of the electromagnetic penguin operator Q_7' is identical to the matching coefficient of the chromomagnetic operator Q_8 since the only difference is in the associated form factors.

5.5.4 Phenomenology of a generic model with heavy vector-like quarks

The phenomenology of the UV completion outlined in the previous section follows similar steps as described in previous sections for an effective theory with only a chromoelectric

operator. The main differences are as follows: There are additional effective operators on the $|\Delta B| = 1$ side, namely Q_7' and Q_8', which lead to additional constraints from experiments. Moreover, there is also a direct contribution to the Q^{RR} operator on the $|\Delta B| = 2$ side, which impacts the constraints from M_{12}.

On the $|\Delta B| = 1$ side, which leads to our prediction of Γ_{12}, the main difference to the theory used in Section 5.4.4 is that the starting point at M_{NP} now has non-vanishing contributions from the three Wilson coefficients C_4', C_7' and C_8'. This does not change the numerical value of Γ_{12} significantly because the corrections from C_8' are in general small. A new feature is the impact on $b \to s\gamma$ from $C_{7,\text{eff}}'$. In $B(B \to X_s\gamma)$ and $B(B \to K^*\gamma)$ there are no interference terms between the SM contribution and the new physics effective operators because the right-handed operators produce the photon with the opposite helicity compared to the left-handed Standard Model ones, so there are no strong constraints from those decays. However, in the time-dependent CP asymmetry $\mathcal{A}^{CP}(B(t) \to X_s\gamma)$ the new physics operator contribution to $B \to K^*\gamma$ interferes with the SM contribution to $\bar{B} \to \bar{K}^*\gamma$ (and vice versa), if the K^* is detected in $K^* \to \pi^0 K^0$. However, we find that also this constraint is less stringent than those considered in Section 5.4.4.

The calculation of the $|\Delta B| = 2$ Hamiltonian, which leads to M_{12}, differs from that shown in Section 5.2.2 due to the fact that our UV theory produces a non-zero matching coefficient $C_Q^{RR}(M_{\text{NP}})$ before integrating out Standard Model particles. This increases the impact on M_{12} from the new physics. For the B_s mesons, the constraints from ΔM_s place stringent bounds on the allowed new physics contributions. This is because the direct contribution from the box diagrams in Fig. 5.9 is sizeable, which limits the potential BSM effects in $\Delta\Gamma_s$. On the other hand, there is an allowed new physics contribution to $\Delta\Gamma_d$ of up to 2%, corresponding to $|C_4'^d| \sim \mathcal{O}(10^{-3})$, while the possible corrections to a_{fs}^d are of the sub-percent level. Compared to the B_s system, the allowed effects of the UV model in the B_d system are greater because the bounds from ΔM_d are less stringent. In order to find UV completions with a more sizeable effects on $\Delta\Gamma_d$, one needs a more efficient suppression mechanism for M_{12}.

6 Phenomenology of B Meson Decays

In this chapter, the NNLO results of the lifetime ratios for B mesons, $\tau(B^+)/\tau(B_d)$, and Ξ_b baryons, $\tau(\Xi_b^0)/\tau(\Xi_b^-)$, are presented. First, the calculation approach for these particular observables and the input parameters are discussed. The main part of the chapter then focuses on the numerical analysis of the lifetime ratios, comparing the theoretical predictions to measurements and analysing the relative size of different contributions to the Standard Model predictions. The results presented here will be published in Ref. [192].

6.1 Calculation strategy

In this thesis, the lifetime ratios

$$\frac{\tau(B^+)}{\tau(B_d)} \qquad \text{and} \qquad \frac{\tau(\Xi_b^0)}{\tau(\Xi_b^-)} \tag{6.1}$$

are considered to the first non-trivial order in the HQE. The main focus is on the B meson ratio, for which the corrections $\delta\Gamma$ in Eq. (2.146) are calculated. With these corrections, the lifetime ratio for the B mesons can be written as

$$\begin{aligned}\frac{\tau(B^+)}{\tau(B_d)} &= 1 + \left[\delta\Gamma(B_d) - \delta\Gamma(B^+)\right] \times \tau(B^+) \\ &= 1 + \left[\frac{G_F^2 m_b^2 |V_{cb}|^2}{12\pi} f_B^2 M_B \left(|V_{ud}|^2 \vec{F}^u + |V_{cd}|^2 \vec{F}^c - \vec{F}^d\right) \cdot \vec{B}\right] \times \tau(B^+)\,, \end{aligned} \tag{6.2}$$

where the matching coefficients $\vec{F}^q$ are calculated in this thesis.

As outlined in Section 3.2.4, the leading-CKM matching coefficients $\vec{F}^u$ and $\vec{F}^d$ are calculated from the uc current-current operators up to NNLO while the sub-leading matching coefficients $\vec{F}^c$ are calculated up to NLO from the cc current-current operators. The penguin operators are included at leading order in diagrams with one penguin and one current-current operator. They are also sub-leading in the CKM factor. It is necessary to include the penguin contributions in order to obtain the correct scale-separated matching coefficients from the solution of the RGE

$$\vec{F}^c(\mu_2) = \vec{F}^c(\mu_1)\, U(\mu_1, \mu_2)\,, \tag{6.3}$$

as the right-hand side would otherwise not be independent of μ_1 at $\mathcal{O}(\alpha_s)$ due to the mixing of penguin and current-current operators. Doubly Cabibbo-suppressed contributions are negligible and not considered. Since we do not calculate $\vec{F}^c$ at NNLO, the approximation we use at that order is $|V_{cd}| = 0$ and $|V_{ud}| = 1$.

The lifetime ratio for the Ξ_b baryons is influenced by the same matching coefficients as the B mesons; however, the decay of the s valence quark will impact the lifetime through $s \to u$ transitions in decays like $\Xi_b^- \to \Lambda_b \pi^-$, $\Xi_b^- \to \Lambda_b \bar{\nu}_e e^-$ and $\Xi_b^0 \to \Lambda_b \pi^0$ [58]. Hence, we define the modified lifetimes and decay widths

$$\overline{\Gamma}(\Xi_b) \equiv \Gamma(\Xi_b) - \Gamma(\Xi_b \to \Lambda_b X) = \frac{1 - B(\Xi_b \to \Lambda_b X)}{\tau(\Xi_b)} \equiv \frac{1}{\overline{\tau}(\Xi_b)} \tag{6.4}$$

to remove the decays from $s \to u$ transitions with the branching fraction $B(\Xi_b \to \Lambda_b X)$. The branching fraction of the decays involving an $s \to u$ transition is less than 10^{-3}, so the modified lifetime is very close to the actual lifetime [162]. The observable we calculate is

$$\frac{\overline{\tau}(\Xi_b^0)}{\overline{\tau}(\Xi_b^-)} = 1 + \left[\frac{G_F^2 m_b^2 |V_{cb}|^2}{12\pi} f_B^2 M_B \left(|V_{ud}|^2 \vec{F}^u + |V_{cd}|^2 \vec{F}^c - \vec{F}^d \right) \cdot \vec{B}^{\Xi_b} \right] \times \overline{\tau}(\Xi_b^0) \,, \tag{6.5}$$

where the bag parameters $\vec{B}^{\Xi_b} \equiv (L_1, L_{1S}, L_2, L_{2S})^T$ are related to the hadronic matrix elements through

$$\begin{aligned}
\left\langle \Xi_b^0 \left| \left(Q^u - Q^d \right) \right| \Xi_b^0 \right\rangle &= f_B^2 \, M_B \, M_{\Xi_b} \, L_1 \,, \\
\left\langle \Xi_b^0 \left| \left(Q_S^u - Q_S^d \right) \right| \Xi_b^0 \right\rangle &= f_B^2 \, M_B \, M_{\Xi_b} \, L_{1S} \,, \\
\left\langle \Xi_b^0 \left| \left(T^u - T^d \right) \right| \Xi_b^0 \right\rangle &= f_B^2 \, M_B \, M_{\Xi_b} \, L_2 \,, \\
\left\langle \Xi_b^0 \left| \left(T_S^u - T_S^d \right) \right| \Xi_b^0 \right\rangle &= f_B^2 \, M_B \, M_{\Xi_b} \, L_{2S} \,.
\end{aligned} \tag{6.6}$$

Similar to the calculation of the B meson mixing observables, the matching coefficients are obtained as an expansion in the mass ratio $z = m_c^2/m_b^2$ up to z^{10}. All undetermined constants $a, b, \ldots f$ in the definitions of the evanescent operators in Section 2.5 have been set to zero for the numerical analysis. This is consistent with the basis chosen in Ref. [60], which calculates the hadronic matrix elements for the B mesons. In general, the basis definitions of the perturbative and non-perturbative calculations must be the same, but there are more degrees of freedom for the $|\Delta B| = 0$ transition operator than for the $|\Delta B| = 2$ transition operator as Fierz symmetry is not required here, see Sections 2.4.2 and 2.5.

6.2 Power-suppression of the baryonic matrix elements

The hadronic matrix elements of the Ξ baryons are not all independent to leading power in Λ_{QCD}/m_b. Therefore, the perturbative relations between the linearly dependent matrix elements or, equivalently, bag parameters need to be calculated. The reason for this linear dependence is rooted in the spin symmetry of the heavy bottom quark. Since there are no interactions with the spin of the bottom quark in the heavy quark limit, the matrix element

$$\frac{1}{2M_{\Xi_b}}\left\langle \Xi_b\middle|\left(\bar{b}^a\gamma^\mu\gamma_5 b^b\right)\left(\bar{q}^c\gamma_\mu P_L q^d\right)\middle|\Xi_b\right\rangle = \mathcal{O}\left(\frac{\Lambda_{\text{QCD}}}{m_b}\right) \tag{6.7}$$

is power-suppressed [57]. The indices a, b, c and d denote colour indices in the equation above. The power-suppression is applicable to linear combinations of the operators Q, Q_S, T and T_S after using a Fierz identity on the expression in Eq. (6.7),

$$\left(\bar{b}^a\gamma^\mu\gamma_5 b^b\right)\left(\bar{q}^c\gamma_\mu P_L q^d\right) = -2\left(\bar{b}^a P_L q^d\right)\left(\bar{q}^c P_R b^b\right) - \left(\bar{b}^a\gamma^\mu P_L q^c\right)\left(\bar{q}^c\gamma_\mu P_L b^b\right). \tag{6.8}$$

Therefore, the matrix elements

$$\begin{aligned}\langle\Xi_b|2Q_S^q + Q^q|\Xi_b\rangle &= \mathcal{O}\left(\frac{\Lambda_{\text{QCD}}}{m_b}\right),\\ \langle\Xi_b|2T_S^q + T^q|\Xi_b\rangle &= \mathcal{O}\left(\frac{\Lambda_{\text{QCD}}}{m_b}\right),\end{aligned} \tag{6.9}$$

with $q \in \{u, d, s\}$ vanish to leading-power. However, there are perturbative corrections to the power-suppressed matrix elements, which depend on the renormalisation scheme. In particular, in the $\overline{\text{MS}}$ scheme, a finite renormalisation is required to ensure the power-suppression of Eq. (6.9). Since the power suppressed matrix elements are discarded in the calculation, two of the four operators $\{Q, Q_S, T, T_S\}$ can be removed from the transition operator. Hence, the finite renormalisation constants are used to eliminate Q_S and T_S up to leading power. This can be implemented via

$$\begin{pmatrix}\langle\Xi_b^0|(Q_S^u - Q_S^d)|\Xi_b^0\rangle^{\overline{\text{MS}}}\\ \langle\Xi_b^0|(T_S^u - T_S^d)|\Xi_b^0\rangle^{\overline{\text{MS}}}\end{pmatrix} = \left[A + \frac{\alpha_s}{4\pi}B + \left(\frac{\alpha_s}{4\pi}\right)^2 C\right]\begin{pmatrix}\langle\Xi_b^0|(Q^u - Q^d)|\Xi_b^0\rangle^{\overline{\text{MS}}}\\ \langle\Xi_b^0|(T^u - T^d)|\Xi_b^0\rangle^{\overline{\text{MS}}}\\ \langle\Xi_b^0|(\vec{E}^u - \vec{E}^d)|\Xi_b^0\rangle^{\overline{\text{MS}}}\end{pmatrix}, \tag{6.10}$$

up to power-suppressed terms. Here, the matrix A corresponds to the LO relation encoded in Eq. (6.9), and part of B has been calculated in Ref. [58]. The vector on the right-hand side contains the evanescent operators of the first and second generation for Q and T, denoted by $\vec{E}$, which are needed to remove IR poles of the form $\langle E\rangle/\epsilon$. To obtain the finite renormalisation constants in A, B and C, the renormalised matrix elements as obtained in the $\overline{\text{MS}}$ scheme are substituted, and Eq. (6.9) is used for the tree-level matrix elements

of Q_S and T_S to discard power-suppressed terms. Analogous relations hold for linear combinations of evanescent operators, i.e.

$$\langle \Xi_b | 2E[O_S] + E[O] | \Xi_b \rangle = \mathcal{O}\left(\frac{\Lambda_{\text{QCD}}}{m_b}\right) . \tag{6.11}$$

Since the finite renormalisation constants in A, B and C relate UV-finite quantities, any IR divergences must cancel. The spurious IR poles we encounter are of the form

$$\frac{b - b_S}{\epsilon} \langle \Xi_b^0 | (Q^u - Q^d) | \Xi_b^0 \rangle^{\overline{\text{MS}}} \qquad \text{and} \qquad \frac{b - b_S}{\epsilon} \langle \Xi_b^0 | (T^u - T^d) | \Xi_b^0 \rangle^{\overline{\text{MS}}} , \tag{6.12}$$

where b and b_S were introduced in Section 2.5 to parametrise the definitions of the evanescent operators at higher orders in ϵ. They must be chosen such that $b = b_S$. This constraint stems from the use of a Fierz identity in Eq. (6.8). As mentioned before, in our numerical analysis, we set all constants $a, b, \ldots f$ equal to zero, which is a definition compatible with the power suppression in Eq. (6.9). After cancelling the IR poles, any tree-level matrix elements of evanescent operators in Eq. (6.10) can be discarded.

While the matrices A, B and C are useful to convert the results of the matching calculation for the B meson lifetime ratio to the appropriate basis for the Ξ_b baryons, it is instructive to connect them to the finite renormalisation constants. By transforming the matrix elements from the $\overline{\text{MS}}$ scheme to the scheme where the power-suppression of Eq. (6.9) holds, the finite renormalisation constants $\widetilde{Z}_{ij}$ are introduced:

$$\begin{aligned}
\langle 2Q_S^q + Q^q \rangle^{\text{new}} &= \langle 2Q_S^q + Q^q \rangle^{\overline{\text{MS}}} + \widetilde{Z}_{13} \langle Q^q \rangle^{\overline{\text{MS}}} + \widetilde{Z}_{14} \langle T^q \rangle^{\overline{\text{MS}}} + \text{ev.} = \mathcal{O}\left(\frac{\Lambda_{\text{QCD}}}{m_b}\right) , \\
\langle 2T_S^q + T^q \rangle^{\text{new}} &= \langle 2T_S^q + T^q \rangle^{\overline{\text{MS}}} + \widetilde{Z}_{23} \langle Q^q \rangle^{\overline{\text{MS}}} + \widetilde{Z}_{24} \langle T^q \rangle^{\overline{\text{MS}}} + \text{ev.} = \mathcal{O}\left(\frac{\Lambda_{\text{QCD}}}{m_b}\right) ,
\end{aligned} \tag{6.13}$$

where the shorthand notation $\langle O \rangle \equiv \langle \Xi_b^0 | O | \Xi_b^0 \rangle$ was used and the finite renormalisation constants multiplying evanescent matrix elements have been omitted for brevity. Setting the right-hand side to zero and rearranging these equations for $\langle Q_S^q \rangle$ and $\langle T_S^q \rangle$ leads to Eq. (6.10), specifically

$$B = -\frac{1}{2} \begin{pmatrix} \widetilde{Z}_{13}^{(1)} & \widetilde{Z}_{14}^{(1)} & \widetilde{Z}_{15}^{(1)} & \widetilde{Z}_{16}^{(1)} & \widetilde{Z}_{17}^{(1)} & \widetilde{Z}_{18}^{(1)} \\ \widetilde{Z}_{23}^{(1)} & \widetilde{Z}_{24}^{(1)} & \widetilde{Z}_{25}^{(1)} & \widetilde{Z}_{26}^{(1)} & \widetilde{Z}_{27}^{(1)} & \widetilde{Z}_{28}^{(1)} \end{pmatrix} , \tag{6.14}$$

$$C = -\frac{1}{2} \begin{pmatrix} \widetilde{Z}_{13}^{(2)} & \widetilde{Z}_{14}^{(2)} & \widetilde{Z}_{15}^{(2)} & \widetilde{Z}_{16}^{(2)} & \widetilde{Z}_{17}^{(2)} & \widetilde{Z}_{18}^{(2)} \\ \widetilde{Z}_{23}^{(2)} & \widetilde{Z}_{24}^{(2)} & \widetilde{Z}_{25}^{(2)} & \widetilde{Z}_{26}^{(2)} & \widetilde{Z}_{27}^{(2)} & \widetilde{Z}_{28}^{(2)} \end{pmatrix} , \tag{6.15}$$

where the superscripts (1) and (2) denote the order in α_s, see Section 2.1.2. The operators corresponding to the indices 5 through 8 are $E^{(1)}[Q]$, $E^{(1)}[T]$, $E^{(2)}[Q]$ and $E^{(2)}[T]$. The

equations obtained from Eq. (6.10) or equivalently Eq. (6.13) are solved order by order in α_s, and we obtain at leading order

$$A = \begin{pmatrix} -1/2 & 0 & 0 & 0 & 0 & 0 \\ 0 & -1/2 & 0 & 0 & 0 & 0 \end{pmatrix} , \tag{6.16}$$

and

$$B = \begin{pmatrix} -\frac{28}{3} - 4\,\ell_1 & -7 - 3\,\ell_1 & -\frac{10}{1263} & \frac{1283}{3368} & -\frac{1}{10104} & \frac{1}{13472} \\ -\frac{14}{9} - \frac{2}{3}\,\ell_1 & \frac{7}{2} + \frac{3}{2}\,\ell_1 & \frac{1283}{15156} & \frac{1243}{20208} & \frac{1}{60624} & -\frac{1}{80832} \end{pmatrix} \tag{6.17}$$

at NLO for $N_c = 3$. These constants are in agreement with Ref. [58], where the scale $\mu_1 = m_b$ was chosen. We also provide the explicit scale dependence in the logarithm $\ell_1 \equiv \ln(\mu_1^2/m_b^2)$, where the mass m_b is in the on-shell scheme. The last four columns are needed to cancel IR poles and to obtain the novel NNLO renormalisation constants, which read

$$\begin{aligned} C_{11} &= -\frac{1742971}{5052} - \frac{55\pi^2}{18} - \frac{1685}{9}\,\ell_1 - 29\,\ell_1^2 + \mathcal{O}\left(\frac{m_c}{m_b}\right) , \\ C_{12} &= -\frac{359267}{842} - \frac{367\pi^2}{72} - \frac{32\pi^2}{3}\ln(2) + 16\zeta(3) - \frac{1411}{6}\,\ell_1 - \frac{159}{4}\,\ell_1^2 + \mathcal{O}\left(\frac{m_c}{m_b}\right) , \\ C_{21} &= -\frac{16994}{3789} - \frac{493\pi^2}{324} + \frac{224\pi^2}{27}\ln(2) - \frac{112}{9}\zeta(3) + \frac{47}{27}\,\ell_1 + \frac{1}{6}\,\ell_1^2 + \mathcal{O}\left(\frac{m_c}{m_b}\right) , \\ C_{22} &= \frac{905701}{13472} + \frac{1025\pi^2}{432} - \frac{40\pi^2}{9}\ln(2) + \frac{20}{3}\zeta(3) + \frac{463}{24}\,\ell_1 + \frac{9}{8}\,\ell_1^2 + \mathcal{O}\left(\frac{m_c}{m_b}\right) , \end{aligned} \tag{6.18}$$

for the physical operators. A cross-check with an IR regulator is required since the definition of the third generation evanescent operator appears in the renormalisation constants. The matrix elements are shown here for $N_c = 3$ and $N_f = 5$ up to zeroth order in m_c/m_b, but all entries have been extracted up to $\mathcal{O}(m_c^{20}/m_b^{20})$ for the phenomenological analysis.

6.3 Input values and renormalisation scales

In this section, the required inputs for the numerical evaluation of the discussed lifetime ratios are presented, and the choice of renormalisation scales is discussed. In Tab. 6.1, all input parameters aside from the bag parameters and CKM elements are summarised. For the CKM elements, we use the values obtained in Ref. [166] from the global fit with their 1σ uncertainties,

$$\begin{aligned} |V_{ud}| &= 0.974358^{+0.000049}_{-0.000054} , \\ |V_{cd}| &= 0.22484^{+0.00023}_{-0.00022} , \\ |V_{cb}| &= 0.04160^{+0.00020}_{-0.00058} . \end{aligned} \tag{6.19}$$

$\alpha_s(M_Z)$	=	0.1180 ± 0.0009	[162]	G_F	=	$1.166\,378\,7 \times 10^{-5}\,\text{GeV}^{-2}$	[162]
M_W	=	$(80.3629 \pm 0.0133)\,\text{GeV}$	[162]	M_Z	=	$(91.1880 \pm 0.0020)\,\text{GeV}$	[162]
m_t^{OS}	=	$(172.4 \pm 0.7)\,\text{GeV}$	[162]	$\overline{m}_b(\overline{m}_b)$	=	$(4.163 \pm 0.016)\,\text{GeV}$	[163]
$\overline{m}_c(3\,\text{GeV})$	=	$(0.993 \pm 0.008)\,\text{GeV}$	[164]	M_B	=	$(5279.41 \pm 0.07)\,\text{MeV}$	[162]
f_B	=	$(0.1900 \pm 0.0013)\,\text{GeV}$	[167]	$\tau(B^+)$	=	$(1.638 \pm 0.004)\,\text{ps}$	[162]

Table 6.1: Input parameters for the phenomenological analysis.

For the bag parameters of the B mesons, we use the values obtained from QCD sum rules in Ref. [60],

$$\begin{aligned} B_1 &= 1.013^{+0.066}_{-0.059}\,, \\ B_2 &= 1.004^{+0.085}_{-0.081}\,, \\ \epsilon_1 &= -0.098^{+0.026}_{-0.032}\,, \\ \epsilon_2 &= -0.037^{+0.019}_{-0.020}\,, \end{aligned} \tag{6.20}$$

which are given at the scale $\overline{m}_b(\overline{m}_b)$. For the Ξ_b baryons only an exploratory lattice QCD calculation exists [193], which obtains

$$\begin{aligned} L_1(m_b) &= \begin{cases} -0.31 \pm 0.03 & \text{for} \quad am_\pi = 0.74 \pm 0.04 \\ -0.22 \pm 0.04 & \text{for} \quad am_\pi = 0.52 \pm 0.03 \end{cases} \\ L_2(m_b) &= \begin{cases} 0.23 \pm 0.02 & \text{for} \quad am_\pi = 0.74 \pm 0.04 \\ 0.17 \pm 0.02 & \text{for} \quad am_\pi = 0.52 \pm 0.03 \end{cases} \end{aligned} \quad . \tag{6.21}$$

The scale of the bag parameters is not precisely defined in Ref. [193], so we choose the scale-invariant bottom mass $\overline{m}_b(\overline{m}_b)$. Since no continuum extrapolation of the baryonic bag parameters is available, these input values are used for illustrative purposes only.

Lastly, the choice of renormalisation scales and the chosen schemes for the quark masses need to be discussed. The renormalisation scales encountered are μ_0, the matching scale of the $|\Delta B| = 1$ Hamiltonian, μ_1, the matching scale of the $|\Delta B| = 0$ transition operator, μ_2, the scale of the hadronic matrix elements, and the mass renormalisation scales μ_c and μ_b. With the exception of μ_2, we choose the same scales as for the B meson mixing, i.e. $\mu_0 = 165\,\text{GeV}$ and $\mu_c = \mu_b = \mu_1$. For the scale of the bag parameters, we use $\mu_2 = \overline{m}_b(\overline{m}_b) = 4.163\,\text{GeV}$ since the results of Ref. [60] are given at that scale. The mass ratio $z = m_c^2/m_b^2$ is evaluated in the $\overline{\text{MS}}$ scheme with five active flavours, and for the overall factor of m_b^2, we calculate our results in the same three schemes as for the B meson mixing. The pole scheme refers to the case of substituting the OS mass for m_b while in the $\overline{\text{MS}}$ and PS schemes we first convert the OS mass and then substitute the corresponding bottom quark mass. To estimate the perturbative uncertainty, the scales $\mu_1 = \mu_c = \mu_b$ are varied simultaneously between 2.1 GeV and 8.4 GeV, and the central value is extracted at 4.2 GeV.

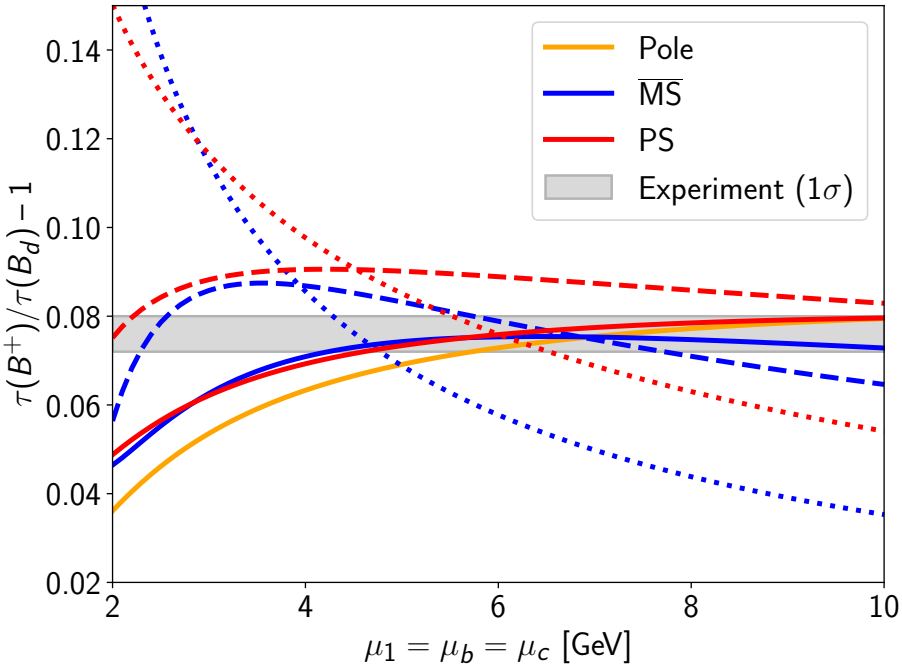

Figure 6.1: Renormalisation scale dependence of $\tau(B^+)/\tau(B_d) - 1$ at LO (short dashes), NLO (long dashes) and NNLO (solid) for the simultaneous scale variation of $\mu_1 = \mu_b = \mu_c$. The experimental value shown is $\tau(B^+)/\tau(B_d) = 1.076 \pm 0.004$ from Ref. [26].

6.4 The lifetime ratio $\tau(B^+)/\tau(B_d)$

The scale variation of the lifetime ratio is shown in Fig. 6.1, and we obtain the central values

$$\begin{aligned}
\frac{\tau(B^+)}{\tau(B_d)} &= 1.065^{+0.013}_{-0.026\text{scale}} \pm 0.017_{\text{bag}} \pm 0.001_{|V_{cb}|} \pm 0.001_{\text{input}}\,(\text{pole})\,, \\
\frac{\tau(B^+)}{\tau(B_d)} &= 1.072^{+0.004}_{-0.024\text{scale}} \pm 0.017_{\text{bag}} \pm 0.001_{|V_{cb}|} \pm 0.002_{\text{input}}\,(\overline{\text{MS}})\,, \\
\frac{\tau(B^+)}{\tau(B_d)} &= 1.070^{+0.009}_{-0.020\text{scale}} \pm 0.018_{\text{bag}} \pm 0.001_{|V_{cb}|} \pm 0.001_{\text{input}}\,(\text{PS})\,. \qquad (6.22)
\end{aligned}$$

Here, the uncertainties of the bag parameters given in Eq. (6.20) have been combined for the "bag" uncertainty, and all remaining inputs apart from $|V_{cb}|$ have been added in quadrature. The largest source of uncertainty is in the bag parameters while the perturbative uncertainty of the NNLO result is only sub-leading. All other input uncertainties are negligible in comparison.

Comparing the LO, NLO and NNLO curves, we observe that the perturbative series has a reduced scale dependence, confirming the convergence of the expansion in the strong

coupling. In the $\overline{\text{MS}}$ scheme for example, the variation of the LO result is around 78% of the central value. This is reduced to 20% at NLO and 19% at NNLO, all computed over the interval [2.1 GeV, 8.4 GeV]. For the PS scheme, the scale variation decrease from 45% at LO to 7% at NLO before increasing again to 20% at NNLO. However, the results of the $\overline{\text{MS}}$ and PS schemes are much closer together over the entire interval at NNLO than at NLO, and they are closer to the experimental value. Therefore, the increased scale dependence for the PS scheme is not an indication of a bad convergence of the perturbative series. Moreover, the $\overline{\text{MS}}$ and PS schemes show a smaller scale dependence and better agreement with the measurement than the pole scheme, confirming that the former schemes yield better results.

As stated in Section 6.1, the contributions to $\vec{F}^c$ are CKM-suppressed, and they only have a minor impact on the numerical result. In the $\overline{\text{MS}}$ scheme, the contributions make up 0.005% of the central value while for the PS scheme the value is 0.06%. This is well below the scale uncertainty, which justifies the approximation at NNLO to neglect $\vec{F}^c$, and to only consider the singly Cabibbo-suppressed contributions. However, this suppression is not only due to the small value of $|V_{cd}|$ but also due to cancellations between LO and NLO since the LO contributions to proportional to $|V_{cd}|$ make up 0.4% and 0.5% in the $\overline{\text{MS}}$ and PS scheme respectively. The penguin operators at LO also have a negligible numerical impact, which is 0.03% and 0.04% for the $\overline{\text{MS}}$ and PS schemes respectively. This confirms that the penguin operators do not need to be included beyond LO at the current level of precision.

The central values of the $\overline{\text{MS}}$ and PS scheme results are averaged to compare to experiment. While the pole scheme is shown for reference in Fig. 6.1, we do not include it in our final result due to the renormalon ambiguity of order Λ_{QCD} in the pole mass. The uncertainty of our final theory prediction is obtained by adding the upper and lower bounds separately in quadrature, symmetrising and then averaging across the two schemes. We obtain

$$\frac{\tau(B^+)}{\tau(B_d)} = 1.071 \pm 0.023\,, \tag{6.23}$$

which agrees within the uncertainty with the experimental value [26]

$$\left(\frac{\tau(B^+)}{\tau(B_d)}\right)^{\text{exp}} = 1.076 \pm 0.004\,. \tag{6.24}$$

Since any BSM effects in the lifetime ratios are expected to be of the per mille level [27, 32], the observed agreement between experiment and theory provides evidence for the validity of the HQE. This is crucial because this expansion forms the basis of many calculations in flavour physics. Discrepancies between experiment and the prediction obtained from the HQE could stem from non-perturbative contributions in the case of quark-hadron duality (QHD) violation [194–196]. Therefore, our results also support the validity of QHD.

The theoretical prediction is at this point less accurate than the measurement. Further improvements in the accuracy require more accurate calculations of the bag parameters as well as a deeper expansion of the perturbative series. Additionally, higher order terms in the HQE have been neglected and might be required to match the precision of the experiment. The contribution from dimension-seven operators, i.e. the next order in the HQE, is calculated to be –0.007 in Ref. [32].

Our results may also be compared to previous calculations using the HQE. Ref. [32] obtains

$$\frac{\tau(B^+)}{\tau(B_d)} = 1.086 \pm 0.022 \tag{6.25}$$

at NLO, using an older determination of the non-perturbative matrix elements and including power-suppressed contributions from dimension-seven operators. We find agreement within the respective uncertainties. The uncertainty given in Ref. [32] is smaller than the one given in Eq. (6.23) since the scale variation was done in a different way and over a smaller interval in Ref. [32].

To enable future calculations with different bag parameters, the coefficients of each bag parameter in

$$\frac{\tau(B^+)}{\tau(B_d)} - 1 = F_{B_1} B_1 + F_{B_2} B_2 + F_{\epsilon_1} \epsilon_1 + F_{\epsilon_2} \epsilon_2 \tag{6.26}$$

are given in the three renormalisation schemes. For the pole scheme, we obtain

$$\begin{aligned}
F_{B_1}^{\text{pole}} &= 0.0184^{+0.0098}_{-0.0167\text{scale}} \pm 0.0003_{|V_{cb}|} \pm 0.0006_{\text{input}}\,, \\
F_{B_2}^{\text{pole}} &= -0.0038^{+0.0022}_{-0.0062\text{scale}} \pm 0.0001_{|V_{cb}|} \pm 0.0003_{\text{input}}\,, \\
F_{\epsilon_1}^{\text{pole}} &= -0.5501^{+0.0345}_{-0.0122\text{scale}} \pm 0.0103_{|V_{cb}|} \pm 0.0097_{\text{input}}\,, \\
F_{\epsilon_2}^{\text{pole}} &= 0.1084^{+0.0077}_{-0.0056\text{scale}} \pm 0.0020_{|V_{cb}|} \pm 0.0017_{\text{input}}\,.
\end{aligned} \tag{6.27}$$

In the $\overline{\text{MS}}$ scheme, the results read

$$\begin{aligned}
F_{B_1}^{\overline{\text{MS}}} &= 0.0231^{+0.0034}_{-0.0152\text{scale}} \pm 0.0004_{|V_{cb}|} \pm 0.0009_{\text{input}}\,, \\
F_{B_2}^{\overline{\text{MS}}} &= -0.0026^{+0.0022}_{-0.0076\text{scale}} \pm 0.0000_{|V_{cb}|} \pm 0.0002_{\text{input}}\,, \\
F_{\epsilon_1}^{\overline{\text{MS}}} &= -0.5646^{+0.0275}_{-0.0011\text{scale}} \pm 0.0106_{|V_{cb}|} \pm 0.0103_{\text{input}}\,, \\
F_{\epsilon_2}^{\overline{\text{MS}}} &= 0.1157^{+0.0019}_{-0.0032\text{scale}} \pm 0.0022_{|V_{cb}|} \pm 0.0018_{\text{input}}\,,
\end{aligned} \tag{6.28}$$

and finally for the PS scheme we have

$$\begin{aligned}
F_{B_1}^{\text{PS}} &= 0.0216^{+0.0067}_{-0.0127\text{scale}} \pm 0.0004_{|V_{cb}|} \pm 0.0008_{\text{input}}\,, \\
F_{B_2}^{\text{PS}} &= -0.0032^{+0.0020}_{-0.0056\text{scale}} \pm 0.0001_{|V_{cb}|} \pm 0.0003_{\text{input}}\,, \\
F_{\epsilon_1}^{\text{PS}} &= -0.5709^{+0.0137}_{-0.0011\text{scale}} \pm 0.0107_{|V_{cb}|} \pm 0.0105_{\text{input}}\,, \\
F_{\epsilon_2}^{\text{PS}} &= 0.1152^{+0.0049}_{-0.0031\text{scale}} \pm 0.0022_{|V_{cb}|} \pm 0.0018_{\text{input}}\,.
\end{aligned} \tag{6.29}$$

Comparing the results across the three schemes, the pole scheme has the largest perturbative uncertainty for all coefficients, which is consistent with the expected poor convergence of the perturbative series. For each scheme, the four coefficients differ in the relative size of the perturbative uncertainty. Interestingly, the coefficients of the larger bag parameters $B_{1,2}$ also have a larger relative perturbative uncertainty, with that of B_2 exceeding 100%. The coefficient F_{B_2} is small compared to F_{B_1} because the contribution to F_S^d vanishes to LO whereas it gives a sizeable contribution to F^d. Therefore, more accurate results of the lifetime ratio could be achieved by calculating higher orders in perturbation theory of selected matching coefficients.

6.5 The lifetime ratio $\tau(\Xi_b^0)/\tau(\Xi_b^-)$

The modified lifetime ratio for the Ξ_b baryons as defined via Eq. (6.4) is given by

$$\begin{aligned}
\frac{\overline{\tau}(\Xi_b^0)}{\overline{\tau}(\Xi_b^-)} &= 0.872^{+0.011}_{-0.006\text{scale}} \pm 0.017_{\text{bag}} \pm 0.001_{|V_{cb}|} \pm 0.001_{\text{input}}\,(\text{pole})\,,\\
\frac{\overline{\tau}(\Xi_b^0)}{\overline{\tau}(\Xi_b^-)} &= 0.867^{+0.005}_{-0.000\text{scale}} \pm 0.017_{\text{bag}} \pm 0.001_{|V_{cb}|} \pm 0.002_{\text{input}}\,(\overline{\text{MS}})\,,\\
\frac{\overline{\tau}(\Xi_b^0)}{\overline{\tau}(\Xi_b^-)} &= 0.866^{+0.006}_{-0.002\text{scale}} \pm 0.018_{\text{bag}} \pm 0.001_{|V_{cb}|} \pm 0.001_{\text{input}}\,(\text{PS})\,, \qquad (6.30)
\end{aligned}$$

for the bag parameters $L_{1,2}$ obtained from the lattice configuration in Eq. (6.21) with $am_\pi = 0.74 \pm 0.04$. The scale variation is shown in Fig. 6.2. In the case of $am_\pi = 0.52 \pm 0.03$, we calculate

$$\begin{aligned}
\frac{\overline{\tau}(\Xi_b^0)}{\overline{\tau}(\Xi_b^-)} &= 0.906^{+0.008}_{-0.004\text{scale}} \pm 0.017_{\text{bag}} \pm 0.001_{|V_{cb}|} \pm 0.001_{\text{input}}\,(\text{pole})\,,\\
\frac{\overline{\tau}(\Xi_b^0)}{\overline{\tau}(\Xi_b^-)} &= 0.902^{+0.004}_{-0.000\text{scale}} \pm 0.017_{\text{bag}} \pm 0.001_{|V_{cb}|} \pm 0.002_{\text{input}}\,(\overline{\text{MS}})\,,\\
\frac{\overline{\tau}(\Xi_b^0)}{\overline{\tau}(\Xi_b^-)} &= 0.901^{+0.004}_{-0.001\text{scale}} \pm 0.018_{\text{bag}} \pm 0.001_{|V_{cb}|} \pm 0.001_{\text{input}}\,(\text{PS})\,, \qquad (6.31)
\end{aligned}$$

with the scale variation shown in Fig. 6.3. In both cases, the NNLO scale variation of the PS scheme follows that of the $\overline{\text{MS}}$ scheme below $\sim 5\,\text{GeV}$ and that of the pole scheme above $\sim 7\,\text{GeV}$. The uncertainties were grouped in the same way as for the B meson lifetime ratios, and they are similarly dominated by the bag parameters. The uncertainties of the bag parameters given here only take into account the uncertainties of the individual results at the two values of am_π in Eq. (6.21). However, the implied uncertainty on physical observables calculated from these bag parameters is larger since they were obtained in an exploratory lattice QCD study which did not extrapolate to the continuum.

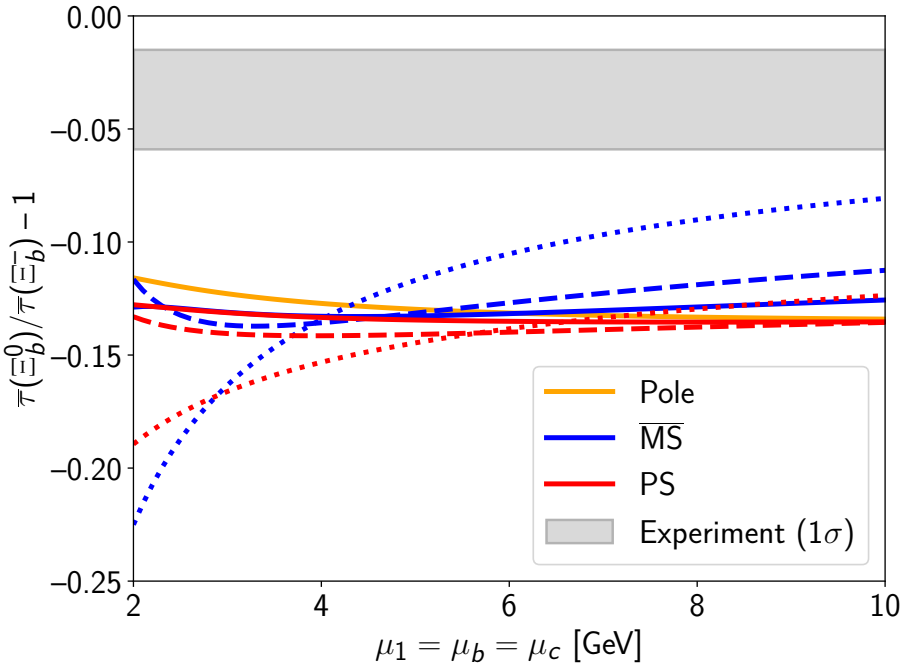

Figure 6.2: Renormalisation scale dependence of $\overline{\tau}(\Xi_b^0)/\overline{\tau}(\Xi_b^-) - 1$ at LO (short dashes), NLO (long dashes) and NNLO (solid) with the bag parameters at $am_\pi = 0.74 \pm 0.04$. The experimental value shown is $\tau(\Xi_b^0)/\tau(\Xi_b^-) = 0.963 \pm 0.022$ from Ref. [26].

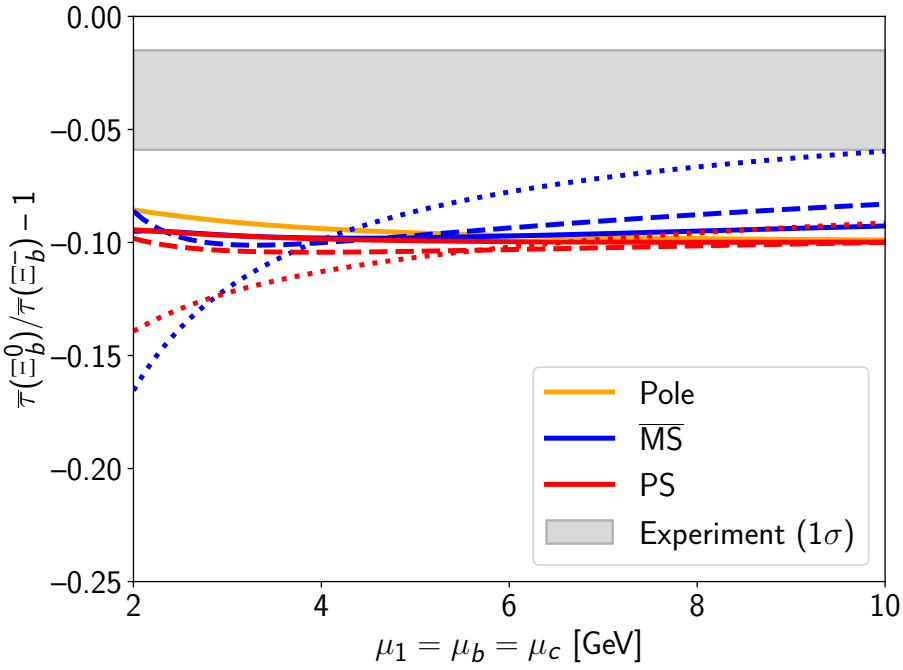

Figure 6.3: Renormalisation scale dependence of $\overline{\tau}(\Xi_b^0)/\overline{\tau}(\Xi_b^-) - 1$ analogous to Fig. 6.2 at $am_\pi = 0.52 \pm 0.03$.

As for the B meson lifetime ratios, we observe a good convergence of the perturbative series from the reduced scale dependence in the interval [2.1 GeV, 8.4 GeV] at higher orders in the strong coupling. To illustrate this point, consider the results for $am_\pi = 0.52 \pm 0.03$. In the $\overline{\text{MS}}$ scheme, the LO scale variation is close to 50%, which is reduced to 7% at NLO and 2% at NNLO. For the PS scheme, the behaviour is similar as for the mesonic lifetime ratios, with the scale variation of 20% at LO decreasing to 2.4% at NLO and 2.6% at NNLO. While the NNLO result in the PS scheme does not exhibit a reduced scale dependence over the considered interval, the agreement with the $\overline{\text{MS}}$ results is improved as compared with the NLO results. The renormalisation scale dependence of the pole scheme is worse, demonstrating the impact of the renormalon uncertainty.

The CKM-suppressed contributions in $\vec{F}^c$ are more significant for the Ξ_b baryon lifetime ratio than for the B meson lifetime ratio, but they are still small. In the $\overline{\text{MS}}$ and PS schemes with $am_\pi = 0.52 \pm 0.03$, these contributions make up 1% of the result for $\overline{\tau}(\Xi_b^0)/\overline{\tau}(\Xi_b^-) - 1$. Therefore, we expect the NNLO contributions from $\vec{F}^c$ to be tiny, justifying our approximation to set $|V_{cd}| = 0$ at that order in perturbation theory. The penguin operators specifically contribute less than 0.1%, so neglecting them at NLO is a good approximation too.

To compare our predictions with experiment, we average the central values of the $\overline{\text{MS}}$ and PS scheme results. Similar to the meson lifetime ratios, the uncertainties for the upper and lower bounds are separately added in quadrature before symmetrising and averaging across the two schemes. The final results read

$$\frac{\overline{\tau}(\Xi_b^0)}{\overline{\tau}(\Xi_b^-)} = \begin{cases} 0.867 \pm 0.018 & \text{for} \quad am_\pi = 0.74 \pm 0.04 \\ 0.902 \pm 0.018 & \text{for} \quad am_\pi = 0.52 \pm 0.03 \end{cases} , \tag{6.32}$$

which can be compared to the experimental value [26]

$$\left(\frac{\tau(\Xi_b^0)}{\tau(\Xi_b^-)}\right)^{\text{exp}} = 0.936 \pm 0.022 \,. \tag{6.33}$$

The branching fraction of the decays into $\Lambda_b X$ from Ref. [162] less than 10^{-3}, and hence we do not need to correct for those terms in Eq. (6.4). Moreover, the corrections to the modified lifetimes largely cancel in the lifetime ratio due to isospin symmetry. The theoretical prediction obtained from lattice results at $am_\pi = 0.52 \pm 0.03$ agrees with the experimental value within the given 1σ uncertainties. The results calculated with the lattice configuration of $am_\pi = 0.74 \pm 0.04$ only agrees within the 2σ intervals, and in both cases the theoretical uncertainty is dominated by the uncertainties of the bag parameters. This clearly shows that more accurate determinations of the bag parameters are required to make conclusive statements about the agreement with the experiment.

The results obtained here may also be compared with previous calculations of the baryon lifetime ratio. In Ref. [33], the NLO result

$$\frac{\tau(\Xi_b^0)}{\tau(\Xi_b^-)} = 0.929 \pm 0.028 \tag{6.34}$$

was obtained using the non-relativistic constituent quark model, which agrees within the 1σ uncertainty with our prediction with the bag parameters at $am_\pi = 0.52 \pm 0.03$. We are able to calculate the lifetime ratio to higher accuracy due to the reduced perturbative uncertainty of the NNLO matching coefficients.

The results obtained in this thesis can be combined with future determinations of the bag parameters to yield more accurate predictions of the lifetime ratio. For this purpose, the coefficients F_1 and F_2 in

$$\frac{\overline{\tau}(\Xi_b^0)}{\overline{\tau}(\Xi_b^-)} - 1 = F_1 L_1 + F_2 L_2 \tag{6.35}$$

are extracted for each of the three renormalisation schemes. For the pole scheme, we obtain

$$\begin{aligned} F_1^{\text{pole}} &= 0.016^{+0.007}_{-0.011\text{scale}} \pm 0.000_{|V_{cb}|} \pm 0.001_{\text{input}}\,, \\ F_2^{\text{pole}} &= -0.534^{+0.033}_{-0.015\text{scale}} \pm 0.010_{|V_{cb}|} \pm 0.009_{\text{input}}\,, \end{aligned} \tag{6.36}$$

and in the $\overline{\text{MS}}$ scheme we have

$$\begin{aligned} F_1^{\overline{\text{MS}}} &= 0.019^{+0.002}_{-0.009\text{scale}} \pm 0.000_{|V_{cb}|} \pm 0.001_{\text{input}}\,, \\ F_2^{\overline{\text{MS}}} &= -0.552^{+0.023}_{-0.000\text{scale}} \pm 0.010_{|V_{cb}|} \pm 0.010_{\text{input}}\,. \end{aligned} \tag{6.37}$$

Finally, the results in the PS scheme are

$$\begin{aligned} F_1^{\text{PS}} &= 0.018^{+0.005}_{-0.008\text{scale}} \pm 0.000_{|V_{cb}|} \pm 0.001_{\text{input}}\,, \\ F_2^{\text{PS}} &= -0.557^{+0.013}_{-0.002\text{scale}} \pm 0.010_{|V_{cb}|} \pm 0.010_{\text{input}}\,. \end{aligned} \tag{6.38}$$

Similar to the corresponding coefficients for the B meson lifetime ratios, the $\overline{\text{MS}}$ and PS schemes lead to a reduced perturbative uncertainty as compared to the pole scheme. Additionally, we observe that the coefficient F_2 is about 30 times larger than the coefficient F_1. Therefore, assuming that L_1 and L_2 are of the same order of magnitude, it is possible to extract a benchmark for the bag parameter L_2 from the current experimental measurement by neglecting F_1. For this purpose, the results for F_2 are averaged across the $\overline{\text{MS}}$ and PS schemes,

$$F_2 = -0.554 \pm 0.019\,, \tag{6.39}$$

and with the experimental result from Eq. (6.33), the prediction for the bag parameter is

$$L_2 = 0.115 \pm 0.040\,. \tag{6.40}$$

The uncertainty here is dominated by the measurement of the lifetime ratio. This result provides a benchmark for future non-perturbative calculations of the bag parameters.

Overall, we find good agreement of the Standard Model predictions for the lifetime ratios $\tau(B^+)/\tau(B_d)$ and $\tau(\Xi_b^0)/\tau(\Xi_b^-)$ from the leading-power HQE terms with the values obtained from experiments. Therefore, the lifetime ratios provide supporting evidence for the validity of the HQE and do not show signs of the violation of QHD.

7 Discussion and Conclusion

In this thesis, the NNLO perturbative QCD corrections to the matching coefficients of the $|\Delta B| = 2$ and $|\Delta B| = 0$ transition operators relevant for Γ_{12} and the lifetime ratios of B mesons and Ξ_b baryons were calculated. To extract these matching coefficients, advancements in the technical tools applicable to a broader range of calculations have been made, e.g. spinor projectors for up to eleven γ matrices on two spin lines were developed and subtleties regarding the preservation of Fierz symmetry and the renormalisation with Λ_{QCD}/m_b-suppressed operators have been resolved.

The perturbative results were also used to discuss the phenomenology of B meson mixing and the lifetime ratios. In particular, the most precise predictions of $\Delta\Gamma$, a_{fs}, $\tau(B^+)/\tau(B_d)$ and $\tau(\Xi_b^0)/\tau(\Xi_b^-)$ to date are obtained from the NNLO matching coefficients. Additionally, the results of this thesis can be used in combination with experimental measurements of the observables a_{fs}^d and $\Delta\Gamma_d/\Delta\Gamma_s$ to yield stringent constraints for the apex of the CKM unitarity triangle. This motivates more precise measurements of these observables, which can then be used to test the Standard Model from B meson mixing observables alone.

Areas for future research with respect to the theoretical predictions of the observables considered here lie mainly in the non-perturbative matrix elements and power-suppressed matching coefficients. For the $|\Delta B| = 2$ transition operator, the leading-power matching coefficients have been fully computed to NNLO, and the next order in perturbation theory would involve a four-loop calculation of a two-point amplitude with the scales m_c and m_b. These corrections are expected to be difficult to calculate in the near future. The Λ_{QCD}/m_b-suppressed contributions are a larger source of uncertainty and should be prioritised. Here, both the hadronic matrix elements as well as their matching coefficients, which are only known to leading order, would benefit from more accurate calculations.

For the lifetime ratios, further improvements in the CKM-suppressed leading-power matching coefficients are possible, but the biggest lever to reduce the theoretical uncertainty is in the non-perturbative matrix elements. Future calculations of non-perturbative matrix elements can be readily combined with the matching coefficients of this thesis to make more accurate predictions of the lifetime ratios. For the baryonic matrix elements, non-perturbative calculations can be checked against the benchmark extracted in this thesis. Additionally, the matching coefficients obtained for the B meson lifetime ratio can be used to calculate the corresponding lifetime ratio for D mesons. Since the power-suppressed

terms in the HQE of the charm mass have a more pronounced impact on the observables than for the bottom mass, the size of the power-suppressed contributions can be estimated by combining the matching coefficients with measurements of the D meson lifetime ratios.

Overall, the results are in good agreement with the Standard Model of particle physics. Moreover, the Heavy Quark Expansion appears to be a good approximation and quark-hadron duality holds. In the future, more stringent tests of the Standard Model and different classes of BSM models will be possible through the combination of the perturbative coefficients of this thesis, more accurate non-perturbative calculations and updated experimental measurements.

A Renormalisation Constants for the $|\Delta B| = 1$ Theory

This appendix contains the renormalisation constants which describe the operator mixing for the weak effective Hamiltonian up to α_s^2. The renormalisation matrices are presented in the CMM basis for all dimension-five and -six operators, which are used for the calculation of the mixing observables in Chapter 4, and in the historical basis for the current-current operators, which are used for the calculation of the lifetime ratios in Chapter 6. The renormalisation constants are given based on the results of Refs. [101, 103, 158]. In Ref. [103] the transformation between the renormalisation matrices in the historical and CMM bases are discussed. The renormalisation constants for the particular choice of evanescent operators in the historical basis follow Ref. [61].

We write the renormalisation constants as a series expansion in α_s and ϵ,

$$Z = \sum_{i=0}^{\infty} \sum_{k=-\infty}^{i} \left(\frac{\alpha_s}{4\pi}\right)^i \frac{1}{\epsilon^k} Z^{(i,k)} \,, \tag{A.1}$$

and for the purpose of better visualisation, the sub-matrices for the physical and evanescent operators are defined via

$$Z \equiv \begin{pmatrix} Z_{QQ} & Z_{QE} \\ Z_{EQ} & Z_{EE} \end{pmatrix} \,, \tag{A.2}$$

which is used to renormalise the Wilson coefficients according to

$$\vec{C}^0 = \vec{C} Z \,. \tag{A.3}$$

To calculate physical amplitudes with the weak effective Hamiltonian, the renormalisation constants of the evanescent operators in Z_{EQ} and Z_{EE} are not required, and hence they are not presented here. The matrices can be found in Refs. [103, 158].

A.1 Renormalisation constants in the historical basis

For the historical basis, we only consider the current-current operator contributions, so we limit the physical operators to

$$\{O_1, O_2, O_1^{cu}, O_2^{cu}, O_1^{uc}, O_2^{uc}, O_1^{uu}, O_2^{uu}\} \,, \tag{A.4}$$

and for the evanescent operators only

$$\begin{aligned}\Big\{&\tilde{E}_1^{(1)}, \tilde{E}_2^{(1)}, \tilde{E}_1^{(1),cu}, \tilde{E}_2^{(1),cu}, \tilde{E}_1^{(1),uc}, \tilde{E}_2^{(1),uc}, \tilde{E}_1^{(1),uu}, \tilde{E}_2^{(1),uu},\\ &\tilde{E}_1^{(2)}, \tilde{E}_2^{(2)}, \tilde{E}_1^{(2),cu}, \tilde{E}_2^{(2),cu}, \tilde{E}_1^{(2),uc}, \tilde{E}_2^{(2),uc}, \tilde{E}_1^{(2),uu}, \tilde{E}_2^{(2),uu}\Big\}\end{aligned} \tag{A.5}$$

need to be considered. In the following, the renormalisation matrices will be presented for the operators

$$\{O_1, O_2, \tilde{E}_1^{(1)}, \tilde{E}_2^{(1)}, \tilde{E}_1^{(2)}, \tilde{E}_2^{(2)}\} \tag{A.6}$$

only as the matrices are identical across the different up-type quark flavours, and there is no mixing between them.

The $\mathcal{O}(\alpha_s^1)$ renormalisation matrix for the current-current operators and their respective evanescent operators with the number of colours fixed to $N_c = 3$ is given by

$$Z^{(1,1)} = \begin{pmatrix} -1 & 3 & \frac{7}{12} & \frac{1}{4} & 0 & 0 \\ 3 & -1 & \frac{1}{2} & -\frac{1}{6} & 0 & 0 \\ 0 & 0 & -\frac{59}{3} & -5 & \frac{7}{12} & \frac{1}{4} \\ 0 & 0 & -13 & \frac{13}{3} & \frac{1}{2} & -\frac{1}{6} \\ 0 & 0 & -\frac{1888}{3} & 96 & \frac{41}{3} & -9 \\ 0 & 0 & -288 & \frac{1568}{3} & 3 & -\frac{67}{3} \end{pmatrix}, \tag{A.7}$$

together with the finite renormalisation of the evanescent operators

$$Z^{(1,0)} = \begin{pmatrix} 0 & 0 & 0 & 0 & 0 & 0 \\ 0 & 0 & 0 & 0 & 0 & 0 \\ 16 & -48 & 0 & 0 & 0 & 0 \\ -24 & -56 & 0 & 0 & 0 & 0 \\ 512 & -1536 & 0 & 0 & 0 & 0 \\ -768 & -1792 & 0 & 0 & 0 & 0 \end{pmatrix}. \tag{A.8}$$

The corresponding renormalisation constants $Z^{(2,2)}$ and $Z^{(2,1)}$ at $\mathcal{O}(\alpha_s^2)$ are shown on the next page.

$$Z^{(2,2)} = \begin{pmatrix} \frac{21}{2}-\frac{N_f}{3} & -\frac{39}{2}+N_f & -\frac{91}{9}+\frac{7N_f}{36} & \frac{N_f}{12}-\frac{8}{3} & \frac{67}{288} & \frac{5}{96} \\ N_f-\frac{39}{2} & \frac{21}{2}-\frac{N_f}{3} & \frac{N_f}{6}-\frac{143}{24} & -\frac{17}{72}\frac{N_f}{18} & \frac{5}{48} & \frac{11}{144} \\ 0 & 0 & \frac{229}{2}-\frac{59N_f}{9} & \frac{955}{6}-\frac{5N_f}{3} & \frac{7N_f}{36}-\frac{35}{6} & \frac{N_f}{12}-\frac{53}{6} \\ 0 & 0 & \frac{227}{6}-\frac{13N_f}{3} & \frac{13N_f}{9}-\frac{3}{2} & \frac{N_f}{6}-\frac{55}{24} & -\frac{35}{24}-\frac{N_f}{18} \\ 0 & 0 & \frac{13360}{9}-\frac{1888N_f}{9} & \frac{5200}{3}+32N_f & \frac{41N_f}{9}-\frac{2273}{6} & \frac{907}{6}-3N_f \\ 0 & 0 & \frac{1424}{3}-96N_f & \frac{1568N_f}{9}-\frac{63248}{9} & N_f-\frac{793}{6} & \frac{1675}{6}-\frac{67N_f}{9} \end{pmatrix}, \tag{A.9}$$

$$Z^{(2,1)} = \begin{pmatrix} -\frac{23}{24}-\frac{N_f}{18} & \frac{N_f}{6}-\frac{161}{8} & \frac{323}{36}-\frac{7N_f}{216} & \frac{7}{12}-\frac{N_f}{72} & -\frac{1}{36} & -\frac{5}{48} \\ \frac{55}{8}+\frac{N_f}{6} & -\frac{239}{24}-\frac{N_f}{18} & \frac{51}{8}-\frac{N_f}{36} & \frac{115}{72}+\frac{N_f}{108} & -\frac{35}{384} & -\frac{77}{1152} \\ \frac{16N_f}{3}-212 & 252-16N_f & \frac{353N_f}{54}-\frac{1279}{24} & -\frac{697}{8}-\frac{N_f}{18} & \frac{145}{24}-\frac{7N_f}{216} & \frac{49}{24}-\frac{N_f}{72} \\ 96-8N_f & 256-\frac{56N_f}{3} & \frac{67N_f}{18}-\frac{1963}{24} & \frac{2753}{24}-\frac{259N_f}{54} & \frac{89}{12}-\frac{N_f}{36} & -\frac{1}{12}+\frac{N_f}{108} \\ \frac{512N_f}{3}-3968 & 11904-512N_f & \frac{32488}{9}+\frac{4280N_f}{27} & 1704-\frac{40N_f}{3} & \frac{9257}{24}+\frac{427N_f}{54} & -\frac{2817}{8}-\frac{3N_f}{2} \\ 4992-256N_f & 16768-\frac{1792N_f}{3} & 80N_f-\frac{12748}{3} & \frac{101644}{9}-\frac{3280N_f}{27} & \frac{6985}{24}+\frac{7N_f}{2} & \frac{2117}{24}-\frac{383N_f}{54} \end{pmatrix}. \tag{A.10}$$

The finite renormalisation constants for the evanescent operators at $\mathcal{O}(\alpha_s^2)$ are

$$Z^{(2,0)} = \begin{pmatrix} 0 & 0 & 0 & 0 & 0 & 0 \\ 0 & 0 & 0 & 0 & 0 & 0 \\ \frac{202796}{115} - \frac{50488 N_f}{1035} & \frac{1037132}{115} - \frac{25544 N_f}{345} & 0 & 0 & 0 & 0 \\ -\frac{15148 N_f}{345} - \frac{39856}{115} & \frac{46028 N_f}{1035} + \frac{39904}{23} & 0 & 0 & 0 & 0 \\ \frac{4098848}{1035} - \frac{1561184 N_f}{1035} & \frac{1154912 N_f}{345} - \frac{1011808}{15} & 0 & 0 & 0 & 0 \\ \frac{56192 N_f}{69} - \frac{34695184}{345} & \frac{6995584 N_f}{1035} - \frac{282282736}{1035} & 0 & 0 & 0 & 0 \end{pmatrix}. \tag{A.11}$$

A.2 Renormalisation constants in the CMM basis

The renormalisation matrix for the physical operators with the number of colours $N_c = 3$ and the number of flavours N_f at order $\mathcal{O}(\alpha_s^1)$ is given by

$$Z_{QQ}^{(1,1)} = \begin{pmatrix} -2 & \frac{4}{3} & 0 & 0 & 0 & 0 & 0 & 0 & 0 & -\frac{1}{9} & 0 & 0 & \frac{167}{648} \\ 6 & 0 & 0 & 0 & 0 & 0 & 0 & 0 & 0 & \frac{2}{3} & 0 & 0 & \frac{19}{27} \\ 0 & 0 & -2 & \frac{4}{3} & 0 & 0 & 0 & 0 & 0 & 0 & 0 & 0 & 0 \\ 0 & 0 & 6 & 0 & 0 & 0 & 0 & 0 & 0 & 0 & 0 & 0 & 0 \\ 0 & 0 & 0 & 0 & -2 & \frac{4}{3} & 0 & 0 & 0 & 0 & 0 & 0 & 0 \\ 0 & 0 & 0 & 0 & 6 & 0 & 0 & 0 & 0 & 0 & 0 & 0 & 0 \\ 0 & 0 & 0 & 0 & 0 & 0 & -2 & \frac{4}{3} & 0 & -\frac{1}{9} & 0 & 0 & \frac{167}{648} \\ 0 & 0 & 0 & 0 & 0 & 0 & 6 & 0 & 0 & \frac{2}{3} & 0 & 0 & \frac{19}{27} \\ 0 & 0 & 0 & 0 & 0 & 0 & 0 & 0 & 0 & -\frac{26}{3} & 0 & 1 & \frac{92}{27} \\ 0 & 0 & 0 & 0 & 0 & 0 & 0 & 0 & -\frac{20}{9} & \frac{2N_f}{3} - \frac{80}{9} & \frac{2}{9} & \frac{5}{12} & -\frac{37 N_f}{216} - \frac{427}{324} \\ 0 & 0 & 0 & 0 & 0 & 0 & 0 & 0 & 0 & -\frac{128}{3} & 0 & 10 & 9N_f + \frac{2192}{27} \\ 0 & 0 & 0 & 0 & 0 & 0 & 0 & 0 & -\frac{128}{9} & \frac{20 N_f}{3} - \frac{272}{9} & \frac{20}{9} & -\frac{1}{3} & \frac{55 N_f}{27} - \frac{1906}{81} \\ 0 & 0 & 0 & 0 & 0 & 0 & 0 & 0 & 0 & 0 & 0 & 0 & \frac{2N_f}{3} - \frac{19}{3} \end{pmatrix}, \tag{A.12}$$

where the rows and columns follow the ordering of the operators

$$\{Q_1, Q_2, Q_1^{cu}, Q_2^{cu}, Q_1^{uc}, Q_2^{uc}, Q_1^{uu}, Q_2^{uu}, Q_3, Q_4, Q_5, Q_6, Q_8\}. \tag{A.13}$$

The current-current operators involving up quarks do not mix with the penguin operators, and they only mix with the physical and evanescent current-current operators of the same CKM factor.

At order $\mathcal{O}(\alpha_s^2)$, the renormalisation matrix for the physical operators is shown on the next page.

$$Z_{QQ}^{(2,2)} = \begin{pmatrix}
17-\frac{2N_f}{3} & \frac{4N_f}{9}-\frac{26}{3} & 0 & 0 & 0 & 0 & 0 & 0 & \frac{10}{81} & \frac{269}{162}-\frac{2N_f}{27} & -\frac{1}{81} & -\frac{5}{216} & * \\
2N_f-39 & 4 & 0 & 0 & 0 & 0 & 0 & 0 & -\frac{20}{27} & \frac{4N_f}{9}-\frac{188}{27} & \frac{2}{27} & \frac{5}{36} & * \\
0 & 0 & 17-\frac{2N_f}{3} & \frac{4N_f}{9}-\frac{26}{3} & 0 & 0 & 0 & 0 & 0 & 0 & 0 & 0 & * \\
0 & 0 & 2N_f-39 & 4 & 0 & 0 & 0 & 0 & 0 & 0 & 0 & 0 & * \\
0 & 0 & 0 & 0 & 17-\frac{2N_f}{3} & \frac{4N_f}{9}-\frac{26}{3} & 0 & 0 & 0 & 0 & 0 & 0 & * \\
0 & 0 & 0 & 0 & 2N_f-39 & 4 & 0 & 0 & 0 & 0 & 0 & 0 & * \\
0 & 0 & 0 & 0 & 0 & 0 & 17-\frac{2N_f}{3} & \frac{4N_f}{9}-\frac{26}{3} & \frac{10}{81} & \frac{269}{162}-\frac{2N_f}{27} & -\frac{1}{81} & -\frac{5}{216} & * \\
0 & 0 & 0 & 0 & 0 & 0 & 2N_f-39 & 4 & -\frac{20}{27} & \frac{4N_f}{9}-\frac{188}{27} & \frac{2}{27} & \frac{5}{36} & * \\
0 & 0 & 0 & 0 & 0 & 0 & 0 & 0 & \frac{68}{27} & \frac{1919}{27}-\frac{22N_f}{9} & \frac{4}{27} & \frac{N_f}{3}-\frac{269}{36} & * \\
0 & 0 & 0 & 0 & 0 & 0 & 0 & 0 & \frac{1550}{81}-\frac{40N_f}{27} & \frac{4N_f^2}{9}-\frac{67N_f}{6}+\frac{7046}{81} & \frac{4N_f}{27}-\frac{283}{162} & \frac{5N_f}{18}-\frac{455}{108} & * \\
0 & 0 & 0 & 0 & 0 & 0 & 0 & 0 & -\frac{640}{27} & \frac{44N_f}{9}+\frac{7376}{27} & \frac{172}{27} & \frac{10N_f}{3}-\frac{590}{9} & * \\
0 & 0 & 0 & 0 & 0 & 0 & 0 & 0 & \frac{9248}{81}-\frac{328N_f}{27} & \frac{40N_f^2}{9}-\frac{788N_f}{9}+\frac{25904}{81} & \frac{40N_f}{27}-\frac{1292}{81} & \frac{23N_f}{18}-\frac{11}{27} & * \\
0 & 0 & 0 & 0 & 0 & 0 & 0 & 0 & 0 & 0 & 0 & 0 & \frac{4N_f^2}{9}-10N_f+\frac{494}{9}
\end{pmatrix}, \quad \text{(A.14)}$$

$$Z_{QQ}^{(2,1)} = \begin{pmatrix}
\frac{4N_f}{9}+\frac{79}{12} & \frac{10N_f}{27}-\frac{205}{18} & 0 & 0 & 0 & 0 & 0 & 0 & -\frac{353}{243} & -\frac{1567}{972} & \frac{67}{486} & -\frac{35}{648} & * \\
\frac{5N_f}{3}+\frac{83}{4} & 3 & 0 & 0 & 0 & 0 & 0 & 0 & -\frac{104}{81} & \frac{338}{81} & \frac{14}{81} & \frac{35}{108} & * \\
0 & 0 & \frac{4N_f}{9}+\frac{79}{12} & \frac{10N_f}{27}-\frac{205}{18} & 0 & 0 & 0 & 0 & 0 & 0 & 0 & 0 & * \\
0 & 0 & \frac{5N_f}{3}+\frac{83}{4} & 3 & 0 & 0 & 0 & 0 & 0 & 0 & 0 & 0 & * \\
0 & 0 & 0 & 0 & \frac{4N_f}{9}+\frac{79}{12} & \frac{10N_f}{27}-\frac{205}{18} & 0 & 0 & 0 & 0 & 0 & 0 & * \\
0 & 0 & 0 & 0 & \frac{5N_f}{3}+\frac{83}{4} & 3 & 0 & 0 & 0 & 0 & 0 & 0 & * \\
0 & 0 & 0 & 0 & 0 & 0 & \frac{4N_f}{9}+\frac{79}{12} & \frac{10N_f}{27}-\frac{205}{18} & -\frac{353}{243} & -\frac{1567}{972} & \frac{67}{486} & -\frac{35}{648} & * \\
0 & 0 & 0 & 0 & 0 & 0 & \frac{5N_f}{3}+\frac{83}{4} & 3 & -\frac{104}{81} & \frac{338}{81} & \frac{14}{81} & \frac{35}{108} & * \\
0 & 0 & 0 & 0 & 0 & 0 & 0 & 0 & -\frac{1117}{81} & -\frac{13N_f}{9}-\frac{29129}{324} & \frac{100}{81} & \frac{3493}{432}-\frac{N_f}{18} & * \\
0 & 0 & 0 & 0 & 0 & 0 & 0 & 0 & \frac{92N_f}{81}-\frac{6839}{486} & \frac{667N_f}{162}-\frac{79409}{972} & \frac{509}{1944}-\frac{2N_f}{81} & \frac{13499}{2592}-\frac{5N_f}{108} & * \\
0 & 0 & 0 & 0 & 0 & 0 & 0 & 0 & -\frac{40N_f}{9}-\frac{81280}{81} & -\frac{730N_f}{9}-\frac{127076}{81} & \frac{4N_f}{9}+\frac{8659}{81} & \frac{37N_f}{9}+\frac{13463}{54} & * \\
0 & 0 & 0 & 0 & 0 & 0 & 0 & 0 & \frac{74840}{243}-\frac{316N_f}{81} & -\frac{634N_f}{81}-\frac{222446}{243} & \frac{100N_f}{81}-\frac{13001}{243} & \frac{311N_f}{54}+\frac{59429}{648} & * \\
0 & 0 & 0 & 0 & 0 & 0 & 0 & 0 & 0 & 0 & 0 & 0 & \frac{623N_f}{108}-\frac{95}{9}
\end{pmatrix}. \quad \text{(A.15)}$$

The entries marked with an asterisk $*$ are unknown and not needed for the calculations in this thesis since they are $\mathcal{O}(\alpha_s^3)$ effects due to the mixing of the Wilson coefficient of the chromomagnetic operator into the other physical operator Wilson coefficients.

The sub-matrix that describes the mixing of the evanescent into physical Wilson coefficients at $\mathcal{O}(\alpha_s)$ is

$$Z_{QE}^{(1,1)} = \begin{pmatrix}
\frac{5}{12} & \frac{2}{9} & 0 & 0 & 0 & 0 & 0 & 0 & 0 & 0 & 0 & 0 & 0 & 0 & 0 & 0 & 0 & 0 & 0 & 0 \\
1 & 0 & 0 & 0 & 0 & 0 & 0 & 0 & 0 & 0 & 0 & 0 & 0 & 0 & 0 & 0 & 0 & 0 & 0 & 0 \\
0 & 0 & \frac{5}{12} & \frac{2}{9} & 0 & 0 & 0 & 0 & 0 & 0 & 0 & 0 & 0 & 0 & 0 & 0 & 0 & 0 & 0 & 0 \\
0 & 0 & 1 & 0 & 0 & 0 & 0 & 0 & 0 & 0 & 0 & 0 & 0 & 0 & 0 & 0 & 0 & 0 & 0 & 0 \\
0 & 0 & 0 & 0 & \frac{5}{12} & \frac{2}{9} & 0 & 0 & 0 & 0 & 0 & 0 & 0 & 0 & 0 & 0 & 0 & 0 & 0 & 0 \\
0 & 0 & 0 & 0 & 1 & 0 & 0 & 0 & 0 & 0 & 0 & 0 & 0 & 0 & 0 & 0 & 0 & 0 & 0 & 0 \\
0 & 0 & 0 & 0 & 0 & 0 & \frac{5}{12} & \frac{2}{9} & 0 & 0 & 0 & 0 & 0 & 0 & 0 & 0 & 0 & 0 & 0 & 0 \\
0 & 0 & 0 & 0 & 0 & 0 & 1 & 0 & 0 & 0 & 0 & 0 & 0 & 0 & 0 & 0 & 0 & 0 & 0 & 0 \\
0 & 0 & 0 & 0 & 0 & 0 & 0 & 0 & 0 & 0 & 0 & 0 & 0 & 0 & 0 & 0 & 0 & 0 & 0 & 0 \\
0 & 0 & 0 & 0 & 0 & 0 & 0 & 0 & 0 & 0 & 0 & 0 & 0 & 0 & 0 & 0 & 0 & 0 & 0 & 0 \\
0 & 0 & 0 & 0 & 0 & 0 & 0 & 0 & 0 & 1 & 0 & 0 & 0 & 0 & 0 & 0 & 0 & 0 & 0 & 0 \\
0 & 0 & 0 & 0 & 0 & 0 & 0 & 0 & \frac{2}{9} & \frac{5}{12} & 0 & 0 & 0 & 0 & 0 & 0 & 0 & 0 & 0 & 0 \\
0 & 0 & 0 & 0 & 0 & 0 & 0 & 0 & 0 & 0 & 0 & 0 & 0 & 0 & 0 & 0 & 0 & 0 & 0 & 0
\end{pmatrix}, \tag{A.16}$$

where the ordering of the evanescent operators is

$$\begin{aligned}\Big\{ & E_1^{(1)}, E_2^{(1)}, E_1^{(1),cu}, E_2^{(1),cu}, E_1^{(1),uc}, E_2^{(1),uc}, E_1^{(1),uu}, E_2^{(1),uu}, E_3^{(1)}, E_4^{(1)}, \\ & E_1^{(2)}, E_2^{(2)}, E_1^{(2),cu}, E_2^{(2),cu}, E_1^{(2),uc}, E_2^{(2),uc}, E_1^{(2),uu}, E_2^{(2),uu}, E_3^{(2)}, E_4^{(2)} \Big\}.\end{aligned} \tag{A.17}$$

At $\mathcal{O}(\alpha_s^2)$, the matrix is given by the matrices on the following page.

$$Z_{QE}^{(2,2)} = \begin{pmatrix}
\frac{5N_f}{36}-\frac{25}{6} & \frac{2N_f}{27}-\frac{31}{18} & 0 & 0 & 0 & 0 & 0 & 0 & 0 & 0 & \frac{19}{96} & \frac{5}{108} & 0 & 0 & 0 & 0 & 0 & 0 & 0 & 0 \\
\frac{N_f}{3}-\frac{31}{4} & 0 & 0 & 0 & 0 & 0 & 0 & 0 & 0 & 0 & \frac{5}{24} & \frac{1}{9} & 0 & 0 & 0 & 0 & 0 & 0 & 0 & 0 \\
0 & 0 & \frac{5N_f}{36}-\frac{25}{6} & \frac{2N_f}{27}-\frac{31}{18} & 0 & 0 & 0 & 0 & 0 & 0 & 0 & 0 & \frac{19}{96} & \frac{5}{108} & 0 & 0 & 0 & 0 & 0 & 0 \\
0 & 0 & \frac{N_f}{3}-\frac{31}{4} & 0 & 0 & 0 & 0 & 0 & 0 & 0 & 0 & 0 & \frac{5}{24} & \frac{1}{9} & 0 & 0 & 0 & 0 & 0 & 0 \\
0 & 0 & 0 & 0 & \frac{5N_f}{36}-\frac{25}{6} & \frac{2N_f}{27}-\frac{31}{18} & 0 & 0 & 0 & 0 & 0 & 0 & 0 & 0 & \frac{19}{96} & \frac{5}{108} & 0 & 0 & 0 & 0 \\
0 & 0 & 0 & 0 & \frac{N_f}{3}-\frac{31}{4} & 0 & 0 & 0 & 0 & 0 & 0 & 0 & 0 & 0 & \frac{5}{24} & \frac{1}{9} & 0 & 0 & 0 & 0 \\
0 & 0 & 0 & 0 & 0 & 0 & \frac{5N_f}{36}-\frac{25}{6} & \frac{2N_f}{27}-\frac{31}{18} & 0 & 0 & 0 & 0 & 0 & 0 & 0 & 0 & \frac{19}{96} & \frac{5}{108} & 0 & 0 \\
0 & 0 & 0 & 0 & 0 & 0 & \frac{N_f}{3}-\frac{31}{4} & 0 & 0 & 0 & 0 & 0 & 0 & 0 & 0 & 0 & \frac{5}{24} & \frac{1}{9} & 0 & 0 \\
0 & 0 & 0 & 0 & 0 & 0 & 0 & 0 & \frac{1}{9} & \frac{5}{24} & 0 & 0 & 0 & 0 & 0 & 0 & 0 & 0 & 0 & 0 \\
0 & 0 & 0 & 0 & 0 & 0 & 0 & 0 & \frac{5}{108} & \frac{19}{96} & 0 & 0 & 0 & 0 & 0 & 0 & 0 & 0 & 0 & 0 \\
0 & 0 & 0 & 0 & 0 & 0 & 0 & 0 & -\frac{4}{9} & \frac{N_f}{3}-\frac{5}{4} & 0 & 0 & 0 & 0 & 0 & 0 & 0 & 0 & \frac{1}{9} & \frac{5}{24} \\
0 & 0 & 0 & 0 & 0 & 0 & 0 & 0 & \frac{2N_f}{27}-\frac{77}{18} & \frac{5N_f}{36}-\frac{137}{72} & 0 & 0 & 0 & 0 & 0 & 0 & 0 & 0 & \frac{5}{108} & \frac{19}{96} \\
0 & 0 & 0 & 0 & 0 & 0 & 0 & 0 & 0 & 0 & 0 & 0 & 0 & 0 & 0 & 0 & 0 & 0 & 0 & 0
\end{pmatrix}, \quad \text{(A.18)}$$

$$Z_{QE}^{(2,1)} = \begin{pmatrix}
\frac{1531}{288}-\frac{5N_f}{216} & -\frac{N_f}{81}-\frac{1}{72} & 0 & 0 & 0 & 0 & 0 & 0 & 0 & 0 & \frac{1}{384} & -\frac{35}{864} & 0 & 0 & 0 & 0 & 0 & 0 & 0 & 0 \\
\frac{119}{16}-\frac{N_f}{18} & \frac{8}{9} & 0 & 0 & 0 & 0 & 0 & 0 & 0 & 0 & -\frac{35}{192} & -\frac{7}{72} & 0 & 0 & 0 & 0 & 0 & 0 & 0 & 0 \\
0 & 0 & \frac{1531}{288}-\frac{5N_f}{216} & -\frac{N_f}{81}-\frac{1}{72} & 0 & 0 & 0 & 0 & 0 & 0 & 0 & 0 & \frac{1}{384} & -\frac{35}{864} & 0 & 0 & 0 & 0 & 0 & 0 \\
0 & 0 & \frac{119}{16}-\frac{N_f}{18} & \frac{8}{9} & 0 & 0 & 0 & 0 & 0 & 0 & 0 & 0 & -\frac{35}{192} & -\frac{7}{72} & 0 & 0 & 0 & 0 & 0 & 0 \\
0 & 0 & 0 & 0 & \frac{1531}{288}-\frac{5N_f}{216} & -\frac{N_f}{81}-\frac{1}{72} & 0 & 0 & 0 & 0 & 0 & 0 & 0 & 0 & \frac{1}{384} & -\frac{35}{864} & 0 & 0 & 0 & 0 \\
0 & 0 & 0 & 0 & \frac{119}{16}-\frac{N_f}{18} & \frac{8}{9} & 0 & 0 & 0 & 0 & 0 & 0 & 0 & 0 & -\frac{35}{192} & -\frac{7}{72} & 0 & 0 & 0 & 0 \\
0 & 0 & 0 & 0 & 0 & 0 & \frac{1531}{288}-\frac{5N_f}{216} & -\frac{N_f}{81}-\frac{1}{72} & 0 & 0 & 0 & 0 & 0 & 0 & 0 & 0 & \frac{1}{384} & -\frac{35}{864} & 0 & 0 \\
0 & 0 & 0 & 0 & 0 & 0 & \frac{119}{16}-\frac{N_f}{18} & \frac{8}{9} & 0 & 0 & 0 & 0 & 0 & 0 & 0 & 0 & -\frac{35}{192} & -\frac{7}{72} & 0 & 0 \\
0 & 0 & 0 & 0 & 0 & 0 & 0 & 0 & -\frac{7}{72} & -\frac{35}{192} & 0 & 0 & 0 & 0 & 0 & 0 & 0 & 0 & 0 & 0 \\
0 & 0 & 0 & 0 & 0 & 0 & 0 & 0 & -\frac{35}{864} & \frac{1}{384} & 0 & 0 & 0 & 0 & 0 & 0 & 0 & 0 & 0 & 0 \\
0 & 0 & 0 & 0 & 0 & 0 & 0 & 0 & \frac{23}{18} & \frac{51}{4}-\frac{N_f}{18} & 0 & 0 & 0 & 0 & 0 & 0 & 0 & 0 & -\frac{7}{72} & -\frac{35}{192} \\
0 & 0 & 0 & 0 & 0 & 0 & 0 & 0 & \frac{7}{6}-\frac{N_f}{81} & \frac{317}{72}-\frac{5N_f}{216} & 0 & 0 & 0 & 0 & 0 & 0 & 0 & 0 & -\frac{35}{864} & \frac{1}{384} \\
0 & 0 & 0 & 0 & 0 & 0 & 0 & 0 & 0 & 0 & 0 & 0 & 0 & 0 & 0 & 0 & 0 & 0 & 0 & 0
\end{pmatrix}. \quad \text{(A.19)}$$

B Renormalisation Constants for the $|\Delta B| = 0$ Theory

The renormalisation constants which are needed to renormalise the Wilson coefficients of the physical operators up to NNLO are given below for $N_c = 3$ and with the $\mathcal{O}(\epsilon)$ constants in the definition of the evanescent operators kept arbitrary.

At $\mathcal{O}(\alpha_s)$, the renormalisation matrix in the parametrisation given in Eqs. (2.22) to (2.25) reads

$$Z_{QQ}^{(1,1)} = \begin{pmatrix} 0 & 6 & 0 & 0 \\ \frac{4}{3} & -2 & 0 & 0 \\ 0 & 0 & -8 & 0 \\ 0 & 0 & 0 & 1 \end{pmatrix} , \tag{B.1}$$

which agrees with the results found in the literature, see for example Ref. [57]. Note that the matrix indices correspond to the ordered list

$$\{Q, T, Q_S, T_S\} , \tag{B.2}$$

where the superscript q was dropped as the renormalisation constants do not depend on the external quark flavour. To $\mathcal{O}(\alpha_s^2)$, we require the additional renormalisation constants

$$Z_{QQ}^{(2,2)} = \begin{pmatrix} 4 & 2N_f - 39 & 0 & 0 \\ \frac{4N_f}{9} - \frac{26}{3} & 17 - \frac{2N_f}{3} & 0 & \\ 0 & 0 & 76 - \frac{8N_f}{3} & 0 \\ 0 & 0 & 0 & \frac{N_f}{3} - 5 \end{pmatrix} \tag{B.3}$$

and

$$Z_{QQ}^{(2,1)} = \begin{pmatrix} \frac{b-5}{9} & \frac{5b+650}{24} + \frac{N_f}{3} & 0 & 0 \\ \frac{5b-646}{108} + \frac{2N_f}{27} & \frac{19b+904}{96} - \frac{N_f}{9} & 0 & 0 \\ 0 & 0 & \frac{b_S-476}{9} + \frac{20N_f}{9} & \frac{5b_S-1318}{24} + 2N_f \\ 0 & 0 & \frac{5b_S+1274}{108} + \frac{4N_f}{9} & \frac{19b_S+2716}{96} - \frac{17N_f}{18} \end{pmatrix} . \tag{B.4}$$

The sub-matrix mixing the Wilson coefficients of the evanescent operators into the Wilson coefficients of the physical operators has the NLO contributions

$$Z_{QE}^{(1,1)} = \begin{pmatrix} 0 & -1 & 0 & 0 & 0 & 0 & 0 & 0 & 0 & 0 & 0 & 0 \\ -\frac{2}{9} & -\frac{5}{12} & 0 & 0 & 0 & 0 & 0 & 0 & 0 & 0 & 0 & 0 \\ 0 & 0 & 0 & -1 & 0 & 0 & 0 & 0 & 0 & 0 & 0 & 0 \\ 0 & 0 & -\frac{2}{9} & -\frac{5}{12} & 0 & 0 & 0 & 0 & 0 & 0 & 0 & 0 \end{pmatrix}, \tag{B.5}$$

where the ordering of the evanescent operators corresponds to

$$\begin{aligned} &\left\{E^{(1)}[Q],\, E^{(1)}[T],\, E^{(1)}[Q_S],\, E^{(1)}[T_S],\right. \\ &\left.\quad E^{(2)}[Q],\, E^{(2)}[T],\, E^{(2)}[Q_S],\, E^{(2)}[T_S]\right\}, \end{aligned} \tag{B.6}$$

and only the first generation matters for the renormalisation of the physical operators. For the NNLO contributions, the second generation becomes relevant, and the renormalisation constants are

$$Z_{QE}^{(2,2)} = \begin{pmatrix} -\frac{20}{9} & \frac{43}{12} - \frac{N_f}{3} & 0 & 0 & \frac{1}{9} & \frac{5}{24} & 0 & 0 \\ \frac{43}{54} - \frac{2N_f}{27} & \frac{5}{24} - \frac{5N_f}{36} & 0 & 0 & \frac{5}{108} & \frac{19}{96} & 0 & 0 \\ 0 & 0 & -\frac{16}{9} & \frac{28}{3} - \frac{N_f}{3} & 0 & 0 & \frac{1}{9} & \frac{5}{24} \\ 0 & 0 & \frac{2}{27} - \frac{2N_f}{27} & \frac{17}{72} - \frac{5N_f}{36} & 0 & 0 & \frac{5}{108} & \frac{19}{96} \end{pmatrix} \tag{B.7}$$

and

$$Z_{QE}^{(2,1)} = \begin{pmatrix} \frac{83}{18} & \frac{N_f}{18} + \frac{23}{8} & 0 & 0 & -\frac{7}{72} & -\frac{35}{192} & 0 & 0 \\ \frac{N_f}{81} + \frac{83}{36} & \frac{5N_f}{216} + \frac{139}{144} & 0 & 0 & -\frac{35}{864} & \frac{1}{384} & 0 & 0 \\ 0 & 0 & \frac{38}{9} & \frac{N_f}{18} + 1 & 0 & 0 & -\frac{7}{72} & -\frac{35}{192} \\ 0 & 0 & \frac{N_f}{81} + \frac{17}{9} & \frac{5N_f}{216} + \frac{173}{144} & 0 & 0 & -\frac{35}{864} & \frac{1}{384} \end{pmatrix}. \tag{B.8}$$

For the renormalisation of the evanescent operators, we will have to consider the set of operators up to third generation,

$$\begin{aligned} &\left\{E^{(1)}[Q],\, E^{(1)}[T],\, E^{(1)}[Q_S],\, E^{(1)}[T_S], E^{(2)}[Q],\, E^{(2)}[T],\, E^{(2)}[Q_S],\, E^{(2)}[T_S]\right. \\ &\left.\quad E^{(3)}[Q],\, E^{(3)}[T],\, E^{(3)}[Q_S],\, E^{(3)}[T_S]\right\}, \end{aligned} \tag{B.9}$$

as the first generation evanescent operators need to be renormalised to NNLO and the second generation to NLO for the matching of the $|\Delta B| = 0$ transition operator. Focusing on the corresponding rows for the first and second generation only, the relevant off-diagonal

sub-matrix at $\mathcal{O}(\alpha_s)$ is

$$Z_{EQ}^{(1,0)} = \begin{pmatrix} 64 & -b-16 & 0 & 0 \\ -\frac{2b}{9}-\frac{32}{9} & -\frac{5b}{12}-\frac{152}{3} & 0 & 0 \\ 0 & 0 & -64 & -b_S-112 \\ 0 & 0 & -\frac{2b_S}{9}-\frac{224}{9} & -\frac{5b_S}{12}-\frac{8}{3} \\ -\frac{64b}{3}-\frac{2560}{3} & -12b-e-768 & 0 & 0 \\ -\frac{24b+2e}{9}-\frac{512}{3} & \frac{29b}{3}-\frac{5e}{12}+\frac{800}{3} & 0 & 0 \\ 0 & 0 & -512 & 4b_S-e_S-512 \\ 0 & 0 & \frac{8b_S-2e_S}{9}-\frac{1024}{9} & \frac{20b_S-5e_S}{12}+\frac{416}{3} \end{pmatrix}, \tag{B.10}$$

and at $\mathcal{O}(\alpha_s^2)$ only the first generation rows need to be considered, which are given on the next page.

$$Z_{EQ}^{(2,1)} = \begin{pmatrix} -\frac{8b}{9}+\frac{e}{9}+\frac{64N_f}{3}-\frac{2720}{9} & -\frac{bN_f}{3}-\frac{5b}{4}+\frac{5e}{24}-\frac{16N_f}{3}-192 & 0 & 0 \\ -\frac{2bN_f}{27}+\frac{67b}{18}+\frac{5e}{108}-\frac{32N_f}{27}+\frac{640}{3} & -\frac{5bN_f}{36}-\frac{17b}{36}+\frac{19e}{96}-\frac{152N_f}{9}+\frac{2608}{9} & 0 & 0 \\ 0 & 0 & -\frac{20b_S}{9}+\frac{e_S}{9}-\frac{64N_f}{3}+\frac{3424}{9} & -\frac{b_SN_f}{3}-\frac{b_S}{2}+\frac{5e_S}{24}-\frac{112N_f}{3}+320 \\ 0 & 0 & -\frac{2b_SN_f}{27}+\frac{17b_S}{9}+\frac{5e_S}{108}-\frac{224N_f}{27}+\frac{1792}{9} & -\frac{5b_SN_f}{36}-\frac{5b_S}{9}+\frac{19e_S}{96}-\frac{8N_f}{9}-\frac{1424}{9} \end{pmatrix}, \tag{B.11}$$

$$Z_{EQ}^{(2,0)} = \begin{pmatrix} Z_1 & Z_2 \end{pmatrix}, \tag{B.12}$$

where

$$Z_1 = \begin{pmatrix} -\frac{272a}{9}+\frac{7b}{9}+\frac{4c}{9}-\frac{7e}{72}+\frac{f}{9}+\frac{32N_f}{9}+\frac{1600}{3} & \frac{8aN_f}{3}+64a+\frac{bN_f}{18}-\frac{427b}{48}-\frac{cN_f}{3}-\frac{13c}{4}-\frac{35e}{192}+\frac{5f}{24}+\frac{248N_f}{9}-\frac{3214}{3} \\ \frac{16aN_f}{27}-\frac{664a}{9}+\frac{bN_f}{81}-\frac{67b}{216}-\frac{2cN_f}{27}+\frac{77c}{18}-\frac{35e}{864}+\frac{5f}{108}+\frac{496N_f}{81}-\frac{1820}{27} & \frac{10aN_f}{9}-\frac{199a}{18}+\frac{5bN_f}{216}-\frac{821b}{288}-\frac{5cN_f}{36}+\frac{c}{36}+\frac{e}{384}+\frac{19f}{96}+\frac{244N_f}{27}-\frac{2561}{9} \\ 0 & 0 \\ 0 & 0 \end{pmatrix}, \tag{B.13}$$

and

$$Z_2 = \begin{pmatrix} 0 & 0 \\ 0 & 0 \\ \frac{32a_SN_f}{9}+\frac{32a_S}{3}+\frac{35b_S}{18}-\frac{20c_S}{9}-\frac{7e_S}{72}+\frac{f_S}{9}+\frac{224N_f}{9}-\frac{4592}{9} & \frac{16a_SN_f}{3}-\frac{154a_S}{3}+\frac{b_SN_f}{18}-\frac{157b_S}{48}-\frac{c_SN_f}{3}+\frac{c_S}{2}-\frac{35e_S}{192}+\frac{5f_S}{24}+\frac{392N_f}{9}-\frac{2662}{3} \\ \frac{32a_SN_f}{27}-\frac{308a_S}{27}+\frac{b_SN_f}{81}+\frac{203b_S}{216}-\frac{2c_SN_f}{27}+\frac{c_S}{9}-\frac{35e_S}{864}+\frac{5f_S}{108}+\frac{784N_f}{81}-\frac{2444}{27} & -\frac{2a_SN_f}{9}+\frac{509a_S}{18}+\frac{5b_SN_f}{216}-\frac{1025b_S}{288}-\frac{5c_SN_f}{36}-\frac{5c_S}{36}+\frac{e_S}{384}+\frac{19f_S}{96}+\frac{28N_f}{27}-\frac{1543}{9} \end{pmatrix}. \tag{B.14}$$

The renormalisation constants for the mixing between the evanescent operators are needed for the renormalisation of the first and second generation operators to $\mathcal{O}(\alpha_s)$, and the corresponding rows in the final sub-matrix are

$$Z_{EE}^{(1,1)} = \begin{pmatrix} 0 & 14 & 0 & 0 & 0 & -1 & 0 & 0 & 0 & 0 & 0 & 0 \\ \frac{28}{9} & \frac{4}{3} & 0 & 0 & -\frac{2}{9} & -\frac{5}{12} & 0 & 0 & 0 & 0 & 0 & 0 \\ 0 & 0 & \frac{8}{3} & 16 & 0 & 0 & 0 & -1 & 0 & 0 & 0 & 0 \\ 0 & 0 & \frac{32}{9} & \frac{1}{3} & 0 & 0 & -\frac{2}{9} & -\frac{5}{12} & 0 & 0 & 0 & 0 \\ \frac{1280}{3} & 336 & 0 & 0 & -\frac{64}{3} & -6 & 0 & 0 & 0 & -1 & 0 & 0 \\ \frac{224}{3} & -\frac{460}{3} & 0 & 0 & -\frac{4}{3} & \frac{23}{3} & 0 & 0 & -\frac{2}{9} & -\frac{5}{12} & 0 & 0 \\ 0 & 0 & \frac{512}{3} & 144 & 0 & 0 & -8 & 4 & 0 & 0 & 0 & -1 \\ 0 & 0 & 32 & -\frac{172}{3} & 0 & 0 & \frac{8}{9} & \frac{8}{3} & 0 & 0 & -\frac{2}{9} & -\frac{5}{12} \end{pmatrix}, \tag{B.15}$$

and at $\mathcal{O}(\alpha_s^2)$ only the renormalisation constants for the first generation are needed, which are presented on the next page.

$$Z_{EE}^{(2,2)} = \begin{pmatrix} -\frac{140}{9} & \frac{14N_f}{3}+9 & 0 & 0 & -\frac{8}{9} & -\frac{N_f}{3}-\frac{5}{4} & 0 & 0 & \frac{1}{9} & \frac{5}{24} & 0 & 0 \\ \frac{28N_f}{27}-78 & \frac{4N_f}{9}+\frac{179}{18} & 0 & 0 & \frac{67}{18}-\frac{2N_f}{27} & -\frac{5N_f}{36}-\frac{17}{36} & 0 & 0 & \frac{5}{108} & \frac{19}{96} & 0 & 0 \\ 0 & 0 & \frac{8N_f}{9}+\frac{4}{3} & \frac{16N_f}{3}-\frac{106}{3} & 0 & 0 & -\frac{20}{9} & -\frac{N_f}{3}-\frac{1}{2} & 0 & 0 & \frac{1}{9} & \frac{5}{24} \\ 0 & 0 & \frac{32N_f}{27}-\frac{1076}{27} & \frac{N_f}{9}+\frac{407}{18} & 0 & 0 & \frac{17}{9}-\frac{2N_f}{27} & -\frac{5N_f}{36}-\frac{5}{9} & 0 & 0 & \frac{5}{108} & \frac{19}{96} \end{pmatrix}, \tag{B.16}$$

$$Z_{EE}^{(2,1)} = \begin{pmatrix} 93-\frac{32N_f}{9} & \frac{293}{3}-\frac{73N_f}{9} & 0 & 0 & \frac{7}{9} & \frac{N_f}{18}-\frac{427}{48} & 0 & 0 & -\frac{7}{72} & -\frac{35}{192} & 0 & 0 \\ \frac{3358}{27}-\frac{146N_f}{81} & \frac{1751}{72}-\frac{32N_f}{27} & 0 & 0 & \frac{N_f}{81}-\frac{67}{216} & \frac{5N_f}{216}-\frac{821}{288} & 0 & 0 & -\frac{35}{864} & \frac{1}{384} & 0 & 0 \\ 0 & 0 & \frac{346}{9}-\frac{52N_f}{27} & \frac{340}{3}-\frac{62N_f}{9} & 0 & 0 & \frac{35}{18} & \frac{N_f}{18}-\frac{157}{48} & 0 & 0 & -\frac{7}{72} & -\frac{35}{192} \\ 0 & 0 & \frac{1256}{27}-\frac{124N_f}{81} & \frac{521}{12}-\frac{97N_f}{54} & 0 & 0 & \frac{N_f}{81}+\frac{203}{216} & \frac{5N_f}{216}-\frac{1025}{288} & 0 & 0 & -\frac{35}{864} & \frac{1}{384} \end{pmatrix}. \tag{B.17}$$

C Derivation of Fierz Identities

Fierz identities are used in four dimensions to decompose bilinear spinor covariants in terms of independent basis elements and are therefore required to determine the linear combination of spinors such that evanescent operators are $\mathcal{O}(\epsilon)$. In this appendix, a derivation of such Fierz identities is presented, following Ref. [72]. We first derive the general Fierz identity and then apply it to prove the example relation

$$(P_R)_{\alpha\beta}(P_R)_{\gamma\delta} = \frac{1}{8}(\sigma^{\mu\nu}P_R)_{\alpha\delta}(\sigma_{\mu\nu}P_R)_{\gamma\beta} + \frac{1}{2}(P_R)_{\alpha\delta}(P_R)_{\gamma\beta}\,. \tag{C.1}$$

The general Fierz identity can be derived directly from the completeness relation of the Dirac algebra in four dimensions. For chiral relations it is most convenient to work with a basis of bilinears spanned by $\Gamma^A \otimes \Gamma_A$, where

$$\begin{aligned}\Gamma^A &\in \left\{P_R, P_L, P_R\,\gamma^\mu, P_L\,\gamma^\mu, \sigma^{\mu\nu}\right\},\\ \Gamma_A &\in \left\{P_R, P_L, \gamma_\mu\,P_R, \gamma_\mu\,P_L, \frac{1}{2}\sigma_{\mu\nu}\right\}.\end{aligned} \tag{C.2}$$

Note that the dual elements with lowered indices have lowered Lorentz indices, a different ordering of the chirality projectors and a factor of $1/2$ for the last element. This is to preserve the normalisation of the inner product, which is defined as

$$\left\langle \Gamma^A, \Gamma_B \right\rangle \equiv \frac{1}{2}\mathsf{Tr}\left(\Gamma^A\,\Gamma_B\right) \stackrel{!}{=} \delta^A_B\,. \tag{C.3}$$

Equipped with the basis definitions in Eq. (C.2), we can write down a general Fierz relation for any two basis elements as

$$\Gamma^A \otimes \Gamma^B = \sum_{C,D} C^{AB}_{CD}\,\Gamma^C \,\widetilde{\otimes}\, \Gamma^D\,, \tag{C.4}$$

where the tilde serves as a shorthand notation for the fact that the spinor indices on the spin lines have been swapped. Explicitly with the spinor indices shown, this relation reads

$$\left(\Gamma^A\right)_{\alpha\beta}\left(\Gamma^B\right)_{\gamma\delta} = \sum_{C,D} C^{AB}_{CD}\,\left(\Gamma^C\right)_{\alpha\delta}\left(\Gamma^D\right)_{\gamma\beta}\,. \tag{C.5}$$

The coefficients C^{AB}_{CD} can be determined by multiplying with

$$\left(\Gamma_E\right)_{\delta\alpha}\left(\Gamma_F\right)_{\beta\gamma}\,, \tag{C.6}$$

and using the definition of the inner product Eq. (C.3), which leads to

$$C_{EF}^{AB} = \frac{1}{4}\,\mathrm{Tr}\left(\Gamma_E\,\Gamma^A\,\Gamma_F\,\Gamma^B\right)\,. \tag{C.7}$$

Together with Eq. (C.4), this completes the general Fierz identity, which is used in this thesis to obtain vanishing finite parts in the evanescent operators.

To prove Eq. (C.1), one can start by applying the general Fierz relation from Eqs. (C.4) and (C.7) to the first term on the right-hand side, which yields

$$\begin{aligned}(\sigma^{\mu\nu}P_R)_{\alpha\delta}\,\left(\sigma_{\mu\nu}P_R\right)_{\gamma\beta} = 6\,(P_R)_{\alpha\delta}\,(P_R)_{\gamma\beta} - (\sigma^{\mu\nu})_{\alpha_\delta}\,\left(\sigma_{\mu\nu}\right)_{\gamma\beta}\\ -\frac{1}{2}\,(\sigma^{\mu_1\mu_2})_{\alpha_\delta}\,(\sigma^{\mu_3\mu_4})_{\gamma\beta}\,\epsilon_{\mu_1\mu_3\mu_2\mu_4}\,.\end{aligned} \tag{C.8}$$

Applying the general Fierz identity to the second term in Eq. (C.1) leads to

$$\begin{aligned}(P_R)_{\alpha\delta}\,(P_R)_{\gamma\beta} = \frac{1}{2}\,(P_R)_{\alpha\delta}\,(P_R)_{\gamma\beta} + \frac{1}{4}\,(\sigma^{\mu\nu})_{\alpha_\delta}\,\left(\sigma_{\mu\nu}\right)_{\gamma\beta}\\ +\frac{1}{8}\,(\sigma^{\mu_1\mu_2})_{\alpha_\delta}\,(\sigma^{\mu_3\mu_4})_{\gamma\beta}\,\epsilon_{\mu_1\mu_3\mu_2\mu_4}\,,\end{aligned} \tag{C.9}$$

which can be added to Eq. (C.8) with a factor of 4 to give the desired result stated in Eq. (C.1).

D Basis Elements of the Spinor Vector Spaces

When applying the projectors introduced in Section 3.3, we make use of an appropriate subset of the basis elements listed below. As outlined earlier, three distinct cases must be treated separately:

(i) The first spin line is longer while the second spin line has length n. In this case, we select a basis comprising all elements with up to n total γ matrices on each spin line, together with the structure containing an additional slashed momentum on the first spin line in addition to the n pure γ matrices; that is, we include all elements up to and including $B_{4(n+1)-2}$.

(ii) The second spin line is longer, or both spin lines have equal length, with the first spin line containing n total γ matrices. Here, the basis includes all elements with up to n total γ matrices on each spin line, as well as the structure with an extra slashed momentum on the second spin line in addition to the n pure γ matrices; that is, we include all elements up to and including $B_{4(n+1)-1}$ but omit $B_{4(n+1)-2}$.

(iii) Both spin lines have length eleven and contain at least one slashed momentum. This represents the most complex structure that must be resolved. To avoid excessively long traces, we employ a specialised basis that includes all elements up to and including B_{45} (generally $B_{4(n+1)+1}$, where n denotes the maximum number of pure γ matrices), while excluding B_{43} ($B_{4(n+1)-1}$ in general). Although B_{42} (corresponding to $B_{4(n+1)-2}$ in the general case) is not required for the projection itself, it must be retained to ensure the invertibility of the Gram matrix. This complication arises because the bilinear map ϕ_p introduced in Section 3.3.3 is not positive-definite.

When dealing with tadpole integrals, for example in the calculation of renormalisation amplitudes, the basis is simplified significantly. Only the basis elements B_{4k+1} are needed, where k takes values from zero up to the number of γ matrices on the shorter of the two spin lines.

The explicit definition of the basis elements is:

$$
\begin{aligned}
B_1 &= \mathbb{1} \otimes \mathbb{1}\,, & B_2 &= \not{e}_q \otimes \mathbb{1}\,,\\
B_3 &= \mathbb{1} \otimes \not{e}_q\,, & B_4 &= \not{e}_q \otimes \not{e}_q\,,\\
B_5 &= \gamma_{\mu_1} \otimes \gamma^{\mu_1}\,, & B_6 &= \gamma_{\mu_1}\not{e}_q \otimes \gamma^{\mu_1}\,,\\
B_7 &= \gamma_{\mu_1} \otimes \gamma^{\mu_1}\not{e}_q\,, & B_8 &= \gamma_{\mu_1}\not{e}_q \otimes \gamma^{\mu_1}\not{e}_q\,,\\
B_9 &= \gamma_{\mu_1}\gamma_{\mu_2} \otimes \gamma^{\mu_2}\gamma^{\mu_1}\,, & B_{10} &= \gamma_{\mu_1}\gamma_{\mu_2}\not{e}_q \otimes \gamma^{\mu_2}\gamma^{\mu_1}\,,\\
B_{11} &= \gamma_{\mu_1}\gamma_{\mu_2} \otimes \gamma^{\mu_2}\gamma^{\mu_1}\not{e}_q\,, & B_{12} &= \gamma_{\mu_1}\gamma_{\mu_2}\not{e}_q \otimes \gamma^{\mu_2}\gamma^{\mu_1}\not{e}_q\,,\\
B_{13} &= \gamma_{\mu_1}\dots\gamma_{\mu_3} \otimes \gamma^{\mu_3}\dots\gamma^{\mu_1}\,, & B_{14} &= \gamma_{\mu_1}\dots\gamma_{\mu_3}\not{e}_q \otimes \gamma^{\mu_3}\dots\gamma^{\mu_1}\,,\\
B_{15} &= \gamma_{\mu_1}\dots\gamma_{\mu_3} \otimes \gamma^{\mu_3}\dots\gamma^{\mu_1}\not{e}_q\,, & B_{16} &= \gamma_{\mu_1}\dots\gamma_{\mu_3}\not{e}_q \otimes \gamma^{\mu_3}\dots\gamma^{\mu_1}\not{e}_q\,,\\
B_{17} &= \gamma_{\mu_1}\dots\gamma_{\mu_4} \otimes \gamma^{\mu_4}\dots\gamma^{\mu_1}\,, & B_{18} &= \gamma_{\mu_1}\dots\gamma_{\mu_4}\not{e}_q \otimes \gamma^{\mu_4}\dots\gamma^{\mu_1}\,,\\
B_{19} &= \gamma_{\mu_1}\dots\gamma_{\mu_4} \otimes \gamma^{\mu_4}\dots\gamma^{\mu_1}\not{e}_q\,, & B_{20} &= \gamma_{\mu_1}\dots\gamma_{\mu_4}\not{e}_q \otimes \gamma^{\mu_4}\dots\gamma^{\mu_1}\not{e}_q\,,\\
B_{21} &= \gamma_{\mu_1}\dots\gamma_{\mu_5} \otimes \gamma^{\mu_5}\dots\gamma^{\mu_1}\,, & B_{22} &= \gamma_{\mu_1}\dots\gamma_{\mu_5}\not{e}_q \otimes \gamma^{\mu_5}\dots\gamma^{\mu_1}\,,\\
B_{23} &= \gamma_{\mu_1}\dots\gamma_{\mu_5} \otimes \gamma^{\mu_5}\dots\gamma^{\mu_1}\not{e}_q\,, & B_{24} &= \gamma_{\mu_1}\dots\gamma_{\mu_5}\not{e}_q \otimes \gamma^{\mu_5}\dots\gamma^{\mu_1}\not{e}_q\,,\\
B_{25} &= \gamma_{\mu_1}\dots\gamma_{\mu_6} \otimes \gamma^{\mu_6}\dots\gamma^{\mu_1}\,, & B_{26} &= \gamma_{\mu_1}\dots\gamma_{\mu_6}\not{e}_q \otimes \gamma^{\mu_6}\dots\gamma^{\mu_1}\,,\\
B_{27} &= \gamma_{\mu_1}\dots\gamma_{\mu_6} \otimes \gamma^{\mu_6}\dots\gamma^{\mu_1}\not{e}_q\,, & B_{28} &= \gamma_{\mu_1}\dots\gamma_{\mu_6}\not{e}_q \otimes \gamma^{\mu_6}\dots\gamma^{\mu_1}\not{e}_q\,,\\
B_{29} &= \gamma_{\mu_1}\dots\gamma_{\mu_7} \otimes \gamma^{\mu_7}\dots\gamma^{\mu_1}\,, & B_{30} &= \gamma_{\mu_1}\dots\gamma_{\mu_7}\not{e}_q \otimes \gamma^{\mu_7}\dots\gamma^{\mu_1}\,,\\
B_{31} &= \gamma_{\mu_1}\dots\gamma_{\mu_7} \otimes \gamma^{\mu_7}\dots\gamma^{\mu_1}\not{e}_q\,, & B_{32} &= \gamma_{\mu_1}\dots\gamma_{\mu_7}\not{e}_q \otimes \gamma^{\mu_7}\dots\gamma^{\mu_1}\not{e}_q\\
B_{33} &= \gamma_{\mu_1}\dots\gamma_{\mu_8} \otimes \gamma^{\mu_8}\dots\gamma^{\mu_1}\,, & B_{34} &= \gamma_{\mu_1}\dots\gamma_{\mu_8}\not{e}_q \otimes \gamma^{\mu_8}\dots\gamma^{\mu_1}\,,\\
B_{35} &= \gamma_{\mu_1}\dots\gamma_{\mu_8} \otimes \gamma^{\mu_8}\dots\gamma^{\mu_1}\not{e}_q\,, & B_{36} &= \gamma_{\mu_1}\dots\gamma_{\mu_8}\not{e}_q \otimes \gamma^{\mu_8}\dots\gamma^{\mu_1}\not{e}_q\,,\\
B_{37} &= \gamma_{\mu_1}\dots\gamma_{\mu_9} \otimes \gamma^{\mu_9}\dots\gamma^{\mu_1}\,, & B_{38} &= \gamma_{\mu_1}\dots\gamma_{\mu_9}\not{e}_q \otimes \gamma^{\mu_9}\dots\gamma^{\mu_1}\,,\\
B_{39} &= \gamma_{\mu_1}\dots\gamma_{\mu_9} \otimes \gamma^{\mu_9}\dots\gamma^{\mu_1}\not{e}_q\,, & B_{40} &= \gamma_{\mu_1}\dots\gamma_{\mu_9}\not{e}_q \otimes \gamma^{\mu_9}\dots\gamma^{\mu_1}\not{e}_q\,,\\
B_{41} &= \gamma_{\mu_1}\dots\gamma_{\mu_{10}} \otimes \gamma^{\mu_{10}}\dots\gamma^{\mu_1}\,, & B_{42} &= \gamma_{\mu_1}\dots\gamma_{\mu_{10}}\not{e}_q \otimes \gamma^{\mu_{10}}\dots\gamma^{\mu_1}\,,\\
B_{43} &= \gamma_{\mu_1}\dots\gamma_{\mu_{10}} \otimes \gamma^{\mu_{10}}\dots\gamma^{\mu_1}\not{e}_q\,, & B_{44} &= \gamma_{\mu_1}\dots\gamma_{\mu_{10}}\not{e}_q \otimes \gamma^{\mu_{10}}\dots\gamma^{\mu_1}\not{e}_q\,,\\
B_{45} &= \gamma_{\mu_1}\dots\gamma_{\mu_{11}} \otimes \gamma^{\mu_{11}}\dots\gamma^{\mu_1}\,. & & \qquad\qquad (D.1)
\end{aligned}
$$

Here, the normalised external momentum

$$\not{e}_q \equiv \frac{\not{q}}{\sqrt{q^2}} \qquad (D.2)$$

was used.

E Individual Uncertainty Sources of *B* Meson Mixing Observables

To show the impact of all input values used in the calculation of $\Delta\Gamma/\Delta M$, a_{fs} and r_{ds} in Chapter 4, we give the individual contributions from each input variable in Tab. E.1 in the $\overline{\text{MS}}$ scheme.

Parameter	$\Delta\Gamma_s/\Delta M_s$	$\Delta\Gamma_d/\Delta M_d$	a_{fs}^s	a_{fs}^d	r_{ds}
$\alpha_s(M_Z)$	5.04×10^{-6}	3.08×10^{-6}	1.85×10^{-7}	4.22×10^{-6}	2.12×10^{-4}
M_W	2.40×10^{-7}	2.31×10^{-7}	1.40×10^{-7}	3.19×10^{-8}	1.25×10^{-7}
M_Z	2.30×10^{-9}	1.41×10^{-9}	8.44×10^{-11}	1.93×10^{-9}	9.66×10^{-8}
m_t^{OS}	2.74×10^{-5}	2.64×10^{-5}	1.38×10^{-7}	3.15×10^{-6}	1.17×10^{-7}
$\overline{m}_b(\overline{m}_b)$	4.02×10^{-5}	3.92×10^{-5}	7.96×10^{-8}	1.81×10^{-6}	9.64×10^{-5}
$\overline{m}_c(3\,\text{GeV})$	2.08×10^{-5}	2.09×10^{-5}	4.11×10^{-7}	9.38×10^{-6}	1.89×10^{-4}
f_{B_s}/f_{B_d}	0	0	0	0	2.23×10^{-3}
ξ	0	0	0	0	2.29×10^{-4}
ξ_S	0	0	0	0	1.12×10^{-2}
ζ	0	0	0	0	3.50×10^{-2}
B_{B_s}	7.38×10^{-6}	0	8.95×10^{-8}	0	1.24×10^{-3}
B_{B_d}	0	1.97×10^{-6}	0	2.43×10^{-6}	0
$\widetilde{B}_{S,B_s}$	1.17×10^{-4}	0	6.83×10^{-8}	0	1.00×10^{-3}
$\widetilde{B}_{S,B_d}$	0	1.12×10^{-4}	0	1.58×10^{-6}	0
B_{R_0}	2.27×10^{-4}	2.50×10^{-4}	7.44×10^{-8}	1.89×10^{-6}	2.23×10^{-3}
B_{R_1}	7.35×10^{-6}	0	2.41×10^{-9}	0	7.20×10^{-5}
$B_{\widetilde{R}_1}$	1.15×10^{-5}	0	3.77×10^{-9}	0	1.13×10^{-4}
$B_{\widetilde{R}_2}$	7.49×10^{-4}	7.55×10^{-4}	2.04×10^{-8}	4.83×10^{-7}	7.55×10^{-3}
B_{R_3}	1.11×10^{-5}	1.11×10^{-5}	2.38×10^{-7}	5.53×10^{-6}	9.63×10^{-5}
$B_{\widetilde{R}_3}$	2.63×10^{-5}	2.64×10^{-5}	5.65×10^{-7}	1.31×10^{-5}	2.29×10^{-4}
$\text{Re}(\lambda_u^s/\lambda_t^s)$	5.18×10^{-7}	0	3.62×10^{-10}	0	1.12×10^{-4}
$\text{Im}(\lambda_u^s/\lambda_t^s)$	3.20×10^{-10}	0	4.58×10^{-7}	0	6.94×10^{-8}
$\text{Re}(\lambda_u^d/\lambda_t^d)$	0	1.28×10^{-5}	0	2.04×10^{-7}	2.88×10^{-3}
$\text{Im}(\lambda_u^d/\lambda_t^d)$	0	1.74×10^{-7}	0	1.09×10^{-5}	3.91×10^{-5}

Table E.1: Uncertainties from individual input parameters in the $\overline{\text{MS}}$ scheme.

F Double Ratio Without Explicit $SU(3)_F$ Breaking

We present the results obtained for the double ratio $(\Delta\Gamma_d/\Delta M_d)/(\Delta\Gamma_s/\Delta M_s)$ from Section 4.5 using the same input parameters as for the calculations carried out in the B_s and B_d systems separately:

$$
\begin{aligned}
r_{ds} &= 0.963^{+0.010}_{-0.014\,\text{scale, comb.}} \pm 0.039_{B\widetilde{B}_S} \pm 0.085_{1/m_b} \pm 0.003_{\text{input}}\ (\text{pole})\,, \\
r_{ds} &= 0.965^{+0.008}_{-0.008\,\text{scale, comb.}} \pm 0.037_{B\widetilde{B}_S} \pm 0.076_{1/m_b} \pm 0.003_{\text{input}}\ (\overline{\text{MS}})\,, \\
r_{ds} &= 0.964^{+0.009}_{-0.010\,\text{scale, comb.}} \pm 0.037_{B\widetilde{B}_S} \pm 0.076_{1/m_b} \pm 0.003_{\text{input}}\ (\text{PS})\,. \qquad \text{(F.1)}
\end{aligned}
$$

To be explicit, we do not make use of the more accurately determined ratios of the bag parameters of the leading-power matrix elements or the decay constants. However, we also do not need to introduce a parametrisation of the $SU(3)_F$-breaking effects in the Λ_{QCD}/m_b-suppressed matrix elements.

Bibliography

[1] S. L. Glashow. "Partial Symmetries of Weak Interactions". In: *Nucl. Phys.* 22 (1961), pp. 579–588. DOI: 10.1016/0029-5582(61)90469-2.

[2] Abdus Salam. "Weak and Electromagnetic Interactions". In: *Conf. Proc. C* 680519 (1968), pp. 367–377. DOI: 10.1142/9789812795915_0034.

[3] Steven Weinberg. "A Model of Leptons". In: *Phys. Rev. Lett.* 19 (1967), pp. 1264–1266. DOI: 10.1103/PhysRevLett.19.1264.

[4] H. Fritzsch, Murray Gell-Mann, and H. Leutwyler. "Advantages of the Color Octet Gluon Picture". In: *Phys. Lett. B* 47 (1973), pp. 365–368. DOI: 10.1016/0370-2693(73)90625-4.

[5] David J. Gross and Frank Wilczek. "Ultraviolet Behavior of Nonabelian Gauge Theories". In: *Phys. Rev. Lett.* 30 (1973). Ed. by J. C. Taylor, pp. 1343–1346. DOI: 10.1103/PhysRevLett.30.1343.

[6] H. David Politzer. "Reliable Perturbative Results for Strong Interactions?" In: *Phys. Rev. Lett.* 30 (1973). Ed. by J. C. Taylor, pp. 1346–1349. DOI: 10.1103/PhysRevLett.30.1346.

[7] Nora Brambilla et al. "The *XYZ* states: experimental and theoretical status and perspectives". In: *Phys. Rept.* 873 (2020), pp. 1–154. DOI: 10.1016/j.physrep.2020.05.001. arXiv: 1907.07583 [hep-ex].

[8] S. W. Herb et al. "Observation of a Dimuon Resonance at 9.5 GeV in 400 GeV Proton-Nucleus Collisions". In: *Phys. Rev. Lett.* 39 (1977), pp. 252–255. DOI: 10.1103/PhysRevLett.39.252.

[9] F. Abe et al. "The CDF Detector: An Overview". In: *Nucl. Instrum. Meth. A* 271 (1988), pp. 387–403. DOI: 10.1016/0168-9002(88)90298-7.

[10] A. J. Bevan et al. "The Physics of the B Factories". In: *Eur. Phys. J. C* 74 (2014), p. 3026. DOI: 10.1140/epjc/s10052-014-3026-9. arXiv: 1406.6311 [hep-ex].

[11] W. Altmannshofer et al. "The Belle II Physics Book". In: *PTEP* 2019.12 (2019). Ed. by E. Kou and P. Urquijo. [Erratum: PTEP 2020, 029201 (2020)], p. 123C01. DOI: 10.1093/ptep/ptz106. arXiv: 1808.10567 [hep-ex].

[12] A. Augusto Alves Jr. et al. "The LHCb Detector at the LHC". In: *JINST* 3 (2008), S08005. DOI: 10.1088/1748-0221/3/08/S08005.

[13] A. Abulencia et al. "Observation of $B_s^0 - \bar{B}_s^0$ Oscillations". In: *Phys. Rev. Lett.* 97 (2006), p. 242003. DOI: 10.1103/PhysRevLett.97.242003. arXiv: hep-ex/0609040.

[14] V. Weisskopf and Eugene P. Wigner. "Calculation of the natural brightness of spectral lines on the basis of Dirac's theory". In: *Z. Phys.* 63 (1930), pp. 54–73. DOI: 10.1007/BF01336768.

[15] T. D. Lee, R. Oehme, and Chen-Ning Yang. "Remarks on Possible Noninvariance Under Time Reversal and Charge Conjugation". In: *Phys. Rev.* 106 (1957), pp. 340–345. DOI: 10.1103/PhysRev.106.340.

[16] Ulrich Nierste. "Three Lectures on Meson Mixing and CKM phenomenology". In: *Helmholz International Summer School on Heavy Quark Physics*. Mar. 2009, pp. 1–38. arXiv: 0904.1869 [hep-ph].

[17] Ulrich Nierste. "Meson-antimeson mixing". In: (Oct. 2025). arXiv: 2510.11716 [hep-ph].

[18] Marina Artuso, Guennadi Borissov, and Alexander Lenz. "CP violation in the B_s^0 system". In: *Rev. Mod. Phys.* 88.4 (2016). [Addendum: Rev.Mod.Phys. 91, 049901 (2019)], p. 045002. DOI: 10.1103/RevModPhys.88.045002. arXiv: 1511.09466 [hep-ph].

[19] Ulrich Nierste. "CP asymmetry in flavor-specific B decays". In: *39th Rencontres de Moriond on Electroweak Interactions and Unified Theories*. June 2004, pp. 445–450. arXiv: hep-ph/0406300.

[20] Marvin Gerlach, Ulrich Nierste, Pascal Reeck, Vladyslav Shtabovenko, and Matthias Steinhauser. "Current-current operator contribution to the decay matrix in B-meson mixing at next-to-next-to-leading order of QCD". In: *JHEP* 10 (2025), p. 162. DOI: 10.1007/JHEP10(2025)162. arXiv: 2505.22740 [hep-ph].

[21] Nicola Cabibbo. "Unitary Symmetry and Leptonic Decays". In: *Phys. Rev. Lett.* 10 (1963), pp. 531–533. DOI: 10.1103/PhysRevLett.10.531.

[22] Makoto Kobayashi and Toshihide Maskawa. "CP Violation in the Renormalizable Theory of Weak Interaction". In: *Prog. Theor. Phys.* 49 (1973), pp. 652–657. DOI: 10.1143/PTP.49.652.

[23] R. E. Cutkosky. "Singularities and discontinuities of Feynman amplitudes". In: *J. Math. Phys.* 1 (1960), pp. 429–433. DOI: 10.1063/1.1703676.

[24] S. L. Glashow, J. Iliopoulos, and L. Maiani. "Weak Interactions with Lepton-Hadron Symmetry". In: *Phys. Rev. D* 2 (1970), pp. 1285–1292. DOI: 10.1103/PhysRevD.2.1285.

[25] R. Aaij et al. "Precise determination of the B_s^0–$\overline{B}_s^0$ oscillation frequency". In: *Nature Phys.* 18.1 (2022), pp. 1–5. DOI: 10.1038/s41567-021-01394-x. arXiv: 2104.04421 [hep-ex].

[26] Swagato Banerjee et al. "Averages of b-hadron, c-hadron, and τ-lepton properties as of 2023". In: (Nov. 2024). arXiv: 2411.18639 [hep-ex].

[27] Johannes Albrecht, Florian Bernlochner, Alexander Lenz, and Aleksey Rusov. "Lifetimes of b-hadrons and mixing of neutral B-mesons: theoretical and experimental status". In: *Eur. Phys. J. ST* 233.2 (2024), pp. 359–390. DOI: 10.1140/epjs/s11734-024-01124-3. arXiv: 2402.04224 [hep-ph].

[28] Marvin Gerlach, Ulrich Nierste, Vladyslav Shtabovenko, and Matthias Steinhauser. "Width Difference in the $B-\bar{B}$ System at Next-to-Next-to-Leading Order of QCD". In: *Phys. Rev. Lett.* 129.10 (2022), p. 102001. DOI: 10.1103/PhysRevLett.129.102001. arXiv: 2205.07907 [hep-ph].

[29] Marvin Gerlach. "Meson width differences and asymmetries - Calculations of higher order contributions to neutral B-meson mixing". PhD thesis. Karlsruher Institut für Technologie (KIT), 2022. 163 pp. DOI: 10.5445/IR/1000146636.

[30] Yasmine Sara Amhis et al. "Averages of b-hadron, c-hadron, and τ-lepton properties as of 2021". In: *Phys. Rev. D* 107.5 (2023), p. 052008. DOI: 10.1103/PhysRevD.107.052008. arXiv: 2206.07501 [hep-ex].

[31] Gonzalo Alonso-Álvarez, Gilly Elor, and Miguel Escudero. "Collider signals of baryogenesis and dark matter from B mesons: A roadmap to discovery". In: *Phys. Rev. D* 104.3 (2021), p. 035028. DOI: 10.1103/PhysRevD.104.035028. arXiv: 2101.02706 [hep-ph].

[32] Alexander Lenz, Maria Laura Piscopo, and Aleksey V. Rusov. "Disintegration of beauty: a precision study". In: *JHEP* 01 (2023), p. 004. DOI: 10.1007/JHEP01(2023)004. arXiv: 2208.02643 [hep-ph].

[33] James Gratrex et al. "Quark-hadron duality at work: lifetimes of bottom baryons". In: *JHEP* 04 (2023), p. 034. DOI: 10.1007/JHEP04(2023)034. arXiv: 2301.07698 [hep-ph].

[34] Alexander Lenz and Ulrich Nierste. "Theoretical update of $B_s-\bar{B}_s$ mixing". In: *JHEP* 06 (2007), p. 072. DOI: 10.1088/1126-6708/2007/06/072. arXiv: hep-ph/0612167.

[35] J. Charles et al. "CP violation and the CKM matrix: Assessing the impact of the asymmetric B factories". In: *Eur. Phys. J. C* 41.1 (2005), pp. 1–131. DOI: 10.1140/epjc/s2005-02169-1. arXiv: hep-ph/0406184.

[36] Martin Beneke, Gerhard Buchalla, Alexander Lenz, and Ulrich Nierste. "CP Asymmetry in Flavor Specific B Decays beyond Leading Logarithms". In: *Phys. Lett. B* 576 (2003), pp. 173–183. DOI: 10.1016/j.physletb.2003.09.089. arXiv: hep-ph/0307344.

[37] Guido Altarelli, G. Martinelli, S. Petrarca, and F. Rapuano. "Failure of local duality in inclusive nonleptonic heavy flavor decays". In: *Phys. Lett. B* 382 (1996), pp. 409–414. DOI: 10.1016/0370-2693(96)00637-5. arXiv: hep-ph/9604202.

[38] Hai-Yang Cheng. "A Phenomenological analysis of heavy hadron lifetimes". In: *Phys. Rev. D* 56 (1997), pp. 2783–2798. DOI: 10.1103/PhysRevD.56.2783. arXiv: hep-ph/9704260.

[39] Toshiaki Ito, Masahisa Matsuda, and Yoshimitsu Matsui. "New possibility of solving the problem of lifetime ratio $\tau(\Lambda_b)/\tau(B_d)$". In: *Prog. Theor. Phys.* 99 (1998), pp. 271–280. DOI: 10.1143/PTP.99.271. arXiv: hep-ph/9705402.

[40] R. J. Dowdall et al. "Neutral B-meson mixing from full lattice QCD at the physical point". In: *Phys. Rev. D* 100.9 (2019), p. 094508. DOI: 10.1103/PhysRevD.100.094508. arXiv: 1907.01025 [hep-lat].

[41] A. Bazavov et al. "B- and D-meson leptonic decay constants from four-flavor lattice QCD". In: *Phys. Rev. D* 98.7 (2018), p. 074512. DOI: 10.1103/PhysRevD.98.074512. arXiv: 1712.09262 [hep-lat].

[42] C. Hughes, C. T. H. Davies, and C. J. Monahan. "New methods for B meson decay constants and form factors from lattice NRQCD". In: *Phys. Rev. D* 97.5 (2018), p. 054509. DOI: 10.1103/PhysRevD.97.054509. arXiv: 1711.09981 [hep-lat].

[43] A. Bussone et al. "Mass of the b quark and B meson decay constants from N_f=2+1+1 twisted-mass lattice QCD". In: *Phys. Rev. D* 93.11 (2016), p. 114505. DOI: 10.1103/PhysRevD.93.114505. arXiv: 1603.04306 [hep-lat].

[44] R. J. Dowdall, C. T. H. Davies, R. R. Horgan, C. J. Monahan, and J. Shigemitsu. "B-Meson Decay Constants from Improved Lattice Nonrelativistic QCD with Physical u, d, s, and c Quarks". In: *Phys. Rev. Lett.* 110.22 (2013), p. 222003. DOI: 10.1103/PhysRevLett.110.222003. arXiv: 1302.2644 [hep-lat].

[45] M. Kirk, A. Lenz, and T. Rauh. "Dimension-six matrix elements for meson mixing and lifetimes from sum rules". In: *JHEP* 12 (2017). [Erratum: JHEP 06, 162 (2020)], p. 068. DOI: 10.1007/JHEP12(2017)068. arXiv: 1711.02100 [hep-ph].

[46] Luca Di Luzio, Matthew Kirk, Alexander Lenz, and Thomas Rauh. "ΔM_s theory precision confronts flavour anomalies". In: *JHEP* 12 (2019), p. 009. DOI: 10.1007/JHEP12(2019)009. arXiv: 1909.11087 [hep-ph].

[47] M. Beneke, G. Buchalla, and I. Dunietz. "Width Difference in the $B_s - \bar{B}_s$ System". In: *Phys. Rev. D* 54 (1996). [Erratum: Phys.Rev.D 83, 119902 (2011)], pp. 4419–4431. DOI: 10.1103/PhysRevD.54.4419. arXiv: hep-ph/9605259.

[48] A. S. Dighe, T. Hurth, C. S. Kim, and T. Yoshikawa. "Measurement of the lifetime difference of B_d mesons: Possible and worthwhile?" In: *Nucl. Phys. B* 624 (2002), pp. 377–404. DOI: 10.1016/S0550-3213(01)00655-1. arXiv: hep-ph/0109088.

[49] M. Beneke, G. Buchalla, C. Greub, A. Lenz, and U. Nierste. "Next-to-leading order QCD corrections to the lifetime difference of B_s mesons". In: *Phys. Lett. B* 459 (1999), pp. 631–640. DOI: 10.1016/S0370-2693(99)00684-X. arXiv: hep-ph/9808385.

[50] M. Ciuchini, E. Franco, V. Lubicz, F. Mescia, and C. Tarantino. "Lifetime differences and CP violation parameters of neutral B mesons at the next-to-leading order in QCD". In: *JHEP* 08 (2003), p. 031. DOI: 10.1088/1126-6708/2003/08/031. arXiv: hep-ph/0308029.

[51] H. M. Asatrian, Artyom Hovhannisyan, Ulrich Nierste, and Arsen Yeghiazaryan. "Towards next-to-next-to-leading-log accuracy for the width difference in the B_s–$\bar{B}_s$ system: fermionic contributions to order $(m_c/m_b)^0$ and $(m_c/m_b)^1$". In: *JHEP* 10 (2017), p. 191. DOI: 10.1007/JHEP10(2017)191. arXiv: 1709.02160 [hep-ph].

[52] Hrachia M. Asatrian et al. "Penguin contribution to the width difference and *CP* asymmetry in B_q-$\bar{B}_q$ mixing at order $\alpha_s^2 N_f$". In: *Phys. Rev. D* 102.3 (2020), p. 033007. DOI: 10.1103/PhysRevD.102.033007. arXiv: 2006.13227 [hep-ph].

[53] Artyom Hovhannisyan and Ulrich Nierste. "Addendum to: Towards next-to-next-to-leading-log accuracy for the width difference in the B_s–$\overline{B}_s$ system: fermionic contributions to order $(m_c/m_b)^0$ and $(m_c/m_b)^1$". In: *JHEP* 06 (2022), p. 090. DOI: 10.1007/JHEP06(2022)090. arXiv: 2204.11907 [hep-ph].

[54] Marvin Gerlach, Ulrich Nierste, Vladyslav Shtabovenko, and Matthias Steinhauser. "The width difference in B–$\bar{B}$ mixing at order α_s and beyond". In: *JHEP* 04 (2022), p. 006. DOI: 10.1007/JHEP04(2022)006. arXiv: 2202.12305 [hep-ph].

[55] Andrzej J. Buras, Matthias Jamin, and Peter H. Weisz. "Leading and Next-to-leading QCD Corrections to ϵ Parameter and $B^0 - \bar{B}^0$ Mixing in the Presence of a Heavy Top Quark". In: *Nucl. Phys. B* 347 (1990), pp. 491–536. DOI: 10.1016/0550-3213(90)90373-L.

[56] Martin Lang, Alexander Lenz, Ali Mohamed, Maria Laura Piscopo, and Aleksey V. Rusov. "B-meson decay width up to $1/m_b^3$ corrections within and beyond the Standard Model". In: (Dec. 2025). arXiv: 2512.14635 [hep-ph].

[57] M. Neubert and Christopher T. Sachrajda. "Spectator effects in inclusive decays of beauty hadrons". In: *Nucl. Phys. B* 483 (1997), pp. 339–370. DOI: 10.1016/S0550-3213(96)00559-7. arXiv: hep-ph/9603202.

[58] Martin Beneke, Gerhard Buchalla, Christoph Greub, Alexander Lenz, and Ulrich Nierste. "The $B^+ - B_d^0$ Lifetime Difference Beyond Leading Logarithms". In: *Nucl. Phys. B* 639 (2002), pp. 389–407. DOI: 10.1016/S0550-3213(02)00561-8. arXiv: hep-ph/0202106.

[59] E. Franco, V. Lubicz, F. Mescia, and C. Tarantino. "Lifetime ratios of beauty hadrons at the next-to-leading order in QCD". In: *Nucl. Phys. B* 633 (2002), pp. 212–236. DOI: 10.1016/S0550-3213(02)00262-6. arXiv: hep-ph/0203089.

[60] Matthew Black, Martin Lang, Alexander Lenz, and Zachary Wüthrich. "HQET sum rules for matrix elements of dimension-six four-quark operators for meson lifetimes within and beyond the Standard Model". In: *JHEP* 04 (2025), p. 081. DOI: 10.1007/JHEP04(2025)081. arXiv: 2412.13270 [hep-ph].

[61] Manuel Egner, Matteo Fael, Kay Schönwald, and Matthias Steinhauser. "Non-leptonic B-meson decays to next-to-next-to-leading order". In: *JHEP* 10 (2024). [Erratum: JHEP 02, 147 (2025)], p. 144. DOI: 10.1007/JHEP10(2024)144. arXiv: 2406.19456 [hep-ph].

[62] Manuel Egner et al. "Total decay rates of B mesons at NNLO-QCD". In: *JHEP* 04 (2025), p. 106. DOI: 10.1007/JHEP04(2025)106. arXiv: 2412.14035 [hep-ph].

[63] Alexey A. Petrov and Andrew E. Blechman. *Effective Field Theories*. WSP, 2016. DOI: 10.1142/8619.

[64] Andrzej Buras. *Gauge Theory of Weak Decays*. Cambridge University Press, June 2020. DOI: 10.1017/9781139524100.

[65] Thomas Appelquist and J. Carazzone. "Infrared Singularities and Massive Fields". In: *Phys. Rev. D* 11 (1975), p. 2856. DOI: 10.1103/PhysRevD.11.2856.

[66] Kenneth G. Wilson. "Nonlagrangian models of current algebra". In: *Phys. Rev.* 179 (1969), pp. 1499–1512. DOI: 10.1103/PhysRev.179.1499.

[67] K. G. Wilson and W. Zimmermann. "Operator product expansions and composite field operators in the general framework of quantum field theory". In: *Commun. Math. Phys.* 24 (1972), pp. 87–106. DOI: 10.1007/BF01878448.

[68] Edward Witten. "Short Distance Analysis of Weak Interactions". In: *Nucl. Phys. B* 122 (1977), pp. 109–143. DOI: 10.1016/0550-3213(77)90428-X.

[69] Wolfhart Zimmermann. "Normal products and the short distance expansion in the perturbation theory of renormalizable interactions". In: *Annals Phys.* 77 (1973), pp. 570–601. DOI: 10.1016/0003-4916(73)90430-2.

[70] Enrico Fermi. "Tentativo di una teoria dell'emissione dei raggi beta". In: *Ric. Sci.* 4 (1933), pp. 491–495.

[71] E. Fermi. "An attempt of a theory of beta radiation. 1." In: *Z. Phys.* 88 (1934), pp. 161–177. DOI: 10.1007/BF01351864.

[72] Michael E. Peskin and Daniel V. Schroeder. *An Introduction to quantum field theory*. Reading, USA: Addison-Wesley, 1995. DOI: 10.1201/9780429503559.

[73] P. A. Baikov, K. G. Chetyrkin, and J. H. Kühn. "Quark Mass and Field Anomalous Dimensions to $\mathcal{O}(\alpha_s^5)$". In: *JHEP* 10 (2014), p. 076. DOI: 10.1007/JHEP10(2014)076. arXiv: 1402.6611 [hep-ph].

[74] Thomas Luthe, Andreas Maier, Peter Marquard, and York Schröder. "Five-loop quark mass and field anomalous dimensions for a general gauge group". In: *JHEP* 01 (2017), p. 081. DOI: 10.1007/JHEP01(2017)081. arXiv: 1612.05512 [hep-ph].

[75] P. A. Baikov, K. G. Chetyrkin, and J. H. Kühn. "Five-loop fermion anomalous dimension for a general gauge group from four-loop massless propagators". In: *JHEP* 04 (2017), p. 119. DOI: 10.1007/JHEP04(2017)119. arXiv: 1702.01458 [hep-ph].

[76] Thomas Luthe, Andreas Maier, Peter Marquard, and York Schroder. "Complete renormalization of QCD at five loops". In: *JHEP* 03 (2017), p. 020. DOI: 10.1007/JHEP03(2017)020. arXiv: 1701.07068 [hep-ph].

[77] K. G. Chetyrkin, G. Falcioni, F. Herzog, and J. A. M. Vermaseren. "Five-loop renormalisation of QCD in covariant gauges". In: *JHEP* 10 (2017). [Addendum:

JHEP 12, 006 (2017)], p. 179. DOI: 10.1007/JHEP10(2017)179. arXiv: 1709.08541 [hep-ph].

[78] Peter Marquard, Alexander V. Smirnov, Vladimir A. Smirnov, and Matthias Steinhauser. "Quark Mass Relations to Four-Loop Order in Perturbative QCD". In: *Phys. Rev. Lett.* 114.14 (2015), p. 142002. DOI: 10.1103/PhysRevLett.114.142002. arXiv: 1502.01030 [hep-ph].

[79] Matteo Fael, Kay Schönwald, and Matthias Steinhauser. "Exact results for Z_m^{OS} and Z_2^{OS} with two mass scales and up to three loops". In: *JHEP* 10 (2020), p. 087. DOI: 10.1007/JHEP10(2020)087. arXiv: 2008.01102 [hep-ph].

[80] M. Beneke. "A Quark mass definition adequate for threshold problems". In: *Phys. Lett. B* 434 (1998), pp. 115–125. DOI: 10.1016/S0370-2693(98)00741-2. arXiv: hep-ph/9804241.

[81] Alexander V. Smirnov, Vladimir A. Smirnov, and Matthias Steinhauser. "Three-loop static potential". In: *Phys. Rev. Lett.* 104 (2010), p. 112002. DOI: 10.1103/PhysRevLett.104.112002. arXiv: 0911.4742 [hep-ph].

[82] C. Anzai, Y. Kiyo, and Y. Sumino. "Static QCD potential at three-loop order". In: *Phys. Rev. Lett.* 104 (2010), p. 112003. DOI: 10.1103/PhysRevLett.104.112003. arXiv: 0911.4335 [hep-ph].

[83] Florian Herren and Matthias Steinhauser. "Version 3 of RunDec and CRunDec". In: *Comput. Phys. Commun.* 224 (2018), pp. 333–345. DOI: 10.1016/j.cpc.2017.11.014. arXiv: 1703.03751 [hep-ph].

[84] M. Beneke, A. Maier, J. Piclum, and T. Rauh. "The bottom-quark mass from non-relativistic sum rules at NNNLO". In: *Nucl. Phys. B* 891 (2015), pp. 42–72. DOI: 10.1016/j.nuclphysb.2014.12.001. arXiv: 1411.3132 [hep-ph].

[85] Andrzej J. Buras and Peter H. Weisz. "QCD Nonleading Corrections to Weak Decays in Dimensional Regularization and 't Hooft-Veltman Schemes". In: *Nucl. Phys. B* 333 (1990), pp. 66–99. DOI: 10.1016/0550-3213(90)90223-Z.

[86] J. S. R. Chisholm. "Relativistic scalar products of γ matrices". In: *Il Nuovo Cimento (1955-1965)* 30.1 (Oct. 1963), pp. 426–428. ISSN: 1827-6121. DOI: 10.1007/BF02750778.

[87] Stefan Herrlich and Ulrich Nierste. "Evanescent operators, scheme dependences and double insertions". In: *Nucl. Phys. B* 455 (1995), pp. 39–58. DOI: 10.1016/0550-3213(95)00474-7. arXiv: hep-ph/9412375.

[88] Michael J. Dugan and Benjamin Grinstein. "On the vanishing of evanescent operators". In: *Phys. Lett. B* 256 (1991), pp. 239–244. DOI: 10.1016/0370-2693(91)90680-O.

[89] Mikolaj Misiak and Jorg Urban. "QCD corrections to FCNC decays mediated by Z penguins and W boxes". In: *Phys. Lett. B* 451 (1999), pp. 161–169. DOI: 10.1016/S0370-2693(99)00150-1. arXiv: hep-ph/9901278.

[90] P. A. Baikov, K. G. Chetyrkin, and J. H. Kühn. "Five-Loop Running of the QCD coupling constant". In: *Phys. Rev. Lett.* 118.8 (2017), p. 082002. DOI: 10.1103/PhysRevLett.118.082002. arXiv: 1606.08659 [hep-ph].

[91] F. Herzog, B. Ruijl, T. Ueda, J. A. M. Vermaseren, and A. Vogt. "The five-loop beta function of Yang-Mills theory with fermions". In: *JHEP* 02 (2017), p. 090. DOI: 10.1007/JHEP02(2017)090. arXiv: 1701.01404 [hep-ph].

[92] Thomas Luthe, Andreas Maier, Peter Marquard, and York Schroder. "The five-loop Beta function for a general gauge group and anomalous dimensions beyond Feynman gauge". In: *JHEP* 10 (2017), p. 166. DOI: 10.1007/JHEP10(2017)166. arXiv: 1709.07718 [hep-ph].

[93] P. Breitenlohner and D. Maison. "Dimensionally Renormalized Green's Functions for Theories with Massless Particles. 1." In: *Commun. Math. Phys.* 52 (1977), p. 39. DOI: 10.1007/BF01609070.

[94] P. Breitenlohner and D. Maison. "Dimensionally Renormalized Green's Functions for Theories with Massless Particles. 2." In: *Commun. Math. Phys.* 52 (1977), p. 55. DOI: 10.1007/BF01609071.

[95] P. Breitenlohner and D. Maison. "Dimensional Renormalization and the Action Principle". In: *Commun. Math. Phys.* 52 (1977), pp. 11–38. DOI: 10.1007/BF01609069.

[96] Guy Bonneau. "Consistency in Dimensional Regularization With γ_5". In: *Phys. Lett. B* 96 (1980), pp. 147–150. DOI: 10.1016/0370-2693(80)90232-4.

[97] Guy Bonneau. "Preserving Canonical Ward Identities in Dimensional Regularization With a Nonanticommuting γ_5". In: *Nucl. Phys. B* 177 (1981), pp. 523–527. DOI: 10.1016/0550-3213(81)90185-1.

[98] Gerard 't Hooft and M. J. G. Veltman. "Regularization and Renormalization of Gauge Fields". In: *Nucl. Phys. B* 44 (1972), pp. 189–213. DOI: 10.1016/0550-3213(72)90279-9.

[99] Warren Siegel. "Supersymmetric Dimensional Regularization via Dimensional Reduction". In: *Phys. Lett. B* 84 (1979), pp. 193–196. DOI: 10.1016/0370-2693(79)90282-X.

[100] Gerhard Buchalla, Andrzej J. Buras, and Markus E. Lautenbacher. "Weak Decays beyond Leading Logarithms". In: *Rev. Mod. Phys.* 68 (1996), pp. 1125–1144. DOI: 10.1103/RevModPhys.68.1125. arXiv: hep-ph/9512380.

[101] Konstantin G. Chetyrkin, Mikolaj Misiak, and Manfred Munz. "$|\Delta F| = 1$ nonleptonic effective Hamiltonian in a simpler scheme". In: *Nucl. Phys. B* 520 (1998), pp. 279–297. DOI: 10.1016/S0550-3213(98)00131-X. arXiv: hep-ph/9711280.

[102] Christoph Bobeth, Mikolaj Misiak, and Jorg Urban. "Photonic penguins at two loops and m_t dependence of $BR[B \to X_s l^+ l^-]$". In: *Nucl. Phys. B* 574 (2000), pp. 291–330. DOI: 10.1016/S0550-3213(00)00007-9. arXiv: hep-ph/9910220.

[103] Martin Gorbahn and Ulrich Haisch. "Effective Hamiltonian for non-leptonic $|\Delta F| = 1$ decays at NNLO in QCD". In: *Nucl. Phys. B* 713 (2005), pp. 291–332. DOI: 10.1016/j.nuclphysb.2005.01.047. arXiv: hep-ph/0411071.

[104] Mikolaj Misiak and Matthias Steinhauser. "Three loop matching of the dipole operators for $b \to s\gamma$ and $b \to sg$". In: *Nucl. Phys. B* 683 (2004), pp. 277–305. DOI: 10.1016/j.nuclphysb.2004.02.006. arXiv: hep-ph/0401041.

[105] Martin Gorbahn, Ulrich Haisch, and Mikolaj Misiak. "Three-loop mixing of dipole operators". In: *Phys. Rev. Lett.* 95 (2005), p. 102004. DOI: 10.1103/PhysRevLett.95.102004. arXiv: hep-ph/0504194.

[106] Matthias Neubert. "Heavy quark symmetry". In: *Phys. Rept.* 245 (1994), pp. 259–396. DOI: 10.1016/0370-1573(94)90091-4. arXiv: hep-ph/9306320.

[107] Martin Gorbahn, Sebastian Jager, Ulrich Nierste, and Stephanie Trine. "The supersymmetric Higgs sector and $B - \bar{B}$ mixing for large tan β". In: *Phys. Rev. D* 84 (2011), p. 034030. DOI: 10.1103/PhysRevD.84.034030. arXiv: 0901.2065 [hep-ph].

[108] Robert V. Harlander and Fabian Lange. "Effective electroweak Hamiltonian in the gradient-flow formalism". In: *Phys. Rev. D* 105.7 (2022), p. L071504. DOI: 10.1103/PhysRevD.105.L071504. arXiv: 2201.08618 [hep-lat].

[109] Matthew Black et al. "Using Gradient Flow to Renormalise Matrix Elements for Meson Mixing and Lifetimes". In: *PoS* LATTICE2023 (2024), p. 263. DOI: 10.22323/1.453.0263. arXiv: 2310.18059 [hep-lat].

[110] Matthew Black et al. "Gradient Flow Renormalisation for Meson Mixing and Lifetimes". In: *PoS* LATTICE2024 (2025), p. 243. DOI: 10.22323/1.466.0243. arXiv: 2409.18891 [hep-lat].

[111] Daniel King, Alexander Lenz, and Thomas Rauh. "SU(3) breaking effects in B and D meson lifetimes". In: *JHEP* 06 (2022), p. 134. DOI: 10.1007/JHEP06(2022)134. arXiv: 2112.03691 [hep-ph].

[112] Daniel James King. "Three loop corrections to HQET Sum Rules for the Bag Parameter". PhD thesis. Durham U., 2022.

[113] Pascal Reeck, Vladyslav Shtabovenko, and Matthias Steinhauser. "B meson mixing at NNLO: technical aspects". In: *JHEP* 08 (2024), p. 002. DOI: 10.1007/JHEP08(2024)002. arXiv: 2405.14698 [hep-ph].

[114] Paulo Nogueira. "Automatic Feynman Graph Generation". In: *J. Comput. Phys.* 105 (1993), pp. 279–289. DOI: 10.1006/jcph.1993.1074.

[115] Marvin Gerlach, Florian Herren, and Martin Lang. "tapir: A tool for topologies, amplitudes, partial fraction decomposition and input for reductions". In: *Comput. Phys. Commun.* 282 (2023), p. 108544. DOI: 10.1016/j.cpc.2022.108544. arXiv: 2201.05618 [hep-ph].

[116] J. A. M. Vermaseren. "New features of FORM". In: (Oct. 2000). arXiv: math-ph/0010025.

[117] M. Tentyukov and J. A. M. Vermaseren. "The Multithreaded version of FORM". In: *Comput. Phys. Commun.* 181 (2010), pp. 1419–1427. DOI: 10.1016/j.cpc.2010.04.009. arXiv: hep-ph/0702279.

[118] J. Kuipers, T. Ueda, J. A. M. Vermaseren, and J. Vollinga. "FORM version 4.0". In: *Comput. Phys. Commun.* 184 (2013), pp. 1453–1467. DOI: 10.1016/j.cpc.2012.12.028. arXiv: 1203.6543 [cs.SC].

[119] Ben Ruijl, Takahiro Ueda, and Jos Vermaseren. "FORM version 4.2". In: (July 2017). arXiv: 1707.06453 [hep-ph].

[120] R. Harlander, T. Seidensticker, and M. Steinhauser. "Complete corrections of $\mathcal{O}(\alpha\alpha_s)$ to the decay of the Z boson into bottom quarks". In: *Phys. Lett. B* 426 (1998), pp. 125–132. DOI: 10.1016/S0370-2693(98)00220-2. arXiv: hep-ph/9712228.

[121] T. Seidensticker. "Automatic application of successive asymptotic expansions of Feynman diagrams". In: *6th International Workshop on New Computing Techniques in Physics Research: Software Engineering, Artificial Intelligence Neural Nets, Genetic Algorithms, Symbolic Algebra, Automatic Calculation*. May 1999. arXiv: hep-ph/9905298.

[122] T. van Ritbergen, A. N. Schellekens, and J. A. M. Vermaseren. "Group theory factors for Feynman diagrams". In: *Int. J. Mod. Phys. A* 14 (1999), pp. 41–96. DOI: 10.1142/S0217751X99000038. arXiv: hep-ph/9802376.

[123] F. V. Tkachov. "A Theorem on Analytical Calculability of Four Loop Renormalization Group Functions". In: *Phys. Lett. B* 100 (1981), pp. 65–68. DOI: 10.1016/0370-2693(81)90288-4.

[124] K. G. Chetyrkin and F. V. Tkachov. "Integration by Parts: The Algorithm to Calculate beta Functions in 4 Loops". In: *Nucl. Phys. B* 192 (1981), pp. 159–204. DOI: 10.1016/0550-3213(81)90199-1.

[125] T. Gehrmann and E. Remiddi. "Differential equations for two-loop four-point functions". In: *Nucl. Phys. B* 580 (2000), pp. 485–518. DOI: 10.1016/S0550-3213(00)00223-6. arXiv: hep-ph/9912329.

[126] Philipp Maierhöfer, Johann Usovitsch, and Peter Uwer. "Kira—A Feynman integral reduction program". In: *Comput. Phys. Commun.* 230 (2018), pp. 99–112. DOI: 10.1016/j.cpc.2018.04.012. arXiv: 1705.05610 [hep-ph].

[127] Jonas Klappert, Fabian Lange, Philipp Maierhöfer, and Johann Usovitsch. "Integral reduction with Kira 2.0 and finite field methods". In: *Comput. Phys. Commun.* 266 (2021), p. 108024. DOI: 10.1016/j.cpc.2021.108024. arXiv: 2008.06494 [hep-ph].

[128] Fabian Lange, Johann Usovitsch, and Zihao Wu. "Kira 3: integral reduction with efficient seeding and optimized equation selection". In: (May 2025). arXiv: 2505.20197 [hep-ph].

[129] R. H. Lewis. *Computer Algebra System Fermat*. https://home.bway.net/lewis.

[130] Jonas Klappert and Fabian Lange. "Reconstructing rational functions with FireFly". In: *Comput. Phys. Commun.* 247 (2020), p. 106951. DOI: 10.1016/j.cpc.2019.106951. arXiv: 1904.00009 [cs.SC].

[131] Jonas Klappert, Sven Yannick Klein, and Fabian Lange. "Interpolation of dense and sparse rational functions and other improvements in FireFly". In: *Comput. Phys. Commun.* 264 (2021), p. 107968. DOI: 10.1016/j.cpc.2021.107968. arXiv: 2004.01463 [cs.MS].

[132] A. V. Smirnov and V. A. Smirnov. "How to choose master integrals". In: *Nucl. Phys. B* 960 (2020), p. 115213. DOI: 10.1016/j.nuclphysb.2020.115213. arXiv: 2002.08042 [hep-ph].

[133] Matteo Fael, Fabian Lange, Kay Schönwald, and Matthias Steinhauser. "A semi-analytic method to compute Feynman integrals applied to four-loop corrections to the $\overline{\text{MS}}$-pole quark mass relation". In: *JHEP* 09 (2021), p. 152. DOI: 10.1007/JHEP09(2021)152. arXiv: 2106.05296 [hep-ph].

[134] Matteo Fael, Fabian Lange, Kay Schönwald, and Matthias Steinhauser. "Massive Vector Form Factors to Three Loops". In: *Phys. Rev. Lett.* 128.17 (2022), p. 172003. DOI: 10.1103/PhysRevLett.128.172003. arXiv: 2202.05276 [hep-ph].

[135] Matteo Fael, Fabian Lange, Kay Schönwald, and Matthias Steinhauser. "Singlet and nonsinglet three-loop massive form factors". In: *Phys. Rev. D* 106.3 (2022), p. 034029. DOI: 10.1103/PhysRevD.106.034029. arXiv: 2207.00027 [hep-ph].

[136] Matteo Fael, Fabian Lange, Kay Schönwald, and Matthias Steinhauser. "Massive three-loop form factors: Anomaly contribution". In: *Phys. Rev. D* 107.9 (2023), p. 094017. DOI: 10.1103/PhysRevD.107.094017. arXiv: 2302.00693 [hep-ph].

[137] Xiao Liu and Yan-Qing Ma. "AMFlow: A Mathematica package for Feynman integrals computation via auxiliary mass flow". In: *Comput. Phys. Commun.* 283 (2023), p. 108565. DOI: 10.1016/j.cpc.2022.108565. arXiv: 2201.11669 [hep-ph].

[138] Inc. Wolfram Research. *Mathematica, Version 14.3*. Champaign, IL, 2025. URL: https://www.wolfram.com/mathematica.

[139] Matthias Steinhauser. "MATAD: A Program package for the computation of MAssive TADpoles". In: *Comput. Phys. Commun.* 134 (2001), pp. 335–364. DOI: 10.1016/S0010-4655(00)00204-6. arXiv: hep-ph/0009029.

[140] Marvin Gerlach, Ulrich Nierste, Vladyslav Shtabovenko, and Matthias Steinhauser. "Two-loop QCD penguin contribution to the width difference in B_s–$\overline{B}_s$ mixing". In: *JHEP* 07 (2021), p. 043. DOI: 10.1007/JHEP07(2021)043. arXiv: 2106.05979 [hep-ph].

[141] M. Beneke and Vladimir A. Smirnov. "Asymptotic expansion of Feynman integrals near threshold". In: *Nucl. Phys. B* 522 (1998), pp. 321–344. DOI: 10.1016/S0550-3213(98)00138-2. arXiv: hep-ph/9711391.

[142] Vladimir A. Smirnov. *Analytic tools for Feynman integrals*. Vol. 250. 2012. DOI: 10.1007/978-3-642-34886-0.

[143] V. A. Smirnov. *Feynman integral calculus*. Berlin, Heidelberg: Springer, 2006.

[144] Tiziano Peraro and Lorenzo Tancredi. "Tensor decomposition for bosonic and fermionic scattering amplitudes". In: *Phys. Rev. D* 103.5 (2021), p. 054042. DOI: 10.1103/PhysRevD.103.054042. arXiv: 2012.00820 [hep-ph].

[145] Lorenzo Tancredi. "Tensor decomposition for multiloop, multileg helicity amplitudes". In: *PoS* LL2022 (2022), p. 020. DOI: 10.22323/1.416.0020.

[146] Oliver Schnetz. "Notes on color reductions and γ traces". In: (Apr. 2025). arXiv: 2504.05853 [hep-ph].

[147] A. N. Vasiliev, Sergey E. Derkachov, and N. A. Kivel. "A Technique for calculating the gamma matrix structures of the diagrams of a total four fermion interaction with infinite number of vertices in $d = (2 + \epsilon)$-dimensional regularization". In: *Theor. Math. Phys.* 103 (1995), pp. 487–495. DOI: 10.1007/BF02274026.

[148] J. Fleischer and M. Yu. Kalmykov. "ON-SHELL2: FORM based package for the calculation of two loop selfenergy single scale Feynman diagrams occurring in the standard model". In: *Comput. Phys. Commun.* 128 (2000), pp. 531–549. DOI: 10.1016/S0010-4655(99)00532-9. arXiv: hep-ph/9907431.

[149] Johannes M. Henn. "Multiloop integrals in dimensional regularization made simple". In: *Phys. Rev. Lett.* 110 (2013), p. 251601. DOI: 10.1103/PhysRevLett.110.251601. arXiv: 1304.1806 [hep-th].

[150] Roman N. Lee. "Reducing differential equations for multiloop master integrals". In: *JHEP* 04 (2015), p. 108. DOI: 10.1007/JHEP04(2015)108. arXiv: 1411.0911 [hep-ph].

[151] Christoph Meyer. "Transforming differential equations of multi-loop Feynman integrals into canonical form". In: *JHEP* 04 (2017), p. 006. DOI: 10.1007/JHEP04(2017)006. arXiv: 1611.01087 [hep-ph].

[152] Andrei I. Davydychev and Vladimir A. Smirnov. "Threshold expansion of the sunset diagram". In: *Nucl. Phys. B* 554 (1999), pp. 391–414. DOI: 10.1016/S0550-3213(99)00269-2. arXiv: hep-ph/9903328.

[153] Kirill Melnikov. Private communication. 2023.

[154] Manuel Egner, Matteo Fael, Kay Schönwald, and Matthias Steinhauser. "Revisiting semileptonic B meson decays at next-to-next-to-leading order". In: *JHEP* 09 (2023), p. 112. DOI: 10.1007/JHEP09(2023)112. arXiv: 2308.01346 [hep-ph].

[155] Ulrich Nierste, Pascal Reeck, Vladyslav Shtabovenko, and Matthias Steinhauser. "Complete next-to-next-to-leading order QCD corrections to the decay matrix in B-meson mixing at leading power". In: (Dec. 2025). arXiv: 2512.07949 [hep-ph].

[156] Andrzej J. Buras, Matthias Jamin, M. E. Lautenbacher, and Peter H. Weisz. "Effective Hamiltonians for $\Delta S = 1$ and $\Delta B = 1$ nonleptonic decays beyond the leading logarithmic approximation". In: *Nucl. Phys. B* 370 (1992). [Addendum:

Nucl.Phys.B 375, 501 (1992)], pp. 69–104. DOI: 10.1016/0550-3213(92)90345-C.

[157] Andrzej J. Buras, Matthias Jamin, Markus E. Lautenbacher, and Peter H. Weisz. "Two loop anomalous dimension matrix for $\Delta S = 1$ weak nonleptonic decays I: $\mathcal{O}(\alpha_s^2)$". In: *Nucl. Phys. B* 400 (1993), pp. 37–74. DOI: 10.1016/0550-3213(93)90397-8. arXiv: hep-ph/9211304.

[158] Paolo Gambino, Martin Gorbahn, and Ulrich Haisch. "Anomalous dimension matrix for radiative and rare semileptonic B decays up to three loops". In: *Nucl. Phys. B* 673 (2003), pp. 238–262. DOI: 10.1016/j.nuclphysb.2003.09.024. arXiv: hep-ph/0306079.

[159] Marco Ciuchini, E. Franco, V. Lubicz, and F. Mescia. "Next-to-leading order QCD corrections to spectator effects in lifetimes of beauty hadrons". In: *Nucl. Phys. B* 625 (2002), pp. 211–238. DOI: 10.1016/S0550-3213(02)00006-8. arXiv: hep-ph/0110375.

[160] Marvin Gerlach. "Meson width differences and asymmetries - Calculations of higher order contributions to neutral B-meson mixing". PhD thesis. KIT, Karlsruhe, EKP, 2022.

[161] T. Inami and C. S. Lim. "Effects of Superheavy Quarks and Leptons in Low-Energy Weak Processes $K_L \to \mu\bar{\mu}$, $K^+ \to \pi^+\nu\bar{\nu}$ and $K^0 \leftrightarrow \bar{K}^0$". In: *Prog. Theor. Phys.* 65 (1981). [Erratum: Prog.Theor.Phys. 65, 1772 (1981)], p. 297. DOI: 10.1143/PTP.65.297.

[162] S. Navas et al. "Review of particle physics". In: *Phys. Rev. D* 110.3 (2024), p. 030001. DOI: 10.1103/PhysRevD.110.030001.

[163] K. Chetyrkin et al. "Precise Charm- and Bottom-Quark Masses: Theoretical and Experimental Uncertainties". In: *Theor. Math. Phys.* 170 (2012), pp. 217–228. DOI: 10.1007/s11232-012-0024-7. arXiv: 1010.6157 [hep-ph].

[164] Konstantin G. Chetyrkin et al. "Addendum to "Charm and bottom quark masses: An update"". In: (Oct. 2017). [Addendum: Phys.Rev.D 96, 116007 (2017)]. DOI: 10.1103/PhysRevD.96.116007. arXiv: 1710.04249 [hep-ph].

[165] Christine T. H. Davies et al. "Lattice QCD matrix elements for the $B_s^0 - \bar{B}_s^0$ width difference beyond leading order". In: *Phys. Rev. Lett.* 124.8 (2020), p. 082001. DOI: 10.1103/PhysRevLett.124.082001. arXiv: 1910.00970 [hep-lat].

[166] CKMfitter Group (J. Charles et al.) "Updated results and plots available at: http://ckmfitter.in2p3.fr". In: *Eur. Phys. J* C41 (2005), pp. 1–131. arXiv: hep-ph/0406184.

[167] Y. Aoki et al. "FLAG Review 2024". In: (Nov. 2024). arXiv: 2411.04268 [hep-lat].

[168] Marzia Bordone, Bernat Capdevila, and Paolo Gambino. "Three loop calculations and inclusive Vcb". In: *Phys. Lett. B* 822 (2021), p. 136679. DOI: 10.1016/j.physletb.2021.136679. arXiv: 2107.00604 [hep-ph].

[169] Jon A. Bailey et al. "B→D$\ell\nu$ form factors at nonzero recoil and $|V_{cb}|$ from 2+1-flavor lattice QCD". In: *Phys. Rev. D* 92.3 (2015), p. 034506. DOI: 10.1103/PhysRevD.92.034506. arXiv: 1503.07237 [hep-lat].

[170] Heechang Na, Chris M. Bouchard, G. Peter Lepage, Chris Monahan, and Junko Shigemitsu. "$B \to Dl\nu$ form factors at nonzero recoil and extraction of $|V_{cb}|$". In: *Phys. Rev. D* 92.5 (2015). [Erratum: Phys.Rev.D 93, 119906 (2016)], p. 054510. DOI: 10.1103/PhysRevD.93.119906. arXiv: 1505.03925 [hep-lat].

[171] A. Bazavov et al. "Semileptonic form factors for $B \to D^*\ell\nu$ at nonzero recoil from $2+1$-flavor lattice QCD: Fermilab Lattice and MILC Collaborations". In: *Eur. Phys. J. C* 82.12 (2022). [Erratum: Eur.Phys.J.C 83, 21 (2023)], p. 1141. DOI: 10.1140/epjc/s10052-022-10984-9. arXiv: 2105.14019 [hep-lat].

[172] Y. Aoki et al. "$B \to D^*\ell\nu_\ell$ semileptonic form factors from lattice QCD with Möbius domain-wall quarks". In: *Phys. Rev. D* 109.7 (2024), p. 074503. DOI: 10.1103/PhysRevD.109.074503. arXiv: 2306.05657 [hep-lat].

[173] Bernard Aubert et al. "Measurement of $|V_{cb}|$ and the Form-Factor Slope in $\bar{B} \to D\ell^-\bar{\nu}_\ell$ Decays in Events Tagged by a Fully Reconstructed B Meson". In: *Phys. Rev. Lett.* 104 (2010), p. 011802. DOI: 10.1103/PhysRevLett.104.011802. arXiv: 0904.4063 [hep-ex].

[174] R. Glattauer et al. "Measurement of the decay $B \to D\ell\nu_\ell$ in fully reconstructed events and determination of the Cabibbo-Kobayashi-Maskawa matrix element $|V_{cb}|$". In: *Phys. Rev. D* 93.3 (2016), p. 032006. DOI: 10.1103/PhysRevD.93.032006. arXiv: 1510.03657 [hep-ex].

[175] E. Waheed et al. "Measurement of the CKM matrix element $|V_{cb}|$ from $B^0 \to D^{*-}\ell^+\nu_\ell$ at Belle". In: *Phys. Rev. D* 100.5 (2019). [Erratum: Phys.Rev.D 103, 079901 (2021)], p. 052007. DOI: 10.1103/PhysRevD.100.052007. arXiv: 1809.03290 [hep-ex].

[176] M. T. Prim et al. "Measurement of differential distributions of $B \to D^*\ell\bar{\nu}_\ell$ and implications on $|V_{cb}|$". In: *Phys. Rev. D* 108.1 (2023), p. 012002. DOI: 10.1103/PhysRevD.108.012002. arXiv: 2301.07529 [hep-ex].

[177] I. Adachi et al. "Determination of $|V_{cb}|$ using $\bar{B}^0 \to D^{*+}\ell^-\bar{\nu}_\ell$ decays with Belle II". In: *Phys. Rev. D* 108.9 (2023), p. 092013. DOI: 10.1103/PhysRevD.108.092013. arXiv: 2310.01170 [hep-ex].

[178] Florian Bernlochner et al. "First extraction of inclusive V_{cb} from q^2 moments". In: *JHEP* 10 (2022), p. 068. DOI: 10.1007/JHEP10(2022)068. arXiv: 2205.10274 [hep-ph].

[179] Alexander Lenz and Gilberto Tetlalmatzi-Xolocotzi. "Model-independent bounds on new physics effects in non-leptonic tree-level decays of B-mesons". In: *JHEP* 07 (2020), p. 177. DOI: 10.1007/JHEP07(2020)177. arXiv: 1912.07621 [hep-ph].

[180] Lincoln Wolfenstein. "Parametrization of the Kobayashi-Maskawa Matrix". In: *Phys. Rev. Lett.* 51 (1983), p. 1945. DOI: 10.1103/PhysRevLett.51.1945.

[181] Andrzej J. Buras, Markus E. Lautenbacher, and Gaby Ostermaier. "Waiting for the top quark mass, $K^+ \to \pi^+ \nu\bar{\nu}$, $B_s^0 - \bar{B}_s^0$ mixing and CP asymmetries in B decays". In: *Phys. Rev. D* 50 (1994), pp. 3433–3446. DOI: 10.1103/PhysRevD.50.3433. arXiv: hep-ph/9403384.

[182] Sandrine Laplace, Zoltan Ligeti, Yosef Nir, and Gilad Perez. "Implications of the CP asymmetry in semileptonic B decay". In: *Phys. Rev. D* 65 (2002), p. 094040. DOI: 10.1103/PhysRevD.65.094040. arXiv: hep-ph/0202010.

[183] M. Lang, U. Nierste, and P. Reeck. (In preparation).

[184] Carlos Miró, Miguel Escudero, and Miguel Nebot. "How large could the CP violation in neutral B-meson mixing be? Implications for baryogenesis and upcoming searches". In: *Phys. Rev. D* 110.11 (2024), p. 115033. DOI: 10.1103/PhysRevD.110.115033. arXiv: 2410.13936 [hep-ph].

[185] Chung Kao, David Atwood, and Amarjit Soni. "Parity violation in bottom quark pair production at polarized hadron colliders". In: *Phys. Lett. B* 395 (1997), pp. 327–333. DOI: 10.1016/S0370-2693(97)00082-8. arXiv: hep-ph/9608383.

[186] H. Simma. "Equations of motion for effective Lagrangians and penguins in rare B decays". In: *Z. Phys. C* 61 (1994), pp. 67–82. DOI: 10.1007/BF01641888. arXiv: hep-ph/9307274.

[187] Andrzej J. Buras, Mikolaj Misiak, and Jorg Urban. "Two loop QCD anomalous dimensions of flavor changing four quark operators within and beyond the standard model". In: *Nucl. Phys. B* 586 (2000), pp. 397–426. DOI: 10.1016/S0550-3213(00)00437-5. arXiv: hep-ph/0005183.

[188] Frederick J. Gilman and Mark B. Wise. "Effective Hamiltonian for $\Delta S = 1$ Weak Nonleptonic Decays in the Six Quark Model". In: *Phys. Rev. D* 20 (1979), p. 2392. DOI: 10.1103/PhysRevD.20.2392.

[189] Stefan Herrlich and Ulrich Nierste. "The Complete $|\Delta S| = 2$ Hamiltonian in the next-to-leading order". In: *Nucl. Phys. B* 476 (1996), pp. 27–88. DOI: 10.1016/0550-3213(96)00324-0. arXiv: hep-ph/9604330.

[190] Yong-Yeon Keum and Ulrich Nierste. "Probing penguin coefficients with the lifetime ratio $\tau(B_s)/\tau(B_d)$". In: *Phys. Rev. D* 57 (1998), pp. 4282–4289. DOI: 10.1103/PhysRevD.57.4282. arXiv: hep-ph/9710512.

[191] Georges Aad et al. "Search for new phenomena in events with an energetic jet and missing transverse momentum in pp collisions at $\sqrt{s}$ =13 TeV with the ATLAS detector". In: *Phys. Rev. D* 103.11 (2021), p. 112006. DOI: 10.1103/PhysRevD.103.112006. arXiv: 2102.10874 [hep-ex].

[192] F. Moretti, U. Nierste, P. Reeck, and M. Steinhauser. (In preparation).

[193] Massimo Di Pierro, Christopher T Sachrajda, and Christopher Michael. "An Exploratory lattice study of spectator effects in inclusive decays of the Λ_b baryon". In: *Phys. Lett. B* 468 (1999). [Erratum: Phys.Lett.B 525, 360–360 (2002)], p. 143. DOI: 10.1016/S0370-2693(99)01166-1. arXiv: hep-lat/9906031.

[194] E. C. Poggio, Helen R. Quinn, and Steven Weinberg. "Smearing the Quark Model". In: *Phys. Rev. D* 13 (1976), p. 1958. DOI: 10.1103/PhysRevD.13.1958.

[195] Mikhail A. Shifman. "Quark hadron duality". In: *8th International Symposium on Heavy Flavor Physics*. Vol. 3. Singapore: World Scientific, July 2000, pp. 1447–1494. DOI: 10.1142/9789812810458_0032. arXiv: hep-ph/0009131.

[196] Ikaros I. Y. Bigi and Nikolai Uraltsev. "A Vademecum on quark hadron duality". In: *Int. J. Mod. Phys. A* 16 (2001), pp. 5201–5248. DOI: 10.1142/S0217751X01005535. arXiv: hep-ph/0106346.

Acknowledgments

Completing a PhD thesis is a challenging endeavour, but I was lucky to have the support of many people along the way. First of all, I would like to thank my supervisor, Matthias Steinhauser, for putting his trust in me, presenting me with interesting physics problems, and always being there to answer all of my questions. I particularly enjoyed the close collaboration on the papers underlying the research presented in this thesis. I am also grateful for Ulrich Nierste who helped shape the direction of the research in relation to the field theoretic aspects and phenomenological applications.

I would like to thank my colleagues with whom I spent many hours discussing physics problems. When it came to anything related to B meson mixing, I was glad to be able to ask Vladyslav Shtabovenko for advice, who also patiently produced many cross-checks of my work. For the work done on the lifetime ratios, I want to thank Francesco Moretti for the fruitful collaboration, which lead to the completion of the project in record time. Last but not least I want to express my gratitude to Martin Lang for the collaboration on the BSM project as well as his invaluable advice when it came to field theories or coding.

One person whom I simply cannot thank enough for all of his support is Manuel Egner. It has been a lot of fun sharing an office together, and even the toughest days were filled with laughter in office 11/18. Manuel, you been one of the best friends I have ever had; thank you for the countless runs, dinners and pub crawls over the last couple of years!

During my time at KIT, I have made extensive use of the computing facilities, pressure testing them at times. Therefore, I would like to express my gratitude to all the IT admins over the years, whether it was for advice or for providing first aid to a cluster machine. Thank you Manuel Egner, Dominik Grau, Martin Lang, Fabian Lange and Jonas Matuszak!

This thesis has seen many iterations, and I am indebted to a number of people who have proofread parts of it: Manuel Egner, Martin Lang, Francesco Moretti, Ulrich Nierste, Vladyslav Shtabovenko, Matthias Steinhauser and Eike Stolze. I am incredibly grateful for all the feedback.

Finally, I want to thank my parents for supporting me throughout this journey not just during my PhD but ever since I decided to pursue my interest in physics. I would not have made it this far without you both.